

# Multiscale Study of a Conjugated Polymer as an Organic Sulfur Host Cathode for Lithium-sulfur Batteries

Inaugural-Dissertation  
to obtain the academic degree  
Doctor rerum naturalium (Dr. rer. nat.)

submitted to the Department of Biology, Chemistry, Pharmacy  
of Freie Universität Berlin

by

**Yannik Schütze**

**2024**

1<sup>nd</sup> reviewer: **Prof. Dr. Annika Bande**  
Leibniz Universität Hannover  
Institut für Anorganische Chemie  
Callinstr. 9, 30167 Hannover

and

Helmholtz-Zentrum Berlin für Materialien und Energie GmbH  
Theorie der Elektronendynamik und Spektroskopie  
Hahn-Meitner Platz 1, 14109 Berlin

2<sup>st</sup> reviewer: **Prof. Dr. Beate Paulus**  
Freie Universität Berlin  
Institute of Chemistry and Biochemistry  
Physical & Theoretical Chemistry  
Arnimallee 22, 14195 Berlin

date of defense: 03.06.2024

The research of this thesis was carried out under the direction of Prof. Dr. Annika Bande and Prof. Dr. Joachim Dzubiella at the Helmholtz-Zentrum Berlin für Materialien und Energie between November 2019 and February 2024.

# Declaration of Independence

I hereby declare that I alone am responsible for the content of my doctoral dissertation titled "Multiscale Study of a Conjugated Polymer as an Organic Sulfur Host Cathode for Lithium-sulfur Batteries" and that I have only used the sources or references cited in said dissertation. I confirm that I have not already submitted this dissertation as part of another doctoral procedure.

---

Yannik Schütze

Berlin, March 6, 2024



# *List of Publications*

- 1. Combined First-principles Statistical Mechanics Approach to Sulfur Structure in Organic Cathode Hosts for Polymer Based Lithium–sulfur (Li–S) Batteries**  
Schütze, Y.<sup>†</sup>; de Oliveira Silva, R.; Ning, J.; Rappich, J.; Lu, Y.; Ruiz, V. G.; Bande, A.; Dzubiella, J.  
*Phys. Chem. Chem. Phys.* **2021**, 23, 26709–26720
- 2. Constructing Binder- and Carbon Additive-Free Organosulfur Cathodes Based on Conducting Thiol-Polymers through Electropolymerization for Lithium-sulfur Batteries**  
Ning, J.<sup>†</sup>; Yu, H.<sup>†</sup>; Mei, S.; Schütze, Y.; Risse, S.; Kardjilov, N.; Hilger, A.; Manke, I.; Bande, A.; Ruiz, V. G.; Dzubiella, J.; Meng, H.; Lu, Y.  
*ChemSusChem* **2022**, 15, e202200434
- 3. How Regiochemistry Influences Aggregation Behavior and Charge Transport in Conjugated Organosulfur Polymer Cathodes for Lithium-sulfur Batteries**  
Schütze, Y.<sup>†</sup>; Gayen, D.; Palczynski, K.; de Oliveira Silva, R.; Lu, Y.; Tovar, M.; Partovi-Azar, P.; Bande, A.; Dzubiella, J.  
*ACS Nano* **2023**, 17, 8, 7889–7900
- 4. Solvation Structure of Conjugated Organosulfur Polymers for Lithium-sulfur Battery Cathodes**  
Gayen, D.<sup>†</sup>; Schütze, Y.; Groh, S.; Dzubiella, J.  
*ACS Appl. Polym. Mater.* **2023**, 5, 7, 4799–4810

---

First-authorship is labelled †.

# *Abstract*

Lithium-sulfur (Li-S) batteries have the potential to become one of the energy storage systems of the future due to their ability to store significantly more energy than current battery types today. Furthermore, sulfur is an abundant element that is cheap and environmentally friendly in its processing, making it an optimal material for sustainable energy systems. However, this type of battery also has some disadvantages, mainly related to the sulfur-containing cathode.

This dissertation comprises the results of three research projects that investigated the structural and electronic properties of a polymer-based cathode material. The individual studies employ a combination of different theoretical multiscale approaches, which are further compared and discussed with experimental measurements.

In the first project, the novel fabrication route for the polymer cathode, which combines the processes of electro-polymerization and vulcanization, is presented. The structural evolution of the material during the synthesis is theoretically rationalized, and experiments show that using this material helps to overcome the typical problems associated with Li-S batteries. The second project focuses on the structure of the vulcanized polymer representing the initial stage of a charged cathode. A combination of electronic structure theory and statistical mechanics is used to bridge between the microscopic description of the vulcanization of polymer and sulfur and the derivation of the macroscopic properties of the cathode. This study reveals that the electronic stability on a microscopic level most likely leads to a sulfur cross-linking of neighboring polymer chains, which is experimentally supported. Furthermore, we find that the extent of cross-linking on a macroscopic scale can be controlled by the amount of sulfur and the temperature during vulcanization.

The third project covers the interplay between the polymer's structural morphology and its electronic properties. Here, we focus on the influence of regiochemistry on the polymer's aggregation behavior and charge transport. A multiscale approach comprising classical molecular dynamic simulation, electronic band structure calculations, and statistical charge transport theory demonstrates the polymer's ability to form well-ordered crystalline phases, allowing fast charge transport. The comparison of experimental and simulated X-ray diffractograms confirms the presence of crystalline phases in the electro-polymerized polymer.

Overall, this thesis's findings help advance the understanding of a polymer material in the context of its application as a Li-S battery cathode. Furthermore, this work demonstrates the benefit of using multiscale approaches to investigate such a system's structural and electronic properties.

# *Zusammenfassung*

Lithium-Schwefel (Li-S) Batterien haben das Potenzial, eines der Energiespeichersysteme der Zukunft zu werden, da sie wesentlich mehr Energie speichern können als heutige Batterietypen. Darüber hinaus ist Schwefel ein reichlich vorhandenes Element, das in seiner Verarbeitung kostengünstig und umweltfreundlich ist, was es zu einem optimalen Material für nachhaltige Energiesysteme macht. Diese Art von Batterie hat jedoch auch einige Nachteile, die hauptsächlich mit der schwefelhaltigen Kathode zusammenhängen.

Diese Dissertation umfasst die Ergebnisse von drei Forschungsprojekten, die die strukturellen und elektronischen Eigenschaften eines polymerbasierten Kathodenmaterials untersucht haben. Die einzelnen Studien kombinieren verschiedene theoretische Multiskalenansätze, die mit experimentellen Messungen verglichen und diskutiert werden.

Im ersten Projekt wird ein neuartiges Herstellungsverfahren für die Polymerkathode vorgestellt, welches den Prozess der Elektropolymerisation und Vulkanisation miteinander kombiniert. Die strukturelle Entwicklung des Materials während der Synthese wird theoretisch begründet, und Experimente zeigen, dass die Verwendung dieses Materials dazu beiträgt, die typischen Probleme im Zusammenhang mit Li-S Batterien zu überwinden. Das zweite Projekt konzentriert sich auf die Struktur des vulkanisierten Polymers, welches den Anfangszustand einer geladenen Kathode darstellt. Eine Kombination aus Elektronenstrukturtheorie und statistischer Mechanik wird verwendet, um eine Brücke zwischen der mikroskopischen Beschreibung der Vulkanisierung von Polymer und Schwefel und der Ableitung von makroskopischen Kathodeneigenschaften zu schlagen. Diese Studie zeigt, dass die elektronische Stabilität auf mikroskopischer Ebene höchstwahrscheinlich zu einer Vernetzung von benachbarten Polymerketten durch Schwefel führt, was experimentell bestätigt wird. Darüber hinaus stellen wir fest, dass das Ausmaß der Vernetzung auf makroskopischer Ebene durch die Schwefelmenge und die Temperatur während der Vulkanisation gesteuert werden kann.

Das dritte Projekt befasst sich mit der Wechselwirkung zwischen der strukturellen Morphologie des Polymers und seinen elektronischen Eigenschaften. Hier konzentrieren wir uns auf den Einfluss der Regiochemie auf das Aggregationsverhalten und den Ladungstransport des Polymers. Ein Multiskalenansatz, der klassische molekulardynamische Simulationen, elektronische Bandstrukturberechnungen und statistische Ladungstransporttheorie umfasst, zeigt die Fähigkeit der Polymere, geordnete kristalline Phasen zu bilden, die einen schnellen Ladungstransport ermöglichen. Der Vergleich von experimentellen und simulierten Röntgendiffrak-

togrammen bestätigt das Vorhandensein von kristallinen Phasen in dem elektropolymerisierten Polymer.

Insgesamt tragen die Ergebnisse dieser Arbeit dazu bei, das Verständnis eines Polymermaterials im Zusammenhang mit seiner Anwendung als Li-S Batteriekathode zu verbessern. Darüber hinaus zeigt diese Arbeit den Nutzen der Verwendung von Multiskalenansätzen zur Untersuchung der strukturellen und elektronischen Eigenschaften eines solchen Systems.

# *Acknowledgements*

You rarely write a doctoral thesis alone, and although my name is on the title page, many people made it possible for me and contributed to the fact that this work came out in the end. I want to take this opportunity to thank these people. First, I thank my two supervisors, Annika Bande and Joachim Dzubiella. Due to their different expertise, I was practically forced to move between the disciplines and combine different approaches repeatedly. But when I look back now, I am very grateful to have had the opportunity to explore so many different areas. The overall purpose of a doctorate is to learn to think independently, and I am glad that Annika and Joe gave me the freedom and confidence to do so.

Although physically apart, I had the pleasure of working with wonderful colleagues who helped me with scientific topics at any time and were always there to talk to. Many of my colleagues at the Helmholtz-Zentrum Berlin and the University of Freiburg have become good friends with whom I have shared many great moments. In particular, I would like to thank Victor Ruiz and Karol Palczynski for their help in learning new scientific concepts and Diptesh Gayen and Sebastian Milster, who always made the visits to Freiburg something special.

I also had the opportunity to work with many people from different backgrounds, which helped me to look at problems from various perspectives. Here, I want to thank Ranielle de Oliveira Silva and Sunel de Kock for the countless discussions, which greatly broadened my knowledge.

Last but not least, I would like to thank my family, Steffi, Anuk, Leosch, and my friends for their constant support. Having these people around me whom I can rely on in difficult times always helped me find a balance between work and life.



# Contents

<b>List of Publications</b>	<b>i</b>
<b>Abstract</b>	<b>ii</b>
<b>Zusammenfassung</b>	<b>iii</b>
<b>Acknowledgements</b>	<b>v</b>
<b>Table of Contents</b>	<b>vi</b>
<b>1 Introduction</b>	<b>1</b>
1.1 Motivation . . . . .	1
1.2 Outline . . . . .	3
<b>2 Fundamentals</b>	<b>7</b>
2.1 Li-S Batteries . . . . .	7
2.2 Organic polymers as cathode materials . . . . .	10
2.3 Multiscale modeling and simulation . . . . .	14
2.3.1 Density functional theory . . . . .	15
2.3.2 Classical molecular dynamics . . . . .	22
2.3.3 Statistical mechanics . . . . .	27
2.4 Statistical binding model of a vulcanized polymer . . . . .	30
2.5 Charge transport in conjugated polymers . . . . .	32
2.5.1 Electronic band structure of conjugated systems . . . . .	33
2.5.2 Band-like transport regime . . . . .	39
<b>3 Results and Conclusions</b>	<b>47</b>
<b>A Publications</b>	<b>65</b>
A.1 Constructing Binder- and Carbon Additive-Free Organosulfur Cathodes Based on Conducting Thiol-Polymers through Electropolymerization for Lithium-sulfur Batteries . . . . .	65
A.2 Combined First-principles Statistical Mechanics Approach to Sulfur Structure in Organic Cathode Hosts for Polymer Based Lithium-sulfur (Li-S) Batteries . . . . .	92
A.3 How Regiochemistry Influences Aggregation Behavior and Charge Transport in Conjugated Organosulfur Polymer Cathodes for Lithium-sulfur Batteries . . . . .	113
<b>Bibliography</b>	<b>153</b>



## CHAPTER 1

# Introduction

"A daunting task lies ahead for scientists and engineers to guide society towards environmentally sustainable management during the era of the Anthropocene."

Paul J. Crutzen

## 1.1 Motivation

The term ‘Anthropocene’ describes our present geological epoch, governed by humankind’s growing influence on the environment.<sup>1</sup> It was popularized by Nobel laureate Paul J. Crutzen in the early 2000s. Since then, the term has found its way into the public discussion as it defines the dominant impact of humans on all natural systems on planet Earth. Crutzen uses the concept of the ‘Anthropocene’ not only to describe the destructive effects of human activity, *e.g.*, on the global climate. The narrative highlights humanity’s responsibility for planetary stewardship to mitigate the climate crisis and prevent further worldwide effects.<sup>2,3</sup>

Grand societal efforts need to be undertaken to mitigate and adapt to global warming. Innovative technologies and new materials in the renewable energy sector are needed to replace fossil fuels and meet the energy demand of a post-carbon society. One of the most critical aspects in the transition towards a future-oriented and sustainable energy supply is the storage of electrical power through batteries. The applications of rechargeable batteries are already enormous today and will most likely increase in the years to come. From the mobility sector to powering motors and machines in the industry to stabilizing large electricity grids, the performance of batteries will play a key factor in the decarbonization of our energy systems.

Throughout history, rechargeable batteries have undergone significant advancements in capacity, efficiency, and safety. The lead-acid battery,<sup>4</sup> invented by Gaston Planté in 1859, paved the way for these improvements as the first-ever

rechargeable battery. In 1899, Waldemar Junger developed the Nickel-cadmium<sup>5</sup> (Ni-Cd) battery, whose commercialization in Sweden started in 1910 and 1946 in the United States. Later in the 1970s, they gained use in consumer electronics, but their widespread adoption was limited due to the negative environmental impact of cadmium. The nickel-metal hydride<sup>6</sup> (NiMH) battery was introduced in the 1980s as a more environmentally friendly alternative to Ni-Cd batteries. NiMH batteries provided better performance and were widely used in various electronic devices. In 1991, Sony made a significant impact on the battery industry with the introduction of lithium-ion (Li-ion) batteries.<sup>7,8</sup> The development of the Li-ion battery by Akira Yoshino involved replacing the lithium cobalt oxide cathode with a safer and more stable lithium manganese oxide cathode. This breakthrough resulted in batteries with higher energy density, longer-lasting charges, and a lower risk of overheating and explosion. Sony's Li-ion battery became the preferred option for many portable electronic devices, leading to the evolution of rechargeable batteries and the creation of modern gadgets and electric vehicles.

Nowadays, Li-ion batteries (LIB) are the cornerstone of energy storage devices, especially in transportation. While a substantial part of modern battery research still focuses on optimizing LIBs, an increasing body of research is now being dedicated to a new generation of batteries using other materials and technologies. Three key performance characteristics for future battery systems are an increased energy density, a longer life span, and more environmentally friendly and sustainable components. One of the most promising battery types among the diverse pool of future candidates is the lithium-sulfur (Li-S) battery, offering significant advantages in terms of energy density, cost-effectiveness, and environmental sustainability. Sulfur is the tenth most abundant element on Earth,<sup>9</sup> making it an optimal feedstock for synthesizing novel materials. With an annually generated surplus in the order of seven million tons,<sup>10</sup> elemental sulfur is a suitable resource for future scaling-up technologies. The chemistry of sulfur in combination with a lithium anode allows it to carry more charge density, leading to a substantially higher energy density per unit weight compared to competitor technologies, thus allowing to produce lighter batteries.

Although the concept of a Li-S battery can be traced back to 1962 when Herbert and Ulam<sup>11</sup> introduced a sulfur cathode, the technology stood under the radar in the decades since - in part due to the success of other battery types. It was only in the last decade, after a breakthrough report of Nazar et al.<sup>12</sup> in 2009, that the Li-S battery experienced a revival with a drastic increase in research interest since then. Despite the promising advantages, Li-S batteries have not yet found their way into our everyday lives. This technology has not achieved widespread commercialization because of several issues that mainly stem from the cathode that

contains sulfur. As will be discussed in the following chapter, the main challenges lay in the insulation of elemental sulfur, leading to low reaction kinetics and bad performance, the shuttle effect of dissolvable lithium polysulfides leading to a loss of active material and a reduced cycle life, and the volumetric change of sulfur during the charge/discharge resulting in fracturing of the cathode. To maximize the benefits offered by Li-S chemistry, researchers have investigated all the different components of the battery.<sup>13–20</sup> Yet, the greatest potential to improve the overall cell performance lies in the sulfur cathode material.<sup>21–24</sup> Finding a suitable candidate that enhances the electrical conductivity, suppresses the shuttle effect, and accommodates the volume change has been the main goal up to now.

This doctoral work was started ten years after the publication of Nazar et al.’s article and continues the investigation of new materials suitable to further improve the performance of Li-S batteries. In the field of material sciences, the role of theory is two-fold. On the one hand, theoretical frameworks that build on principles of physics and chemistry can give a systematic way to study the relationships between a material’s structure, composition, and behavior. This can guide researchers to design and optimize new materials with specific functionalities. On the other hand, theoretical models aid in interpreting experimental results, enabling scientists to uncover underlying mechanisms and propose hypotheses for further exploration. In both ways, theory is particularly powerful when it combines multiple frameworks applied to phenomena on different lengths and time scales. Such multiscale approaches give a more holistic view of the functioning of the material.

## 1.2 Outline

This thesis comprises a set of studies on thiophenyl benzenethiol, which is used as a polymeric cathode material within a Li-S battery. The projects present a combination of different multiscale approaches conceived and applied by me, together with experimental measurements of my colleagues explaining the structural and electronic behaviors of the polymer material and its functioning in the battery.

Before discussing the results of these works, in Chapter 2, the reader is first introduced to the field of Li-S batteries and the application of polymeric cathode materials therein. Furthermore, I will discuss the fundamentals of the three theoretical concepts of density functional theory (DFT), classical molecular dynamics (MD), and statistical mechanics. At the end of that chapter, I describe how I combined these concepts into different multiscale approaches.

Chapter 3 then presents the main findings of the three research projects comprised in this thesis. Here, I will highlight my contributions and connect the results with

each other to draw a bigger picture. In the following, I give an overview of the three studies. The first project (App. A.1) is a joint experimental and theoretical study on a new fabrication concept to construct a vulcanized conjugated polymer material. Vulcanization is a method to embed elemental sulfur into a polymer chemically. The material is analyzed with several characterization techniques, and its application as a Li-S cathode is demonstrated with battery performance measurements. From a theoretical point of view, I start by investigating the smallest possible subsystem of the vulcanized polymer, which is the monomer unit covalently bonded to a sulfur chain. I rationalize the synthesis process on a microscopic scale and derive some basic electronic properties from the model system to support the experimental findings on the conducting behavior of the polymer.

In the second study (App. A.2), I continue the structural investigation of the vulcanized polymer. I start again with a fragmentation of the polymer, but here, the model allows to distinguish between different ways sulfur can bind to the polymer. Using DFT, I investigate the structural stability of the vulcanized polymer and derive a statistical mechanics model using these microscopic insights as inputs. My model describes the outcome of the vulcanization process as a statistical equilibrium of an ensemble of many microscopic states (the polymer fragments). I then derive average numbers for the length of covalently bonded sulfur chains depending on the temperature and the amount of embedded sulfur. Furthermore, my theoretical findings are supported by experimental Raman spectroscopy measurements of the monomer and polymer.

For the last project (App. A.3), I study the interplay between microstructure and electrical properties of the material by investigating the charge-transfer processes in the conjugated polymer. Here, I extend the dimensions of the theoretical model from small chain fragments to several polymer chains. In order to study the aggregation behavior of these systems, I parameterize an all-atomistic MD force field. The results of the MD simulations are fed back to band structure calculations, which allows a connection between the electronic properties of the material and its transport behavior on a nanoscale. Furthermore, I calculate X-ray diffractograms, which enable the direct comparison of the microscopic structure with the experiment. Once again, I use a statistical method to investigate the transport properties further. Based on the structural characterization, I employ the Boltzmann transport equation (BTE),<sup>25</sup> which describes the movement of charges through a material by a probability distribution function. This theory captures the behavior of particles on an intermediate scale, where particle interactions are important, but the system is not yet fully described by continuum equations. In order to capture the particle interaction on a microscopic level, I combine this method with the so-called deformation potential (DP) theory.<sup>26</sup> This

concept from solid-state physics describes the interaction between electrons and lattice vibrations (phonons) in crystalline materials. By integrating this theory into the approach, I finally calculate electrical conductivities in dependency of charge carrier concentrations.

Finally, I will discuss the main findings by putting the advancements I have made into context. The thesis concludes with a scope of possible directions for future studies.



# Fundamentals

The main research objective of this work is to understand the structural and electronic properties of the polymeric cathode material poly(4-thiophen-3-yl)benzenethiol) (PTBT) in a Li-S battery. This is done by applying theories and methods from theoretical chemistry and physics. In order to give the reader a better understanding of the subject, this chapter comprises the most relevant fundamental concepts of the materials and methods used throughout this work. First, I will introduce the general working principle of a Li-S battery, its benefits, and the most common technical challenges. Focusing on the cathode, I will present a brief overview of the history of organic polymers in the context of Li-S battery research and discuss the advantages of utilizing them as cathode materials. Further, I will cover the basics of the three main methodological concepts I have applied for my investigations: DFT, classical MD, and statistical mechanics. Finally, I present two multiscale modeling approaches that I conceived to study the structure of the polymer and the charge transport herein.

## 2.1 Li-S Batteries

A lithium-based rechargeable battery's most general working principle involves the movement of lithium ions between two electrodes during charging and discharging cycles.<sup>27</sup> Between the electrodes (anode and cathode), an electrolyte facilitates the transport of the lithium ions. During the charging process, an external power source applies a voltage to the battery. The lithium ions are extracted from the cathode material and move through the electrolyte toward the anode, where they are stored. By creating a concentration gradient of lithium ions between the anode and cathode, energy gets stored in the battery. The process is reversed during discharge: lithium ions are released at the anode side and move back towards the cathode. Simultaneously, the movement of the ions releases the stored en-

ergy in the form of an electrical current, which then powers an external device. Conventional LIBs involve the insertion and de-insertion of ions into the electrodes. In LIBs, these so-called intercalations are only possible at specific sites in the host materials, limiting the charge-storage capacity and energy density of the battery.<sup>28</sup> This is one of the reasons why lithium-ion batteries, although they have dominated portable electronics over the past three decades, will not satisfy the high-energy requirement for a global transition towards electric transportation and next-generation energy storage.<sup>29</sup>

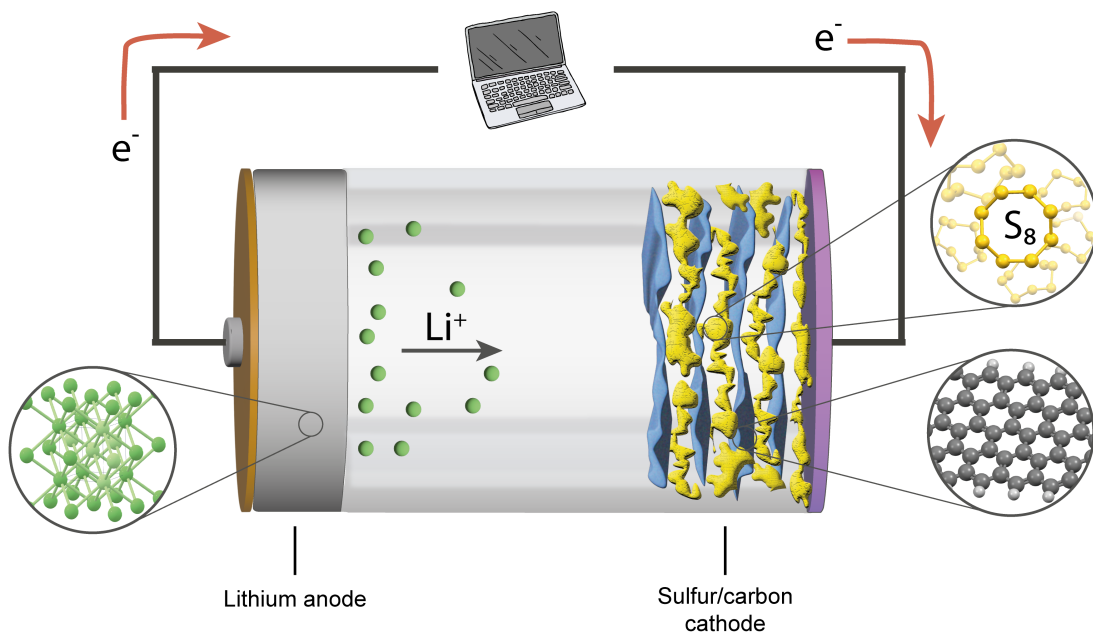


Figure 2.1: A scheme of a conventional Li-S battery where the cathode is made of sulfur integrated in a conductive carbon based material. During discharge, Li ions migrate from the anode into the electrolyte towards the cathode while the electrons conduct through an external circuit powering a device (*e.g.* a computer). At the cathode, Li ions and electrons react with sulfur in a multi-step process.

Compared to LIBs, Li-S batteries are based on a different cell chemistry. Instead of being intercalated, lithium ions undergo a conversion reaction mechanism with sulfur. In a conventional Li-S battery, the anode is made of lithium metal since it has the highest specific capacity among all anode materials,<sup>30</sup> and the cathode consists of sulfur (*cf.* Fig. 2.1). Sulfur atoms are known to form long homoatomic chains or homocyclic rings.<sup>31</sup> At room temperature, octasulfur (cyclo-S<sub>8</sub>), which crystallizes as orthorhombic  $\alpha$ -S<sub>8</sub>, is the most stable allotrope. During discharge, the lithium metal anode gets oxidized and releases ions into

the electrolyte.<sup>27</sup> At the cathode side, sulfur gets reduced by accepting these ions and electrons. In a multistep redox reaction,  $S_8$  and lithium ions react to form intermediate lithium polysulfide species  $Li_2S_n$  of different sulfur chain lengths  $n$  with lithium sulfide  $Li_2S$  as the end product. During charge,  $Li_2S$  is converted back to  $S_8$  and Li-ions, resulting in a reversible cycle. Because this reaction incorporates two electrons per sulfur atom compared to one or less than one electron per transition-metal ion in intercalation-based cathode materials, Li-S batteries yield a theoretical specific capacity of 1675 mAh/g, ten times higher than that of LIBs.<sup>18</sup> The product of capacity and working voltage (which at 2.2 V is relatively low compared to that of LIBs at 3.5 V<sup>32</sup>) yields an extremely high theoretical gravimetric energy density of around 2600 Wh/kg for a Li-S battery. Although assembled into a full battery cell, this value drops down to about 400 Wh/kg for current state-of-the-art commercial cell designs,<sup>33</sup> it is already twice as high compared to current Li-ion cells. The promise for future Li-S batteries is to increase this value beyond 500 Wh/kg. Therefore, Li-S batteries can be made much lighter, which opens up possibilities for the electrification of aviation and large vehicles. Another benefit is the low cost of sulfur, which is one of the most abundant elements on Earth.<sup>9</sup> This will allow to reduce prices compared to LIBs, where much of the cost is due to the use of metals such as nickel and cobalt for the cathode. Removing these transition metals will also have a positive environmental impact since their mining and processing are known to have severe consequences for humans and ecosystems.<sup>34</sup>

Despite all these advantages, and although the number of companies announcing the commercialization of Li-S batteries has steadily grown over the last few years, there are still some unmet challenges with this battery type - not only regarding scaling up but also on a fundamental level. Some of these challenges are directly related to the intrinsic properties of sulfur, including the most prominent problem of the so-called shuttle effect that concerns the cycle life span of the battery.<sup>35</sup> During the conversion reaction between sulfur and lithium ions, the cathode material undergoes a phase transition from solid ( $S_8$ ) to liquid ( $Li_2S_n$ ,  $n \geq 2$ ) back to solid ( $Li_2S$ ). Especially the longer intermediate lithium polysulfides  $Li_2S_n$  ( $6 \leq n \leq 8$ ) are soluble in the ether-based electrolytes commonly used for Li-S batteries.<sup>36</sup> Because of this, these species can dissolve into the electrolyte and move from the cathode to the anode, where they react with the lithium metal. The long or high-order polysulfides reduce to low-order polysulfides, migrate back to the cathode, form high-order polysulfides again, and so on.<sup>37</sup> This shuttling leads to a loss of active material and, in turn, a capacity fading over time. Another problem stems from the insulating behavior of elemental sulfur  $S_8$  and the discharge product lithium sulfide  $Li_2S$ . Both have a very low conductivity for elec-

trons and lithium ions, which prevents efficient charge-transfer and leads to very slow redox kinetics.<sup>38</sup> A third challenge is the volume expansion of sulfur during lithiation. Upon full lithiation, sulfur undergoes a significant volume expansion of about 80 % due to its higher density of 2.07 g/cm<sup>3</sup> compared to lithium sulfide of 1.66 g/cm<sup>3</sup>.<sup>39</sup> This can cause mechanical stress on the electrode, eventually leading to degradation after repeated cycles.

Over the last decade, much effort has been devoted to overcoming these obstacles. Herein, all sorts of strategies were pursued by investigating the different parts of the battery. Still, the most impactful yet challenging part is searching for a suitable sulfur cathode material that suppresses the shuttle effect, enhances the electrical conductivity, and accommodates the volume change. One class of materials that has received increasing attention due to its ability to fulfill all three requirements while being relatively cheap and environmentally friendly is organic polymers. The following chapter presents the benefits of organic polymers as cathode materials for Li-S batteries.

## 2.2 Organic polymers as cathode materials

Various methods have been explored to overcome the above-mentioned problems of using sulfur as the active cathode material. One common approach is to combine sulfur with a substrate with high electrical conductivity, like carbon, to enhance electrical contact. Additionally, porous substrates are often used to absorb the polysulfides that form during cycling and effectively restrain the sulfur on the cathode side. To buffer the volume change of sulfur, flexible substrates with retained cavities or porous structures have proven advantageous.

In their pioneering work, Nazar *et al.* used CMK-3, a mesoporous carbon material, to host the elemental sulfur.<sup>12</sup> Due to the unique architecture of hollow carbon nanorods in which the sulfur was confined, they could, for the first time, demonstrate stable cycling over 20 cycles. Although this marked a great breakthrough, 20 cycles is far from relevant for any practical application. In the following years, great progress has been made in modifying such carbon-based host materials, for example, by using 1- or 2D materials such as carbon nanofibers<sup>40,41</sup> or graphene.<sup>42,43</sup> Still, the cycling performance remained unsatisfactory, which could mainly be attributed to the nonpolar carbon surface that only provides weak physical adsorption of the polar lithium polysulfides. This led to the emergence of polymers as an organic cathode material. Due to their diversity of functional groups and tunable topologies, one has precise control of chemically confining the sulfur, and at the same time, their flexible nature accommodates the volume changes.

Interestingly, the investigation of organosulfur compounds for energy storage materials already began in the late 1980s.<sup>44</sup> The development of polymer-based cathode materials can be distinguished into three categories or generations<sup>15</sup> (*cf.* Fig. 2.2). The first organosulfur compounds for batteries were disulfide polymers with the sulfide group integrated into the main chain of the polymer (main-chain organosulfur polymer).<sup>45–47</sup> The main disadvantage of these polymers is that the redox reaction during cycling can lead to an irreversible breakage of the S-S bond, which causes depolymerization. Because of that, such batteries showed a drastic capacity fade after only a few cycles. The damage to the polymer backbone can be circumvented if the disulfide group is attached to the side group (side-chain organosulfur polymer). Such polymers represent the second generation of organosulfur electrodes.<sup>48–51</sup> Here, the redox reaction takes place at the side group without altering the backbone. Thus, these polymers showed much better structural stability upon cycling. Despite the improved performance, disulfide groups offer only a small amount of sulfur compared to the electrochemically inactive polymer backbone. This limits the specific capacity of a battery if one accounts for the extra weight of the organic framework. Therefore, polysulfide polymers with longer sulfur moieties  $-S_n-$  ( $n > 2$ ) received increasing attention during the late 1990s (polysulfide polymers).<sup>52–54</sup>

If sulfur is not a part of the monomeric units that make up the organosulfur polymer, sulfur has to be integrated into the polymeric framework after polymerization. Here, vulcanization is one of the best-known and simplest methods to prepare sulfur-containing polymers. The process of vulcanization was originally invented in the mid-1800s to make natural rubber (consisting of the polymer polyisoprene<sup>56</sup>) more resistant to temperature changes.<sup>57</sup> It describes the chemical cross-linking of natural rubber or related polymers and sulfur. This procedure makes use of sulfurs' unique characteristics at elevated temperatures. If elemental sulfur is heated above a temperature of 159 °C, the  $S_8$  rings start to break, forming liquid chain-like free  $\cdot S_8 \cdot$  radical. The reversible ring-opening polymerization results in linear polysulfides with diradical chain ends  $\cdot(S_8)_n \cdot$  ( $n > 1$ ). This polymeric sulfur depolymerizes into smaller monomeric radicals (*e.g.*,  $\cdot S_8 \cdot$ ,  $\cdot S_6 \cdot$ ) at temperatures above 200 °C.<sup>58–60</sup> At 444 °C, the liquid sulfur starts to boil, and sulfur vapor in the form of  $S_6$ ,  $S_4$ , and  $S_2$  is formed. Depending on the temperature, one can convert elemental sulfur into chain-like free radicals of various lengths. A possible way to prepare the polymer for vulcanization is first to infiltrate it with liquid elemental sulfur and subsequently heating up. The radical ends of the polymeric sulfur can then react with reactive or polymerizable groups of the polymer. A variety of functional groups, such as C-H, OH, C=O, SH, or C=C can polymerize with the sulfur, resulting in a sulfurized polymer where  $S_n$  groups

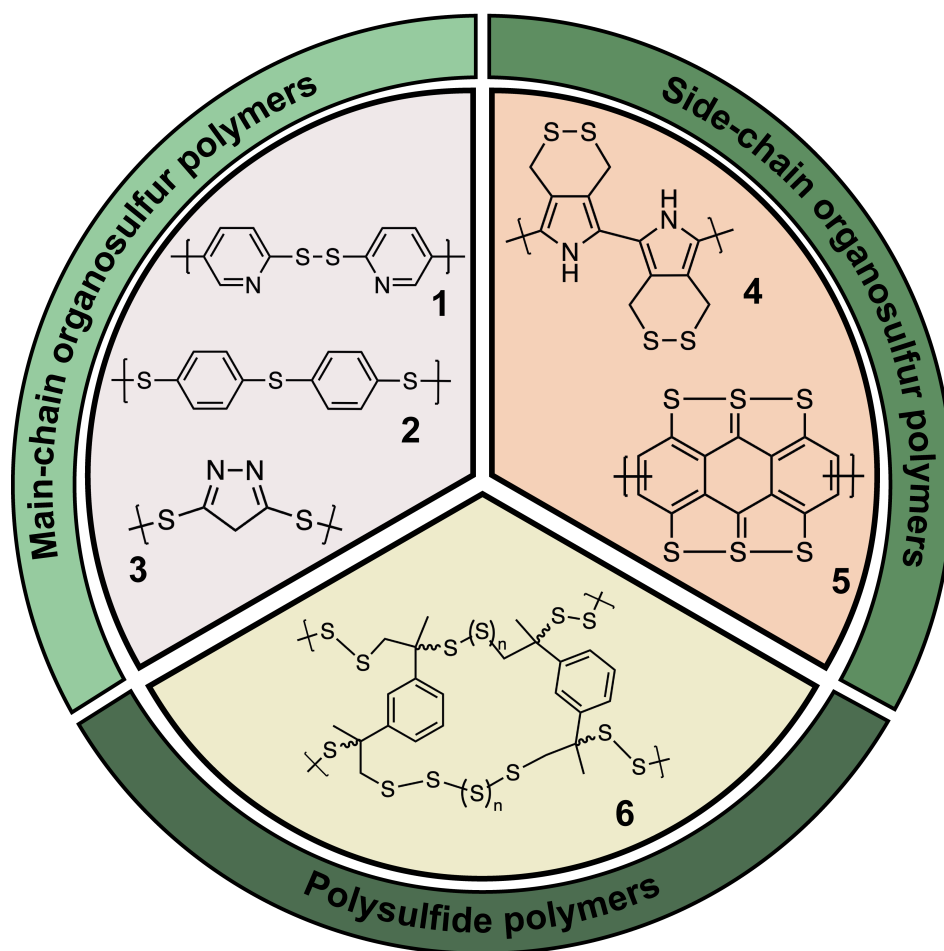


Figure 2.2: Three generations of sulfurized organic polymers: main-chain type polymers with a disulfide link as part of the backbone (Nos. **1**,<sup>46</sup> **2**,<sup>55</sup> **3**<sup>45</sup>). Side-chain type polymers with the disulfide link attached to the side group (Nos. **4**,<sup>51</sup> **5**<sup>48</sup>). Polysulfide polymers (such as the shown poly(S-r-DIB), No. **6**<sup>10</sup>) can be synthesized by inverse vulcanization and feature longer polysulfide chains.

of different length are chemically bonded to the organic framework. Although this synthetic approach led to cathode materials with much better capacity, researchers were trying to increase the sulfur content further. Usually, only a small amount of sulfur is integrated into the polymer host during vulcanization. In 2013, Chung *et al.*<sup>10</sup> changed the mixing ratio of the educts and investigated the effect of vulcanizing a small amount of 1,3-diisopropenylbenzene (DIB) monomers with a large amount of elemental sulfur. This so-called inverse vulcanization yielded a sulfur-rich polymer with a capacity of 1005 mAh/g.<sup>61</sup> Similar to the first-generation organosulfur polymers, the sulfur chains are part of the main framework of this copolymer. Nevertheless, the material showed a stable cycling performance, which the authors attributed to the plasticizing effects of DIB discharge units dispersed in the low-order lithium polysulfides. This copolymerization process is a low-cost technique to produce sulfur-rich polymers, which also enables the choice of differ-

ent cross-linking organic molecules,<sup>62–64</sup> thus making it a very versatile approach. However, the main disadvantage is the random nature of the copolymer’s morphology, which leads to low conductivity. This drawback can be circumvented by using conjugated polymers as a sulfur host material.

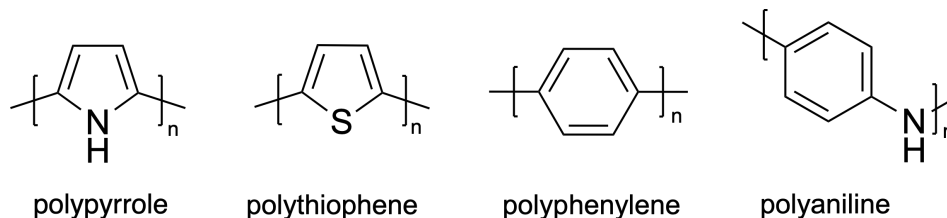


Figure 2.3: Illustration of the repeat units of four different conjugated polymers that have been used as cathode materials for Li-S batteries.

Conjugated polymers are a class of organic macromolecules characterized by a backbone consisting of alternating single- and double-bonds. Historically, polyenes (linear carbon chains with alternating C–C and C=C bonds) were one of the first conjugated polymers studied with the discovery of polyacetylene in 1975 eventually leading to the Nobel prize in chemistry in 2000.<sup>65,66</sup> If, instead of a linear carbon chain, heterocyclic molecules like pyrrole, furan, or thiophene form the backbone of a polymer chain, this can further improve the conductive properties of the material. In section 2.5, I will explain in more detail how I calculated the conductivity of the conjugated PTBT system based on its electronic properties. In search of polymeric cathode materials with both high sulfur content and electrical conductivity, researchers investigated conjugated polymers such as polypyrrole, polythiophene, polyphenylene, or polyaniline<sup>67–71</sup> (*cf.* Fig. 2.3) modified with allyl or thiol groups in order to polymerize them with elemental sulfur.

In summary, numerous strategies to prepare organic cathode materials for Li–S batteries have been explored in recent years, starting from the first organosulfur compounds with low sulfur content and insufficient cycling stability, leading to sulfur-rich vulcanized conjugated polymers with much-improved battery performance. Overall, Li-S batteries have come a long way from the early efforts with pure sulfur cathodes in the 1960s to modern approaches with highly functionalized organic sulfur host materials (*cf.* Fig. 2.4).

Within this work, I investigate a vulcanized conjugated polymer, building on the most recent the current development of sulfur-containing polymer cathodes. To explore the functionality of a new material, it is crucial first to characterize it and understand its properties. Regarding its application as a cathode material, I was interested in the structural and electronic properties of the vulcanized polymer, especially its morphology, ability to chemically confine sulfur, and charge

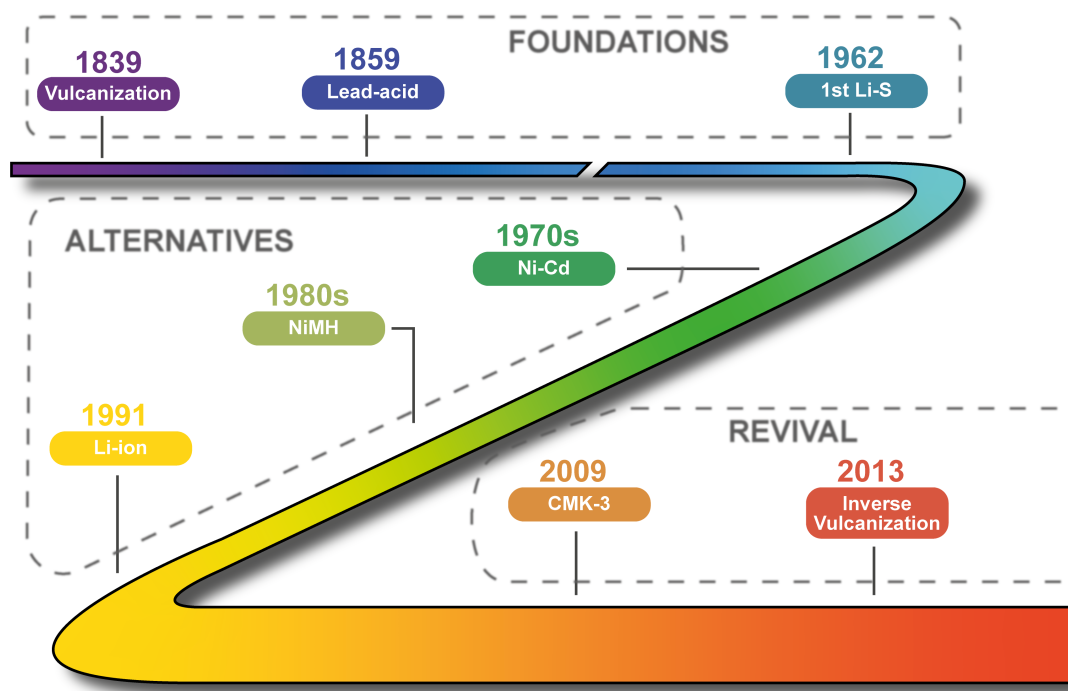


Figure 2.4: A brief history of Li-S batteries: the method of vulcanization (invented 1859) was originally used to hardening rubber; the first rechargeable battery (lead-acid) dates back to the year 1859; the first Li-S battery was invented in 1962; in the following decades, several other battery types have been investigated - particularly noteworthy is the introduction of the Li-ion battery in 1991; a breakthrough study<sup>12</sup> on a mesoporous carbon host material (CMK-3) in 2009 started the revival of Li-S battery research; in 2013, the first Li-S battery with an inverse vulcanized polymer cathode was presented.

transport behavior. For this task, the modeling and simulation of the respective materials provide a direct and fundamental understanding of their properties and their behavior in application.

## 2.3 Multiscale modeling and simulation

This section summarizes the methodological concept of the thesis. Here, I will present the fundamentals of DFT, classical MD, and statistical mechanics and explain how I combined these theories into joint approaches.

The creating and breaking of chemical bonds during the synthesis of a polymer are quantum mechanical processes, as they involve the motion and interaction of particles on an atomic scale. While quantum mechanical calculations can offer high accuracy in describing microscopic processes, they are usually computationally quite expensive (as I explain in the following) and hence limited to small systems.

However, the final product of a vulcanized conjugated polymer represents a macroscopic system. At the same time, its macroscopic properties might originate from processes at different lengths and time scales. To account for these dependencies across multiple scales, the general concept of a multiscale approach builds on the following strategy: using higher precision (but more computationally expensive) techniques at smaller spatial and temporal scales, extracting specific parameters of interest, and feeding them to less computationally expensive methods capable of performing at larger spatial and temporal scales. The benefit of such an approach can be two-fold. Focusing the computationally demanding calculations only on specific regions of interest brings a time advantage. Additionally, a multiscale approach can provide a more holistic understanding of properties that arise from the complex interplay of various processes.

### 2.3.1 Density functional theory

A quantum mechanical description is the basis for a fundamental understanding of our material. In quantum mechanics, we learn that all information we can possibly have about a system is contained in the system's wave function  $\Psi$ . The wave function of a system's ground state is calculated from the time-independent Schrödinger equation (SE)<sup>72</sup>

$$\hat{H}\Psi = E\Psi, \quad (2.1)$$

where  $\hat{H}$  is the Hamiltonian of the system (an operator characterizing the system's energy, referencing the concept of Hamiltonian mechanics<sup>73</sup>), and  $E$  is the total energy of the system.

An analytical solution for the SE can only be derived for one-electron systems such as the hydrogen atom. Over the last century, many powerful methods have been developed to solve this equation for bigger systems approximately. One of the earliest approaches is the Hartree-Fock (HF) method<sup>74-76</sup> in which the many-body wave function is described by a Slater determinant,<sup>77</sup> an anti-symmetric product of one-electron wave functions. The anti-symmetric form of a Slater determinant accounts for the Pauli exclusion principles,<sup>78</sup> which states that two fermions (such as electrons) cannot occupy the same quantum state simultaneously. The interaction that arises due to the Pauli exclusion principle, coupled with the electrostatic repulsion between electrons, is termed the exchange interaction. In the HF method, the electron-electron exchange is approximated by an effective interaction of a mean electronic field evoked by all electrons. However, electrons also feel an additional interaction due to their correlated motion. The mean field approach of the HF method does not capture this correlation interaction. Post-Hartree-Fock

methods such as coupled-cluster<sup>79</sup> or configuration interaction<sup>80</sup> are employed to incorporate electron correlation and generally provide more accurate descriptions of a system's electronic structure. The problem with such methods is the computational effort arising from the many-body problem when dealing with more than one electron.

DFT<sup>81</sup> is a very powerful and versatile alternative. It provides a way to map the many-body problem onto a single-body problem by promoting the particle density to a key variable from which all other observables can be derived. Made popular by Hohenberg and Kohn in 1964,<sup>82</sup> this theory became a cornerstone of computational chemistry and was awarded the Nobel Prize in Chemistry in 1998.<sup>83</sup> In essence, the Kohn-Sham theorems state that the ground state wave function of a system,  $\Psi_0(\mathbf{r}_1, \mathbf{r}_2, \dots, \mathbf{r}_n)$ , is a unique functional of its ground state density  $n_0(\mathbf{r})$

$$\Psi_0(\mathbf{r}_1, \mathbf{r}_2, \dots, \mathbf{r}_n) = \Psi[n_0(\mathbf{r})], \quad (2.2)$$

where [...] denotes a functional. Eq. (2.2) describes the reduction of dimensionality when going from a many-body problem of  $n$  particles (with individual three-dimensional cartesian coordinates  $\mathbf{r}_i$ ) to only one three-dimensional quantity, the ground state density  $n_0(\mathbf{r})$ . As a consequence of the direct correspondence of wave function and density, the expectation value of any observable is also a functional of the density. Among these observables, the ground state energy  $E_0$  is of particular interest. This energy obeys the variational principle

$$E_0 \leq E[n_0] = \langle \Psi[n_0] | \hat{H} | \Psi[n_0] \rangle \leq E[n'], \quad (2.3)$$

which states that for any other density  $n'$  than the ground state density  $n_0$ , one obtains an energy higher than (or equal to) the ground state energy  $E_0$ . Thus, the functional  $E[n']$  gets minimized only by the ground state density  $n_0$ .

In order to use these considerations, one has to specify the Hamiltonian in Eq. (2.3) according to the system of interest. When starting from Schrödinger's equation, using the Born-Oppenheimer approximation<sup>84</sup> allows to separate the description of electrons and nuclei, exploiting the fact that the nuclei are much heavier and slower than the electrons. The nuclear degrees of freedom appear only in the form of a potential acting on the electrons, and the wave function depends only on the electron coordinates. For a system with  $N$  electrons, the electronic Hamilton operator in Eq. (2.1) then reads

$$\hat{H} = \hat{T} + \hat{U} + \hat{V}, \quad (2.4)$$

with the kinetic energy operator  $\hat{T}$ , the operator  $\hat{U}$ , describing the electron-

electron interaction, and the external potential  $\hat{V}$ , which is given by the charges and the spatial arrangement of the nuclei. The nuclear degrees of freedom enter only *via*  $\hat{V}$ , so the wave function  $\Psi$  depends only on the electronic degrees of freedom. An important fact is that  $\hat{T}$  and  $\hat{U}$  are universal operators, meaning they are the same for any non-relativistic system if particles interact *via* Coulomb interactions. Only the non-universal potential  $\hat{V}$  distinguishes whether the system is an atom, a molecule, or a solid.

Translating Eq. (2.4) into a functional form, one can write

$$E[n] = T[n] + U[n] + V[n]. \quad (2.5)$$

A first approximation to this equation was already given by Thomas<sup>85</sup> and Fermi<sup>86</sup> in 1927/28 and was further developed by Kohn and Sham in 1965.<sup>87</sup> The main idea of the Kohn-Sham approach is to decompose the kinetic-energy functional of interacting electrons  $T[n]$  into one part representing the kinetic energy  $T_s[n]$  of non-interacting particles of the density  $n$  and one that represents the rest (the subscript  $s$  stands for ‘single-particle’). In the same way, the full interaction energy functional  $U[n]$  gets separated into the Hartree energy  $U_H[n]$  (the electrostatic interaction energy of a charge density  $n$ ) and a remainder. The full energy functional can then be rewritten as<sup>88</sup>

$$E[n] = T_s[n] + U_H[n] + V[n] + E_{xc}[n], \quad (2.6)$$

where the last term comprises the differences  $T - T_s$  and  $U - U_H$ . This functional,  $E_{xc}[n]$ , is called the exchange-correlation functional, and it contains the energy contributions due to the Pauli exclusion of the electrons (exchange) and the correlation between them. The benefit of going from Eq. (2.5) to 2.6 is that one can use analytical expressions for the Hartree and kinetic energy term. This comes at the cost of introducing  $E_{xc}[n]$ , which now comprises all many-body effects. After the Hohenberg-Kohn theorems replace the wave function description with a density description, the twist of the Kohn-Sham approach is now to introduce again a special kind of wave function, the single-particle orbitals  $\psi_i^{\text{KS}}$  of a fictitious system of non-interaction electrons.<sup>89</sup> The density of the initial many-body system is the one that minimizes Eq. (2.6)

$$0 = \frac{\delta E[n]}{\delta n} = \frac{\delta T_s[n]}{\delta n} + \frac{\delta U_H[n]}{\delta n} + \frac{\delta V[n]}{\delta n} + \frac{\delta E_{xc}[n]}{\delta n} = \frac{\delta T_s[n]}{\delta n} + \nu_H + \nu + \nu_{xc}, \quad (2.7)$$

with the Hartree potential  $\nu_H$ , the external potential the electrons move in  $\nu$ , and the term  $\nu_{xc}$ , which can only be calculated if one knows how to describe the

exchange-correlation functional. This minimization problem can then be translated into a SE for the non-interacting system<sup>88</sup>

$$\left[ \hat{T}_s + \nu_s \right] \psi_i^{\text{KS}} = \epsilon_i \psi_i^{\text{KS}}, \quad (2.8)$$

with an effective potential  $\nu_s = \nu_H + \nu + \nu_{xc}$ . If this potential is so chosen, then Eq. (2.8) yields orbitals that reproduce the density of the original system

$$n \equiv n_s = \sum_i f_i |\psi_i^{\text{KS}}|^2, \quad (2.9)$$

with the occupation number  $f_i$  of the  $i$ 'th orbital. One can summarize the idea of Kohn-Sham DFT as follows: Instead of calculating the density of an interacting (many-body) system in the potential  $\nu$ , which is described by the many-body SE 2.1, one solves the equation of a non-interacting (single-body) system in the potential  $\nu_s$ .

Equation 2.8 is a nonlinear eigenvalue problem since  $\nu_H$  and  $\nu_{xc}$  on the left side depend on  $n$ , which depends on the orbitals  $\Psi_i^{\text{KS}}$  via Eq. (2.9), which in turn depend on  $\nu_s$ . Therefore, one has to solve this equation iteratively in a self-consistent cycle by first guessing an initial density  $n$ , calculating the corresponding  $\nu_s$ , solving the Eq. (2.8) for the  $\Psi_i^{\text{KS}}$ , and updating the density. This process gets repeated until a desired convergence is reached.

With the Kohn-Sham equations at hand, one still faces a couple of questions when trying to actually solve them. The biggest obstacle is the description of the exchange-correlation functional. Formally, Kohn-Sham DFT is an exact theory to the initial many-body problem as long as one can find an expression for  $E_{xc}[n]$ . Unfortunately, an exact form is unknown, so one must find a suitable approximation depending on the specific system. This is where DFT shows its vast diversity. Over the last decades, numerous functional approximations have been developed, and searching for more accurate functionals is an ongoing task.<sup>90</sup> Generally, one can distinguish between local, semi-local or gradient-dependent, and non-local or hybrid functionals. The local density approximation (LDA) resembles the idea of the Thomas-Fermi approach by decomposing the real inhomogeneous electron density into small cells, in each of which the density is locally homogeneous. In LDA, only the local density  $n(\mathbf{r})$  at a point  $\mathbf{r}$  is used to calculate the term  $\nu_{xc}(\mathbf{r})$ . An improvement of LDA is made by also taking into account the gradient of the density at that point in space. This class of functionals is known as generalized gradient approximations (GGA).

Furthermore, one can combine a GGA-functional with a portion of HF exchange interaction to yield a hybrid functional. The mean-field approach of the HF method

gives hybrid functionals a non-local character. This non-locality of the HF portion in the hybrid functional makes the computation much more complex as it involves integrals over the three-dimensional space instead of just taking the density (and its gradient) at a given point.

Therefore, the choice of a functional often depends not only on the system but also on the trade-off between accuracy and computational expenses. Regardless of their local character, one can further distinguish between empirical functionals whose parameters are fitted to experimental data and non-empirical functionals derived through a combination of theoretical considerations and mathematical approximations.

In this work, I have mostly employed the Perdew-Burke-Ernzerhof (PBE) functional,<sup>91</sup> which is one of the most popular non-empirical GGA functionals. It owns its success by its satisfactory description of both condensed matter as well as molecules.<sup>92</sup> For comparison, I also used the PBE0 functional,<sup>93</sup> which mixes 75% of the PBE exchange with 25% of exact Hartree-Fock exchange, and the well-known B3LYP<sup>94</sup> functional, which mixes the GGA functional LYP for correlation with the three-parameter hybrid functional B3<sup>95</sup> for exchange.

Besides the choice of the functional, another key to numerical efficiency and accuracy is how the Kohn Sham orbitals  $\psi_i^{\text{KS}}$  are represented. For this, one has to choose a basis set, that is, a set of basis functions  $\phi_l$  in which the KS orbitals are expanded as a linear combination

$$\psi_i^{\text{KS}} = \sum_j c_{ji} \phi_j. \quad (2.10)$$

Within the basis set, a KS orbital is represented as a vector, the components of which correspond to the coefficients  $c_{ji}$  of the basis functions  $\phi_j$  in the linear expansion. This transforms the differential equation 2.8 into an algebraic eigenvalue problem, which is more suitable to be solved on a computer. Similar to the choice of a functional, selecting a suitable basis set depends on the specific system and the available computational power. The first choice is regarding the number of basis functions. The limit of an infinite number of functions is described as the complete basis set limit. However, this is not practical for an actual DFT calculation. Therefore, the KS orbitals are usually described by a finite set of basis functions. The second choice is regarding the type of basis functions.

Historically, atomic orbitals (AOs) have been the main choice in the chemistry community by linear combining them to construct the wave functions of molecular systems (LCAO method). The atomic orbitals are centered around the nuclei of the constituting atoms of the molecule. Chemical basis functions are then classified with respect to their behavior as a function of the radial coordinate relative

to the nuclei. For example, Slater-type orbitals (STOs) are solutions to the SE of hydrogen-like atoms (atoms with only one valence electron) and decay exponentially away from the nucleus, which closely resembles the behavior of atomic orbitals.<sup>96</sup> In contrast, Gaussian-type orbitals (GTOs) have a Gaussian radial behavior. The benefit here is that they are easier to handle numerically because the product of two GTOs is again a GTO, which is not the case for STOs.

While for the treatment of molecules, basis sets are usually composed of localized functions, solids are usually described within periodic boundary conditions, and therefore, plane-wave basis sets are numerically advantageous.<sup>96</sup> These functions are not associated with any particular atom. Instead, the parameter to control the size of the basis set is the so-called energy cut-off up to which the plane waves are included in the expansion (based on the relation  $E = h\nu = hc/\lambda$ , with the Planck constant  $h$ , the speed of light  $c$ , the frequency  $\nu$  and respective wavelength  $\lambda$  of the wave). By construction, such plane wave basis sets are less suitable for describing spatially isolated molecules. Because of the applied periodic boundary conditions, one has to use large simulation cells with enough vacuum around the molecule to avoid any interactions with the periodic neighbors. This, in turn, increases the computational expenses.

I used the electronic structure code FHI-aims<sup>97–99</sup> in all of my DFT calculations. Here, another type of basis set is employed, namely numeric atom-centered orbitals (NAOs)<sup>97</sup> of the form

$$\phi_j(\mathbf{r}) = \frac{u_j(r)}{r} Y_{lm}(\Omega). \quad (2.11)$$

The radial shape  $u_j(r)$  of these functions is numerically tabulated, which, in principle, allows one to choose any desired shape. In Eq. (2.11),  $Y_{lm}(\Omega)$  describe spherical harmonics. In FHI-aims, a pool of different radial function shapes (*e.g.*, hydrogen-like, cation-like, or atom-like functions) for different chemical environments is used iteratively to construct pre-optimized basis sets for every element, which can be tuned in size to yield the desired accuracy.<sup>97</sup> Starting from a minimal basis set consisting of the free-atom radial functions, one can hierarchically add more functions toward the complete basis set limit. The possibility of using preconstructed defaults makes it very convenient to go from fast qualitative to highly accurate calculations. Another huge benefit is that this approach describes periodic and molecular geometries on the same footing. While NAOs are also localized on the atomic sites, similar to STOs and GTOs, their numerical adjustability is beneficial when solving the SCF cycle for a (periodic) system with varying chemical environments.<sup>97</sup> The fixed analytical forms of STOs and GTOs can make the SCF cycle challenging in periodic DFT calculations, as they may

adapt less efficiently to varying chemical environments than NAOs. Because of the numerical adaptability, the size of an NAO basis set can be smaller, which leads to a speed-up of the calculation without losing accuracy compared to the other two approaches.<sup>100</sup>

Another important part of an accurate DFT-based description of a material is the incorporation of van der Waals (vdW) interactions. Van der Waals interactions are forces that arise between neutral atoms or molecules. They can be both attractive and repulsive depending on the distance of interacting particles. While they are comparatively weaker than covalent or ionic interactions, their cumulative effect can significantly impact the formation and stability of a material. The origin of these non-covalent forces is temporary fluctuations in the electron distribution around the atoms or molecules. These instantaneous dipoles induce polarization in neighboring molecules, which causes an attractive force between them. Especially conjugated (and/or aromatic) systems with extended  $\pi$ -electron distributions, such as the one studied in this work, possess large polarizability, and therefore, the description of vdW interactions plays a crucial role.

Because of the long-range behavior of vdW interactions, they are often underestimated in LDA and GGA exchange-correlation functionals. I, therefore, employed the Tkatchenko-Scheffler (TS) method,<sup>101</sup> which adds a term to the DFT energy (after the SCF is converged) that corrects for the long-range vdW interaction energy. This method adds pairwise interatomic correction terms in the form of London dispersion interaction ( $\sim C_6/R^6$ ) with the dispersion coefficients  $C_6$  and the atom distance  $R$ . The dispersion coefficients are determined by partitioning the DFT electron density into effective volumes for every atom. The total interaction energy is then a sum over all atom pairs in the molecule or solid. This pairwise description is further improved by including many-body dispersion (MBD) effects. In FHI-aims, this is done by building on the TS atomic polarizabilities by separating the dispersion interaction into short- and long-range contributions.<sup>102</sup> The short-range contributions are accounted for by the TS method (together with the respective xc-functional), while the long-range contributions are calculated by mathematically describing the atomic polarizabilities *via* response functions which allow to include higher order (beyond two-body) effects (this concept is adapted from the so-called random phase approximation<sup>103-105</sup> (RPA) which is used to describe long-range electron correlation effects in many-body systems). Since the computational cost of this method is negligible compared to the underlying DFT SCF cycle,<sup>102</sup> the MBD method became my preferred choice for including dispersion interaction effects in my calculations.

To summarize this section, DFT describes the ground state of a quantum mechanical system by using the electron density instead of the many-body wave function, thus leading to a huge dimensionality reduction of the problem. This approach makes it suitable for systems with more than a few electrons. Over the last decades, DFT has been very successful in accurately describing numerous properties of atoms, molecules, and solids, yet at an affordable computational expense. Users of DFT software are faced with two practical concerns: choosing an exchange-correlation functional and a basis set. For both, there is a wide range of options, and the decision has to be based on the experience (and intuition) of the system, the desired accuracy, and the computing costs. In my work, I dealt with both molecular and periodic systems. Therefore, I chose the PBE functional and a basis set based on numeric atom-centered orbitals because of their applicability for both types of systems. Furthermore, I have incorporated van der Waals interactions by using correction methods that account both for pairwise and many-body dispersion effects.

### 2.3.2 Classical molecular dynamics

Although DFT offers an improvement compared to more sophisticated quantum-chemical methods, one quickly realizes that the simulation of a polymeric material on a quantum level is still far from practical. One possible step to reduce the complexity of the system is to disregard the electronic degrees of freedom and the respective electronic structure, allowing the simulation of much larger systems. We then enter the field of classical molecular dynamics simulations.<sup>106</sup> In this classical picture, atoms are represented as spheres with a specific size and partial charge. Their mutual interactions are described by deterministic interatomic potentials, and their trajectories in a simulation are determined by numerically solving Newton's equations of motion.

Although the theoretical basis for MD dates back to the historical works of Newton, Hamilton, and Lagrange, the first simulations of classical many-body systems only began in the 1950s with the development of computers. This is because the equations of motion can only be solved numerically. According to Newton's second law, the acceleration of the  $i$ th particle is given by  $m_i \dot{\mathbf{v}}_i = \mathbf{F}_i$ , and its velocity follows from  $\dot{\mathbf{r}}_i = \mathbf{v}_i$ . The total force  $\mathbf{F}_i$  on the particle is the sum over all forces derived by the individual potentials  $U_i$  according to  $\mathbf{F}_i = -\nabla_i U_i$ . The set of different potentials (although mathematically incorrect) is often referred to as the force field of the system. In the following, I will explain the different contributions included in the force field that I used for my MD simulations.

In general, an atomistic force field can be distinguished into an intra-molecular part describing all interactions between bonded atoms and an inter-molecular part comprising all non-bonded interactions,

$$U_i = U_i^{\text{bonded}} + U_i^{\text{non-bonded}}. \quad (2.12)$$

The intra-molecular contributions of the force field for particle  $i$  are obtained by summing over all bonds, angles, and dihedrals

$$U_i^{\text{bonded}} = \sum_j U_{ij}^{\text{bond}} + \sum_{jk} U_{ijk}^{\text{angl}} + \sum_{jkl} U_{ijkl}^{\text{dih}}. \quad (2.13)$$

From experiments (and quantum mechanical calculations), we know that the distance between two bonded atoms  $i$  and  $j$  varies around an equilibrium value  $r_{ij}^{\text{eq}}$ . The exact bond potential is generally not known, but in many cases a simple harmonic approximation of the form

$$U_{ij}^{\text{bond}} = k_{ij}^{\text{b}} (r_{ij} - r_{ij}^{\text{eq}})^2, \quad (2.14)$$

(with the distance  $r_{ij} = |\mathbf{r}_i - \mathbf{r}_j|$ ) is already sufficient if the bond distance is not too far away from equilibrium (*cf.* upper right diagram in Fig. 2.5). The above equation is analog to Hooke's law for a spring, and one only needs the spring constant  $k_{ij}^{\text{b}}$  and the equilibrium distance  $r_{ij}^{\text{eq}}$  as parameters to describe the bond potential.

The adequate description of a molecule's geometric characteristics possibly having different stable conformations cannot be achieved solely with bond potentials. Besides the two-body contribution, one needs three-body (angles,  $U_{ijk}^{\text{angl}}$ ) and four-body (dihedrals,  $U_{ijkl}^{\text{dih}}$ ) potentials. In my work, I also used a harmonic potential

$$U_{ijk}^{\text{angl}} = k_{ijk}^{\text{angl}} (\phi_{ijk} - \phi_{ijk}^{\text{eq}})^2 \quad (2.15)$$

for the angles, with the angle  $\phi_{ijk}$ . For the description of dihedrals, I employed two analytical forms which use different cosine expansions according to

$$U_{ijkl}^{\text{dih,OPLS}} = \frac{1}{2} \sum_{n=1}^4 K_n (1 + (-1)^{n-1} \cos(n\phi_{ijkl})), \quad (2.16)$$

and

$$U_{ijkl}^{\text{dih,RB}} = \sum_{n=0}^5 C_n \cos(\phi_{ijkl})^n, \quad (2.17)$$

as a result of the force field optimization described in the following.

In order to get valuable insights from an MD simulation, the underlying force field has to be accurate and reliable regarding the physical/chemical system. The ingredients of a force field are the functional forms of the potentials and their parameters. In order to capture the nature of the system in the best way, it is necessary to tune, i.e., parameterize the force field. Each system requires a unique parametrization of the respective force field to capture its dynamics accurately. Over the past decades, numerous force fields have been published, and depending on the physical situation (solid, liquid, molecules, ions, etc.), they all employed different parametrization strategies. Fortunately, in this heuristic approach, one rarely starts by developing a force field from scratch. It is more common to build upon an existing force field, which then gets further fine-tuned following one of the two main strategies. The bottom-up approach, which I employed in my case, uses data from the nanoscopic level, *e.g.*, from quantum-mechanical calculations. Parameters like particle size, charge, and potential constants are fitted to, for example, DFT results obtained for a small subsystem of the material under study. Here, two critical steps are finding a suitable small model system and identifying the important parameters. Alternatively, in the top-down approach, one can start with experimental data from macroscopic properties of the materials and refine the parameters to match the experimental results.

In parts, my work is a continuation of existing studies<sup>107–109</sup> which built on the OPLS force field (optimized potentials for liquid simulations).<sup>110,111</sup> Introduced by Jorgensen and Tirado-Rives in the late 1980s, it has been successful in describing the structural and thermodynamic properties of organic molecules in different environments. Over the years, researchers have refined the force field for their applications (specific elements or functional groups) and improved its accuracy to better reproduce experimental results. Nowadays, the OPLS force field can be applied to a wide range of molecular systems, ranging from small molecules to liquids and proteins. However, the here studied PTBT system contains several dihedrals for which there exists no parametrization in the original or any following study; hence, the first step of this work consisted of finding a suitable parametrization for these dihedrals. In the original form, the dihedral potential is described by  $U_{ijkl}^{\text{dih,OPLS}}$ . One observation while parameterizing the missing dihedral potentials was that Eq. (2.16) was not capable of capturing the full potential sufficiently enough, which is why I chose the fifth-order Ryckaert-Bellmanns function 2.17 for the missing dihedrals instead. The other dihedrals are still described by Eq. (2.16). (an exemplary dihedral potential is shown in the upper left diagram in Fig. 2.5)

Besides the intra-molecular potentials, the description of non-bonded inter-

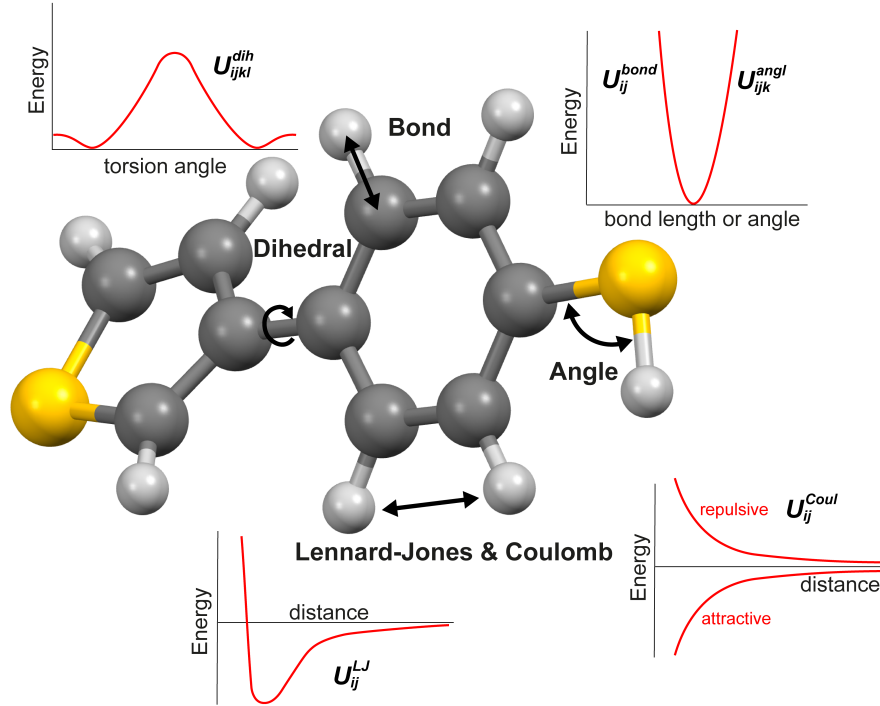


Figure 2.5: The ingredients of a force field presented for the example of a TBt molecule: harmonic bond stretching (Eq. (2.14)) and angle potentials (Eq. (2.15)), exemplary dihedral potential (like Eq. (2.16) or 2.17)), Lennard-Jones potential for van der Waals interactions (Eq. (2.19)), and Coulomb potential for electrostatic attraction and repulsion (Eq. (2.18)).

actions is just as important. Usually, these are composed of two contributions. On the one hand, there are electrostatic interactions between particles of positive/negative partial charges  $q_i$  and  $q_j$ , described by Coulomb's law

$$U_i^{\text{Coul}} = \sum_{j \neq i} U_{ij}^{\text{Coul}} = \sum_{j \neq i} \frac{q_i q_j}{\epsilon r_{ij}}, \quad (2.18)$$

with the dielectric constant  $\epsilon$  (*cf.* lower right diagram in Fig. 2.5). On the other hand, van der Waals interactions are apparent between all atom pairs, even with zero net partial charges. One of the most frequently used implementations to describe these interactions is the Lennard-Jones potential

$$U_i^{\text{LJ}} = \sum_{j \neq i} U_{ij}^{\text{LJ}} = \sum_{j \neq i} 4\epsilon_{ij} \left[ \left( \frac{\sigma_{ij}}{r_{ij}} \right)^{12} - \left( \frac{\sigma_{ij}}{r_{ij}} \right)^6 \right]. \quad (2.19)$$

The specific form of Eq. (2.19) is governed by the effective radius  $\sigma_{ij}$  and the depth of the potential minimum  $\epsilon_{ij}$ . Usually, these two parameters are given for atom pairs of the same species, and one calculates the values for the mixed cases by their geometrical ( $\epsilon_{ij} = \sqrt{\epsilon_{ii}\epsilon_{jj}}$ ) and arithmetic mean ( $\sigma_{ij} = (\sigma_{ii} + \sigma_{jj})/2$ ).<sup>112,113</sup> The first term in Eq. (2.19) describes the repulsive behavior at very short distances

due to the Pauli exclusion principle.<sup>114</sup> The second term characterizes the attraction between particles due to London dispersion forces<sup>115</sup> (*cf.* lower left diagram in Fig. 2.5).

The above discussion only represents a brief introduction to the area of force field development, and besides the discussed interactions, many more sophisticated variations and extensions exist.

Once the functional forms are chosen and all parameters are set, the trajectories of all  $N$  particles can be calculated by numerically solving the set of  $3N$  coupled differential equations for discrete time steps. The choice of a specific time step again depends on the system and the properties one wants to study. In general, the dynamics are limited by the highest frequency vibrations, which is most often the C–H bond stretching in the order of  $3000\text{ cm}^{-1}$  (corresponding to a time scale of  $10^{-14}\text{ s}$ , measured by infrared spectroscopy<sup>116</sup>). Therefore, a common simulation time step is one femtosecond (fs). Another prerequisite is to define an initial state of the system, that is, setting the positions and velocities of all particles. When simulating the dynamics of the system, the MD has to explore a representative region of the phase space (represented by the phase  $\pi = (\mathbf{r}, \mathbf{p})$  of coordinate and momentum). Hence, it is important that the outcome of a simulation does not depend on the initial state, so the simulation has to run for a sufficient long time. The beginning of an MD run is called the equilibration phase, after which there is no memory of the (arbitrarily) selected initial configuration.

The ability of an MD simulation to explore the phase space and yield a representative distribution of states is described by its so-called ergodicity.<sup>117</sup> This concept states that a particle of a dynamical system will eventually visit all states in the phase space during its natural evolution (within the given energy constraints). In order to achieve this, the trajectory of the MD run has to be long enough. A typical analysis of a trajectory consists of sampling, i.e., a series of  $M$  measurements of a particular system property  $A(\mathbf{r}, \mathbf{p}, t_i)$  over times  $t_i$ . From this, one can calculate the time average

$$\langle A \rangle_{\text{time}} = \frac{1}{M} \sum_{i=1}^M A(\mathbf{r}, \mathbf{p}, t_i). \quad (2.20)$$

The benefit of MD compared to quantum mechanical methods is that due to its simpler classical description, much larger systems (thousands of atoms) can be simulated over relatively long time scales (nano to microseconds). This is especially important for systems with high structural complexity, such as conjugated polymers. The ergodic property of the system now plays an important role when we move to the last scale in our multi-scale approach, which is the field of statis-

tical mechanics.

To summarize this section, all-atomistic molecular dynamics simulations offer a versatile computational approach for studying the behavior of molecular systems at the microscopic level. The approach is based on a classical description of particles with a defined spacial position and momentum, and the system's dynamics are obtained by solving Newton's equations of motion. The centerpiece of an MD simulation is the force field, which contains all information about the properties of the particles and their mutual interactions. The force field is parameterized in such a way that it captures specific behaviors that are observed on smaller or larger scales. Either way, using an all-atomistic MD force field, which builds up on information from the nano- or macro-scale, is a prime example of a multi-scale approach. In my work, I employed the OPLS force field for which I parameterized several dihedral potentials based on DFT calculations. I used MD simulations primarily to sample the conformational space of different structural models for the PTBT polymer. I then used these structures again for further quantum mechanical calculations.

### 2.3.3 Statistical mechanics

Statistical mechanics provides a connection between the macroscopic properties of a material and its microscopic behaviors.<sup>118</sup> Historically, this mathematical framework originates from the explanation of the phenomenological theory of thermodynamics. The field of thermodynamics describes macroscopic systems with the help of only a few quantities, such as temperature, pressure, and volume. However, thermodynamics is not a rigorous mathematical theory from which all these variables can be deduced. Instead, it relies on postulates (the thermodynamic laws), which comprise the empiric observation that macroscopic systems aim to go from a non-equilibrium to an equilibrium state. The actual mathematical validation of this observation is a matter of statistical mechanics.<sup>119</sup>

Statistical mechanics describes the macroscopic behavior of a system by an ensemble of many microscopic states. The term 'statistical ensemble' resembles a probability distribution  $\rho(\mathbf{r}, \mathbf{p})$  over all possible states of the system. As a special type, thermodynamic ensembles are those that describe systems in their thermodynamic equilibrium. This means that, although the system's dynamics might still change (the particles might still move) over time, the probability distribution is only a function of coordinates and momenta and is constant in time (stationary). Since any macroscopic system consists of an extremely large number of microscopic particles (1 mole contains  $\approx 10^{23}$  elementary entities), it is impossible to know the exact state (all coordinates and momenta) of all these constituents. Therefore,

statistical mechanics uses the concepts of probability theory to extract all macroscopic observables as averaged quantities from the ensemble. The way how the ensemble is represented depends on the macroscopical constraints. The four thermodynamic ensembles (*cf.* Fig. 2.6) defined by Gibbs<sup>120</sup> are the *microcanonical* ( $NVE$ ) ensemble where the number of particles  $N$ , the volume  $V$ , and the total energy  $E$  of the system is fixed. This only applies to totally isolated systems with no exchange or interaction with the environment, which is strictly not applicable to any realistic experiment. If the system is allowed to exchange energy with the environment in the form of heat (the particle number is still constant), it gets described by the *canonical* ( $NVT$ ) ensemble. Instead of the total energy, which is not exactly known, the temperature  $T$  of the system (the same as for the environment because of the thermal contact) is constant. If the system is entirely open (energy and particle exchange with the environment), it gets represented by the *grand canonical* ( $\mu VT$ ) ensemble, which defines the chemical potential  $\mu$  (that is, the amount of energy which gets absorbed or released due to a change in the number of particles) as constant. Another relevant ensemble is the *isothermal-isobaric* ( $NPT$ ) one, in which the system can change its volume, but the pressure is held constant.

We can now compare the MD approach with these statistical ensembles. Since the Newtonian equations of motion are energy-conserving, conventional MD describes the time evolution of a microcanonical ( $NVE$ ) system. This differs from most experimental scenarios because the system cannot be completely isolated from the environment so that its energy changes. Most often, the system's temperature is kept constant in conjunction with either the volume (canonical ensemble) or the pressure (isothermal-isobaric ensemble). If MD is not only seen as a way of simulating the (classical) nature of a system (based on Newton) but is more regarded as a tool to generate specific thermodynamic equilibrium states, one has to modify the dynamics.<sup>106</sup> This is done by adding so-called thermo- ( $NVT$ ) and barostats ( $NPT$ ) to the equations of motion to mimic the experimental conditions of fixed temperature and volume or pressure. There are different ways to formulate these thermo- and barostats, and the choice for a specific one depends on the system and the goal of the MD simulation. In my work, I used the Nosé-Hoover thermostat<sup>121</sup> and barostat,<sup>122</sup> which are known to give good control over temperature and pressure to maintain realistic conditions. The thermostat is included by adding a degree of freedom for the thermal reservoir, and the interaction strength between the system and bath is controlled by a coupling constant.<sup>121</sup>

Additionally, to solve the equations of motion for the system variables, the velocities are re-scaled by a factor that depends on the strength of the coupling constant. This dynamical velocity re-scaling ensures that the system's kinetic en-

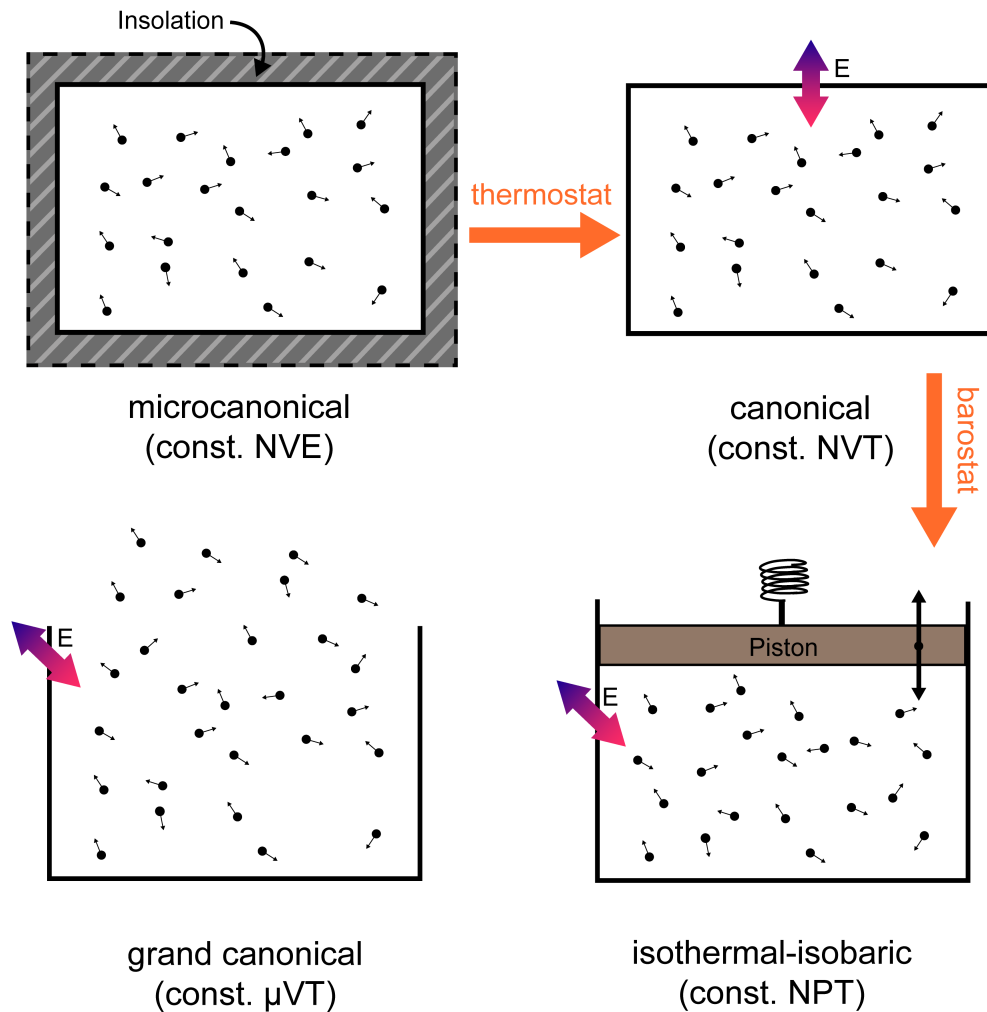


Figure 2.6: Visualization of four thermodynamic ensembles and how MD can transform them: the microcanonical ( $NVE$ ) ensemble is completely isolated from the outside (depicted by the grey border). In the canonical ( $NVT$ ) ensemble, energy exchange happens with the environment. Technically, this is done by applying a thermostat to the  $NVE$  ensemble. In the grand canonical ( $\mu VT$ ) ensemble, the system is completely open, i.e., energy and particle exchange between system and environment. In the isothermal-isobaric ( $NPT$ ) ensemble, the system shares the same constant pressure and temperature with the environment. Instead, its volume can change (depicted by the moving piston). This can be achieved by applying a an additional barostat to the ( $NVT$ ) ensemble.

energy remains close to the desired value, effectively controlling the temperature of the simulated system.<sup>121</sup> This concept can be extended to a barostat by including a reservoir controlling the pressure. Here, the instantaneous pressure of the system is calculated based on the virial theorem,<sup>123</sup> which is then coupled to the desired target pressure by a another coupling constant. A volume scaling factor is also calculated to correct the simulation cell volume. This mimics the action of a piston on a real system (*cf.* Fig. 2.6).

The average of an observable  $A(\mathbf{r}, \mathbf{p})$  in one of these ensembles is now taken over

the ensemble probability distribution of microstates

$$\langle A \rangle_{\text{stat}} = \int d\mathbf{r}d\mathbf{p} A(\mathbf{r}, \mathbf{p})\rho(\mathbf{r}, \mathbf{p}). \quad (2.21)$$

The ergodic hypothesis relates the statistical average 2.21 with the time average 2.20. In other words, the entirety of all ensemble states represents the total time evolution of the dynamical system ( $\langle A \rangle_{\text{time}} \equiv \langle A \rangle_{\text{stat}}$ ) but only if the system is ergodic meaning it eventually will populate every state of the ensemble after a certain time.

## 2.4 Statistical binding model of a vulcanized polymer

The main object of interest in my investigations was the vulcanized PTBT polymer. This system results from the chemical vulcanization reaction between the organic polymer and elemental sulfur. However, the chemical reaction during the vulcanization cannot be captured by a classical force field due to the harmonic bond potential (*cf.* Fig. 2.5). Although there are possibilities to combine quantum mechanics to account for the chemical reactivity together with a force field description (*e.g.*, *ab-initio* MD<sup>124</sup> or QM/MM<sup>125</sup> methods), these approaches are computationally costly. As an alternative approach, I focused on the vulcanization outcome, which I described as a thermodynamic equilibrium. In the following, I will outline how I derived an expression for the probability distribution representing the statistical ensemble of this equilibrium state.

The vulcanization process is thought of as mixing two reactants, the PTBT polymer (characterized by the  $-\text{SH}$  binding sites) and the  $\text{S}_8$  sulfur rings together, to yield a product state, the vulcanized S/PTBT system. The chemical equilibrium of this binding reaction is reached when the chemical composition of the system does not change anymore. According to thermodynamics, this is characterized by the system's free energy being at a minimum. If an isothermal-isobaric ensemble represents the system, the Gibbs free energy  $G(p, T)$  gets minimized. If we consider a general binding reaction



of  $\alpha$  moles of A and  $\beta$  moles of B to form  $\gamma$  moles of a product state AB, the ratio of molar concentrations of product species over reactant species is defined as the reaction quotient<sup>126</sup>

$$Q(t) = \frac{[AB]_t^\gamma}{[A]_t^\alpha [B]_t^\beta}, \quad (2.23)$$

with  $[...]_t$  denoting the instantaneous concentrations of reactants and products. Eq. (2.23) is time-dependent since it gives the instantaneous ratio of the amounts of  $A$ ,  $B$ , and  $AB$ . In the chemical equilibrium,  $Q(t \rightarrow \infty)$  asymptotically approaches a constant value called the equilibrium binding constant  $K^c$ . Note that  $K^c$  has the dimension of concentration ( $\text{mol l}^{-1}$ ) to some power (depending on the molar ratio). It is common to convert this into a dimensionless value by

$$K = \frac{K^c}{C_0}, \quad (2.24)$$

where  $C_0$  is a constant with the same units as  $K^c$ . This conversion is equivalent to defining a reference or standard state.<sup>127</sup>  $K$  is then called the standard state equilibrium constant. It is important to note that the choice of  $C_0$  is arbitrary. However, in experiments, there is the convention to use the standard concentration  $C_0 = 1 \text{ M}$  ( $1 \text{ mol l}^{-1}$ ), corresponding to a standard volume  $v_0 = 1 \text{ mol}^{-1}$ .<sup>127,128</sup> The dimensionless equilibrium constant  $K$  can then be related to the standard Gibbs free energy change  $\Delta G$  of the reaction by<sup>126,129</sup>

$$\Delta G = -k_B T \ln(K). \quad (2.25)$$

As discussed in section 2.2, the final sulfurized polymer consists of sulfur chains  $S_n$  of different lengths covalently bonded to the organic framework. This is due to the characteristic behavior of sulfur forming chain-like free radicals of various lengths depending on the temperature. The situation of different chain lengths in the vulcanized polymer can be described by multiple binding equilibria<sup>126</sup> of a certain amount  $n = 1, 2, 3, \dots, m$  of sulfur atoms  $x$  binding to the polymer  $P$ :



Each equilibrium constant  $K_n^c$  is defined by

$$K_n^c = \frac{[Px_n]}{[P][x]^n}. \quad (2.27)$$

Different sulfur chain lengths are described in the statistical ensemble describing the sulfurized S/PTBT polymer. In total, they are represented by the sum of all respective concentrations of binding products

$$\begin{aligned}
Q_B[P] &= [P] + [Px] + [Px_2] + \dots + [Px_m] \\
Q_B[P] &= [P](1 + K_1^c[x] + K_2^c[x]^2 + \dots + K_m^c[x]^m) \\
\implies Q_B([x]) &= 1 + K_1^c[x] + K_2^c[x]^2 + \dots + K_m^c[x]^m \\
Q_B([x]) &= \sum_{n=0}^m K_n^c[x]^n.
\end{aligned} \tag{2.28}$$

The sum  $Q_B$  is called the binding polynomial. It is describing all possible binding states. With this, one can calculate the probability

$$\rho(n) = \frac{[Px_n]}{Q_B[P]} \tag{2.29}$$

of having the binding state  $n$  in the ensemble. From here, one has access to all other statistical quantities, such as the mean

$$\bar{n} = \sum_n n\rho(n) = \sum_n n \frac{[Px_n]}{Q_B[P]} = Q_B^{-1} \sum_{n=0}^m n K_n^c[x]^n \tag{2.30}$$

or the standard deviation of the distribution

$$\sigma_n = \sqrt{\sum_{n=0}^m (\bar{n} - n)^2 \rho(n)}. \tag{2.31}$$

The equilibrium constants in Eq. (2.29) - (2.31) can now be substituted with the Gibbs free energy of change *via* Eq. (2.25) (while taking care of the dimensions according to Eq. (2.24)). Doing so, the microscopic information  $\Delta G$  representing the thermodynamic favorability of the binding reaction is used in the macroscopic description of the vulcanized polymer as a statistical ensemble. This way, I derive a multi-scale model of the vulcanized polymer system.

## 2.5 Charge transport in conjugated polymers

In section 2.2, I discussed the benefits of using conjugated polymers as a cathode material due to their conducting behavior. In the following, I will explain how this behavior can be rationalized by looking at their electronic structure. Furthermore, I will present the methods that I have used to investigate the charge transport properties of the PTBT polymer based on its electronic properties.

### 2.5.1 Electronic band structure of conjugated systems

The electronic structure of a conjugated molecule can be explained by molecular orbital (MO) theory,<sup>130</sup> which describes the spatial and energetic properties of the electrons as a linear combination of atomic orbitals (LCAO method) surrounding the atoms.

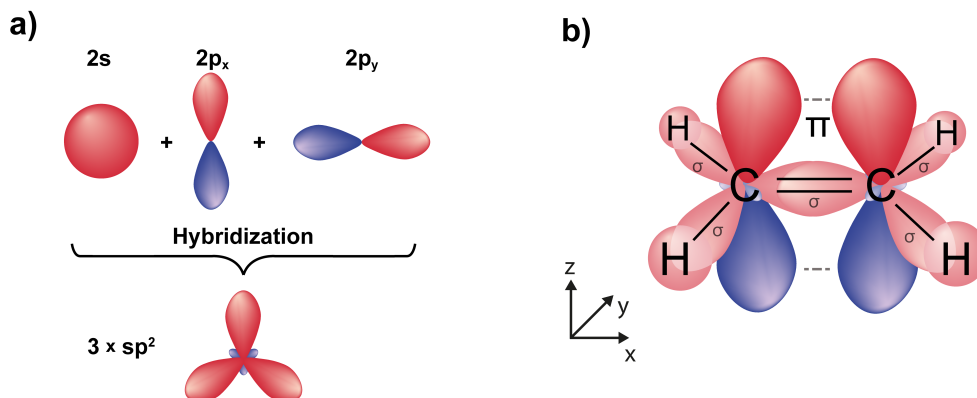


Figure 2.7: a) the hybridization of carbon's 2s orbital with the 2p<sub>x</sub> and 2p<sub>y</sub> orbital results in three planar sp<sup>2</sup> atomic orbitals (red and blue colors depict the positive and negative phases, respectively). b) schematic of the conjugated π electron system of ethylene. Each carbon atom forms a σ-bond with two hydrogen atoms and to the other carbon. Perpendicular to the molecular *xy*-plane, the atomic p<sub>z</sub> orbitals form one bonding molecular π orbital indicated by the dashed grey lines.

The smallest conjugated molecule, ethylene C<sub>2</sub>H<sub>4</sub> (CH<sub>2</sub>=CH<sub>2</sub>), has 12 valence electrons (four from each carbon atom and one from each hydrogen atom). The covalent bonding between the six atoms can be explained by the hybridization of the carbon atomic orbitals (AOs). The ground state electronic configuration of carbon is denoted as 1s<sup>2</sup> 2s<sup>2</sup> 2p<sup>2</sup>. In ethylene, the 2s AO of carbon mixes with two 2p orbitals (2p<sub>x</sub> and 2p<sub>y</sub>) to form three sp<sup>2</sup> orbitals with one remaining 2p<sub>z</sub> orbital (*cf.* Fig. 2.7a). Each carbon atom forms then two covalent C–H bonds by s–sp<sup>2</sup> overlap and the remaining two hybrid orbitals form a single covalent bond between the two carbons. All these single bonds account for 10 of the 12 valence electrons. Since they all lie in the molecular plane (*i.e.*, they are symmetric to the *xy*-plane), they can be categorized into one group, denoted as σ bonds. The remaining two 2p<sub>z</sub> orbitals of the carbons are perpendicular to this plane (*cf.* Fig. 2.7b). Their overlap forms a so-called π bond additionally to the σ bond between the two carbons (resulting in the double bond). Because of the phase of the AOs (depicted as blue and red), the resulting π bond is anti-symmetric to the molecular plane. The separation into σ and π bonds is strictly only valid if there is no overlap between the two, which is only the case in perfectly planar molecules. The Hückel method describes the interaction of these π electrons to give an qual-

itative picture of how the electronic energy levels of a conjugated system depend on its structural topology.<sup>131–134</sup> The Hückel method makes use of the LCAO principle, which predicts the conservation of orbitals. Thus, the number of  $N$  AOs results in the same number of MOs. For the ethylene molecule, this means that the linear in-phase and out-of-phase combination of the two  $2p_z$  AOs results in two MOs, the  $\pi$  and  $\pi^*$  orbital (*cf.* Fig. 2.8a). In the  $\pi$  MO, the in-phase combination of the AOs increases the electron density between the carbon nuclei drawing the atoms closer together and thus leading to a stabilization (equal to a lowering in energy). The two  $2p_z$  electrons (depicted as red arrows) will occupy this MO, hence it is referred to as *bonding*. In contrast, the out-of-phase combination in the  $\pi^*$  MO results in a node between the carbon nuclei along a plane perpendicular to the bond axis (green dashed line). This means, the probability of finding an  $\pi$  electron in this plane is zero which consequently reduces the electron density between the carbons. Therefore, this MO is higher in energy than the bonding MO and is called *anti-bonding*. The  $\pi$  MO represents the highest occupied molecular orbital (HOMO) and the  $\pi^*$  MO as the next available one is denoted as the lowest unoccupied molecular orbital (LUMO).

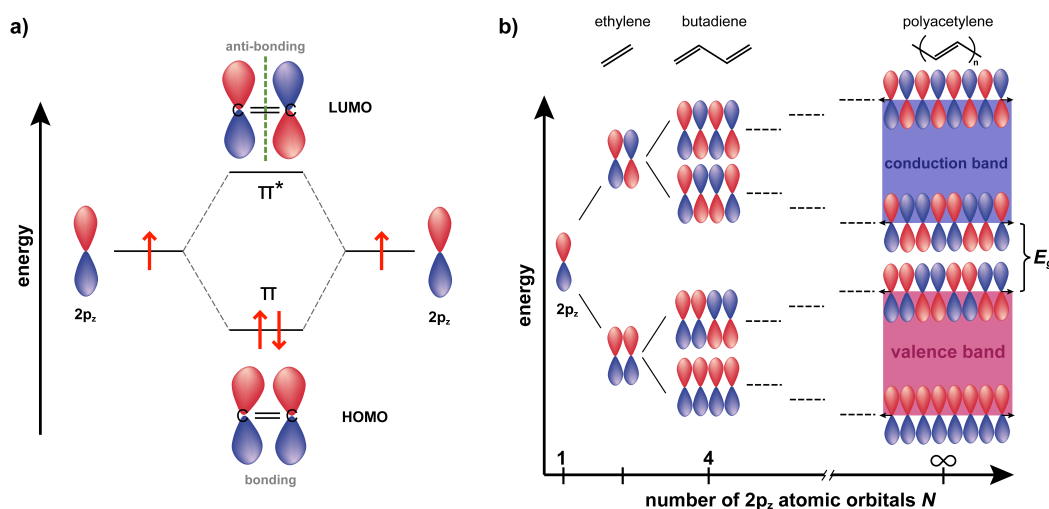


Figure 2.8: a) the in-phase and out-of-phase combination of the electrons (indicated by red arrows) in the two  $2p_z$  AOs results in a doubly occupied, *i.e.* bonding,  $\pi$  MO (HOMO) and an unoccupied anti-bonding  $\pi^*$  MO (LUMO), respectively. The LUMO has a node (dashed green line) between the carbon nuclei along a plane perpendicular to the bond axis. b) schematic illustration of the in-phase and out-of-phase combinations of  $2p_z$  AOs going from ethylene ( $N = 2$ ) to polyacetylene ( $N = \infty$ ). The splitting of the energy levels with increasing chain length results in two bands (a filled valence and an empty conduction band). Their energetical separation is called the band gap  $E_g$ .

Taking the ethylene molecule as the basic unit, we can extend the same concept to longer polyenes molecules. Their  $\pi$  electronic structure can be constructed

by a combination of ethylene sub-units (*cf.* Fig. 2.8b). Starting with two  $2p_z$  AOs, one gets one bonding and one anti-bonding  $\pi$ -MO. Doubling the number of carbon atoms results in the four  $\pi$  MOs of butadiene ( $N = 4$ ). With increasing chain length, the  $2p_z$  AOs overlap over a larger number of carbon atoms. Thus, the resulting MOs span over a larger part of the chain, leading to greater delocalization of the  $\pi$  electrons. In the limit of an infinite long chain ( $N = \infty$ ), the energy splitting between adjacent MOs becomes infinitesimally small that the discrete energy levels evolve into continuous bands. The entirety of all filled MOs is called the valence band (VB) and all empty MOs form the conduction band (CB). Interestingly, this procedure would mean that the HOMO (the top of the VB) and the LUMO (the bottom of the CB) would have the same energy, *i.e.* they would be energetically degenerated, because they are equivalent in the number of bonding and anti-bonding patterns just shifted by one bond. However, in an actual polyacetylene chain, there exists an energetic gap  $E_g$  between the two bands. This can be explained by the so-called Peierls distortion<sup>135</sup> of a one-dimensional periodic chain which in case of the ground state geometry of polyacetylene is seen in a bond length alternation between shorter C=C double-bonds and longer C–C single bonds. Since this geometry is reflected in the bonding–anti-bonding pattern of the HOMO (bonding at double-bonds and anti-bonding at single-bonds), it is energetically stabilized. In the LUMO, in contrast, this pattern is shifted by one bond (anti-bonding at double-bonds and bonding at single-bonds) which makes it energetically less favourable.<sup>136</sup> The band gap of a system describes an energetic region where no electronic states are allowed. If an electron would be added to the polyacetylene system, it would occupy the next energetically available state in the conduction band.

In order to describe the electronic configuration of polyacetylene in mathematical terms, one can make use of the translational symmetry of the system due to its spatial periodicity. The translational symmetry of such a perfectly regular chain would be expressed as

$$\rho(\mathbf{r} + j\mathbf{a}) = \rho(\mathbf{r}). \quad (2.32)$$

Equation 2.32 is called Bloch's theorem<sup>137</sup> describing the equality between the electronic density  $\rho$  at point  $\mathbf{r}$  and any other point  $\mathbf{r} + j\mathbf{a}$  along the chain with  $|\mathbf{a}|$  as the length of the repeating chain pattern (the unit cell) and  $j$  being an integer number. In quantum mechanics, the density of an electron in a particular orbital  $\phi_n$  is given by the square of the wave function, hence Eq. (2.32) translates into

$$|\phi_n(\mathbf{r} + j\mathbf{a})|^2 = |\phi_n(\mathbf{r})|^2. \quad (2.33)$$

Building on the AOs  $\chi_n(\mathbf{r})$ , one can construct so-called Bloch functions

$$\phi_{n\mathbf{k}}(\mathbf{r}) = \sum_j e^{i\mathbf{k}j\mathbf{a}} \chi_n(\mathbf{r} - j\mathbf{a}), \quad (2.34)$$

which represent the molecular orbitals and obey the Bloch theorem. In Eq. (2.34), the signs and amplitudes of the AOs at different sites  $j$ ,  $\chi_n(\mathbf{r} - j\mathbf{a})$  (*e.g.*, the  $2p_z$  orbitals) are modulated by the phase factors  $\exp(i\mathbf{k}j\mathbf{a})$ . Here, the so-called wave vector  $\mathbf{k}$  is a measure for the number of sign changes of the atomic orbitals. Since the exponential has to be a pure number,  $\mathbf{k}$  must have the dimension of inverse length. It is thus defined in the reciprocal space and can be related to the momentum  $\mathbf{p}$  of the electron by the relation  $\mathbf{p} = \hbar\mathbf{k}$  where  $\hbar$  is the reduced Planck constant. At the same time,  $\mathbf{k}$  can be associated with the wavelength  $\lambda$  of the phase factor representing a plane wave *via*  $|\mathbf{k}| = 2\pi/\lambda$ . In general, the wave vector represents a three-dimensional quantity but for a 1D-periodic system, such as polyacetylene, it reduces to a scalar  $k$ .

One can now plot the energy of a Bloch function in dependency of the wave vector  $k$ . It is the dispersion relation between the energy  $\epsilon(k)$  of a particular orbital  $\phi_n$  and the wave vector that defines the electronic bands in the reciprocal space. The entirety of electronic bands originating from all atomic orbitals is called the band structure of the system. Because of the periodicity in direct space, the electronic bands must also be periodic in reciprocal space. Therefore, it is convenient to calculate the dispersion relation only for a range of values between  $k = -\pi/a$  and  $k = \pi/a$  within a unit cell that has the inverse length  $g = 2\pi/a$ . This reciprocal unit cell is called the first Brillouin zone (BZ). Another consequence of Bloch's theorem is that the electronic bands are symmetric to the origin of  $k = 0$ . Thus, one only has to plot the first half of the BZ.

A schematic illustration of the dispersion relation of polyacetylene's  $\pi$  and  $\pi^*$  band is shown in Fig. 2.9. At  $k = 0$ , the  $\pi$  band is fully bonding corresponding to an infinite wavelength (no sign changes of the  $2p_z$  AOs). As  $k$  increases, the energy of the band goes up, maximizing at  $k = \pi/a$  where the MO is bonding at the double-bonds and anti-bonding at the single-bonds. This corresponds to the HOMO of the system and is described by a wavelength of  $\lambda = 2a$ . For the  $\pi^*$  band, this behavior is reversed as it goes down in energy when moving away from the center of the BZ. At  $k = 0$ , the band is fully anti-bonding corresponding to the highest  $\pi^*$  MO while at the edge of the BZ, it describes the system's LUMO. Again, the energy gap  $E_g$  between the two bands at  $k = \pi/a$  is due to the Peierls

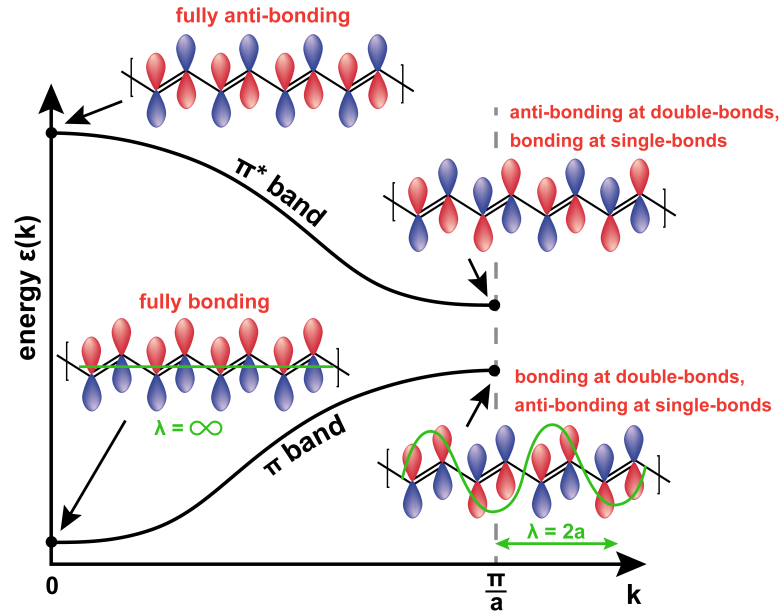


Figure 2.9: Schematic of the energy dispersion relation  $\epsilon(k)$  for the  $\pi$  and  $\pi^*$  band of polyacetylene. The insets show the pattern in sign changes of the contributing  $2p_z$  AOs at the center ( $k = 0$ ) and the edge ( $k = \pi/a$ ) of the BZ. The corresponding wavelengths ( $\lambda = 2\pi/k$ ) are shown in green.

distortion.

The difference of the band energy between the center and the edge of the BZ is described as the band width and is a measure for the degree of overlap of the interacting AOs. This is related to their separation and relative orientation. In case of the  $\pi$  bands of polyacetylene, this simply depends on the carbon atom distances. The closer the atoms are, the greater the overlap between adjacent AOs is, and hence the larger the band width. With greater overlap of the  $2p_z$  AOs, the electrons are more freely to move along the delocalized  $\pi$  orbitals. Hence, it is the inherent property of having a  $\pi$  electron system that imparts electrical conductivity to conjugated polymers. Using heterocyclic rings as part of a polymer backbone (*cf.* Fig. 2.3) enlarges the spatial extend of the  $\pi$  system and can further improve the movement of electrons across the material.

So far, I have discussed the case of a 1D periodic chain to illustrate the concept of electronic bands. For my investigations of the PTBT polymer, I extended this to three dimensions describing the system as a polymeric crystal. Furthermore, I have used DFT instead of the Hückel method to calculate the electronic band structure. For the 3D-case, the Brillouin zone represents generally a polyhedron in reciprocal space depending on the crystal structure in direct space. In Fig. 2.10a), the Brillouin zone for a simple orthorhombic crystal lattice is shown.<sup>138</sup> A common way to display the four-dimensional dispersion relation  $\epsilon(\mathbf{k})$  is to plot the band

energies against  $\mathbf{k}$ -values along straight lines that connect high-symmetry points of the BZ (*e.g.*, the path  $\Gamma - X - S - Y$  in reciprocal space). The exemplary band structure in Fig. 2.10b) describes a system with a band gap where in the ground state the valence band would be filled completely and the conduction band would be empty. The highest occupied state is denoted as the valence band maximum (VBM) and the next available state above the band gap as the conduction band minimum (CBM) for all respective  $\mathbf{k}$ -values.

Given the band structure  $\epsilon(\mathbf{k})$ , one can also calculate the density of states (DOS) by integrating over all  $\mathbf{k}$ -values in the Brillouin zone

$$g(\epsilon) = \int d\mathbf{k} \delta(\epsilon - \epsilon(\mathbf{k})), \quad (2.35)$$

with the Dirac delta function  $\delta(\epsilon - \epsilon(\mathbf{k}))$ . The DOS gives the number of available states per unit volume and energy and is important to determine how many charge carriers are available for transport.

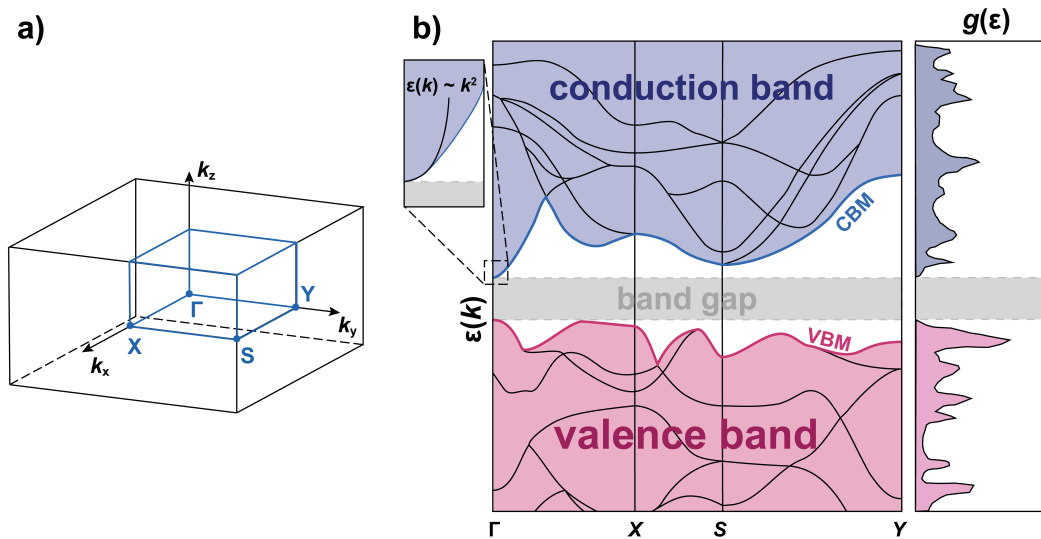


Figure 2.10: a) the Brillouin zone of an orthorhombic crystal unit cell with the high-symmetry  $\mathbf{k}$  points  $\Gamma$ ,  $X$ ,  $S$ , and  $Y$ . b) schematic illustration of an exemplary band structure  $\epsilon(k)$  and the corresponding density of state  $g(\epsilon)$  for a system with a band gap (grey area) separating the VB (red) and CB (blue). The inset shows a magnification of the conduction band minimum at the  $\Gamma$ -point near which the dispersion relation  $\epsilon(\mathbf{k})$  can be approximated to be parabolic.

In a system without an extended  $\pi$  system, where the electrons cannot delocalize and move freely, the ability for electrons to participate in conduction depends on the availability of vacant electronic states. If the valence band is completely filled and no vacant state are available, the electrons would not be able to move and the material would not be conducting. The only way to increase the conductivity would be to excite electrons into higher states in the CB so that they are

able to move. An electron that moves into the CB leaves an empty space in the valence band which allows other electrons to fill it. The conduction of these valence electrons can be described by the movement of the vacancy which is called a hole. If the band gap is small enough, electrons could be already excited thermally into the CB. Materials with such a band structure are known as semiconductors. The density of electrons in the CB and of holes in the VB is given by<sup>139</sup>

$$\rho_e = \int_{\text{CB}} d\epsilon g(\epsilon) f(\epsilon), \text{ and} \quad (2.36)$$

$$\rho_h = \int_{\text{VB}} d\epsilon g(\epsilon) (1 - f(\epsilon)), \quad (2.37)$$

with the Fermi-Dirac function

$$f(\epsilon; T) = \frac{1}{e^{(\epsilon - \mu_{\text{chem}})/k_B T} + 1}, \quad (2.38)$$

describing the probability distribution of an ensemble of many fermionic particles such as electrons or holes. Here,  $T$  denotes the temperature,  $k_B$  the Boltzmann constant, and  $\mu_{\text{chem}}$  the chemical potential describing the energy gain or loss of the system due to a change in the number of electrons. The latter describes the reflection point of the distribution. At zero absolute temperature,  $f(\epsilon; T = 0)$  becomes a step-function at  $\epsilon = \mu_{\text{chem}}$  and the chemical potential is referred to as the Fermi energy  $\epsilon_F$  up to which all electronic states are occupied. For a system with a band gap, the Fermi energy is usually located in the middle of the gap.<sup>140</sup>

## 2.5.2 Band-like transport regime

In the following, I will describe how I calculated the electrical conductivity of a polymer based on its band structure. The underlying charge transport mechanism of this description relies on the delocalized picture of charge carriers which move through the extended  $\pi$ -system of the material and the corresponding regime is called the band transport regime.<sup>141</sup>

In general, the electrical conductivity  $\sigma$  is determined by the concentration of charge carriers  $N$  and their mobility  $\mu$

$$\sigma = qN\mu, \quad (2.39)$$

with  $q$  as the charge of the carrier. The concentration of charge carriers is the net concentration given by the difference of electron and hole density

$$N = \frac{\rho_e - \rho_h}{V_{\text{BZ}}}, \quad (2.40)$$

with the volume of the crystal unit cell  $V_{\text{BZ}}$ . The mobility of a charge carrier describes its ability to move through the material. Regardless of the specific system and the underlying charge transport mechanism, the mobility is defined as the velocity response of a charge carrier to an external electric field

$$\mu_{ij} = \frac{\langle v_i \rangle}{E_j}, \quad (2.41)$$

where  $\langle v_i \rangle$  denotes the  $i$ th component of the time-averaged velocity  $\langle \mathbf{v} \rangle$  of the charge and  $E_j$  as the  $j$ th component of the electric field  $\mathbf{E}$ .<sup>139</sup> In general, both  $\langle \mathbf{v} \rangle$  and  $\mathbf{E}$  are three-dimensional vectors which makes the mobility a tensor of rank 2 but if the velocity response in direction  $i$  only depends on the field strength in that direction, the mobility reduces to a scalar quantity  $\mu$ .

For the later application of the polymer in a battery cathode, the system will be electrochemically doped with electrons during cycling. Therefore, the focus lies in the movement of electrons through the polymer's conduction band. For now, I will only consider a single band and drop the index  $n$  denoting a specific electronic band. Similar to the group velocity of a wave packet moving through a dispersive medium, the velocity of an electron in a particular band can be expressed by the reciprocal space gradient of the dispersion relation

$$\mathbf{v}_{\mathbf{k}} = \nabla_{\mathbf{k}} \epsilon(\mathbf{k}) / \hbar \quad (2.42)$$

In analogy to the classical case of a charged particle in an electric field, one can write a Newtonian equation of motion for the electron that moves through the polymeric system because of the external field

$$F_i = qE_i = \left( \frac{1}{m_{\text{eff},ij}} \right)^{-1} \frac{dv_j}{dt}, \quad (2.43)$$

Here,  $m_{\text{eff},ij}$  is called the effective mass of the electron that is defined as the curvature of the dispersion relation

$$\frac{1}{m_{\text{eff},ij}} = \frac{1}{\hbar^2} \frac{\partial^2 \epsilon(\mathbf{k})}{\partial k_i \partial k_j}. \quad (2.44)$$

In contrast to the rest mass of a free electron, the effective mass incorporates the effect of the crystal's periodic potential in which the electron moves.<sup>139</sup> In general,  $m_{\text{eff},ij}$  is a second rank tensor but often one can apply a transformation into the symmetry-based principal axes of the crystal to only consider the diagonal elements.<sup>142</sup> Note, that Eq. (2.43) is a harmonic approximation and is therefore only valid at the extrema points of the band structure where the dispersion can be described by a parabolic function. In case of electron conduction, these extrema

are the conduction band minima (*cf.* inset in Fig. 2.10b).

For any applied field, Eq. (2.43) would describe an indefinite acceleration of an electron through the material. However, there are other effects which act against the acceleration by the electric field. At finite temperatures  $T$ , the atoms of the crystal are not static but vibrate around their equilibrium positions due to thermal energy. The quantized energy of the collective vibrational motion of the crystal can be described by a quasi-particle, a so-called phonon. The influence of the crystal vibrations on the movement of an electron can be expressed as an elastic scattering event between the two particles.<sup>141</sup> This scenario is called ballistic conduction where the interplay of the acceleration by the electric field and the scattering due to thermal fluctuations leads to a finite velocity of the moving electron. In a more realistic system, one could also consider the scattering of electrons with impurities, that is any structural deviations from the crystal's periodicity. However, here, I will only consider electron-phonon interactions.

To model the charge transport in such a scenario, I employed the Boltzmann transport equation.<sup>141,143,144</sup> This equation describes the statistical ensemble of conducting electrons by a probability distribution function  $f(\mathbf{r}, \mathbf{k}, t)$  in the coordinate and momentum (*i.e.*  $\mathbf{k}$ -) phase space (*cf.* section 2.3.3). This distribution function is defined such that  $f(\mathbf{r}, \mathbf{k}, t)d\mathbf{r}d\mathbf{k}$  gives the number of electrons with position in  $d\mathbf{r}$  around  $\mathbf{r}$  and wave vectors in  $d\mathbf{k}$  around  $\mathbf{k}$  at time  $t$ . The time evolution of  $f(\mathbf{r}, \mathbf{k}, t)$  is governed by three different factors: the external electric field that drives the distribution out of equilibrium, the diffusion of electrons which moves the distribution in time, and the scattering processes with phonons which restore the distribution to equilibrium again. The general BTE describes then the steady-state situation

$$\left(\frac{\partial f}{\partial t}\right)_{\text{field}} + \left(\frac{\partial f}{\partial t}\right)_{\text{diffusion}} + \left(\frac{\partial f}{\partial t}\right)_{\text{scattering}} = 0. \quad (2.45)$$

In order to solve this equation, one usually considers the relative change

$$g(\mathbf{r}, \mathbf{k}, t) = f(\mathbf{r}, \mathbf{k}, t) - f^0(\mathbf{r}, \mathbf{k}, t), \quad (2.46)$$

of the distribution  $f$  against the equilibrium distribution  $f^0$ . In the absence of an external field, the equilibrium distribution is given by a Fermi-Dirac function Eq. (2.38) but it might be described as  $f^0(\mathbf{r}, \mathbf{k}, t)$  because the chemical potential  $\mu_{\text{chem}}(\mathbf{r}, t)$  and temperature  $T(\mathbf{r}, t)$  can in general depend on  $\mathbf{r}$  and  $t$ . For simplicity, I will assume that  $\mu_{\text{chem}}(\mathbf{r}, t)$  and  $T(\mathbf{r}, t)$  are both space- and time-independent which makes the equilibrium distribution function only implicitly dependent on  $\mathbf{k}$ , *i.e.*  $f_{\mathbf{k}}^0 \equiv f^0(\epsilon(\mathbf{k}))$ . Equation 2.45 can then be reduced to

$$-e\mathbf{E}\mathbf{v}_{\mathbf{k}}\frac{\partial f_{\mathbf{k}}^0}{\partial \epsilon} = -\left(\frac{\partial f(\mathbf{r}, \mathbf{k}, t)}{\partial t}\right)_{\text{scattering}}. \quad (2.47)$$

The difficulty in solving this equation lies in the description of the scattering processes between electrons and phonons. A common solution to this problem is the so-called relaxation time approximation (RTA)

$$-\left(\frac{\partial f(\mathbf{r}, \mathbf{k}, t)}{\partial t}\right)_{\text{scattering}} = \frac{g(\mathbf{r}, \mathbf{k}, t)}{\tau}, \quad (2.48)$$

with the relaxation time  $\tau$ . If the external field  $\mathbf{E}$  would be switched off, the 'out of balance'  $g(\mathbf{r}, \mathbf{k}, t)$  of the distribution would decay on the scale of  $\tau$  according to

$$-\frac{\partial g}{\partial t} = \frac{g}{\tau} \implies g(\mathbf{r}, \mathbf{k}, t) = g(\mathbf{r}, \mathbf{k}, 0)e^{-t/\tau}. \quad (2.49)$$

Hence, the physical interpretation of  $\tau$  is that of the average time between scattering events which reset the pertubated distribution  $f$  to its equilibrium  $f^0$ . In general, the relaxation time may depend on the energy of the electrons  $\tau(\epsilon(\mathbf{k}))$  but for simplicity I consider it to be energy-independent.

I will now derive an expression for the macroscopic conductivity of the collective motion of electrons through the material. By integrating over the distribution function in  $\mathbf{k}$ -space, one can calculate the electric current density at point  $\mathbf{r}$  which is given by

$$\mathbf{j}(\mathbf{r}, t) = -e \sum_n \int d\mathbf{k} f_n(\mathbf{r}, \mathbf{k}, t) \mathbf{v}_{n,\mathbf{k}}. \quad (2.50)$$

Here, I reintroduce the band index  $n$  again. The sum over  $n$  considers all electrons in the conduction band that contribute to the current. Using  $f = g + f^0$  from Eq. (2.46) and inserting Eq. (2.47) and (2.48), this can be written as

$$\mathbf{j} = -e^2\tau \sum_n \int d\mathbf{k} \mathbf{v}_{n,\mathbf{k}} \mathbf{v}_{n,\mathbf{k}} \frac{\partial f_{n,\mathbf{k}}^0}{\partial \epsilon_{n,\mathbf{k}}} \mathbf{E}. \quad (2.51)$$

Comparing Eq. (2.51) with Ohm's law  $\mathbf{j} = \boldsymbol{\sigma}\mathbf{E}$ , finally yields an expression for the conductivity

$$\boldsymbol{\sigma} = -e^2\tau \sum_n \int d\mathbf{k} \mathbf{v}_{n,\mathbf{k}} \mathbf{v}_{n,\mathbf{k}} \frac{\partial f_{n,\mathbf{k}}^0}{\partial \epsilon_{n,\mathbf{k}}}. \quad (2.52)$$

For a given band structure, the integral in Eq. (2.52) can be simply calculated by taking the derivatives of the dispersion relation (Eq. (2.42)). In contrast, the

relaxation time  $\tau$  is more complicated to calculate since one has to consider the exact scattering mechanisms between electrons and phonons. Generally, one can distinguish between acoustic and optical phonons.<sup>145</sup> Acoustic phonons are associated with the collective vibrations of atoms in the crystal lattice that involve the entire lattice moving in a coordinated manner. They are usually characterized by longer wavelengths, hence lower frequencies and energies. Optical phonons, in turn, involve vibrations associated with the relative motion of charged particles within the unit cell and therefore feature higher frequencies than acoustic phonons. If the interactions between electrons and these two types of phonons are statistically independent, the total scattering rate, which is the inverse of the relaxation time, is given by Matthiessen's rule<sup>145</sup>

$$\frac{1}{\tau} = \frac{1}{\tau^{\text{acc}}} + \frac{1}{\tau^{\text{op}}}. \quad (2.53)$$

In principal, the rate for a scattering event that relaxes a state  $|n, \mathbf{k}\rangle$ , with band index  $n$  and wave vector  $\mathbf{k}$ , into a state  $|n', \mathbf{k}'\rangle$  can be calculated based on Fermi's golden rule<sup>146</sup>

$$\frac{1}{\tau} = \frac{2\pi}{\hbar} \sum_{n', \mathbf{k}'} |\langle n, \mathbf{k} | \Delta V | n', \mathbf{k}' \rangle|^2 \delta(\epsilon_n(\mathbf{k}) - \epsilon_{n'}(\mathbf{k}')) (1 - \cos \Theta). \quad (2.54)$$

Here,  $\langle n, \mathbf{k} | \Delta V | n', \mathbf{k}' \rangle$  describes the matrix element in Dirac notation<sup>147</sup> of the perturbation  $\Delta V$ , that causes the transition between the initial and final state, and  $(1 - \cos \Theta)$  is a weighting factor for the angle  $\Theta$  between the wave vectors  $\mathbf{k}$  and  $\mathbf{k}'$ . Since the energy of optical phonons is usually higher than that of acoustic phonons, one can make the approximation that the thermal fluctuations of the crystal at room temperature only correspond to the latter ones. For my calculations of the relaxation time, I considered the scattering of electrons with acoustic phonons to be the dominant mechanism. In this approximation, I used the deformation potential theory<sup>26</sup> to describe the matrix element in Eq. (2.54). The physical interpretation of this theory is, that the interactions between electrons and acoustic phonons lead to changes in the volume and shape of the crystal lattice. The perturbation  $\Delta V$  is then a linear function of the strain induced by the lattice deformation with a coupling constant  $\mathbf{D}_{\text{def}}$ , the deformation potential. In this model, the relaxation time  $\tau_i^{\text{acc}}$  along a crystal direction  $i$  can be derived from<sup>148</sup>

$$\tau_i^{\text{acc}} = \frac{C_i \hbar^2}{\sqrt{k_B T m_{\text{eff}, ii}} D_{\text{def}, ii}^2}. \quad (2.55)$$

The deformation potential in direction  $i$ ,  $D_{\text{def},ii}$ , is the response of a single electron's energy (taken at an extremal  $\mathbf{k}$ -point  $\mathbf{k}_e$ ) to a lattice deformation  $\delta l_i$  along direction  $i$

$$D_{\text{def},ii} = \left. \frac{\partial \epsilon(\mathbf{k})}{\partial \delta l_i} \right|_{\mathbf{k}=\mathbf{k}_e}. \quad (2.56)$$

The other factor introduced in Eq. (2.55), is the elastic constant of the crystal,  $C_i$ , which is the response of the total electronic energy to a dilation in direction  $i$

$$C_i = \frac{1}{l_i} \frac{\partial^2 E_{\text{tot}}}{\partial \delta l_i^2}, \quad (2.57)$$

with  $l_i$  as the length of the respective lattice vector of the non-deformed crystal unit cell, and  $E_{\text{tot}}$  as the total electronic energy of the unit cell. Like the effective mass, the deformation potential is also a second rank tensor which I assumed can be diagonalizable due to the crystal's symmetry. I dilated the unit cell of the polymeric crystal along its principal axes and calculated the total electronic energy and the energy of the CBM based on DFT geometry optimizations of the stretched and compressed cell. I then determined the deformation potential and the elastic constant by parabolic and linear fitting procedures based on Eq. (2.56) and (2.57), respectively.

With the relaxation time and the band structure, the conductivity can be determined according to Eq. (2.52). Note, that in this expression, the chemical potential and the temperature which enter through the Fermi-Dirac function (Eq. (2.38)) are still to be determined. For my considerations, I fixed the temperature to  $T = 300$  K and used  $\mu_{\text{chem}}$  as an adjustable parameter. By varying the chemical potential, one can change the charge carrier concentration *via* Eq. (2.36). This assumes that the band structure does not change when the chemical potential is varied so that the conduction band is occupied with electrons or the valence band with holes. In this so-called rigid band approximation,<sup>141</sup> I calculated the conductivity along the individual crystal lattice directions as a function of the charge carrier concentration  $N$  by varying the value of  $\mu_{\text{chem}}$ . Furthermore, I determined the mobilities along the crystal directions using Eq. (2.39).

In summary, I modeled the charge transport through a polymeric crystal in the band-like transport regime. To calculate the electrical conductivity and mobility of the system along its crystal directions, I employed the Boltzmann transport equation which describes the movement of charges in a statistical manner by a probability function. Herein, two parameters need to be determined, namely the effective mass and the relaxation time. The effective mass is directly obtained from the electronic band structure and for the relaxation time, I utilized the deformation

potential theory.



# Results and Conclusions

The following chapter comprises the main results of three projects investigating the structural and electronic properties of the conjugated polymer material PTBT and its function as a battery cathode. In particular, I will emphasize the role of my theoretical contributions and connect them to the fundamentals presented in Chapter 2. Although my work was primarily a theoretical and computational endeavor, it was also conducted in close cooperation with experimental partners. Therefore, the employed multi-scale approaches not only improve the theoretical description of the material but also provide a direct comparison of theory and experiment by the mutual support and complementation of simulated and measured results.

The first study (A.1) presents the novel fabrication process of a vulcanized conjugated poly(4-(thiophene-3-yl)benzenethiol) polymer (S/PTBT) as a cathode material for a Li-S battery. The synthesis consists of a two-step procedure where 4-(thiophene-3-yl)benzenethiol (TBT) monomers are first electro-polymerized onto the surface of a porous Nickel foam (NF) to form a conjugated PTBT polymer network and subsequently, sulfur is incorporated into this framework by vulcanization to yield the final S/PTBT material (*cf.* Fig. 3.1).

From a theoretical point of view, I rationalize the structural evolution of the material during the fabrication process. Starting from the TBT monomer, which features a five-membered heterocyclic thiophene ring, the electro-polymerization can occur through bond creation at the  $\alpha$ - or  $\beta$ - (*i.e.*, 2- or 3-) position (*cf.* right inset in Fig. 3.1). Since in the TBT monomer, the  $\beta$ -position is substituted with a benzenethiol group, it is most likely that the polymerization will form  $\alpha,\alpha$ -linkages, resulting in a conjugated PTBT polymer with the thiophene rings as the main-chain and the benzenethiol groups as the side-chain.<sup>149–152</sup> The alternating single- and double-bonds of the thiophene rings form a conjugated backbone, imparting electrical conductivity to the system, while the thiol groups serve as the binding

sites for incorporating sulfur.

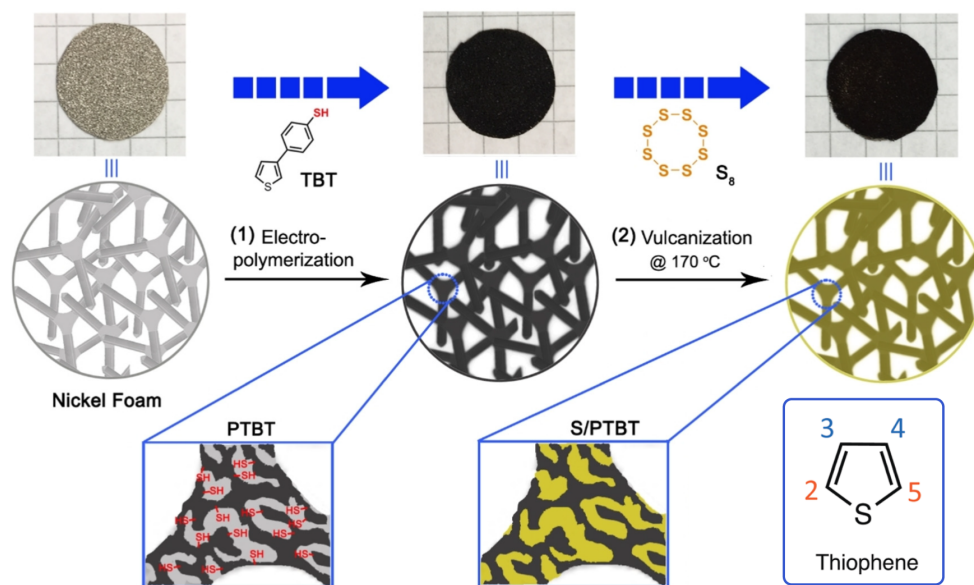


Figure 3.1: Schematic illustration of the fabrication route of the S/PTBT polymer: (1) creation of the conjugated PTBT framework on a porous Nickel foam by electro-polymerization; (2) covalent embedding of sulfur to form the S/PTBT polymer through vulcanization of elemental sulfur with the  $-SH$  binding sites of PTBT. The right inset shows the binding sites of a heterocyclic thiophene ring. Adapted with permission from Wiley-VCH GmbH for Ning *et al.*, A.1, 2022.

As a possible side reaction during this synthesis step, the thiol ( $-SH$ ) groups of two TBT units can react to form a disulfide bond (PTBTS structure in Fig. 3.2). This is indicated by Raman spectroscopy measurements of the PTBT polymer, which already show a clear signature of  $S-S$  vibrational modes before the vulcanization (*cf.* Fig. S6 in A.1).

During the subsequent vulcanization step, the PTBT framework is first infiltrated with elemental sulfur ( $S_8$ ) and then heated up. As described in Section 2.2, increasing the temperature causes the reaction of sulfur with the functional groups of the polymer. The ring-opening polymerization of  $S_8$  yields diradical polysulfide chains. At the same time, the polymer forms a radical (PTBT $'$ ) either by breaking the  $S-H$  bond or by cleavage of the disulfide bond of PTBTS. As a bi-product, the two hydrogen atoms of the thiol groups can react with a sulfur atom to form  $H_2S$  gas.<sup>55,71,153</sup> The vulcanization yields a chemically-bonded organosulfur polymer S/PTBT, which can be directly assembled into a battery setup without further modification.

The benefit of such a two-step synthesis approach is that the structure of the PTBT polymer is already determined before sulfur is incorporated. This way, the conductivity originating from the conjugated PTBT chains will likely be maintained in the final vulcanized S/PTBT system because the vulcanization with

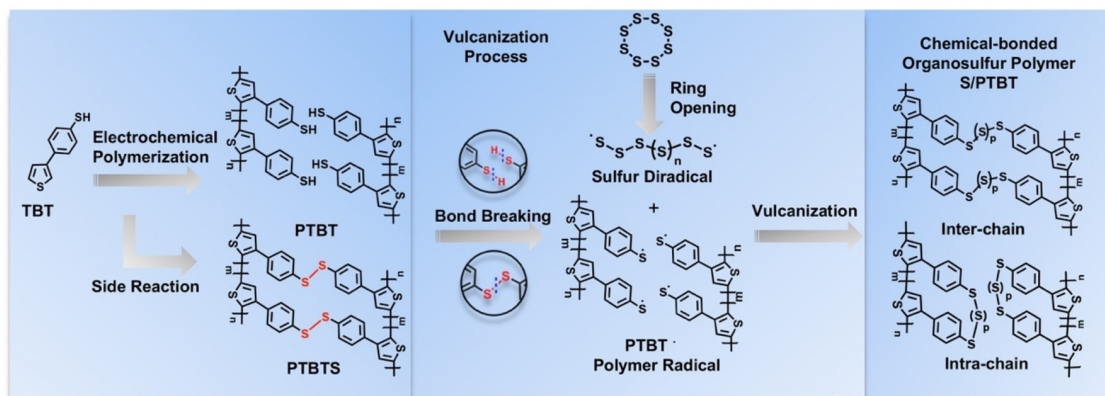


Figure 3.2: Illustration of the molecular structure evolution during the fabrication process. The electro-polymerization of the TBT monomers yields the PTBT framework (which can already form disulfide bridges (PTBTS) as a side reaction). The vulcanization between elemental sulfur and PTBT (or PTBTS) leads to a chemically-bonded organosulfur S/PTBT polymer. Generally, one can distinguish between an *intra-chain* and *inter-chain* sulfur cross-link between two TBT units. Reprint with permission from Wiley-VCH GmbH for Ning *et al.*, A.1, 2022.

sulfur will not alter the polymer backbone. Indeed, electrochemical impedance spectroscopy (EIS) demonstrated that the conductivity of the S/PTBT system with chemically-bonded sulfur is comparable to that of the pristine PTBT polymer (*cf.* Fig. 5a in A.1). Furthermore, the EIS showed a superior conducting behavior of S/PTBT compared to a reference system in which elemental sulfur was only physisorbed to the polymer.

In a first assessment of the polymer's microscopic structure, I considered a minimal model of a single TBT monomer to which a chain of  $n = 2 - 8$  sulfur atoms is attached. Using DFT, I calculated the energetically highest occupied and lowest unoccupied molecular orbitals (HOMOs and LUMOs) of the optimized structures. These calculations provided a qualitative explanation for the EIS results as they showed the reduction of the HOMO-LUMO gap upon extension of the sulfur chain to the TBT monomer (*cf.* Fig. 3.3), suggesting that covalently-bonded sulfur can indeed enhance the conducting properties of the PTBT cathode.

At the same time, the covalent fixing of polysulfides to the thiol groups of the polymer side chains confines the sulfur content within the cathode. In-operando X-ray imaging measurements confirmed the suppression of the shuttle effect by this fixation of sulfur (*cf.* Fig. 7 in A.1), and the improved functionality was also demonstrated in battery performance tests (*cf.* Fig. 5b-e in A.1).

This proof-of-concept project was the starting point for two investigations that ultimately resulted in the following publications. The second study was about the vulcanization process and the question of how sulfur will bind to the polymer. The third investigation dealt with the question of how the structure of the conjugated

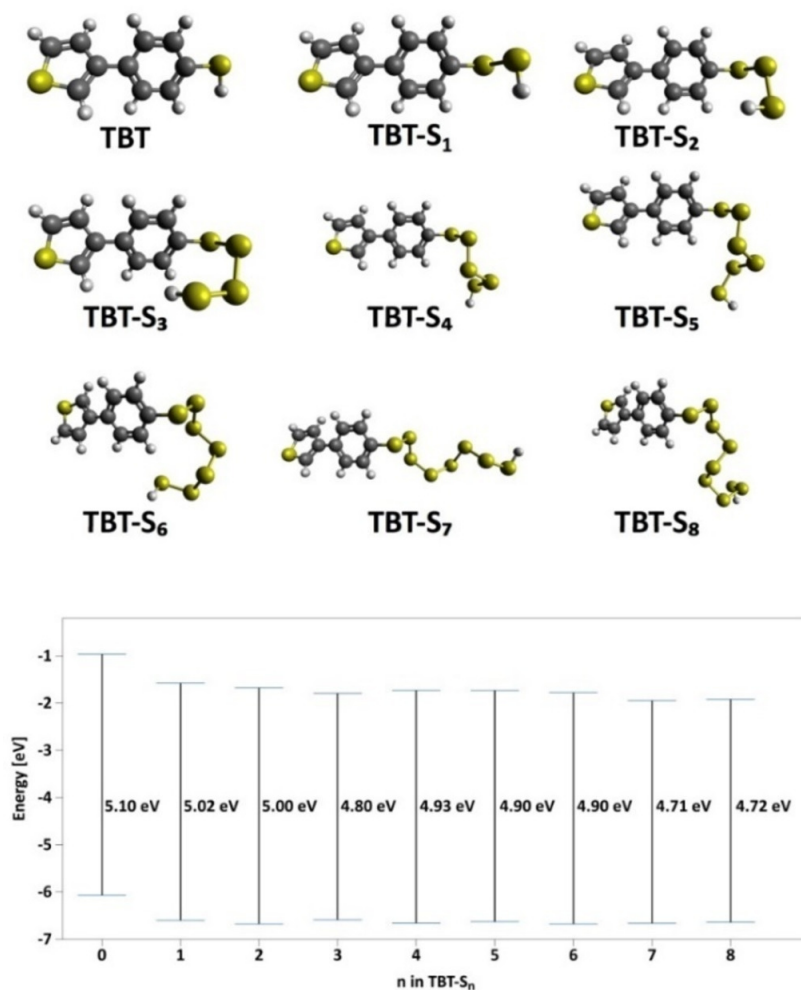


Figure 3.3: Illustration of the most stable structures of a TBT and TBT-S<sub>n</sub> ( $n = 2 - 8$ ) molecules and their respective HOMO-LUMO gaps. Carbon (C), hydrogen (H), and sulfur (S) elements are displayed as spheres in grey, white, and yellow, respectively. Reprint with permission from Wiley-VCH GmbH for Ning *et al.*, A.1, 2022.

polymer influences its conducting behavior.

To increase the capacity of a Li-S battery, the most straightforward measure would be to increase the sulfur loading, that is, the amount of sulfur in the cathode material. As discussed in Section 2.2, this idea led to inverse vulcanization, where a large amount of sulfur is used.<sup>10</sup> In its original sense, this technique does not offer direct control of the morphology of the final polymer since the process of vulcanization happens as a bulk reaction of the mixture of elemental sulfur and monomer units. By contrast, in our approach, we separate the electro-polymerization from the vulcanization process. Thus, the fundamental architecture of the PTBT polymer chains, meaning their backbones and side chains, is already given after the first synthesis step. The open question remains what the final vulcanized polymer

looks like. How does the sulfur bind to the polymer, and how long are the sulfur chains?

To answer these questions, I derived a statistical mechanics model to describe the outcome of the vulcanization process as a thermodynamic equilibrium of bringing two reference states (polymer and elemental sulfur) together that are forming the vulcanized S/PTBT. Based on the structure of the PTBT polymer, I distinguished between two ways in which the polysulfide chains can bind to the TBT units. On the one hand, a sulfur chain can connect two adjacent TBT units of the same polymer chain to form an *intra-chain* sulfur link (*cf.* bottom right picture of Fig. 3.2). On the other hand, as shown above, sulfur can form an *inter-chain* cross-link between TBT monomers that belong to different polymer chains. The binding polynomial  $Q_B([x])$  in Eq. (2.28), describing all binding possibilities of the multiple binding equilibria, takes then the form  $Q_B([x]) = 1 + P^{\text{intra}}([x]) + P^{\text{inter}}([x])$ . It is the sum of the statistical weights of the three scenarios that a binding site can either have an *intra-* or *inter-*configuration or can still be empty (meaning the thiol groups have not reacted). As a further extension of this model, I distinguished the possible reaction products of the vulcanization not only by their binding type (*intra* or *inter*) and sulfur chain length (sulfur rank)  $n$  but also by their conformation  $i$ . This conformational space sampling gives a better estimate of the quantitative structure-stability relationship of the vulcanization products compared to considering only one (potentially most) stable structure for each binding situation. Using Eq. (2.30), I obtained the mean sulfur rank of the *intra-* and *inter-*type binding processes by averaging over the statistical ensemble

$$\bar{n}^{\text{intra/inter}}([x]) = \sum_{n=1}^m \sum_{i=1}^{i_{\text{max}}(n)} n \frac{P_{n,i}^{\text{intra/inter}}([x])}{Q_B([x])}. \quad (3.1)$$

My binding model is then fed by the results of a DFT structure-stability analysis of reaction products. This analysis describes the reaction of forming an *intra-* or *inter-*type link in terms of their vulcanization energies, that is, the electronic energy difference between products and reactants. The corresponding reactions are based on the definition of two reference states: a DiTBT molecule describing two neighboring, covalently bonded TBT monomers as the basic unit of a polymer chain and one-eighth of an  $S_8$  ring for the amount of free sulfur that is going to be embedded into the polymer.

Fig. 3.4 shows the results of the vulcanization energies for sulfur ranks  $n = 1 - 18$  for the *intra-* (red) and *inter-*case (blue). The dashed grey lines denote the minimum and maximum energies of the conformational space sampling which is represented by the colored areas. The solid lines show the averages over all conformers

of a particular sulfur rank. Comparing the solid red and blue curve, the main result is that  $E_{\text{vul}}^{\text{inter}}$  is always lower than  $E_{\text{vul}}^{\text{intra}}$  and for almost the whole range of sulfur ranks the former is negative. This shows that the *inter*-type process chemically stabilizes the sulfur content. In contrast, the *intra*-process leads mostly to energetically unstable products, as can be seen from the almost only positive values for  $E_{\text{vul}}^{\text{intra}}$ . Only for very long chains ( $n > 11$ ), the *intra*-type process results in energetically stable structures. The difference in stability between the two processes can be explained by the induced strain energy due to the structural changes of the reactants. Especially for the *intra*-type reaction products, this additional strain energy increases their internal energy and thus makes them unfavorable to form.

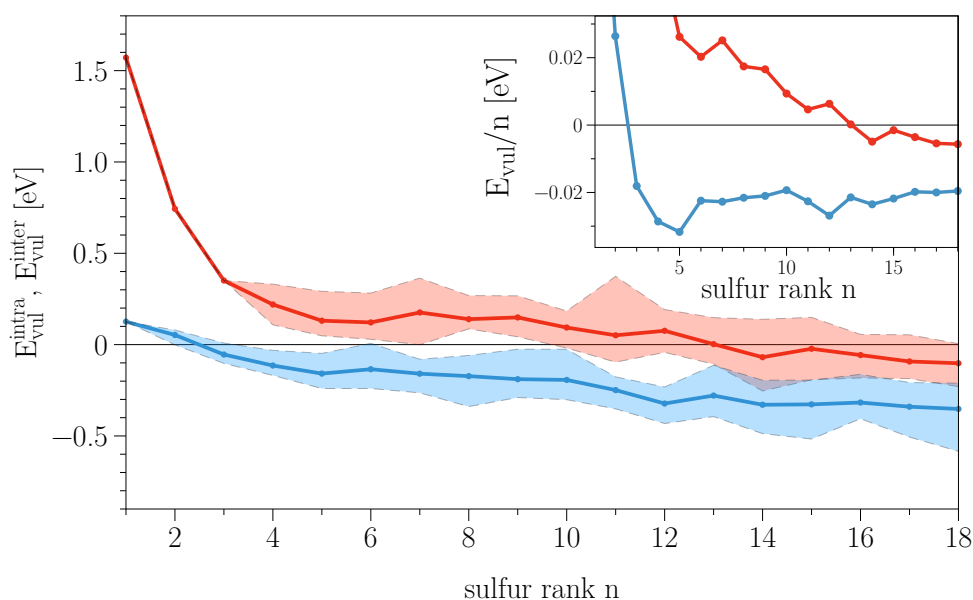


Figure 3.4: The vulcanization energies  $E_{\text{vul}}^{\text{intra}}$  (red) and  $E_{\text{vul}}^{\text{inter}}$  (blue). The dashed grey lines denote the minimum and maximum energies of the colored areas which represent the energies of all sampled conformations. The solid lines show the averaged trends. In the inset, the vulcanization energies normalized by the sulfur rank  $E_{\text{vul}}/n$  are shown. Reprint with permission from the Royal Society of Chemistry in accordance with the creative commons attribution 3.0 unported licence for Y. Schütze *et al.*, A.2, 2021.

The finding that the *inter*-type reaction is more favorable in terms of electronic energies and could, therefore, be the dominant way how sulfur binds to the polymer during vulcanization is experimentally supported by the Raman spectroscopy measurements of the first study. Based on my stability analysis, the S–S signal, which was detected already after electro-polymerization, can be identified with the inter-chain structures (*cf.* PTBTS structure in Fig. 3.2).

I used the information about the energetic stability of the reaction products

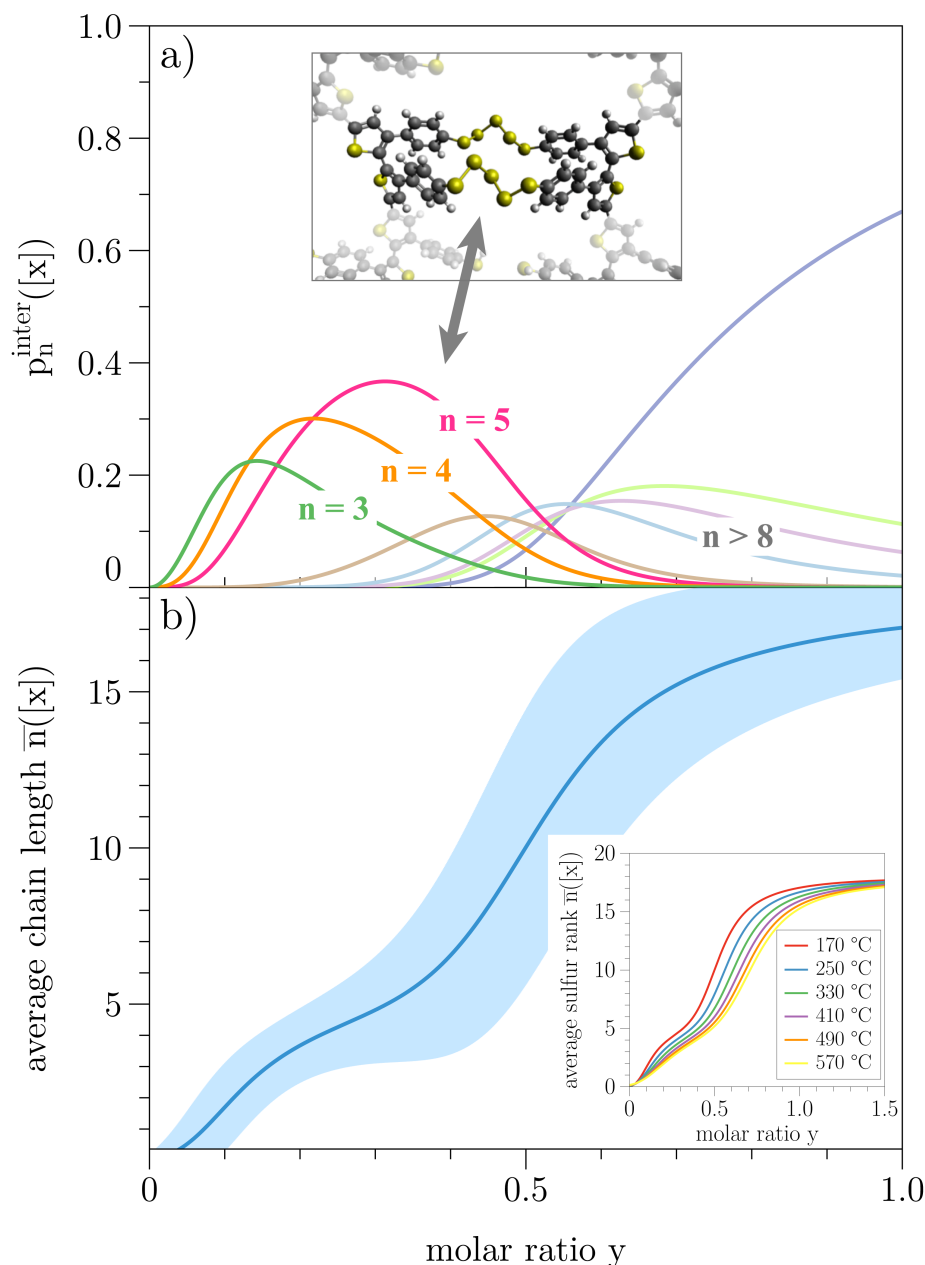


Figure 3.5: a) the individual binding probabilities  $p_n^{\text{inter}}([x])$  in dependence of the molar ratio  $y$  of concentrations of free sulfur and polymer binding sites. The inset in a) shows an example structure of an *inter*-chain sulfur cross-link with a rank  $n = 5$ . b) the average sulfur rank for the *inter*-process (solid line) and its standard deviation (colored area). The inset in b) shows the temperature dependency of the average sulfur rank. Adapted with permission from the Royal Society of Chemistry in accordance with the creative commons attribution 3.0 unported licence for Y. Schütze *et al.*, A.2, 2021.

as an input for my statistical binding model by relating the vulcanization energies with the equilibrium constants through Eq. (2.25) (approximating the free binding energy of change  $\Delta G$  with only the electronic energy differences  $E_{\text{vul}}$ ). This combination of methods allows us not only to look at the energetic stability of

certain reaction products but also to study how the microstructure of the vulcanized polymer behaves depending on the temperature and the mixing ratio of free elemental sulfur to polymer binding sites.

In Fig. 3.5a), the individual binding probabilities for the *inter*-type process are shown in dependency of the molar ratio of concentrations of free sulfur and polymer binding sites  $y = [x]/[\text{BS}]$  (only the binding curves for sulfur ranks, whose maximum probability is over 10%, are shown). The shortest sulfur chains ( $n = 1, 2$ ) do not contribute significantly since they are unfavorable to form (*cf.*  $E_{\text{vul}}^{\text{inter}}$  in Fig 3.4). If we increase the molar ratio  $y$  by increasing the amount of free sulfur, medium-sized chains with  $n = 3 - 5$  will form. Here, the probability of forming a pentasulfide ( $n = 5$ ) cross-link (corresponding to the structure shown in the inset) is highest over a long range of  $y$ . This observation can be related to the minimum of the relative vulcanization energy  $E_{\text{vul}}^{\text{inter}}/n$  at  $n = 5$  (*cf.* the inset in Fig. 3.4 indicating that this sulfur rank maximizes the electronic stability of the vulcanized structure and is thus the most probable outcome for a certain range of free sulfur concentrations. The stability of a pentasulfide chain can also be recognized in the average sulfur rank in Fig. 3.5b) as this shows a plateau around  $\bar{n}[x] \approx 5$  instead of a monotonically increasing curve. Further increasing the amount of free sulfur leads also to the formation of longer sulfur chains  $n \geq 8$ ). This trend is evident from the fact that for the limit of very high sulfur concentrations, only the longest chain I have considered ( $n = 18$ ) contributes to the binding polynomial. Here, the model implies that adding more sulfur in the vulcanization process would always yield longer sulfur cross-links. This is due to the shortcoming of considering only the electronic stability of reaction products, excluding any entropic effects. Especially for longer sulfur chains, the restriction of degrees of freedom due to the binding to the polymer leads to a loss of conformational entropy. Including this contribution means an entropic penalty for longer chains, which causes a destabilization of structures with higher sulfur ranks.

The binding model also allows us to look at the temperature dependency of the average sulfur rank (*cf.* inset in Fig. 3.5b). Here, one sees that increasing the temperature leads to a decrease in the average sulfur rank. Therefore, the optimal temperature to yield longer sulfur chains should be just high enough to initiate the vulcanization process.

To summarize the second study, I showed that the main reaction during vulcanization leads to a sulfur chain cross-linking different PTBT polymer chains (*inter*-chain binding). In contrast, connecting adjacent TBT binding sites *via* a sulfur chain within the same polymer chain (*intra*-chain binding) is not preferable. For *inter*-binding, a sulfur chain length of five atoms seems to be dominant in the

final material, but it would be possible to extend it by increasing the amount of sulfur for the vulcanization process. These results have some interesting implications. From the vulcanization of natural rubber (polyisoprene) or related polymers, it is known that the nature of cross-links plays an important role in determining the physical properties of the resulting material.<sup>154</sup> The extent of cross-linking influences the hardness of the rubber, as excessive cross-linking can convert it into a brittle material. At the same time, the number of sulfur atoms in the cross-links also has an influence. Short cross-links give the rubber better heat resistance, while longer cross-links lead to improved tensile strength, the maximum stress the material can withstand while being deformed.<sup>155,156</sup> Similar to rubber, the polymer inside a battery cathode is also subjected to deformations due to the volume change of sulfur during charge and discharge. The findings on natural rubber suggest that longer polysulfide cross-links would improve the flexibility of a polymeric cathode and hence lower the risk of irreversible deformations induced by the volume change.<sup>157,158</sup>

Furthermore, the results of my binding model show that an increasing temperature decreases the average sulfur chain length. This is in accordance with the behavior of elemental sulfur when heated up (*cf.* Section 2.2) and suggests that an optimal temperature to yield longer cross-links is right above the floor temperature of sulfur to initiate the vulcanization process.

Besides the influence of the sulfur chain length on the mechanical behavior of the cathode, it also determines the electrochemical properties of the electrode. As described in Section 2.1, the conversion reaction between elemental sulfur ( $S_8$ ) and lithium ions leads to the creation of long lithium polysulfide species ( $Li_2S_n$  with  $6 \leq n \leq 8$ ), which are the cause for the shuttle-effect. If the fully charged cathode (as it is prepared after vulcanization) does not contain sulfur cross-links longer than six, this could help to prevent the formation of these longer lithium polysulfides and thus impede the shuttle effect. Hence, the results of the second study provide an excellent explanation for the in-operando X-ray imaging measurements of the first study, which revealed the suppression of the shuttle-effect in the S/PTBT cathode.

Overall, I demonstrated that understanding how sulfur binds to a polymer during vulcanization in a Li-S cathode material is critical for tailoring the battery's properties to meet specific requirements. Here, one must balance different factors such as capacity, cathode stability, and electrochemical performance. The outcome of the vulcanization will, of course, always depend on the choice of the polymeric material. This is another advantage of my binding model, as it can be applied relatively easily to other vulcanized systems to get insights into their microscopic structure.

After studying the structural characteristics of the vulcanized system, I turned to an investigation of the electrical properties of the polymer. The motivation for this project was to understand the origin of the observed conducting behavior of the polymer and the relationship among structure and charge transfer properties. As a first step, I modeled the pure PTBT system before vulcanization. When revisiting the assumptions made in the previous structural models, it became apparent that although the electro-polymerization process gives the overall structure of the polymer chains, thiophene rings forming the backbone with the benzenethiol groups as the side chain, there is an ambiguity regarding the ordering of consecutive monomer units within a chain. This choice in the arrangement of repeating units is described by the regioregularity of the polymer chain.

In order to study the effect of the regioregularity of PTBT chains on their electrical properties, I distinguished two limiting cases, namely a head-to-head/tail-to-tail (HH-TT) and head-to-tail/head-to-tail (HT-HT) regularity (*cf.* Fig. 3.6). Referring back to Fig. 3.1, the terms ‘head’ and ‘tail’ distinguish between the two  $\beta$ -positions (3- and 4-position) of the thiophene rings. The substituted benzenethiol group is depicted as a head (H), and the unsubstituted hydrogen is the tail (T) (green and orange dashed rectangle in Fig. 3.6a).

Compared to the relatively small gas-phase systems from the previous studies, I extended the spatial dimensions of this model, which included one hundred polymer chains in a box with periodic boundary conditions, to study the polymer’s morphology on larger scales. I simulated their self-assembly with classical MD to explore the influence of the polymer chain’s regioregularity on the aggregation behavior of these bigger systems.

Prior to these systems, I studied the behavior of single PTBT chains. Figure 3.6 shows the DFT-optimized structures of a periodic chain with HH-TT and HT-HT regioregularity. The two lower panels show that the polythiophene backbones are not planar. Similar polythiophene systems substituted with bulky aromatic rings as the side group also show such a distortion of the backbone.<sup>159,160</sup> Therefore, the deviation from planarity of the PTBT chains is most likely due to steric effects between neighboring benzenethiol side groups. As discussed in Section 2.2, the conjugated backbone of the polymer chain gives rise to the conductive behavior of the material. Therefore, accurately describing the backbone is crucial when studying the relationship between the polymer’s microstructure and its charge transport properties. For the PTBT system, I identified the backbone torsion between the thiophene rings of neighboring TBT units,  $\Theta_b$ , and the side chain torsion between the thiophene ring and the benzenethiol group of one monomer unit,  $\Theta_s$ , as the two critical dihedrals that will govern the dynamics of the polymer chains (ex-

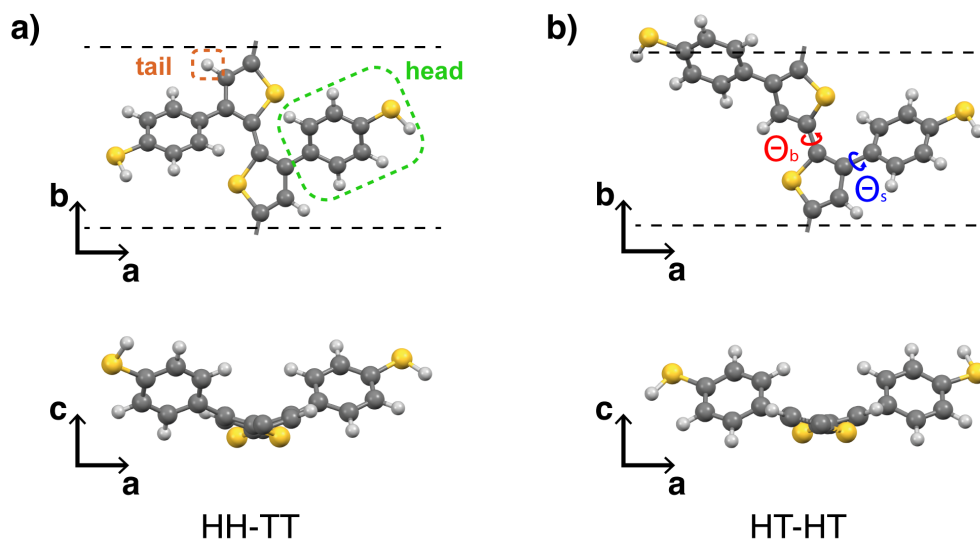


Figure 3.6: Illustration of the two considered regioregularities, (a) HH-TT and (b) HT-HT, of a conjugated PTBT chain. The upper two panels show the side view ( $ab$  plane), and the lower two panels show the top view along the backbone direction ( $ac$  plane). Dashed lines indicate the height of the unit cell along the  $b$  direction. The head and tail groups highlighted by dashed green and orange rectangles, respectively, in the upper left panel. The dihedral of the backbone  $\Theta_b$  and the side chain  $\Theta_s$  are shown in red and blue in the upper right panel. Adapted with permission from the American Chemical Society in accordance with the creative commons attribution 4.0 international licence for Y. Schütze *et al.*, A.3, 2023.

emphified in red and blue in the upper panel of Fig. 3.6b). I reparametrized the dihedrals  $\Theta_b$  and  $\Theta_s$  according to Eq. (2.17) to capture the energetic profiles that govern their rotations (*cf.* Table S1 and Fig. S1-S5 in A.3).

For the simulation of the self-assembly process of the polymer chains, I described the systems in an  $NPT$  ensemble. The aggregation of the chains was modeled by a temperature annealing process; that is, the simulation started at a very high initial temperature and was then cooled down to room temperature while keeping the pressure constant. After the systems were equilibrated, all chains have aggregated into one big cluster, respectively (*cf.* Fig. 3.7). Here, I observe a difference in the aggregation behavior between the two regioregularities.

On the one hand, the HT-HT chains form an ordered region in the center of the cluster, where neighboring chains stack in a face-to-face manner along the  $a$  axis and in a lamellar fashion along the  $c$  axis (blue-colored area in Fig. 3.7a). On the other hand, the HH-TT system does not show any stacking behavior of consecutive chains but rather arrangements of pairs. This difference in aggregation can be related to the backbone dihedral profiles of the two regioregularities (*cf.* Fig. S5 in A.3). For an HH-TT chain, the energy barriers at  $\Theta_b = 180^\circ$  are higher than for an HT-HT chain, which makes it energetically more unfavorable for the

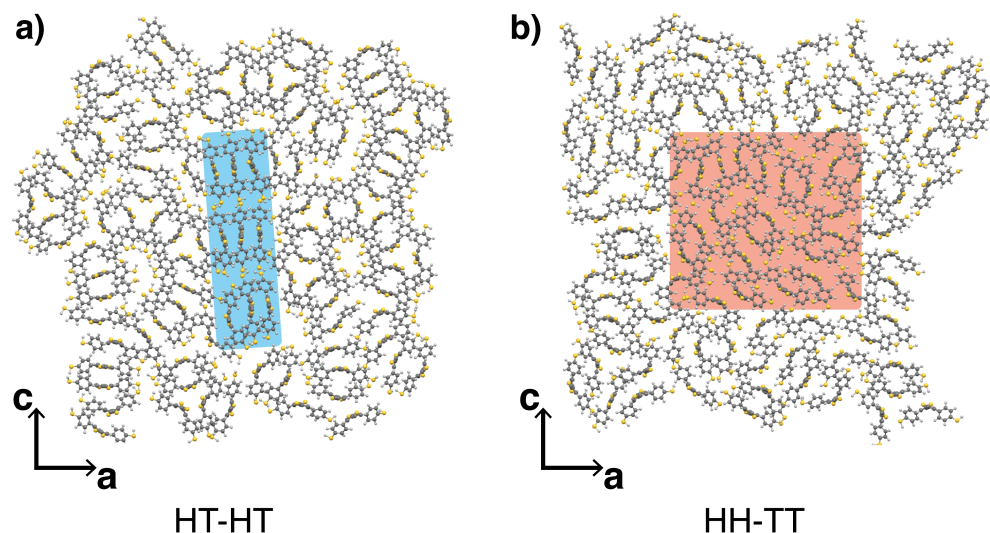


Figure 3.7: Comparison of the grown clusters at  $T = 300$  K after annealing. The systems are shown in the  $ac$  plane with the view along the polymer backbones. (a) The HT-HT system forms an ordered phase with a two-dimensional translational ordering along the  $a$  and  $c$  axes (blue-colored area). (b) The HH-TT system does not show long-range ordering in the  $ac$  plane. For further investigation, we cut out a representative subset of the cluster's center (red-colored area). Reprint with permission from the American Chemical Society in accordance with the creative commons attribution 4.0 international licence for Y. Schütze *et al.*, A.3, 2023.

former to adopt a planar configuration. This explains why the backbones of the HH-TT chains in the cluster simulation are still twisted as for the isolated chain in Fig. 3.6a). These results suggest that polymer chains with HT-HT regioregularity can form crystalline phases due to their ability to aggregate into ordered stacks, whereas HH-TT chains possess a more disordered morphology because of their distorted backbones.

To validate this structural characterization, I extracted a single-crystal structure from the ordered region of the HT-HT cluster and calculated its X-ray diffraction (XRD) patterns based on the DFT-optimized crystal unit cell (*cf.* Fig. 3.8). These were then compared to experimental XRD diffractograms of two samples of the PTBT polymer, measured by my colleagues. The first sample is the polymer attached to the Nickel surface (black line, 'PTBT in Ni' in Fig. 3.8b), which shows strong crystalline peaks. The calculated XRD pattern (blue line) features very similar peaks, which can be related to the structural arrangement of the atoms in the unit cell. Comparing the two diffractograms allows us to distinguish three characteristic regions: a lamellar peak at low Bragg angles corresponding to the stacking of polymer chains along the  $c$  axis, a peak that originates from reflections of the benzenethiol side groups, and the region of higher Bragg angles which stem from the stacking of thiophene backbones along the short  $a$  axis. The stacking of

thiophene rings can be attributed to the interaction of their  $\pi$  orbitals (*cf.* Fig. 2.7), which is known to initiate the crystallization of conjugated polymers during the self-assembly process.<sup>161–164</sup>

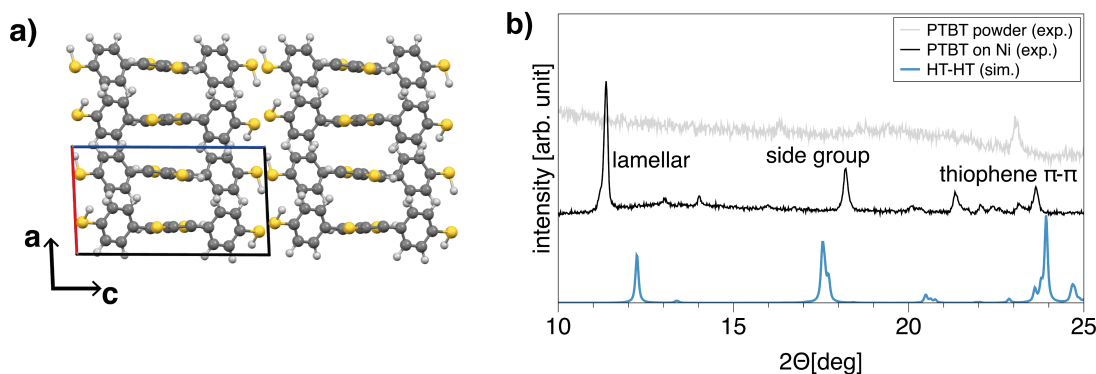


Figure 3.8: a) DFT optimized crystal structure of the HT-HT unit cell. b) Comparison between the simulated X-ray diffraction (XRD) pattern for the theoretical crystal structure of HT-HT (blue) and two experimentally observed diffractograms for the PTBT film on nickel foam (black) and as a powder (gray). Adapted with permission from the American Chemical Society in accordance with the creative commons attribution 4.0 international licence for Y. Schütze *et al.*, A.3, 2023.

In contrast, the second sample (grey line, ‘PTBT powder’ in Fig. 3.8b), which is a collection of material that detached from the growing PTBT film during prolonged electro-polymerization, does not show any crystallinity except for one peak, indicating the  $\pi$ - $\pi$  stacking of thiophene rings. This shows that the duration of electro-polymerization influences the structure of the polymer. While the polymer chains attached to nickel at the early stage of electro-polymerization can form higher regular and crystalline zones, longer chains tend to form more disordered morphologies, causing the loss of structural order in the outer layers of the polymer. The good agreement between the ‘PTBT on Ni’ and the theoretical diffractogram suggests that the crystallinity of this sample can be related to the existence of chains with HT-HT regioregularity forming highly ordered domains. The electronic band structure of the HT-HT system allows us to connect the structural characteristics of the crystalline phase with its charge transport properties. Figure 3.9 shows the HT-HT crystal to have a band gap of 0.58 eV. From the large bandwidth along the  $\Gamma - Y$  direction (corresponding to the direction along the conjugated backbones), one can already see that the main direction for charge transport is along the polymer backbones. Furthermore, the species’ projected DOS confirms that the CB is due to the  $\pi$ -orbitals of the thiophene carbon atoms. Along the  $\pi$ - $\pi$  stacking axis **a** of neighboring chains, the system also features a non-vanishing but smaller bandwidth, indicating a two-dimensional charge transport typical for lamellar-stacked conjugated polymers.<sup>165–167</sup>

I also investigated the electronic properties of the HH-TT system by averaging over several snapshots of an *NPT* MD trajectory of a representative subset of the bigger cluster (*cf.* red shaded area in Fig. 3.7). The comparison of the DOS of the HT-HT and HH-TT system (black solid and red dashed line, respectively, in the right inset of *cf.* Fig. 3.9) shows that their structural differences result in a different electronic behavior. The non-planarity of the HH-TT chains indicates that the spatial periodicity along their conjugated backbones (denoted as the conjugation length<sup>168</sup>) is reduced compared to that of the HT-HT chains, which manifests in an enlarged band gap of the former system.<sup>169,170</sup> Furthermore, the structural disorder in the  $\pi$  stacks of neighboring HH-TT chains (so-called paracrystallinity<sup>171,172</sup>) can be related to the broadening of the DOS near the band gap, which is in contrast to the sharp band edges of the HT-HT system. The larger the width of these tails, the larger the energetic disorder, *i.e.* the variations in the system's energy levels.<sup>170,173</sup> Furthermore, it has been shown that charge carriers, which occupy states in these band tails, are very localized,<sup>174,175</sup> preventing them from contributing to conduction.<sup>176,177</sup>

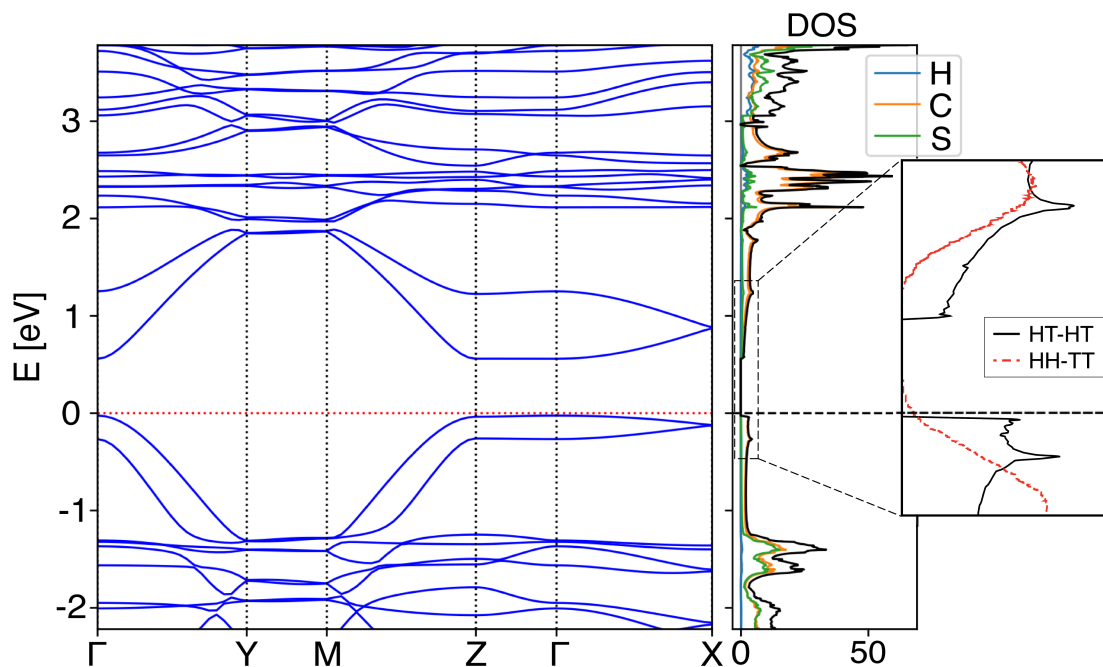


Figure 3.9: Band structure, density of states (DOS), and projected DOS (hydrogen (H), carbon (C), and sulfur (S) are depicted with blue, orange, and green lines, respectively) for the HT-HT crystal. The band energies are shifted relative to the Fermi level. The Fermi level is indicated with a red dotted and black dashed line. The inset on the right shows a magnification of the DOS of the HT-HT crystal (black solid line) compared to the averaged DOS of five representative configurations of the unordered HH-TT phase (red dashed line). Adapted with permission from the American Chemical Society in accordance with the creative commons attribution 4.0 international licence for Y. Schütze *et al.*, A.3, 2023.

For a quantitative assessment of the charge transport properties of the HT-HT system, I described the conduction of electrons through the polymeric crystal in the band-like transport regime. To calculate the conductivity and mobility along the principal crystal axes, I employed the relaxation time approximation of the Boltzmann transport equation (Eq. (2.48)) in combination with the deformation potential theory (Eq. (2.55)). Figure 3.10 shows the band-like conductivity  $\sigma$  as a function of the charge carrier concentration  $N$  for the three principal crystal axes. Changing the chemical potential in the Fermi-Dirac function (Eq. (2.38)) to the left increases the concentration of electrons in the CB (similarly, changing  $\mu_{\text{chem}}$  to the right increases the hole concentration in the VB). Furthermore, I calculated the electron mobilities as the slope of the linear regions according to Eq. (2.39) (indicated by green dashed lines).

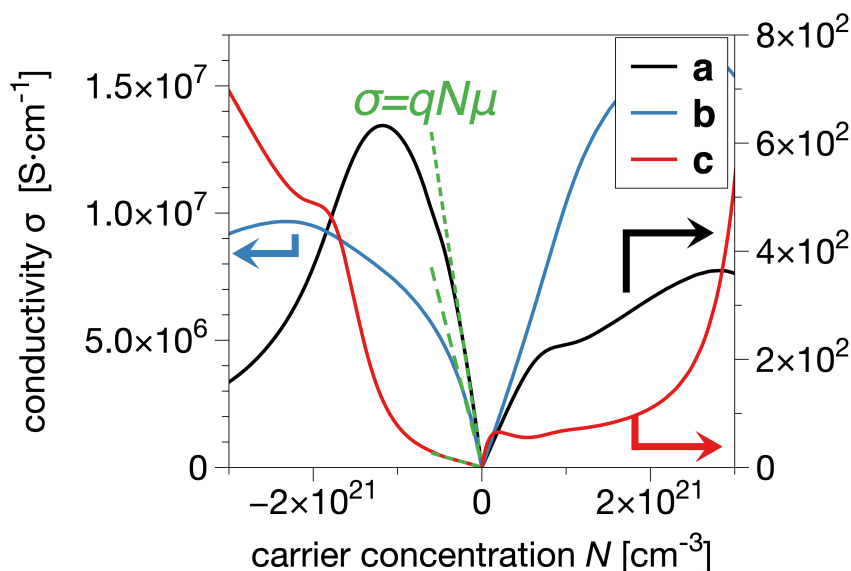


Figure 3.10: Plot of the band-like conductivity  $\sigma$  along the principal crystal axes **a**, **b**, and **c**, respectively, as a function of the charge carrier concentration  $N$  (the colored arrows associate the lines to their corresponding scales on the y-axes). The slope of the positive (negative) linear region of the conductivity over  $N$  gives the hole (electron) mobility according to Eq. (2.39) (green dashed lines). Reprint with permission from the American Chemical Society in accordance with the creative commons attribution 4.0 international licence for Y. Schütze *et al.*, A.3, 2023.

The band-like electron conductivity and mobility along the CB of the polymer backbone (**b** direction) is several orders higher than those for the  $\pi$ - $\pi$  and lamellar stacking direction (**a** and **c** direction) which reveals a high anisotropy of the crystal's charge transport. This is in agreement with recent experimental measurements on other polythiophene-based polymers,<sup>178–180</sup> which showed comparable anisotropic mobilities.<sup>181,182</sup>

Overall, in this third study, I provided insights into the interplay between the

microstructure and the electronic properties of the conjugated PTBT polymer. Using classical MD, I simulated the self-assembly of polymer chains with different regioregularity and found that only an HT-HT regioregularity allowed the formation of crystalline phases. In contrast, the HH-TT system did not show any long-range order, which can be related to increased steric constraints. I calculated the band structure and DOS of the different structural phases and observed that the structural disorder in the HH-TT phase leads to an energetic disorder that could limit charge transport. In contrast, the crystalline HT-HT system shows a high anisotropy, which allows for fast charge transport along the polymer backbones.

The information about the importance of polymer chain regioregularity on charge transport can now be used to reassess the process of electro-polymerization. Knowing that a high degree of HT-HT regioregularity is beneficial for the crystallinity of the polymer, increasing the regioselectivity of the polymerization reactions would be desirable. This gives rise to the concept of controlled electro-polymerization.<sup>183</sup> Furthermore, a systematic optimization of the electrochemical conditions, such as the polymerization current density and the polymerization time, could provide a strategy to yield higher degrees of crystallinity.

The results presented in this thesis shed light on the structural and electronic properties of a conjugated organosulfur polymer cathode for Li-S batteries. In the first project, the novel fabrication process using a combination of electro-polymerization and vulcanization was tested, and the ability of this material to overcome common drawbacks of Li-S batteries was shown experimentally by my colleagues. My contributions helped rationalize the evolution of the microscopic structure during the synthesis.

In the second project, I built on these results and conducted a structural investigation of the vulcanized polymer. I developed a DFT-informed statistical mechanics model of the vulcanization outcome, which describes the vulcanized product in terms of the molar ratio and binding type between sulfur and polymer. I found that the electronic stability on a microscopic scale determines a sulfur cross-linking of adjacent polymer chains and that the amount of sulfur and temperature control the extent of cross-linking on a macroscopic scale.

Using these results, I extended the dimension of the model in the third project to study the interplay between the structural morphology of the PTBT polymer and its charge transport properties. With a combination of classical MD, DFT band structure calculation, and statistical charge transport theory, I showed how the microstructure of individual polymer chains is intertwined with their respective aggregates' electronic behavior. Here, I highlighted the importance of polymer

chain regioregularity to obtain crystalline phases, allowing for fast charge transport.

The next natural step would be the investigation of the charge transport properties of the final vulcanized polymer. A reasonable starting point would be to experimentally investigate how the vulcanization influences the crystallinity of the polymer. Depending on this, the theoretical transport mechanism would have to be reassessed. For a system with a morphological disorder, it might be more appropriate to describe the charge transport herein with different models (*e.g.*, hopping models) instead of a band transport theory. Here, a decisive point is the development of an appropriate structural model for the vulcanized polymer that accounts for the local binding between sulfur and the conjugated nature of the polymer chains on a larger scale.

The investigations in this thesis focused on the characterization of the polymer as a bulk material without boundaries. A future step to add complexity would be to consider the interphase between the cathode and the electrolyte and study the ionic charge transport herein. Ultimately, elucidating the dynamics of the electrochemical processes during the charge and discharge would be desirable. Capturing multiple scales with different theoretical models and complementing them with experiments will help to get a comprehensive view of these processes.



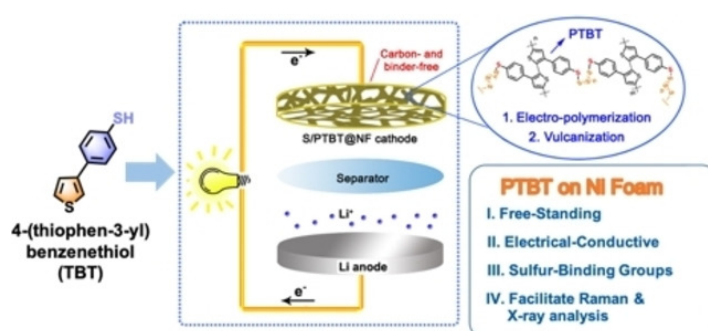
## Publications

### A.1 Constructing Binder- and Carbon Additive-Free Organosulfur Cathodes Based on Conducting Thiol-Polymers through Electropolymerization for Lithium-sulfur Batteries

Jiaoyi Ning, Hongtao Yu, Shilin Mei, Yannik Schütze, Sebastian Risse, Nikolay Kardjilov, André Hilger, Ingo Manke, Annika Bande, Victor G. Ruiz, Joachim Dzubiella, Hong Meng, Yan Lu

*ChemSusChem*, 2022, 15, e202200434

DOI: 10.1002/cssc.202200434



**Author Contributions:** This project was a cooperation between the groups of Yan Lu (YL), Sebastian Risse (SR), and Joachim Dzubiella (JD). The project idea was conceived by YL, SB, and JD. The synthesis was carried out by Hongtao Yu (HY). SEM, TGA, XPS, EDX, and Raman measurements were taken by HY, Shilin Mei (SM), and Jiaoyi Ning (JN). All theoretical calculations were performed by Yannik Schütze (YS). In-operando X-ray imaging was carried out by SR, Nikolay Kardjilov (NK), and André Hilger (AH). The manuscript was mainly

written by HY and JN, with YS responsible for the theoretical contributions, SR responsible for the in-operando chapter, and the remaining authors proofreading. All authors contributed to the final version of the manuscript.

On the following pages, the publication, including the supporting information, is provided with permission of Wiley-VCH GmbH in accordance with the creative commons attribution 4.0 international licence for Jiaoyi Ning *et al.*, A.1, 2022.

# Constructing Binder- and Carbon Additive-Free Organosulfur Cathodes Based on Conducting Thiol-Polymers through Electropolymerization for Lithium-Sulfur Batteries

Jiaoyi Ning<sup>+, [a, b]</sup> Hongtao Yu<sup>+, [a, c]</sup> Shilin Mei,<sup>[a]</sup> Yannik Schütze,<sup>[d, e]</sup> Sebastian Risse,<sup>[a]</sup> Nikolay Kardjilov,<sup>[f]</sup> André Hilger,<sup>[f]</sup> Ingo Manke,<sup>[f]</sup> Annika Bande,<sup>[g]</sup> Victor G. Ruiz,<sup>[d]</sup> Joachim Dzubiella,<sup>[d, h]</sup> Hong Meng,<sup>\*, [b]</sup> and Yan Lu<sup>\*, [a, i]</sup>

Herein, the concept of constructing binder- and carbon additive-free organosulfur cathode was proved based on thiol-containing conducting polymer poly(4-(thiophene-3-yl) benzenethiol) (PTBT). The PTBT featured the polythiophene-structure main chain as a highly conducting framework and the benzenethiol side chain to copolymerize with sulfur and form a crosslinked organosulfur polymer (namely S/PTBT). Meanwhile, it could be in-situ deposited on the current collector by electropolymerization, making it a binder-free and free-standing cathode for Li-S batteries. The S/PTBT cathode exhibited a

reversible capacity of around 870 mAh g<sup>-1</sup> at 0.1 C and improved cycling performance compared to the physically mixed cathode (namely S&PTBT). This multifunction cathode eliminated the influence of the additives (carbon/binder), making it suitable to be applied as a model electrode for operando analysis. Operando X-ray imaging revealed the remarkable effect in the suppression of polysulfides shuttle via introducing covalent bonds, paving the way for the study of the intrinsic mechanisms in Li-S batteries.

## Introduction

Lithium-sulfur (Li-S) batteries, using sulfur as an active cathode material, have attracted considerable attention owing to the superiority of electrode materials, especially the high theoretical capacity ( $\approx 1675 \text{ mAh g}^{-1}$ ) of sulfur, which is simultaneously Earth-abundant, cheap, and environmentally benign.<sup>[1]</sup> However, this superior battery type also suffers from various drawbacks hindering its commercialization, such as the “shuttle effect” of the soluble lithium polysulfides during the charging-discharging

cycle process, the insulating nature of sulfur and lithium sulfide, and the large volume expansion of sulfur ( $\approx 80\%$ ) on its full lithiation.<sup>[2]</sup> To alleviate these issues for improving the performance of Li-S batteries, in particular, the exploitation of high-performance cathode materials is highly desired. So far, plenty of inorganic framework material, such as carbon material (e.g., mesoporous carbon, hollow carbon spheres, carbon nanotubes, and graphene), as well as metal oxides/sulfides/nitrides and metal-organic frameworks have been designed and fabricated through chemical synthesis methods.<sup>[3]</sup> They should prevent the

[a] J. Ning,<sup>+</sup> Dr. H. Yu,<sup>+</sup> Dr. S. Mei, Dr. S. Risse, Prof. Y. Lu  
Department for Electrochemical Energy Storage  
Helmholtz-Zentrum Berlin für Materialien und Energie GmbH  
Hahn-Meitner Platz 1, 14109 Berlin (Germany)  
E-mail: yan.lu@helmholtz-berlin.de

[b] J. Ning,<sup>+</sup> Prof. H. Meng  
School of Advanced Materials, Peking University Shenzhen Graduate School  
Peking University  
Lishui road 2199, Nanshan district, Shenzhen, 518055 (P. R. China)  
E-mail: menghong@pku.edu.cn

[c] Dr. H. Yu<sup>+</sup>  
Guangdong Province Key Laboratory of Durability for Marine Civil Engineering, School of Civil Engineering  
Shenzhen University  
Shenzhen, 518060 (P. R. China)

[d] Y. Schütze, Dr. V. G. Ruiz, Prof. J. Dzubiella  
Research Group Simulation of Energy Materials  
Helmholtz-Zentrum Berlin für Materialien und Energie GmbH  
Hahn-Meitner Platz 1, 14109 Berlin (Germany)

[e] Y. Schütze  
Institute of Chemistry and Biochemistry  
Freie Universität  
Amimallee 22, 14195 Berlin (Germany)

[f] N. Kardjilov, A. Hilger, I. Manke  
Institute for Applied Materials  
Helmholtz-Zentrum Berlin für Materialien und Energie GmbH  
Hahn-Meitner Platz 1, 14109 Berlin (Germany)

[g] A. Bande  
Theory of Electron Dynamics and Spectroscopy  
Helmholtz-Zentrum Berlin für Materialien und Energie GmbH  
Hahn-Meitner Platz 1, 14109 Berlin (Germany)

[h] Prof. J. Dzubiella  
Physikalisches Institut  
Albert-Ludwigs-Universität Freiburg  
Hermann-Herder-Straße 3, 79104 Freiburg (Germany)

[i] Prof. Y. Lu  
Institute of Chemistry  
University of Potsdam  
14467 Potsdam (Germany)

[\*] These two authors contribute equally.

Supporting information for this article is available on the WWW under <https://doi.org/10.1002/cssc.202200434>

© 2022 The Authors. ChemSusChem published by Wiley-VCH GmbH. This is an open access article under the terms of the Creative Commons Attribution License, which permits use, distribution and reproduction in any medium, provided the original work is properly cited.

loss of the soluble polysulfides through physical/chemical confinement as well as increase the electrical conductivity of cathodes. On the other hand, the chemical confinement, through fixing polysulfides via covalent bonds to the cathode host material, has been demonstrated to be extremely efficient in suppressing the shuttle effect. Various organic moieties containing functional groups (e.g., allyl, thiol, or cyano) have been copolymerized with sulfur through inverse vulcanization to form the organosulfur polymers,<sup>[4]</sup> along with the improvement of cycling stability. However, the poor conductivity of most organosulfur compounds has been the main drawback that hampers their advance towards practical use. As a result, conjugated polymers emerge as promising candidates due to their significantly improved conductivity when compared with small organic molecules and non-conjugated polymers, as well as their ability to form chemical bonds with sulfur species.<sup>[5]</sup>

To gain insight into the structure of the organosulfur polymer, a series of *ex-situ* measurements have been combined, such as X-ray photoelectron spectroscopy (XPS), nuclear magnetic resonance (NMR) spectroscopy, and electron paramagnetic resonance (EPR) analysis,<sup>[6]</sup> and confirmed the formation of covalent bonds between sulfur moieties and polymer backbones. However, more direct information based on *operando* analysis is still missing, which is essential to pursuing a comprehensive view of the redox mechanism and structure evolution of the organosulfur polymer during the charge-discharge process, especially the formation of polysulfides and the reversibility of covalent bonding of sulfur species to the polymer. Therefore, developing a highly conductive, flexible, and free-standing organosulfur cathode for *operando* analysis under realistic reaction conditions is of great importance.

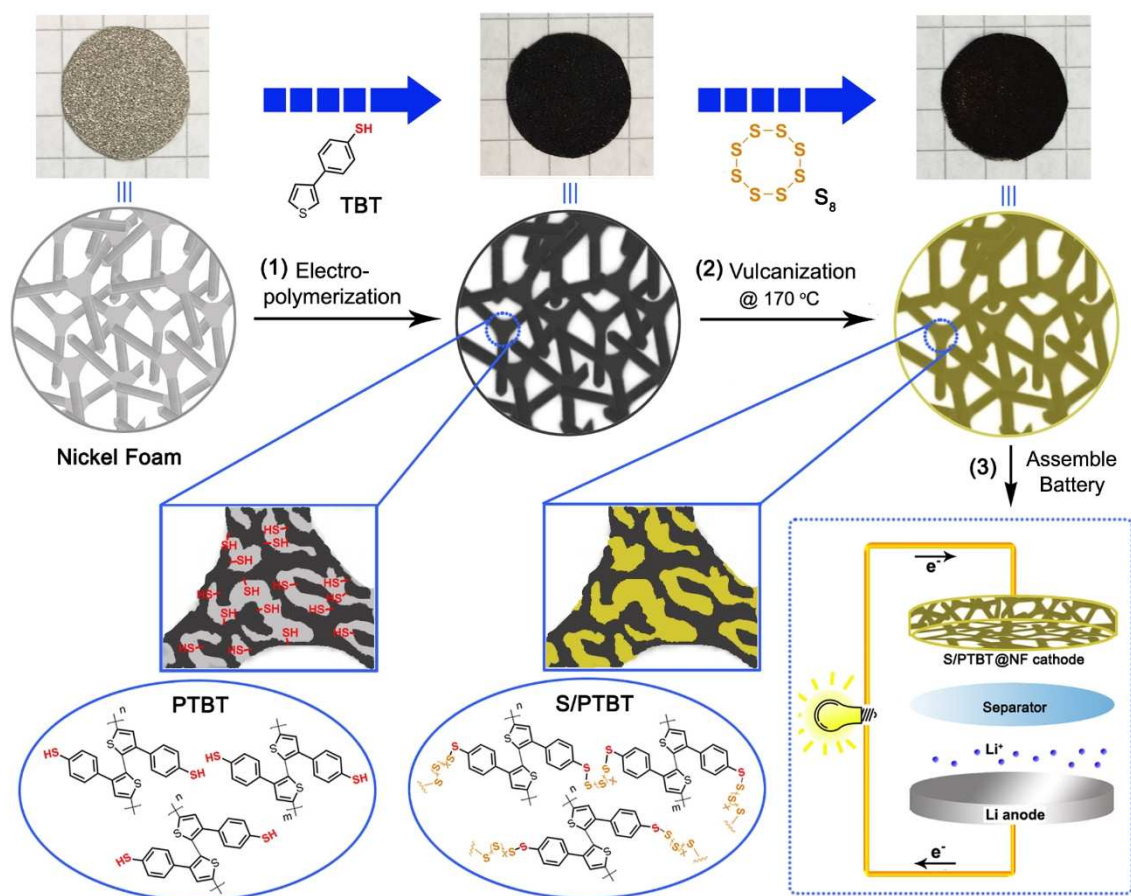
Normally, chemical polymerization is applied for the synthesis of functional conducting polymers and then followed by the traditional fabrication of electrodes containing the binder and additive carbon, the excitation signals of which will disturb the *operando* analysis of the cathode. In addition, the chemical-polymerization method often suffers from poor control of the morphology of the resulting materials. Thus, it is quite a challenge to produce well-designed electrodes with optimized conductivity, diffusion efficiency, and so on. Therefore, some efforts have been devoted to taking advantage of the electro-polymerizable properties of conducting polymers to construct free-standing cathodes *in situ*.<sup>[7]</sup> As is well known, electro-polymerization of conducting monomers on a flexible conducting substrate has been commonly used to design and fabricate functional electronic devices, owing to their low equipment cost, facile operation, and low-temperature process advantages. Meanwhile, Ni foam (NF), a low-cost commercial material, has been widely used as a substrate and support for electrode materials owing to its high electronic conductivity, desirable 3D open-pore structure, and high specific surface area.<sup>[8]</sup> In addition, the porous structure can decrease the loss of X-rays for the *operando* analysis and imaging.<sup>[9]</sup>

Thus, in the present work, we take advantage of the electro-polymerization strategy to construct a free-standing cathode on NF *in situ*. Combined with the electropolymerizable thiophene molecule as the main chain and the benzenethiol containing

thiol group as the lateral chain, 4-(thiophene-3-yl)benzenethiol (TBT) was synthesized. The corresponding polymer with many flexible and active sulfur binding sites was applied as the framework to fabricate a novel binder- and carbon additive-free cathode of Li-S battery by two steps as shown in Scheme 1. In the first step, TBT monomers were electro-polymerized on the surface of flexible NF to form the porous and conducting poly(4-(thiophene-3-yl)benzenethiol) (PTBT) frameworks with many lateral chains of thiol groups, which could serve as chemical binding sites for polysulfides. In the second step, this framework was thoroughly combined with sulfur molecules through vulcanization to obtain an organosulfur S/PTBT@NF cathode, which could be used to assemble Li-S batteries without any further modification. The loose structure of PTBT frameworks and the porous structure of NF are beneficial for the penetration and diffusion of electrolytes; meanwhile, the interconnected conjugate structure can be used as the transfer channels of electrons. Most importantly, this free-standing cathode can be applied as a model system for an *operando* study of the batteries. In this work, *operando* X-ray imaging analysis was applied to detect the sulfur storage manner of the organosulfur cathode during the charge-discharge process. This strategy does not only take advantage of the chemical confinement of the conducting polymer to improve the performance of cathodes but also simplify the fabrication process of electrode materials for Li-S batteries. Moreover, owing to the electro-deposition method, electrodes with different sizes can be easily obtained, as well as substituting NF with other flexible, cheaper, and higher-conductive substrates. We believe this facile fabrication method of free-standing organosulfur cathodes has great potential in the exploitation of highly efficient Li-S batteries in the future.

## Results and Discussion

To fabricate the PTBT through electro-polymerization, the thiol-containing monomer TBT was firstly synthesized as shown in Scheme S1, and the detailed experimental conditions and characterization results are shown in the Supporting Information (S1). The final product of TBT is a light-yellow powder as shown in Figure S1. For the fabrication of the S/PTBT@NF cathode, the flexible nickel foam was used as the substrate for electro-polymerization of TBT as well as the current collector of the cathode. To be more specific, the electro-polymerization of the TBT monomers was carried out in acetonitrile solution to form PTBT on the surface of NF, which leads to the formation of PTBT@NF frameworks. Such frameworks not only provide continuous pathways for electron transport due to the internal conjugated main-chain but also furnish plenty of lateral thiol groups working as active bonding sites, which can fix sulfur and polysulfide through the formation of S–S bonds for their chemical confinement. Figure 1a described the representative electrochemical growth processes of TBT on NF by cyclic voltammetry (CV) for oxidative electro-polymerization in an acetonitrile (ACN) solution containing 2 mg mL<sup>-1</sup> TBT monomer and 0.1 M tetrabutylammonium hexafluorophosphate (TBAPF<sub>6</sub>)



**Scheme 1.** Fabrication route of binder- and carbon additive-free S/PTBT@NF cathode. Schematic illustration describing the fabrication procedure of sulfur crosslinked to a PTBT cathode through a combined electrochemical and vulcanization strategy in situ: (1) creation of the PTBT frameworks on porous NF by electro-polymerization method; (2) crosslink of ring-opening sulfur through vulcanization; and (3) assembly of the Li-S batteries by using the newly gained cathode material.

as the electrolyte, revealing the electroactivity of TBT and the formation of PTBT on the surface of NF. During this process, a dark red-brown PTBT film forming on the surface of NF can be observed (inset of Figure 1a) with the increasing of peak currents in CV curves. The first cycle of the CV curve for the electrochemical property of TBT is shown in Figure S2. After seven cycles, the CV curves becoming stable indicates the maximum deposition of PTBT with a weight of about  $1.0 \text{ mg cm}^{-2}$  after rinsing by ACN and drying at room temperature. With prolonging the electro-polymerization time, the PTBT film became thicker and looser, from which the outer layer was likely to fall off uniformly. Scanning electron microscopy (SEM) images have been taken to investigate the microstructures of the obtained PTBT@NF sample. As shown in Figure 1b,c, the PTBT@NF electrode exhibits a loose structure, where the obtained PTBT layer is composed of some integrated particles with the size of 100–300 nm. The Brunauer-Emmett-Teller (BET) surface area was recorded as  $6.9 \text{ m}^2 \text{ g}^{-1}$  with a range of pore dimensions (3–10 nm) (Figure S3). It is necessary to stress that these particles are homogeneously coated on the NF, which can provide a favorable pathway for charge transfer.

In addition, the loose structure of the polymer can facilitate the quick diffusion of electrolytes.

To produce the S/PTBT@NF cathode with the linear polysulfane along the thiol surface, a two-step vulcanization process was carried out in a sealed vessel: sulfur was first embedded into the PTBT framework at a low-temperature step at  $150 \text{ }^\circ\text{C}$ , followed by further heating to  $170 \text{ }^\circ\text{C}$  leading to ring-opening radical polymerization of elemental sulfur with the thiol groups of PTBT.<sup>[5b]</sup> After rinsing with  $\text{CS}_2$  to remove the physical-adsorbed sulfur and drying at room temperature, the free-standing S/PTBT@NF cathode can be obtained and employed to assemble the Li-S battery without any further modification. A control cathode without heating treatment to sulfur, namely S&PTBT@NF, was employed for comparison. It is instructive that this strategy can be used as an alternative method for the fabrication of organosulfur cathode electrodes without binder and carbon additives. Our design and synthesis of the new conducting thiol-polymer PTBT using the electro-polymerization method could pave the way for the exploration of advanced free-standing cathode materials with the function of covalent fixing of sulfur species.

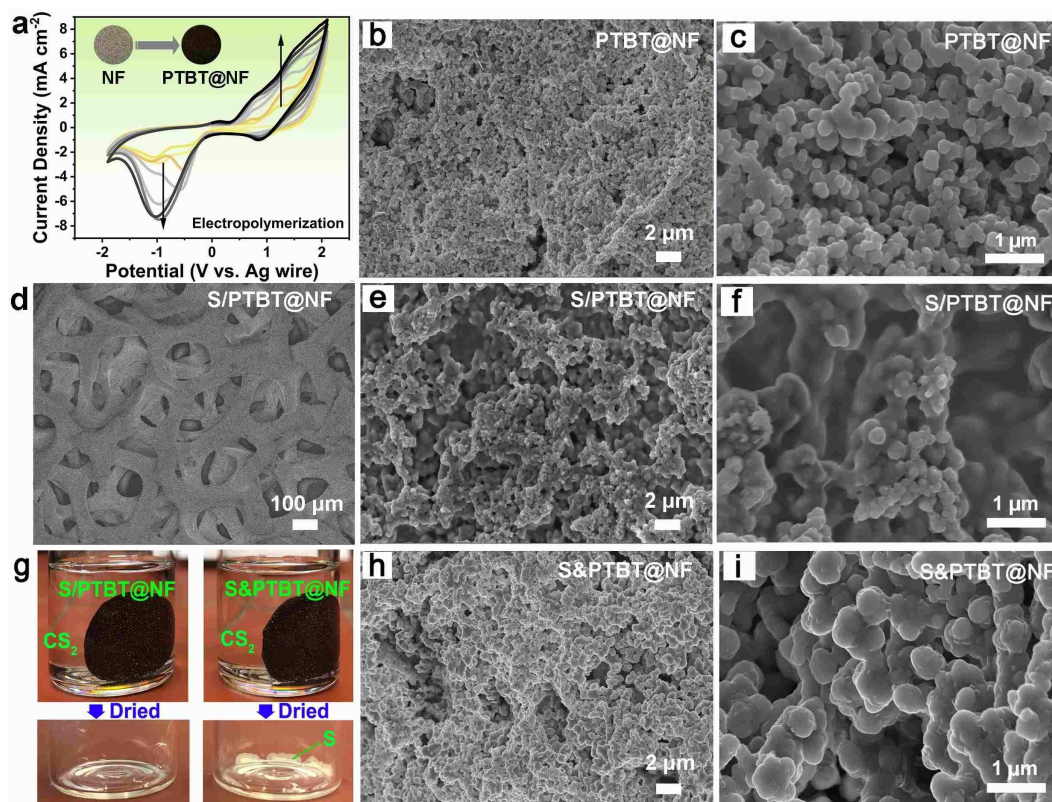


**Figure 1.** (a) Repeated potential scan electro-polymerization of TBT in 0.1 M TBAPF<sub>6</sub>/ACN at 100 mV s<sup>-1</sup> on NF. (b,c) SEM images of PTBT@NF and (d–f) S/PTBT@NF with low and high magnification. (g) Pictures of S/PTBT@NF (left) and S&PTBT@NF (right) electrode immersed in CS<sub>2</sub> and the corresponding product after drying of CS<sub>2</sub>. (h,i) SEM images of S&PTBT@NF with low and high magnification.

In order to vulcanize the PTBT@NF thoroughly, a certain amount of sulfur was dissolved in the CS<sub>2</sub> solution to infiltrate the frameworks in advance. Then the vulcanization process was carried out according to the methods mentioned above. After vulcanization, the S/PTBT@NF electrode with a dark-brown color was obtained as shown in Scheme 1. The SEM images in Figure 1d–f show a smooth surface and disappearance of most of the pores. In addition, the cross-section SEM image in Figure S4 also shows a similar morphology with a thickness of about 17 μm. The S/PTBT@NF electrode is stable in CS<sub>2</sub> solvent without dissolution of sulfur species (Figure 1g), which indicates that the sulfur molecules should be fixed to PTBT through covalent bonds with thiol groups in the polymer. The elemental content and corresponding element maps of PTBT@NF electrodes before and after vulcanization are shown in Figure S5. The element weight percent of S is increased from 14.7 to 66.8% after vulcanization, denoting that plenty of sulfur was loaded in the way of chemical bonding with PTBT. The sulfur loading in S/PTBT@NF is about 1.6 mg cm<sup>-2</sup>. Different from the morphology of PTBT@NF, the physically adsorbed sulfur sample (named S&PTBT@NF) was composed of some larger particles with the size of around 500 nm and most of the pores are still present (Figure 1h,i). The growing size of the particles indicates that the sulfur was prone to distribute and coat on the surface of PTBT, which ensures the full reaction between sulfur and PTBT during vulcanization. In addition, the S&PTBT@NF electrodes are light-

yellow in color, indicating the surface precipitation of sulfur, which can be defined as physical adsorption due to the fact that the sulfur in S&PTBT@NF can be totally removed by CS<sub>2</sub>, and the weight of the eluted sulfur from the electrode is almost the same as the amount of initial addition (Figure 1g).

To deeply investigate the chemical-bonding interaction between sulfur and PTBT in the S/PTBT electrodes, molecular and structural characteristics of the vulcanized PTBT were examined by means of different measurements. Firstly, XPS measurements were carried out to investigate the variation of chemical states and the elemental composition in the vulcanized PTBT. As shown in high-resolution C1s XPS spectra of Figure 2a,b, both samples of PTBT and S/PTBT show two peaks: one peak at 284.6 eV belongs to the C–C/C=C bond of benzol and thiophene skeleton, and the other peak is the C–S bond of thiophene ring and thiol group, respectively.<sup>[5a]</sup> Note that S/PTBT possesses lower binding energy of 285.8 eV for C–S bond than PTBT (286.1 eV) as well as a little increased content, indicating the stronger interaction between the linear sulfur and C–S bond of thiol after vulcanization. The corresponding high-resolution S2p spectra are presented in Figure 2c,d, where three species of sulfur including C–S, –SH, or –S–S– and the sulfate species can be observed at the peaks of 162.7, 163.7, and 168.1 eV with their satellite peaks.<sup>[10]</sup> It is obvious that after vulcanization, the content of –S–S– bond increased distinctly; these increased S–S bonds possess lower binding energy than

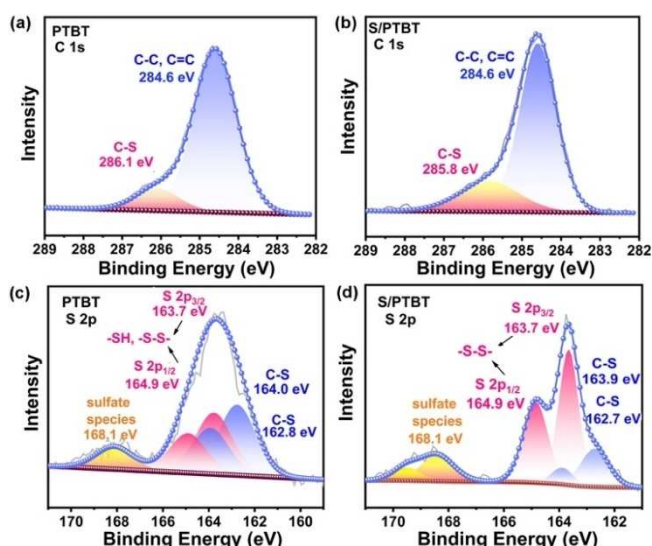


Figure 2. (a,b) C 1s and (c,d) S 2p XPS spectra of PTBT and S/PTBT samples.

that of pure sulfur  $S_8$  (164.0 eV),<sup>[11]</sup> which indicates that the added sulfur molecules in S/PTBT were ring-opened and covalently bonded to the PTBT through the formation of S–S bonds with the thiol groups. Besides, the sulfate species at 168.1 eV attributed to the doping process of the thiophene ring during the electro-polymerization to ensure the conductivity, which is commonly observed in the polythiophene or poly(3,4-ethylene-dioxythiophene)(PEDOT).<sup>[12]</sup>

Then, the thermogravimetric analysis (TGA) curves of different samples in argon are displayed in Figure 3a. The negligible weight loss of PTBT@NF below 200 °C indicates that the PTBT is thermally stable under the condition of vulcanization. Moreover, S/PTBT@NF exhibits a lower sublimation temperature (inset of Figure 3a) and a gentler slope of thermal decomposition than the pure sulfur  $S_8$ . The low sublimation temperature and slow loss process are related to the release of sulfur covalently bonded to the PTBT frameworks.<sup>[4b]</sup> These results support the covalent attachment of sulfur to the PTBT frameworks during the functional fabrication of cathodes in situ for Li-S batteries. Furthermore, the Raman spectra of the PTBT and S/PTBT samples are shown in Figure 3b. After vulcanization, the

characteristic peak of S–S bonds at 474  $\text{cm}^{-1}$  was present with a remarkable intensity in S/PTBT,<sup>[4b,g,13]</sup> which indicates successful chemical bonding of sulfur to the polymer frameworks. The intensities of the peaks in PTBT became relatively weak, including the C–S peaks at 182 and 308  $\text{cm}^{-1}$ , which may be due to the suppression by the fed sulfur.<sup>[14]</sup> Notably, the last peak of PTBT at 480  $\text{cm}^{-1}$  should belong to the disulfides S–S bonds formed between inter-chain thiol groups (–SH...SH–) of PTBT molecules as a side reaction during or after the electrochemical polymerization, which has also been reported in the literature.<sup>[15]</sup> To verify the phenomenon, we have also measured the Raman spectra of a TBT monomer, which is shown in Figure S6. The signal around 2560  $\text{cm}^{-1}$  belongs to the S–H stretching vibration mode of the thiol group in the monomer. After electrochemical polymerization, this signal disappears, and a peak emerges at 480  $\text{cm}^{-1}$  that indicates the formation of disulfide S–S bonds in the PTBT polymer. The shift of the S–S peak position in the Raman spectra of S/PTBT (Figure 3b) shows that the S–S bonds in PTBT (C–S–S–C) are different from the emerged S–S bonds after vulcanization. This fact strongly suggests that the disulfide S–S bonds in PTBT were broken and then reacted with sulfur radicals to form longer polysulfide chains (–S–S–S–) during the vulcanization process. Taking these results into account, we have proposed the rational molecular structure evolution during the whole fabrication process (Figure 4). On the first step of electrochemical polymerization, the monomer TBT was polymerized to form the PTBT polymer, and a side reaction happened between the inter-chain thiol group leading to the disulfide polymer named PTBTs. Next on the vulcanization process, the  $S_8$  monomer undergoes ring-opening polymerization (ROP) into linear polysulfide with diradical chain ends.<sup>[4a]</sup> Meanwhile, the S–H bond of PTBT polymer breaks to form the polymer radical (PTBT·). The lost two hydrogen atoms react with the sulfur atom during the vulcanization, releasing  $H_2S$  gas as a bi-product, which has already been confirmed by experiments.<sup>[16]</sup> For the PTBTs polymer, the cleavage of disulfide S–S bonds leads to the formation of the same polymer radical (PTBT·), which then reacts with the sulfur diradical. Note that no  $H_2S$  gas is produced in this route. Finally, the chemical-bonded organo-sulfur polymer S/PTBT is formed. According to the findings in our recent work, in which we have investigated the initial structure of the cathode using a combination of electronic-

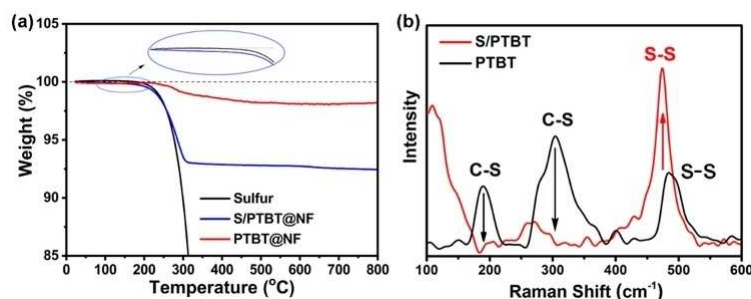


Figure 3. (a) TGA analysis and (b) Raman spectra of PTBT and S/PTBT samples.

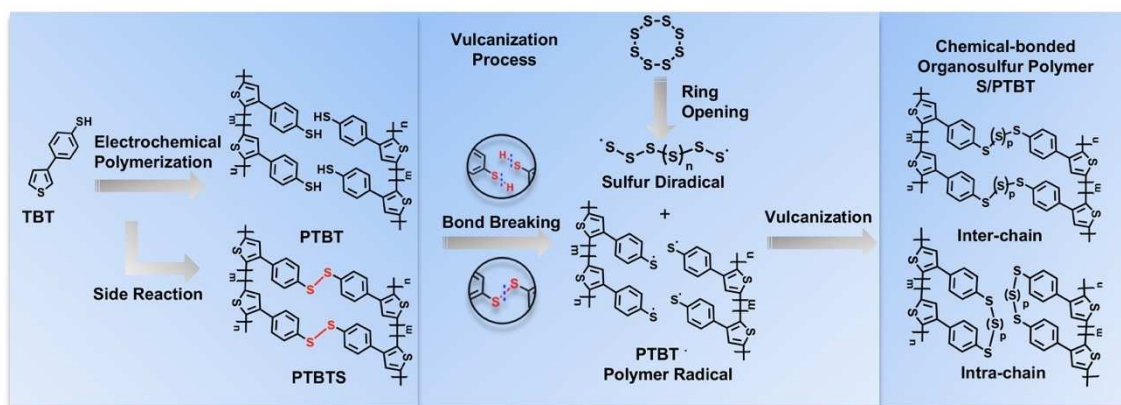
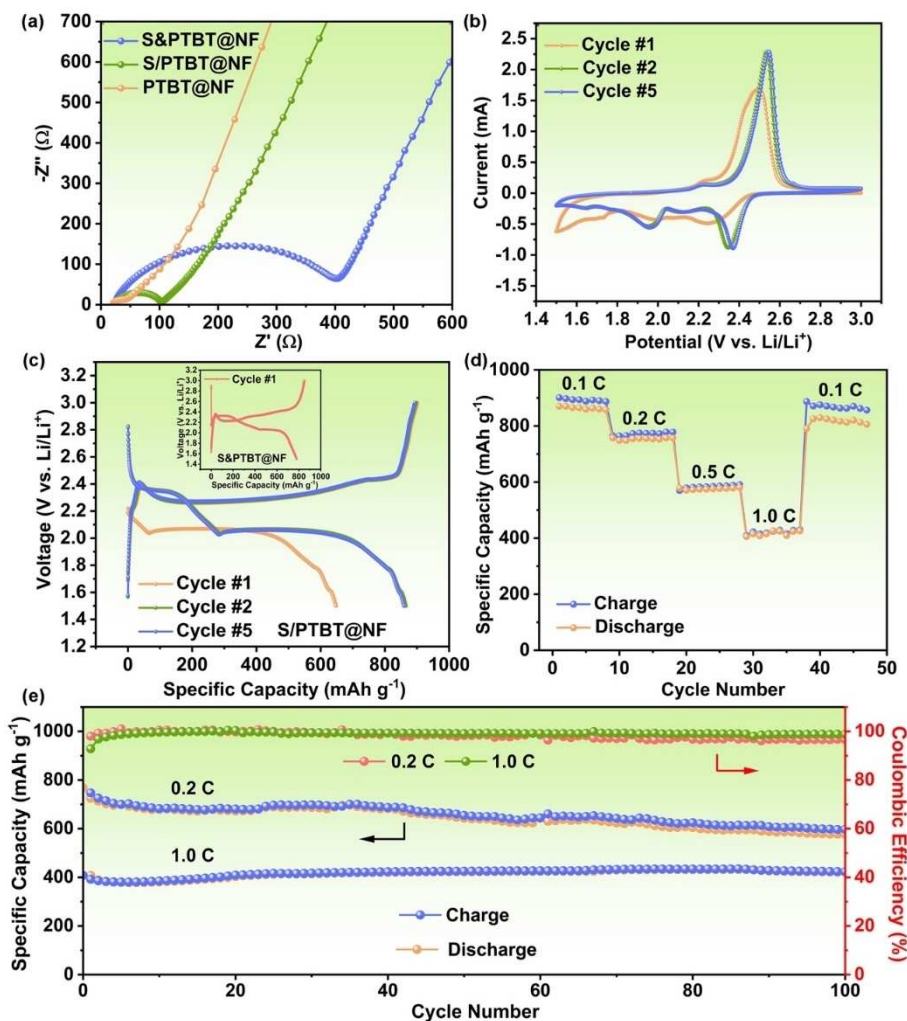


Figure 4. Illustration of the molecular structure evolution during the whole fabrication process.

structure theory and statistical mechanics,<sup>[17]</sup> we have proposed two possible structures for the S/PTBT polymer, named inter-chain and intra-chain, which can be generally distinguished by the way in which the polysulfide chains bind to the TBT units. From these two possible structures, our results showed that pentasulfide ( $p=5$ ) inter-chain crosslinks are dominant after vulcanization.<sup>[17]</sup>

The S/PTBT@NF cathodes without carbon additives and binder are directly applied in the Li-S coin cells. To investigate the effect of interaction between sulfur and PTBT on the conductivity of the cathode, the analysis of the electrochemical impedance spectroscopy (EIS) was first evaluated for Li-S batteries. Figure 5a shows the Nyquist plots of the pristine PTBT@NF, the chemical bonded S/PTBT@NF, and the control sample S&PTBT@NF cathode. All three electrodes show a semicircle in the high-frequency region associated with the charge-transfer resistance ( $R_{ct}$ ). It can be observed that the pristine PTBT@NF shows the smallest  $R_{ct}$  of around 20  $\Omega$ , due to the good conductivity of PTBT polymer. After sulfur embedding, the  $R_{ct}$  of the control cathode S&PTBT@NF increases significantly ( $\sim 400 \Omega$ ), most likely due to the insulating effect of elemental sulfur. Notably, after vulcanization, the  $R_{ct}$  of the S/PTBT@NF cathode decreased remarkably to around 75  $\Omega$ , indicating that covalent crosslinking of sulfur to PTBT leads to enhanced electron conduction in the cathode. This resistance value is comparable to those reported for organosulfur polymers with conductive carbon additives, which are summarized in Table S1, and reflects the good conductivity of the S/PTBT@NF cathode in the absence of additional conducting agents. The decrease of the resistance to electronic conduction in the S/PTBT@NF cathode occurring upon vulcanization can be related to a change in its electronic structure. Density-functional theory (DFT) calculations were carried out to calculate the energy bandgap of a TBT monomer upon attachment of sulfur chains with different numbers of sulfur atoms. Figure 6 shows the optimized structures and the highest occupied molecular orbital (HOMO)-lowest unoccupied molecular orbital (LUMO) gap of TBT monomers after attachment of  $n=2-8$  sulfur atoms, calculated with the PBE0 exchange-correlation functional<sup>[18]</sup> plus van der Waals interactions using the Tkatchenko-Scheffler

method (PBE0+vdW).<sup>[19]</sup> The results show a reduction of the HOMO-LUMO gap upon extension of the sulfur chain, gradually decreasing from 5.10 eV for TBT to 4.72 eV after attachment of an  $S_8$  chain. These results suggest that covalently bonded sulfur could indeed enhance the conducting properties of the PTBT cathode. In addition, it is important to note that the conducting properties of such a polymeric cathode can be further tuned by many synthetic design parameters such as polydispersity, compositional fluctuations, and morphological properties.<sup>[20]</sup> The electrochemical performance of S/PTBT@NF was further studied: Figure 5b exhibits the CV of the S/PTBT@NF cathode, which is similar to a typical Li-S redox curve. But the remarkable thing is at the first cycle, only one broad and weak reduction peak was observed, then two obvious reduction peaks emerged from the following cycles. The repetitive galvanostatic discharge/charge cycling between 1.5 and 3.0 V at 0.1C ( $1C=1675 \text{ mA g}^{-1}$ ) was displayed in Figure 5c. It is notable that there is only one distinct plateau at 2.07 V (vs. Li/Li<sup>+</sup>) during the first discharge process, which is consistent with the CV result, while two plateaus at 2.33 and 2.06 V are present for the control S&PTBT@NF cathode (inset of Figure 5c). According to the previous studies, the two voltage plateaus are attributed to the reduction of  $S_8$  to high-order polysulfides  $\text{Li}_2\text{S}_x$  ( $x=4-8$ ) at 2.35 V and further to low-order polysulfides  $\text{Li}_2\text{S}_2$  and  $\text{Li}_2\text{S}$  at 2.07 V, respectively.<sup>[21]</sup> This result further confirmed that most of the sulfur in the S/PTBT@NF cathode were ring-opened and covalently bonded to the PTBT through forming S-S bonds. This phenomenon is similar to those organosulfur cathodes, for which the ring-opening plateaus in the first discharge process are disappeared.<sup>[4b]</sup> However, this discharge plateau has appeared and is stable at 2.35 V in the following discharge/charge cycles of S/PTBT@NF, which suggests the formation of  $S_8$  molecules after the scission of crosslinked sulfur side chains and regeneration of S-S bonds with cycling. Moreover, the S/PTBT@NF exhibits a low initial discharge capacity of around 650  $\text{mAh g}^{-1}$  and a stable capacity of around 860  $\text{mAh g}^{-1}$  for the following cycles. The reversible discharge/charge capacities at various C-rate are exhibited in Figure 5d. Although the C-rate capability is inferior to the similar sulfur-containing cathodes, S/



**Figure 5.** (a) Nyquist plots of PTBT@NF, S/PTBT@NF, and S&PTBT@NF cathode. (b) CV of S/PTBT@NF cathode at a scan rate of  $0.1 \text{ mVs}^{-1}$ . (c) Representative galvanostatic discharge/charge voltage profiles of the S/PTBT@NF cathode for the 1st, 2nd, and 5th cycles at  $0.1 \text{ C}$ . Discharge/charge voltage profiles of the S&PTBT@NF cathode at the first cycle are also shown as inset. (d) Rate capabilities of the S/PTBT@NF cathode in  $1.5\text{--}3.0 \text{ V}$  at various current densities. (e) Discharge/charge capacities and coulombic efficiencies of the S/PTBT@NF cathodes for 100 cycles (after the first cycle) at the different C rates.

PTBT@NF without the assistance of super P carbon delivered a considerable reversible capacity of around  $870 \text{ mAh g}^{-1}$  at  $0.1 \text{ C}$ ,  $756$  ( $0.2 \text{ C}$ ),  $576$  ( $0.5 \text{ C}$ ),  $417$  ( $1.0 \text{ C}$ ), and back to a reversible capacity of  $820 \text{ mAh g}^{-1}$  at  $0.1 \text{ C}$ . Meanwhile, the S/PTBT@NF exhibited good capacity retention, in which the capacity is conserved at around  $600 \text{ mAh g}^{-1}$  for  $0.2 \text{ C}$  ( $\approx 80\%$ ) and  $400 \text{ mAh g}^{-1}$  for  $1.0 \text{ C}$  ( $\approx 96\%$ ) after 100 cycles, with the coulombic efficiencies of 97 and 99%, respectively, in Figure 5e. It is notable that when cycling at  $0.2 \text{ C}$ , the achieved capacity is higher and the coulombic efficiency declines along with cycling, which can be ascribed to the structural deformation of the electrode materials induced by the larger storage of Li ions. In contrast, when cycling at  $1.0 \text{ C}$ , the lithiation capacity of the electrode materials is limited with minimal structural deformation, and therefore, the cycling stability is enhanced, and the coulombic efficiency does not decay that as rapidly as during cycling at a low rate ( $0.2 \text{ C}$ ). Such phenomenon has been frequently observed in alloy-Si<sup>[22]</sup> or conversion-type

electrode<sup>[23]</sup> materials for Li-ion batteries that undergo significant volume variations during battery charge and discharge. As a comparison, the control S&PTBT@NF, in which the loading sulfur is fixed through physical adsorption, showed a markedly low discharge capacity of below  $400 \text{ mAh g}^{-1}$  for  $0.2 \text{ C}$ , while maintaining around 83% capacity (compared with the first discharge capacity) after 100 cycles with a coulombic efficiency of below 90% throughout, as shown in Figure S7. The significantly improved capacity and coulombic efficiency of S/PTBT@NF when compared to that of S&PTBT@NF should be attributed to the chemical-bonding interaction between sulfur and PTBT. The long-term discharge-charge cycling performance in Figure S8 shows that the capacity of the S/PTBT@NF cathode declined slightly with increasing cycle number at a fading rate of 0.178 and 0.387% per cycle for 200 and 300 cycles. Furthermore, the morphology of the S/PTBT@NF electrode after 100 cycles looks similar to that of the original S/PTBT@NF electrode as shown in Figure S9, which indicates that most of

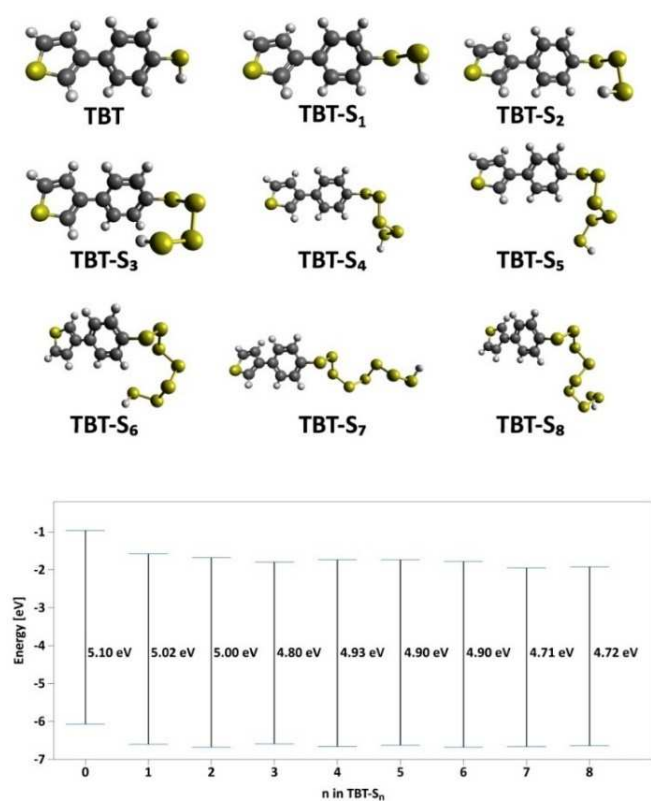


**Figure 6.** PBE0+vdW calculations of the HOMO-LUMO gap of TBT and TBT-S<sub>n</sub> molecules. All the model structures shown correspond to the most stable configuration after optimization of the forces as described in the Experimental Section. Carbon (C), hydrogen (H), and sulfur (S) elements are displayed as spheres in grey, white, and yellow, respectively.

the attached sulfur was confined in the cathode during fully repetitive lithiation and delithiation reactions. In summary, these coin-cell battery performances have verified the S/PTBT@NF cathode can work efficiently in the absence of additional conducting agents.

As a proof of concept, the porous, binder-free, and free-standing cathode without additional carbon additives can work as the model system for operando analysis. X-ray imaging of the operating Li/S cell is a suitable tool to test the effect of the polymer. If sulfur is covalently bonded to the polymer, no macroscopic sulfur particles should appear on the cathode during charge as it was already shown for the conventional Li/S cells.<sup>[24]</sup> However, if free sulfur is added to the PTBT electrode via simple drop-casting of a sulfur-rich CS<sub>2</sub> solution, sulfur particles should form during the charge step. Figure 7 summarizes the operando X-ray study by the device presented in Figure S12 that shows the morphological activity of the Li/S cells around the state of charge ( $\pm 30\%$  state-of-charge) for both cases of sulfur admixture.

For the S/PTBT@NF cathode with covalently bonded sulfur no morphological activity can be detected, while the PTBT cathode with the free sulfur shows a clear formation of sulfur particles (marked by red arrows in Figure 7), especially in the second and third cycle. Video S1 shows the time-dependent

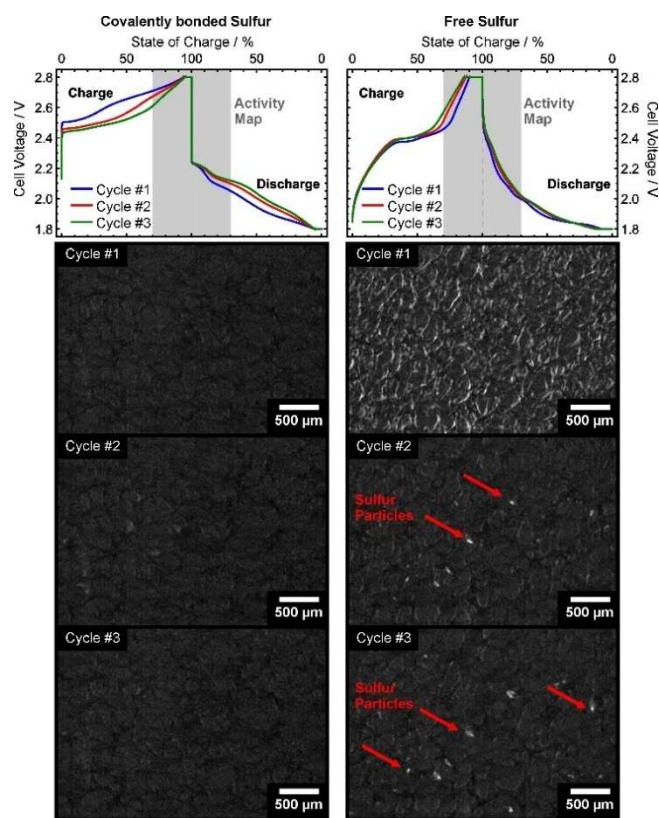


**Figure 7.** Results of the operando X-ray imaging study for covalently bonded sulfur to the PTBT-cathode and free sulfur on the PTBT cathode. The activity map was created from the X-ray images around the charged state ( $\pm 30\%$  state-of-charge).

morphological evolution of the particles during the period of the activity map. Video S2 shows the same time interval, which is extended to the final discharge of the third cycle. Here, also the dissolution of the sulfur particles can be observed. These results clearly reveal the remarkable effect in the suppression of polysulfides shuttle via introducing covalent bonds between sulfur species and the active thiol groups, which leads to a significant improvement in the cycling performance when compared to the physically adsorbed sulfur-based cathode. This work not only demonstrates a new fabrication strategy of the organosulfur cathodes for Li-S batteries but also shows a way for the construction of a model cathode for the operando analysis of Li-S batteries. The significant fixing effect of sulfur species was proven by operando X-ray imaging in real-time for the first time.

## Conclusion

Combined with the electro-polymerization and vulcanization method, a porous framework based on a conducting thiol-polymer was constructed, and the sulfur-rich cathode from elemental sulfur without binder and carbon additives was fabricated in situ. This approach maintains the conductivity and flexibility of the polymer framework. Simultaneously, the thiol

groups on its side chain can realize the covalent bonding with the long sulfur chains to further improve the performance of Li-S batteries through the chemical confinement of polysulfide. This work not only demonstrates a new fabrication strategy of the organosulfur cathodes for Li-S batteries but also shows a way for the construction of a model cathode for the operando analysis of Li-S batteries. The significant fixing effect of sulfur species was proven by operando X-ray imaging in real-time for the first time.

## Experimental Section

### Electro-polymerization of TBT on NF (PTBT@NF)

The commercial Ni foam (thickness: 0.5 mm) was cleaned first with acetone and soaked in 2.0 M HCl for 10 min, then washed subsequently with water and ethanol for several times, and dried in a vacuum oven at room temperature. The monomer TBT was electro-polymerized on the Ni foam in an N<sub>2</sub>-saturated acetonitrile solution containing 2 mg mL<sup>-1</sup> TBT and 0.1 M TBAPF<sub>6</sub> (Tetrabutylammonium hexafluorophosphate). This process was conducted by CV in a three-electrode system at a potential between -1.8–1.8 V (100 mV s<sup>-1</sup>, *n* = 7) using an electrochemical workstation (GAMRY-1100), Ag wire as the reference electrode, and platinum wire as the counter electrode. After electro-polymerization, the electrode was rinsed with acetonitrile several times and then dried in a vacuum oven at room temperature. Finally, a red-brown electrode (PTBT@NF) was obtained, and the mass loading of PTBT is around 1.0 mg cm<sup>-2</sup>.

### Preparation of S/PTBT@NF and S&PTBT@NF cathodes

In advance, a certain weight of sulfur was dissolved in 100  $\mu$ L CS<sub>2</sub>. Then the sulfur was mixed with PTBT@NF through dropping and quickly drying the S/CS<sub>2</sub> solution on a hot stage at 60 °C to obtain the control S&PTBT@NF electrode. After that, the S&PTBT@NF was heated at 150 °C for 1 h under an argon atmosphere, facilitating the melt infiltration of sulfur into the polymer framework. Then followed by further heating at 170 °C for 8 h to form the S/PTBT@NF electrode. Finally, the S/PTBT@NF was rinsed with CS<sub>2</sub> to wash away the physical-adsorbed sulfur. The loading amount of sulfur in S/PTBT@NF is around 1.6 mg cm<sup>-2</sup>, which was calculated through the weight variation of S/PTBT@NF and PTBT@NF. The equivalent sulfur in control S&PTBT@NF electrodes was predetermined by controlling the drop volume of the S/CS<sub>2</sub> solution. The resultant S&PTBT@NF and S/PTBT@NF electrodes exhibited a light-yellow and dark-brown color, respectively.

### Materials characterizations

The morphologies and structures of the samples were examined by SEM (LEO 1530) with an energy-dispersive X-ray spectroscopy (EDX) attachment (Zeiss). XPS (Thermo Scientific, Escalab 250Xi) was employed to analyze the composition of the samples. TGA was performed in a temperature range of 25–800 °C with a heating rate of 10 °C min<sup>-1</sup> under an argon atmosphere. Raman spectra were measured using a Horiba LabRAM HR 800 Raman spectroscopy. Nitrogen adsorption experiments were performed with a Quantachrome Autosorb-1 at liquid nitrogen temperature, and data analysis was performed by Quantachrome software. The specific surface area was calculated using the BET equation. Pore size distribution was determined by Barrett-Joyner-Halenda (BJH) method.

### Battery tests

The Li-S batteries were assembled in an Ar-filled glovebox with the concentration of moisture and oxygen below 1.0 ppm. Coin type (CR 2032) cells were fabricated by assembling an S/PTBT@NF or S&PTBT@NF cathode, a Celgard 2500 diaphragm separator, and a lithium foil anode with 30  $\mu$ L electrolyte [electrolyte/sulfur (E/S) ratio  $\approx$  18.7]. The electrolyte was prepared by dissolving 1 M lithium bis(trifluoromethane)sulfonamide (LiTFSI) and 0.1 M lithium nitride (LiNO<sub>3</sub>) in a mixture solution of 1,3-dioxolane and 1,2-dimethoxyethane (DOL/DME; 1:1 v/v). The galvanostatic charge/discharge tests were performed using a Bio-Logic VMP3 electrochemical workstation at different current densities within a cutoff voltage window of 1.5–3.0 V. The specific capacity is calculated based on the mass of sulfur. EIS was also carried out by applying an AC voltage with a 5 mV amplitude in a frequency of 0.01 to 100 kHz at open-circuit potential.

### Operando X-ray imaging

The operando cell design used for this study is shown in the Supporting Information. The inner geometry of the cell is the same as for CR2032 standard coin cells. The cell was assembled with two lithium chips to achieve a significant electrode pressure. Two Celgard 2500 separators made of porous polypropylene were used to minimize the risk for a short circuit due to the sharp edges of the nickel foam. Subsequently, the respective PTBT cathode either with covalently bonded or free sulfur, with 1.5 mg of sulfur each, was placed in the operando cell. Finally, 50  $\mu$ L of the electrolyte (DOL/DME 1:1 v/v, 1 M LiTFSI, 0.1 M LiNO<sub>3</sub>) was added on the porous Ni foam. After applying a vacuum for less than one minute to achieve a complete filling of the cell by the electrolyte, the additional electrolyte was added onto the Ni-foam cathode until a proper wetting was obtained. This results in 136.6 mg and 90.3 mg of electrolyte in the operando cell for the covalently bonded and free sulfur cathode, respectively. The open-circuit potential for each electrochemical cell was measured immediately after assembling and was 2.939 and 2.623 V for covalently bonded and free sulfur, respectively. The cells were cycled with a C-rate of 0.1C in the voltage window that ranged from 1.8 to 2.8 V. EIS was performed at the end of each charge and discharge step. The X-ray radiography images were recorded by using a laboratory CT setup (Supporting Information). The applied voltage of the tungsten source was 100 keV and the current was set to 100  $\mu$ A. The images were detected with a flat panel argon detector every 20 s with a resolution of approximately 10  $\mu$ m per pixel. The images were post-processed with the freely available open-source software ImageJ. The images were cropped to the region of interest after dark field correction and flat field division. An activity map was created for the first three states of charge to examine the appearance of sulfur crystals in the cell. For this, the standard deviation of all X-ray images was taken that is 30% state-of-charge away from the final charge state. Therefore, bright areas show regions with high activity while darker areas represent fields with low morphological activity. This analysis allows for the detection of particle formation despite the high attenuation of nickel for X-rays. In addition, two videos of the 3rd cycle of the free sulfur cathode were created that clearly show the formation and dissolution of sulfur particles around the charged state. Here, a background image of the Ni foam was created by calculating the mean value image during a period of low activity at the beginning of the charge. This image was subsequently subtracted from the image stack to achieve a better contrast with respect to the formed sulfur particles. Video S1 shows the time period where the activity map of the 3rd cycle of the free sulfur cathode was created from. Video S2 shows the same period but is extended to the end of discharge.

## Theoretical calculations

The computational details of the theoretical calculations can be found in section S2 of the Supporting Information.

## Acknowledgements

Jiaoyi Ning gratefully acknowledges the financial support of the CSC scholarship (No. 202006010282). Hongtao Yu thanks the National Science Foundation for Young Scientists of China (21704040). The authors would like to thank the priority program "Polymer-based Batteries" (SPP 2248) from the Deutsche Forschungsgesellschaft (DFG) (project number 441211139) for financial support. Open Access funding enabled and organized by Projekt DEAL.

## Conflict of Interest

The authors declare no conflict of interest.

## Data Availability Statement

The data that support the findings of this study are available from the corresponding author upon reasonable request.

**Keywords:** electrochemistry · energy storage · lithium-sulfur batteries · operando studies · organosulfur

- [1] A. Manthiram, Y. Fu, Y. Su, *Acc. Chem. Res.* **2013**, *46*, 1125–1134.
- [2] H. Peng, J. Huang, X. Cheng, Q. Zhang, *Adv. Energy Mater.* **2017**, *7*, 1700260.
- [3] a) M. Shi, S. Zhang, Y. Jiang, Z. Jiang, L. Zhang, J. Chang, T. Wei, Z. Fan, *Nano-Micro Lett.* **2020**, *12*, 146; b) L. Xue, L. Zeng, W. Kang, H. Chen, Y. Hu, Y. Li, W. Chen, T. Lei, Y. Yan, C. Yang, A. Hu, X. Wang, J. Xiong, C. Zhang, *Adv. Energy Mater.* **2021**, *11*, 2100420; c) H. Zhang, L. Yang, P. Zhang, C. Lu, D. Sha, B. Yan, W. He, M. Zhou, W. Zhang, L. Pan, Z. Sun, *Adv. Mater.* **2021**, *33*, 2008447; d) J. Qian, Y. Xing, Y. Yang, Y. Li, K. Yu, W. Li, T. Zhao, Y. Ye, L. Li, F. Wu, R. Chen, *Adv. Mater.* **2021**, *33*, 2100810; e) B. Liu, R. Bo, M. Taheri, I. Bernardo, N. Motta, H. Chen, T. Tsuzuki, G. Yu, A. Tricoli, *Nano Lett.* **2019**, *19*, 4391–4399.
- [4] a) W. Chung, J. Griebel, E. Kim, H. Yoon, A. Simmonds, H. Ji, P. Dirlam, R. Glass, J. Wie, N. Nguyen, B. Guralnick, J. Park, Á. Somogyi, P. Theato, M. Mackay, Y. Sung, K. Char, J. Pyun, *Nat. Chem.* **2013**, *5*, 518–524; b) H. Kim, J. Lee, H. Ahn, O. Kim, M. Park, *Nat. Commun.* **2015**, *6*, 7278; c) A. Hoeffling, D. Nguyen, Y. Lee, S. Song, P. Theato, *Mater. Chem. Front.* **2017**, *1*, 1818–1822; d) X. Li, L. Yuan, D. Liu, Z. Li, J. Chen, K. Yuan, J. Xiang, Y. Huang, *Energy Storage Mater.* **2020**, *26*, 570–576; e) R. Guan, L. Zhong, S. Wang, D. Han, M. Xiao, L. Sun, Y. Meng, *ACS Appl. Mater. Interfaces* **2020**, *12*, 8296–8305; f) N. Xu, T. Qian, X. Liu, J. Liu, Y. Chen, C. Yan, *Nano Lett.* **2017**, *17*, 538–543; g) S. Je, T. Hwang, S. Talapaneni, O. Buyukcakir, H. Kim, J. Yu, S. Woo, M. Jang, B. Son, A. Coskun, J. Choi, *ACS Energy Lett.* **2016**, *1*, 566–572; h) H. Hu, B. Zhao, H. Cheng, S. Dai, N. Kane, Y. Yu, M. Liu, *Nano Energy* **2019**, *57*, 2211–2855.
- [5] a) S. Talapaneni, T. Hwang, S. Je, O. Buyukcakir, J. Choi, A. Coskun, *Angew. Chem. Int. Ed.* **2016**, *55*, 3106–3111; *Angew. Chem.* **2016**, *128*, 3158–3163; b) S. Zeng, L. Li, L. Xie, D. Zhao, N. Wang, S. Chen, *ChemSusChem* **2017**, *10*, 3378; c) S. Zeng, L. Li, D. Zhao, J. Liu, W. Niu, N. Wang, S. Chen, *J. Phys. Chem. C* **2017**, *121*, 2495–2503; d) B. Oschmann, J. Park, C. Kim, K. Char, Y. Sung, R. Zentel, *Chem. Mater.* **2015**, *27*, 7011–7017.
- [6] a) M. Weret, C. Kuo, T. Zeleke, T. Beyene, B. Hwang, *Energy Storage Mater.* **2020**, *26*, 483–493; b) C. Huang, K. Lin, Y. Hsieh, W. Su, C. Wang, G. Bruncklaus, M. Winter, J. Jiang, B. Hwang, *ACS Appl. Mater. Interfaces* **2021**, *13*, 14230–14238; c) W. Wang, Z. Cao, G. Elia, Y. Wu, J. Ming, *ACS Energy Lett.* **2018**, *3*, 2899–2907.
- [7] a) T. Schoetz, C. Ponce de Leon, A. Bund, M. Ueda, *Electrochem. Commun.* **2018**, *89*, 52–56; b) P. Bairagi, N. Verma, *Sens. Actuators B* **2019**, *289*, 216–225; c) V. Muniraj, R. Boukherroub, M. Shelke, *ACS Sustainable Chem. Eng.* **2020**, *8*, 6433–6441.
- [8] N. Chaudhari, H. Jin, B. Kim, K. Lee, *Nanoscale* **2017**, *9*, 12231–12247.
- [9] J. Weker, M. Toney, *Adv. Funct. Mater.* **2015**, *25*, 1622–1637.
- [10] J. Senkevich, C. Mitchell, G. Yang, T. Lu, *Langmuir* **2002**, *18*, 1587–1594.
- [11] R. Wang, J. Yang, X. Chen, Y. Zhao, F. Pan et al., *Adv. Energy Mater.* **2020**, *10*, 1903550.
- [12] a) A. Taouil, F. Lallemand, J. Hihn, J. Melot, V. Pattissie, B. Lakard, *Ultrason. Sonochem.* **2011**, *18*, 140–148; b) N. Chanunpanich, A. Ulman, A. Malagon, Y. Strzhemechny, S. Schwarz, A. Janke, T. Kratzmueller, H. Braun, *Langmuir* **2000**, *16*, 3557–3560; c) E. Mittraka, M. Jafari, M. Vagin, X. Liu, M. Fahlman, T. Ederth, M. Berggren, M. Jonsson, X. Crispin, *J. Mater. Chem. A* **2017**, *5*, 4404–4412.
- [13] a) M. Helton, P. Chen, P. Paul, Z. Tyeklar, R. Sommer, L. Zakharov, A. Rheingold, E. Solomon, K. Karlin, *J. Phys. Chem.* **1976**, *80*, 1812–1823.
- [14] Y. You, W. Zeng, Y. Yin, J. Zhang, C. Yang, Y. Zhu, Y. Guo, *J. Mater. Chem. A* **2015**, *3*, 4799–4802.
- [15] S. Revin, S. John, *Electrochim. Acta* **2011**, *56*, 8934–8940.
- [16] P. Sang, Y. Si, Y. Fu, *Chem. Commun.* **2019**, *55*, 4857–4860.
- [17] Y. Schütze, R. Silva, J. Ning, J. Rappich, Y. Lu, V. Ruiz, A. Bande, J. Dzubielia, *Phys. Chem. Chem. Phys.* **2021**, *23*, 26709–26720.
- [18] C. Adamo, V. Barone, *J. Chem. Phys.* **1999**, *110*, 6158.
- [19] A. Tkatchenko, M. Scheffler, *Phys. Rev. Lett.* **2009**, *102*, 073005.
- [20] S. Tajik, H. Beitollahi, F. Nejad, I. Shoaie, M. Shokouhimehr, *RSC Adv.* **2020**, *10*, 37834.
- [21] H. Peng, J. Huang, X. Cheng, Q. Zhang, *Adv. Energy Mater.* **2017**, *7*, 1700260.
- [22] Y. Xu, D. Borsa, F. Mulder, *J. Electrochem. Soc.* **2018**, *166*, A5252.
- [23] T. Quan, Y. Xu, M. Tovar, N. Goubard-Bretesché, Z. Li, Z. Kochovski, H. Kirmse, K. Skrodzky, S. Mei, H. Yu, D. AbouRas, M. Wagemaker, Y. Lu, *Batteries & Supercaps* **2020**, *3*, 747.
- [24] a) S. Risse, C. Jafta, Y. Yang, N. Kardjilov, A. Hilger, I. Manke, M. Ballauff, *Phys. Chem. Chem. Phys.* **2016**, *18*, 10630–10636; b) Y. Yang, S. Risse, S. Mei, C. J. Jafta, Y. Lu, C. Stöcklein, N. Kardjilov, I. Manke, J. Gong, Z. Kochovski, M. Ballauff, *Energy Storage Mater.* **2017**, *9*, 96–104; c) S. Risse, A. Juhl, S. Mascotto, T. Arlt, H. Markötter, A. Hilger, I. Manke, M. Fröba, *J. Phys. Chem. Lett.* **2020**, *11*, 5674–5679.

Manuscript received: March 21, 2022  
Revised manuscript received: April 26, 2022  
Accepted manuscript online: May 7, 2022  
Version of record online: May 30, 2022

# ChemSusChem

Supporting Information

## **Constructing Binder- and Carbon Additive-Free Organosulfur Cathodes Based on Conducting Thiol-Polymers through Electropolymerization for Lithium-Sulfur Batteries**

Jiaoyi Ning<sup>+</sup>, Hongtao Yu<sup>+</sup>, Shilin Mei, Yannik Schütze, Sebastian Risse, Nikolay Kardjilov, André Hilger, Ingo Manke, Annika Bande, Victor G. Ruiz, Joachim Dzubiella, Hong Meng,\* and Yan Lu\* © 2022 The Authors. ChemSusChem published by Wiley-VCH GmbH. This is an open access article under the terms of the Creative Commons Attribution License, which permits use, distribution and reproduction in any medium, provided the original work is properly cited.

**Table S1.** Summary of the reported organosulfur cathode for lithium-sulfur batteries.

Remarks	Sulfur loading (mg cm <sup>-2</sup> )	Composite (active material:carbon additive:binder)	Charge-transfer resistance (R <sub>ct</sub> ) (ohm)	Voltage (V)	First discharge capacity (mAh g <sup>-1</sup> )	Retention, cycles	Ref.
poly(S-r-DIB)	0.8	75:20:5		1.7-2.6	1100 (at 0.1 C)	71 %, 270	[4a]
S-TTCA-I	0.8	60:30:10		1.7-2.7	1210 (at 0.1 C)	83 %, 450	[4b]
poly(S-co-EAE)	0.75	70:15:5		1.5-2.6	650 (at 0.1 C)	64 %, 100	[4c]
STI		80:10:10	43.4	1.7-2.8	1123 (at 0.2 C)	94 %, 350	[4d]
S/P-CTF@rGO	1.5	80:10:10	27.5	1.7-2.8	1130 (at 0.5 C)	81.4 %, 500	[4e]
S-GSH	1.0	70:20:10	65	1.5-2.8	1108 (at 0.2 C)	87 %, 450	[4f]
S-BOP	0.9	60:30:10		1.7-2.7	1149 (at 0.2 C)	92.7 %, 1000	[4g]
OPNS-50 OPNS-72 OPNS-80	1.1	70:20:10	80 90 170	1.7-2.7	650 (at 1 C) 889 (at 1 C) 1100 (at 1 C)	98 %, 200 91 %, 620 72 %, 200	[4h]
S-CTF-1		60:30:10		1.7-2.7	670 (at 0.05 C)	85.8 %, 300	[5a]
cp(S-PMAT)	1.5	80:10:10	48.7	1.5-3.0	1240 (at 0.1 C)	66.9 %, 1000	[5b]
Capped CP(S3BT)/C	1.0	65:25:10	111	1.5-3.0	1362 (at 0.1 C)	75 %, 500	[5c]
(S/S-P3HT/CB	1.0	70:25:5	40	1.7-2.8	1212 (at 0.5 C)	65 %, 100	[5d]
S/PTBT	1.6	Binder and carbon additive-free	75	1.5-3.0	870 (at 0.1 C)	96 %, 100	This work

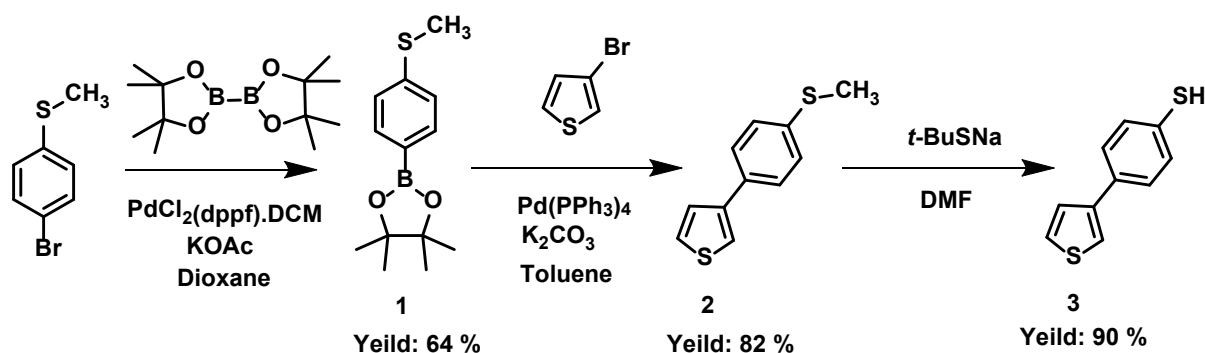
## S1. Synthesis of Monomer TBT:

### 1. Materials

4-Bromothioanisole (97 %, Energy Chemical), bis(pinacolato)diboron ( 98 %, Alligator Reagent), potassium acetate (99 %, Sigma), 1,1'-Bis(diphenylphosphino) ferrocene-palladium(II)dichloride dichloromethane complex (98 %, Energy Chemical), dichloromethane (99.5 %, Aladdin), anhydrous magnesium sulfate (99 %, Aladdin), n-hexane (95 %, Aladdin), 3-bromothiophene (97%, TCI), toluene (99.5 %, Sinopharm Chemical Reagent), potassium carbonate (99.7 %, Aladdin),

tricaprylylmethylammonium chlorid (90 %, Aladdin), tetrakis (triphenylphosphine) palladium ( $\text{Pd}(\text{PPh}_3)_4$ ) (97%, TCI), Sodium 2-methyl-2-propanethiolate (*t*-BuSNa) (90 %, Aldrich), hydrochloric acid (37 %, Sigma-Aldrich), carbon powders (Acros), Chloroform-d (D, 99.8 % + TMS, 0.03 %, Energy Chemical) were commercially available and used as received, the 1,4-dioxane (99.5 %, Aladdin) and N,N-dimethylformamide (99.9 %, Aladdin) were dried by molecular sieves (5A, Energy Chemical).

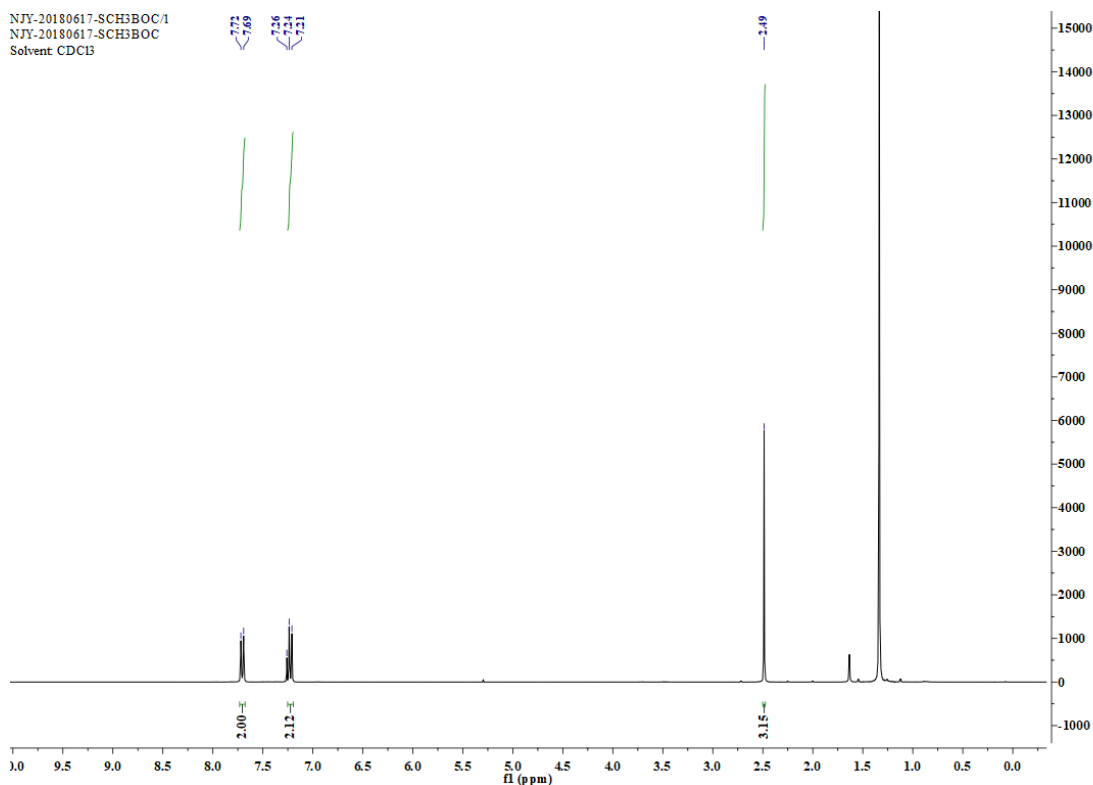
## 2. Experimental Procedures



**Scheme S1.** Synthesis of monomer 4-(thiophene-3-yl)benzenethiol (TBT).

### 4,4,5,5-tetramethyl-2-(4-(methylthio)phenyl)-1,3,2-dioxaborolane (1)

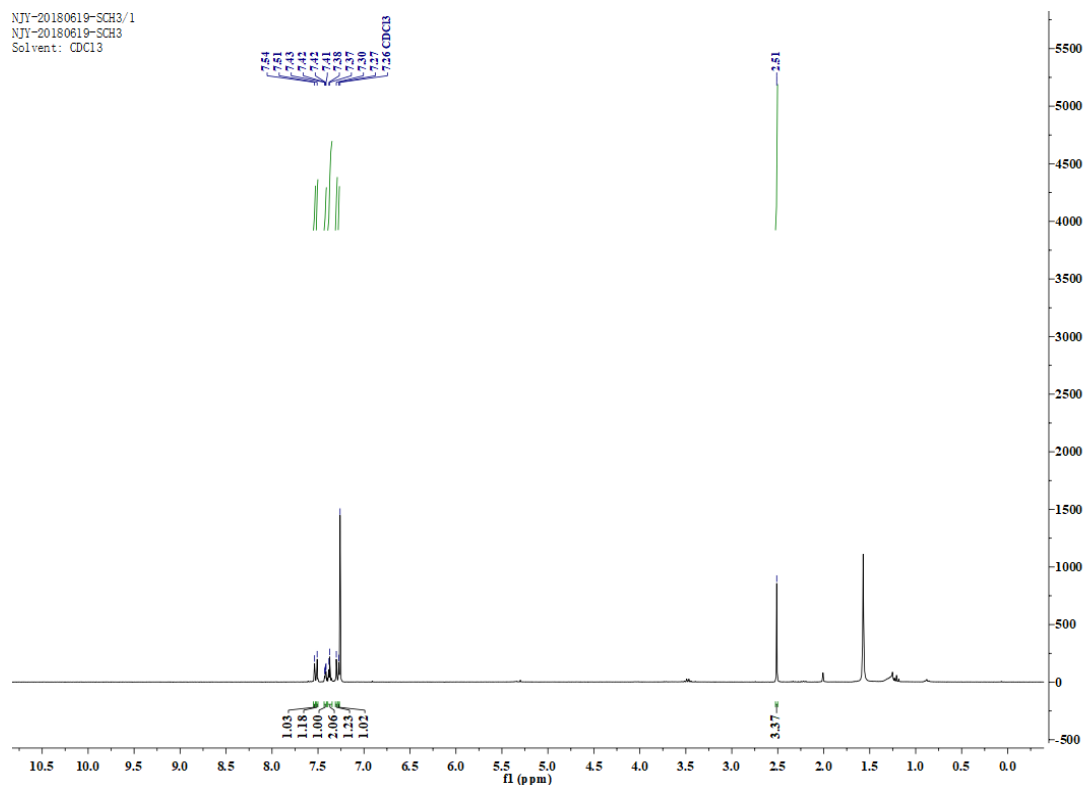
A 250 mL round bottom flask were charged with 4-Bromothiobenzene (10 g, 50 mmol), bis(pinacolato)diboron (16 g, 60 mmol), 200 mL dry 1,4-dioxane was added and bubbled with nitrogen for 15 minutes, then potassium acetate (6 g, 62 mmol) and 1,1'-Bis(diphenylphosphino)ferrocene-palladium(II)dichloride dichloromethane complex (0.8 g, 1mmol) were added quickly. The mixture was heated to reflux for 16 hours under the protection of nitrogen. After the reaction finished, the solvent 1,4-dioxane was moved by rotary evaporation. Then extracted with dichloromethane and water twice, the organic layer was dried with anhydrous magnesium sulfate. Finally purified by silica gel chromatography (eluent: dicholormethane and n-hexane 1:5) to give 1 as yellow oil; yield 64 %.  $^1\text{H NMR}$  (300 MHz, Chloroform-d)  $\delta$  7.71 (d,  $J = 8.3$  Hz, 2H), 7.22 (d,  $J = 8.3$  Hz, 2H), 2.49 (s, 3H).



<sup>1</sup>H NMR (300 MHz, CDCl<sub>3</sub>) spectrum of 4,4,5,5-tetramethyl-2-(4-(methylthio)phenyl)-1,3,2-dioxaborolane.

### 3-(4-(methylthio)phenyl)thiophene (2) (MPT)

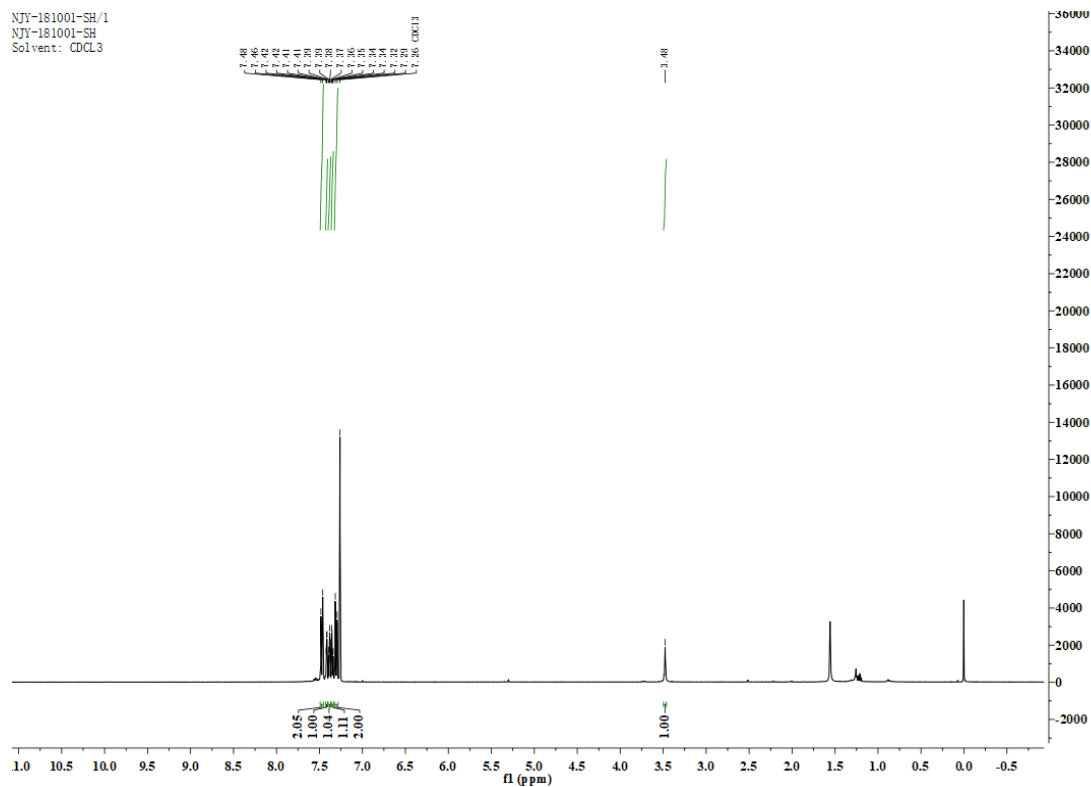
To a 250 mL pressure bottle, 4,4,5,5-tetramethyl-2-(4-(methylthio)phenyl)-1,3,2-dioxaborolane (**1**, 5.8 g, 23.2 mmol) and 3-bromothiophene (4.9 g, 30.16 mmol) were dissolved in 100 mL toluene. Then 35 mL 2 M potassium carbonate aqueous solution was added to the suspension followed by the addition of the phase-transfer agent tricaprylmethylammonium chlorid. The catalyst tetrakis (triphenylphosphine) palladium (Pd(PPh<sub>3</sub>)<sub>4</sub>) (1.33 g, 1.16 mmol) were added to the mixture after bubbling with nitrogen for 15 minutes. The mixture was heated to 110°C for 24 hours. When cooling down to room temperature, the solvent toluene was moved by rotary evaporation, and further purified by silica gel chromatography (eluent: dichloromethane and n-hexane 1:10) to give **2** as white powder; yield 82%. <sup>1</sup>H NMR (300 MHz, Chloroform-d) δ 7.54 (s, 1H), 7.51 (s, 1H), 7.42 (dd, J = 2.8, 1.5 Hz, 1H), 7.38 (d, J = 2.7 Hz, 2H), 7.30 (s, 1H), 7.27 (s, 1H), 2.51 (s, 3H).



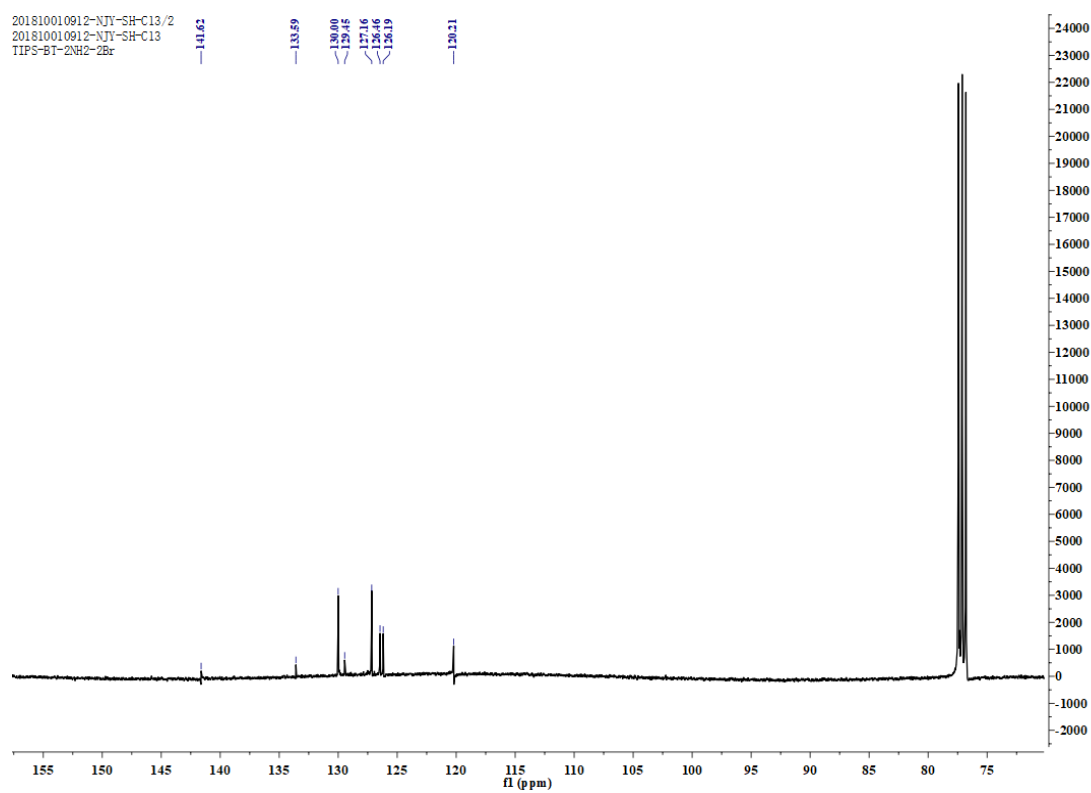
$^1\text{H}$  NMR (300 MHz,  $\text{CDCl}_3$ ) spectrum of 3-(4-(methylthio) phenyl) thiophene.

#### 4-(thiophen-3-yl)benzenethiol (**3**) (TBT)

To a 250mL round bottom flask, the above 3-(4-(methylthio) phenyl) thiophene (**2**, 4 g, 19.2 mmol), Sodium 2-methyl-2-propanethiolate (*t*-BuSNa) (8.8 g, 76.8 mmol) and dry N,N-dimethylformamide (100 mL) were added, the reaction mixture was refluxed for 8 hours under nitrogen atmosphere. The solution was cooled and poured into hydrochloric acid solution (10 %, 100 mL), with the white precipitate subsequently formed. Then filtered and washed by flash chromatography, dried in vacuum oven to give the product **3** as pale yellow solid; yield 90 %. Please noticed the odor of *t*-BuSNa, all the processes should be carried on in the fume hood, and carbon powders were used to absorb residual odor.  $^1\text{H}$  NMR (400 MHz, Chloroform-*d*)  $\delta$  7.47 (d,  $J = 8.5$  Hz, 2H), 7.42 (dd,  $J = 2.9, 1.4$  Hz, 1H), 7.38 (dd,  $J = 5.0, 2.9$  Hz, 1H), 7.35 (dd,  $J = 5.0, 1.4$  Hz, 1H), 7.30 (d,  $J = 8.5$  Hz, 2H), 3.48 (s, 1H).  $^{13}\text{C}$  NMR (101 MHz, Chloroform-*d*)  $\delta$  141.62, 133.59, 130.00, 129.45, 127.16, 126.46, 126.19, 120.21.



<sup>1</sup>H NMR (400 MHz, CDCl<sub>3</sub>) spectrum of 4-(thiophene-3-yl)benzenethiol.



<sup>13</sup>C NMR spectrum of 4-(thiophene-3-yl)benzenethiol.



**Figure S1.** The photograph of the monomer TBT.

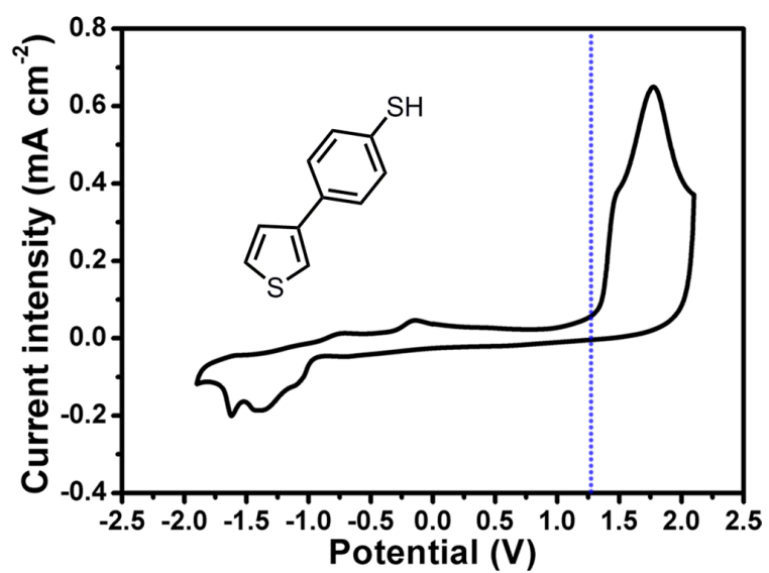


**Figure S2.** The CV curve of monomer TBT.

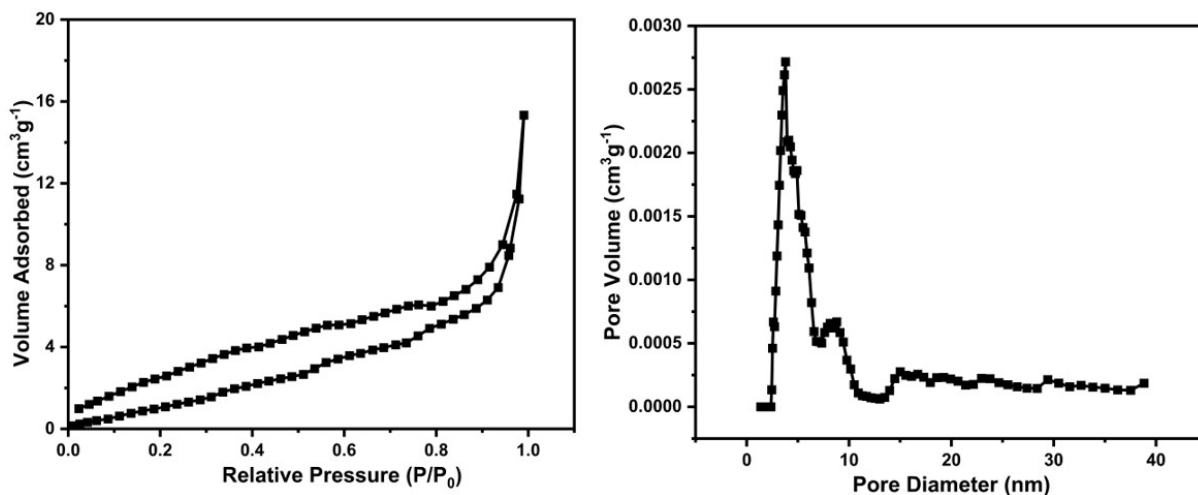


Figure S3. (a) BET Nitrogen adsorption and desorption test for the PTBT polymer, (b) the distribution of pore diameter using Barrett-Joyner-Halenda (BJH) method.

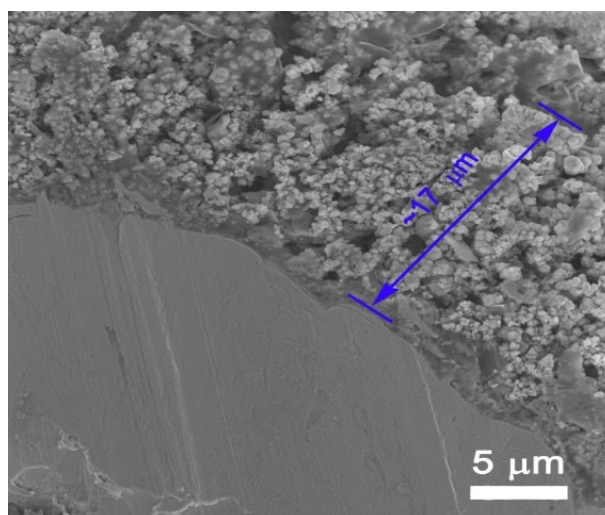
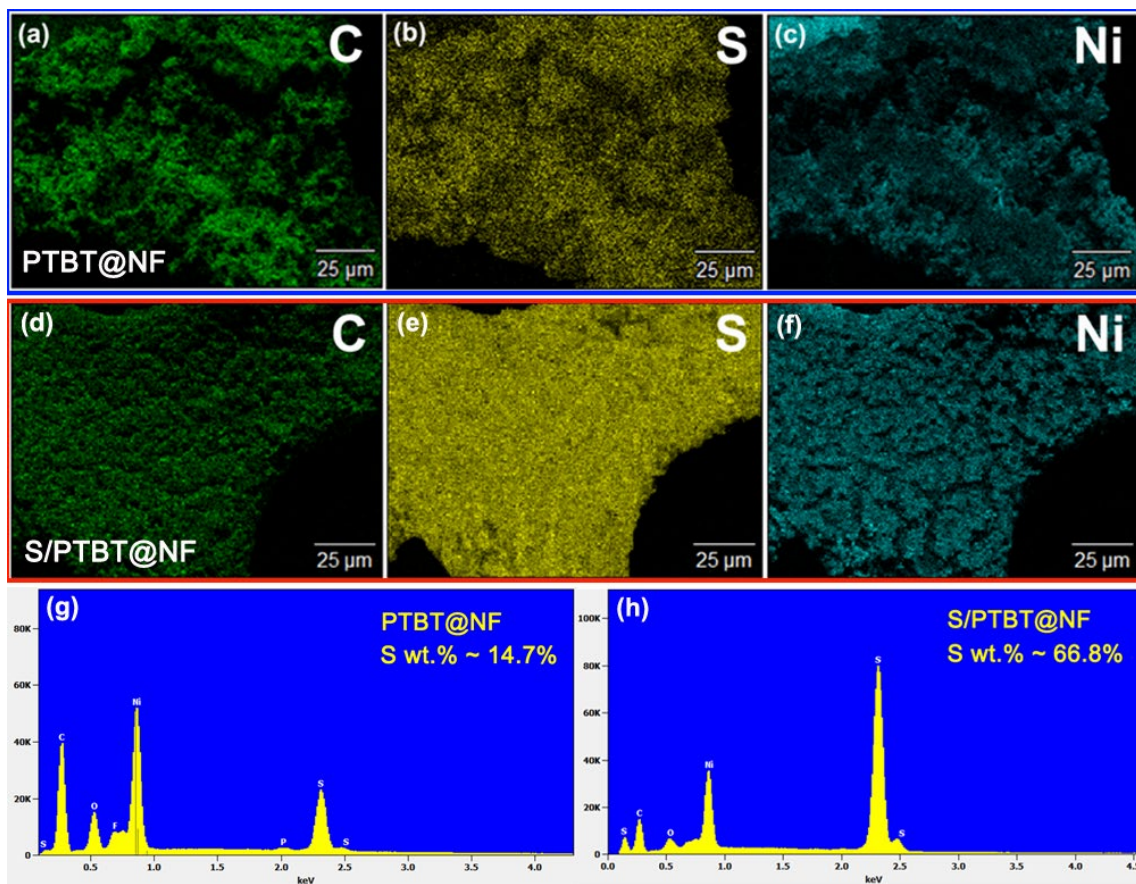


Figure S4. The cross-section SEM image of the S/PTBT@NF.



**Figure S5.** EDX of the PTBT@NF and S/PTBT@NF samples.

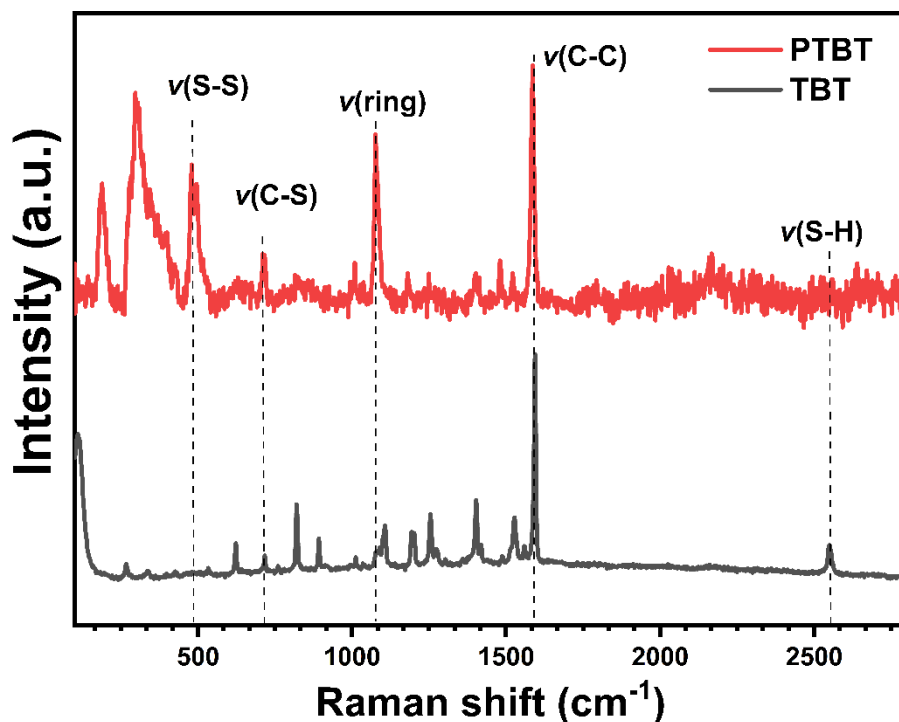


Figure S6. Raman spectra of monomer TBT and polymer PTBT.

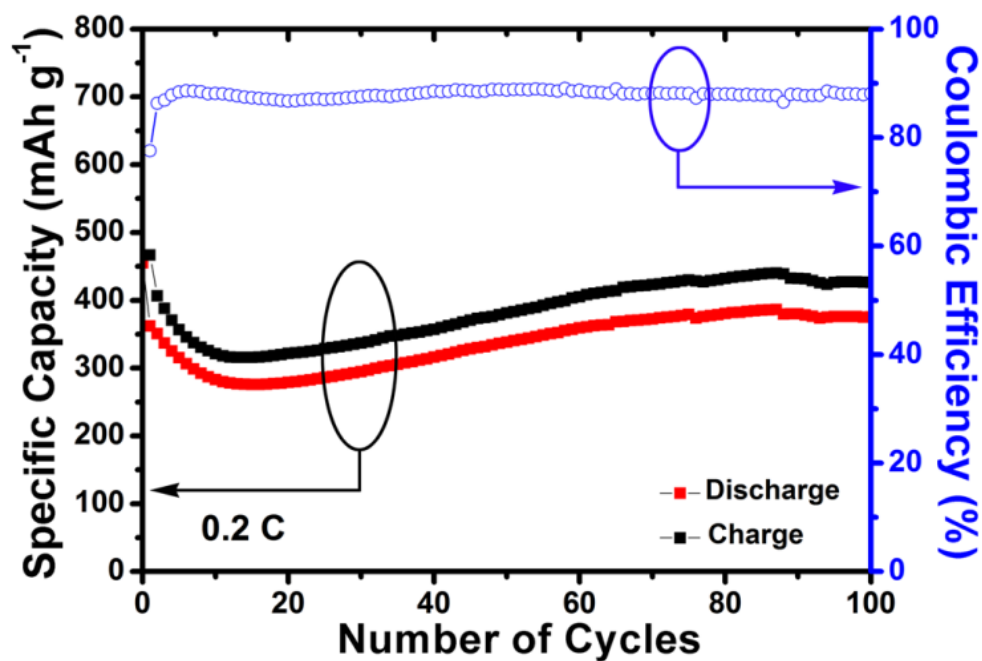
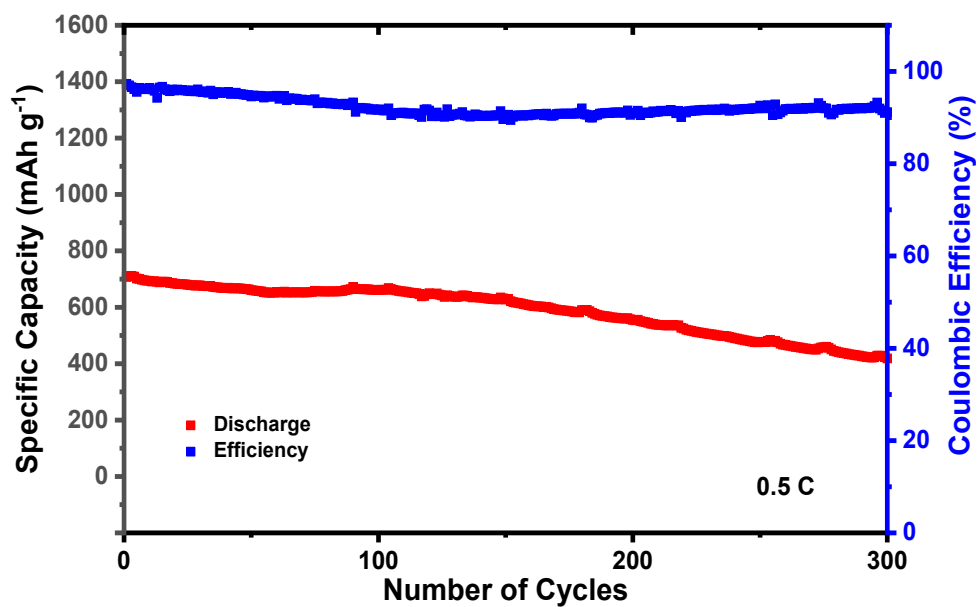
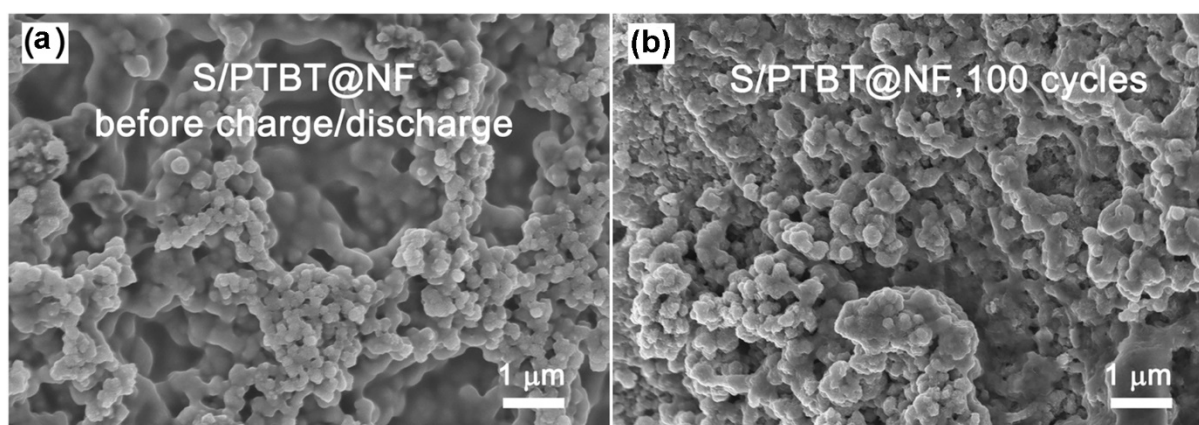


Figure S7 The discharge/charge capacities and coulombic efficiencies of the control S&PTBT@NF cathode for 100 cycles at 0.2 C.



**Figure S8** Long-term discharge profiles of the S/PTBT@NF cathode at 0.5 C rate.



**Figure S9** SEM of the S/PTBT@NF cathode before (a) and after (b) 100 charge/discharge cycles at 0.2 C.

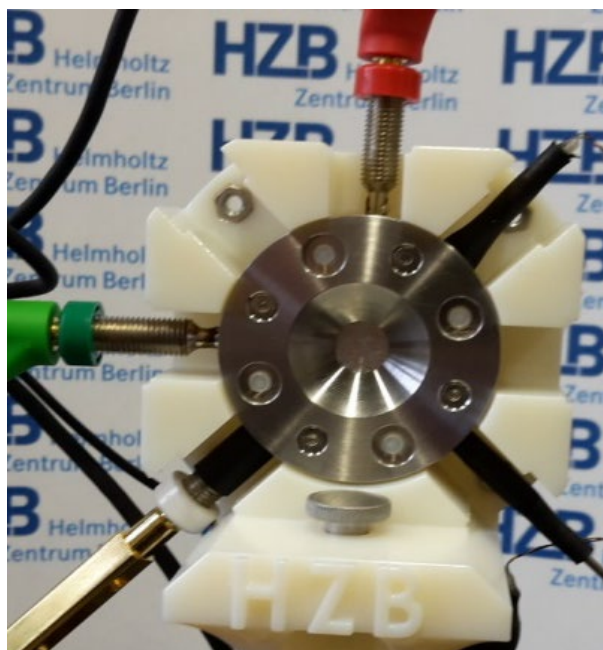
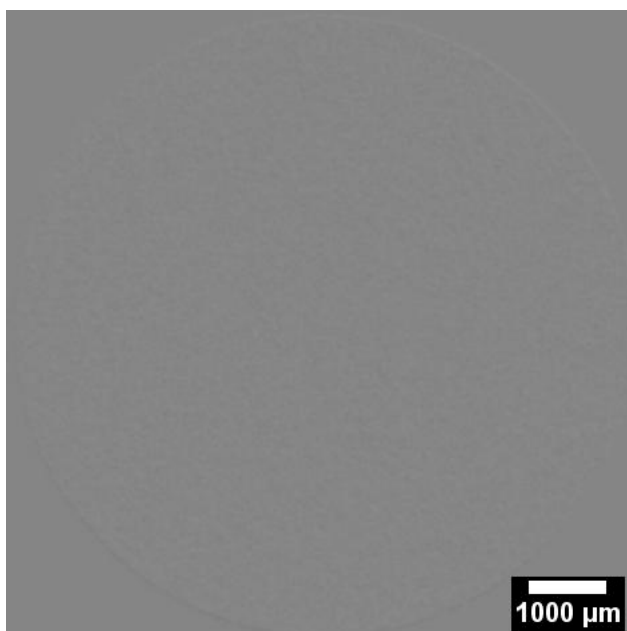
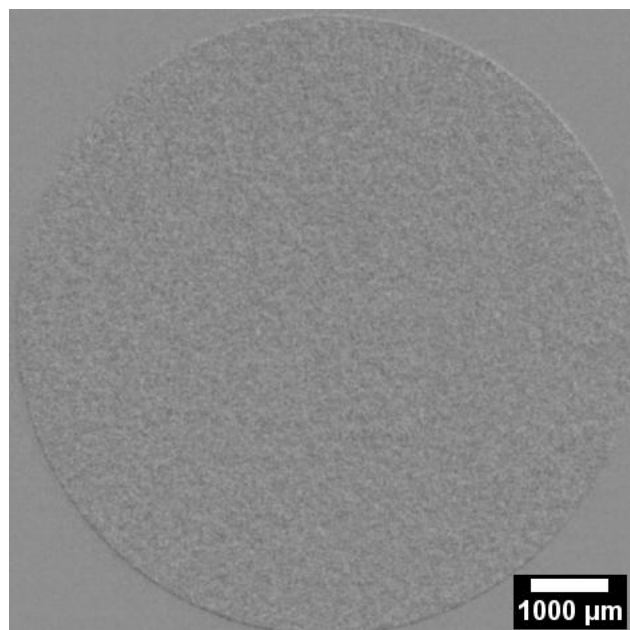


**Figure S10.** Image of the *operando* cell used for the X-ray imaging study.<sup>[7]</sup> The X-ray radiography images were recorded by using a laboratory CT setup.<sup>[8,9]</sup> The cell body consists of stainless steel and a polyether ether ketone (PEEK) ring. The inner geometry is comparable to that of a standard CR2032 coin cell.



**Video S1.** The time-dependent morphological evolution of the particles during the period of the activity map.



**Video S2.** The same time interval, which is extended to the final discharge of the third cycle.

## **S2. Theory calculations**

For the generation of structures, a pre-relaxation was performed with the Avogadro software<sup>[1]</sup> employing the MMFF94 force field<sup>[2]</sup> using steepest descent minimization. Pre-relaxed structures were further optimized with DFT. All DFT calculations were performed using the all-electron, full-potential density functional theory package FHI-aims.<sup>[3]</sup> The exchange-correlation (XC) interactions were treated using the PBE0 functional together with the Tkatchenko-Scheffler method<sup>[1]</sup> to include van der Waals (vdW) interactions. FHI-aims-specific tier 2 basis sets and tight settings have been used. The convergence criterion for the total energy and for the forces was set to  $10^{-6}$  eV and  $10^{-5}$  eV/Å, respectively. The HOMO-LUMO gaps were deduced from the final relaxed structures. HOMO-LUMO gaps using the B3LYP<sup>[4,5]</sup> and PBE<sup>[6]</sup> XC functionals plus vdW interactions (B3LYP+vdW, PBE+vdW) were also computed for comparison (shown in **Figure S11**).

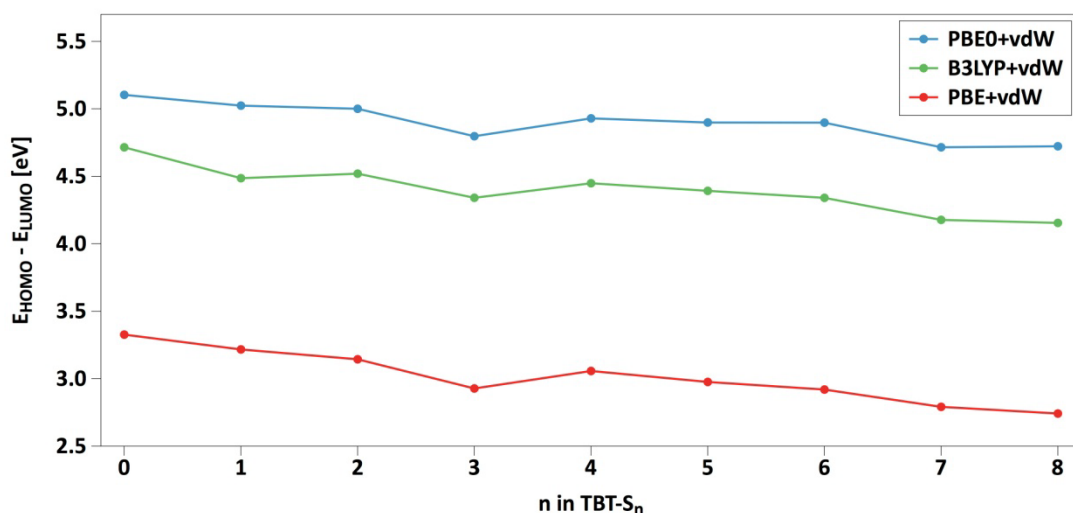


**Figure S11** HOMO-LUMO gap of TBT and TBT-S<sub>n</sub> monomers for  $n = 1, 2, \dots, 8$  using different XC functionals. As expected, hybrid functionals show a larger HOMO-LUMO gap in comparison to PBE+vdW. All numbers correspond to the most stable configuration after optimization of the forces as described in the Methods section.

### References:

- [1] Hanwell, M. D.; Curtis, D. E.; Lonie, D. C.; Vandermeersch T.; Zurek, E.; Hutchison G. R. Avogadro: an advanced semantic chemical editor, visualization, and analysis platform. *Journal of Cheminformatics* **2012**, *4*, 17.
- [2] Halgren T. A. Merck molecular force field. I. Basis, form, scope, parameterization, and performance of MMFF94. *Journal of Computational Chemistry* **1996**, *17*, 490-519.
- [3] Blum, V.; Gehrke R.; Hanke, F.; Havu, P.; Havu, V; Ren, X; Reuter K; Scheffler, M. *Computer Physics Communications*, **2009**, *180*, 2175-2196.
- [4] Becke, A. D. A new mixing of Hartree-Fock and local density-functional theories, *Journal of Chemical Physics*, **1993**, *98*, 5648-5652.

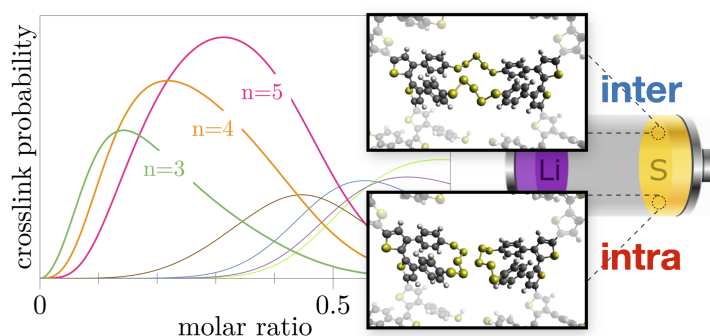
- [5] Stephens P. J.; Devlin, F. J.; Chabalowski, C.F.; Frisch, M.J. *Ab Initio* Calculation of Vibrational Absorption and Circular Dichroism Spectra Using Density Functional Force Fields, *The Journal of Physical Chemistry*, **1994**, 98, 11623-11627.
- [6] Perdew J. P.; Burke K.; Ernzerhof, M. Generalized Gradient Approximation Made Simple, *Physical Review Letters*, **1997**, 78, 1396.
- [7] Risse, S.; Hark, E.; Kent, B.; Ballauff, M. Operando Analysis of a Lithium/Sulfur Battery by Small-Angle Neutron Scattering. *ACS Nano* **2019**, 13, 10233-10241.
- [8] Kardjilov, N.; Hilger, A.; Manke, I.; Woracek, R.; Banhart, J. CONRAD-2: the new neutron imaging instrument at the Helmholtz-Zentrum Berlin. *Journal of Applied Crystallography* **2016**, 49, 195-202.
- [9] Kardjilov, N.; Hilger, A.; Manke, I. CONRAD-2: Cold Neutron Tomography and Radiography at BER II (V7). *Journal of Large-Scale Research Facilities* **2016**, 2 (DOI: 10.17815/jlsrf-2-108).

## A.2 Combined First-principles Statistical Mechanics Approach to Sulfur Structure in Organic Cathode Hosts for Polymer Based Lithium–sulfur (Li–S) Batteries

Yannik Schütze, Ranielle de Oliveira Silva, Jiaoyi Ning, Jörg Rappich, Yan Lu, Victor G. Ruiz, Annika Bande, Joachim Dzubiella

*Phys. Chem. Chem. Phys.*, **2021**, 23, 26709-26720

DOI: 10.1039/D1CP04550D



**Author Contributions:** This project was a cooperation between the groups of Joachim Dzubiella (JD), Yan Lu (YL), and Annika Bande (AB). The project idea was conceived by JD, AB, Victor G. Ruiz (VR), and Yannik Schütze (YS). All synthesis was carried out by Ranielle de Oliveira Silva (RS). Raman spectra were recorded by RS and Jörg Rappich (RP). All theoretical calculations were performed by YS. RS, JP, and YS analyzed the Raman spectra and compared them to the theoretical results. The manuscript was mainly written by YS, with RS responsible for the experimental chapter and the remaining authors proofreading. All authors contributed to the final version of the manuscript.

On the following pages, the publication, including the supporting information, is provided with permission of the Royal Society of Chemistry in accordance with the creative commons attribution 3.0 unported licence for Yannik Schütze *et al.*, A.2, 2021.



Cite this: *Phys. Chem. Chem. Phys.*,  
2021, **23**, 26709

# Combined first-principles statistical mechanics approach to sulfur structure in organic cathode hosts for polymer based lithium–sulfur (Li–S) batteries†

Yannik Schütze,<sup>id</sup><sup>ab</sup> Ranielle de Oliveira Silva,<sup>id</sup><sup>cd</sup> Jiaoyi Ning,<sup>ce</sup> Jörg Rappich,<sup>id</sup><sup>f</sup>  
Yan Lu,<sup>id</sup><sup>cd</sup> Victor G. Ruiz,<sup>id</sup><sup>a</sup> Annika Bande,<sup>id</sup><sup>g</sup> and Joachim Dzubiella<sup>\*ah</sup>

Polymer-based batteries that utilize organic electrode materials are considered viable candidates to overcome the common drawbacks of lithium–sulfur (Li–S) batteries. A promising cathode can be developed using a conductive, flexible, and free-standing polymer, poly(4-thiophen-3-yl)benzenethiol (PTBT), as the sulfur host material. By a vulcanization process, sulfur is embedded into this polymer. Here, we present a combination of electronic structure theory and statistical mechanics to characterize the structure of the initial state of the charged cathode on an atomic level. We perform a stability analysis of differently sulfurized TBT dimers as the basic polymer unit calculated within density-functional theory (DFT) and combine this with a statistical binding model for the binding probability distributions of the vulcanization process. From this, we deduce sulfur chain length (“rank”) distributions and calculate the average sulfur rank depending on the sulfur concentration and temperature. This multi-scale approach allows us to bridge the gap between the local description of the covalent bonding process and the derivation of the macroscopic properties of the cathode. Our calculations show that the main reaction of the vulcanization process leads to high-probability states of sulfur chains cross-linking TBT units belonging to different polymer backbones, with a dominant rank around  $n = 5$ . In contrast, the connection of adjacent TBT units of the same polymer backbone by a sulfur chain is the side reaction. These results are experimentally supported by Raman spectroscopy.

Received 4th October 2021,  
Accepted 18th November 2021

DOI: 10.1039/d1cp04550d

[rsc.li/pccp](http://rsc.li/pccp)

## 1 Introduction

The continued dependency of modern society on fossil fuels is warming the world at an increasing pace while the energy demand is rising steadily at the same time. Hence, the utilization of renewable energies is gaining interest. Within this context, the storage of electrical power is one of the most critical aspects. Lithium–ion batteries have become prominent over the past three decades and are currently the leading practical battery type among other energy storage technologies. However, this technology is approaching its maximum theoretical limits.<sup>1,2</sup> The theoretical gravimetric energy density limit ( $\sim 400 \text{ Wh kg}^{-1}$ ) of a lithium–ion battery has already been reached by today’s commercially available ones.<sup>3</sup> Still, the demand for technologies such as high energy storage systems for renewable energy applications, electric vehicles, or devices increases the interest in batteries with high energy densities.

Lithium–sulfur (Li–S) batteries are considered one of the most viable candidates for next-generation rechargeable batteries owing to their high theoretical specific energy of  $2500 \text{ Wh kg}^{-1}$ .<sup>4</sup> Furthermore, sulfur is a material that is naturally abundant,

<sup>a</sup> Research Group for Simulations of Energy Materials, Helmholtz-Zentrum Berlin für Materialien und Energie GmbH, Hahn-Meitner-Platz 1, Berlin 14109, Germany. E-mail: [yannik.schuetze@helmholtz-berlin.de](mailto:yannik.schuetze@helmholtz-berlin.de)

<sup>b</sup> Institute of Chemistry and Biochemistry, Freie Universität Berlin, Arnimallee 22, Berlin 14195, Germany

<sup>c</sup> Department Electrochemical Energy Storage, Helmholtz-Zentrum für Materialien und Energie GmbH, Hahn-Meitner-Platz 1, Berlin 14109, Germany

<sup>d</sup> Institute of Chemistry, University of Potsdam, Am Neuen Palais 10, Potsdam 14469, Germany

<sup>e</sup> School of Advanced Materials, Peking University Shenzhen Graduate School, Peking University, Shenzhen 518055, China

<sup>f</sup> Institute Si-Photovoltaics, Helmholtz-Zentrum Berlin für Materialien und Energie GmbH, Kekuléstr. 5, Berlin 12489, Germany

<sup>g</sup> Theory of Electron Dynamics and Spectroscopy, Helmholtz-Zentrum Berlin für Materialien und Energie GmbH, Hahn-Meitner-Platz 1, Berlin 14109, Germany

<sup>h</sup> Applied Theoretical Physics – Computational Physics, Physikalisches Institut, Albert-Ludwigs-Universität Freiburg, Hermann-Herder-Straße 3, Freiburg 79104, Germany. E-mail: [joachim.dzubiella@physik.uni-freiburg.de](mailto:joachim.dzubiella@physik.uni-freiburg.de)

† Electronic supplementary information (ESI) available. See DOI: 10.1039/d1cp04550d



readily available, and comparably cheap. Despite its promising potential, several main challenges hinder its practical application so far: the insulation of elemental sulfur,<sup>5</sup> the shuttle effect of dissolvable lithium polysulfides,<sup>6</sup> and the volumetric change of sulfur during the charge/discharge processes.<sup>7,8</sup> In recent years, enormous progress has been made in developing new sulfur host materials, efficient electrolytes, and novel cell configurations.<sup>9–16</sup>

One Li–S battery type that has gained significant attention is polymer-based batteries which utilize organic electrode materials.<sup>17</sup> Numerous studies have been conducted on the usage of different organosulfur compounds as cathode materials.<sup>18–20</sup> Here, conjugated polymers emerged as promising candidates due to their good conductivity,<sup>21,22</sup> ability to suppress the shuttle effect by confining the sulfur content,<sup>23–26</sup> and tolerance to large volume expansion during lithiation.<sup>27–29</sup> Among them, thiol-containing polymers are one example where the –SH groups can be cross-linked with sulfur *via* covalent bonds.<sup>30–33</sup>

Yu *et al.* recently proposed a strategy to construct a free-standing cathode with the conductive and flexible polymer poly(4-thiophen-3-yl)benzenethiol (PTBT) as the sulfur host material. Here, TBT monomers are first electro-polymerized onto the surface of nickel foam to form a porous PTBT network with the thiophene rings as the polymer backbone and benzenethiol as the side chains. In a second inverse vulcanization step,<sup>34</sup> elemental sulfur S<sub>8</sub> gets embedded into this framework. Therefore, it is heated up to 170 °C which causes ring-opening radical polymerization (ROP) of the sulfur with the thiol groups of PTBT. This S/PTBT@NF cathode can then be directly used to assemble Li–S batteries without any further modifications. This fabrication approach seems promising to overcome all typical drawbacks of Li–S batteries, but a detailed investigation of the structural aspects of the cathode is still missing.

Pyun *et al.* investigated the process of inverse vulcanization for the first time in an experimental study with an organic copolymer synthesized with 1,3-diisopropenylbenzene (DIB) monomers and elemental sulfur.<sup>34</sup> Here, the authors analyzed the microstructure of the vulcanized polymer under different synthetic conditions. More precisely, they showed that, depending on the feed ratio of S<sub>8</sub> and DIB monomers, the S-DIB copolymer exhibits varying structural features. The authors observed that, with increasing DIB content, the copolymer morphology changed from semi-crystalline to amorphous. At the same time, the sulfur rank (the number of sulfur units per DIB unit) decreased with increasing DIB content.

Guided by these findings, knowing the most likely outcome of the chemical binding process of sulfur in our PTBT polymer is highly desirable to characterize the initial stage of the charged cathode. In particular, electronic structure theory can give us insights into the structural features at an atomic level leading to a better understanding of the charged state of the cathode. In this work, we present the structural characterization of the charged cathode, that is, the sulfurized polymer, as it is prepared after the vulcanization process, using density functional theory (DFT). However, DFT is limited to minimum energy (0 K) states, and temperature effects (fluctuations and

entropy) are not included. Therefore, we develop a statistical mechanics model that uses DFT energies as the input and calculate configurational distributions at operating temperatures. This novel combination of methods can be considered a multi-scale approach and allows us to bridge the gap between the local description of the covalent bonding process and the derivation of the macroscopic properties of the polymer. We also compare our theoretical analysis to new experimental observations. Raman spectroscopy of the TBT monomer and the electro-polymerized PTBT motivates the reference states of our binding model and supports the results of our combined model approach.

This paper is organized as follows. In the subsequent Section 2, we first give a detailed description of how to derive a statistical binding model describing the vulcanized S/PTBT polymer. The basis of this model is the characterization of the molecular structure of S/PTBT by fragmenting it into different sulfurized TBT dimers. Here, we distinguish between two types of binding (intra and inter) and different sulfur chain lengths. Based on that, we describe the result of the vulcanization reaction as a thermodynamic equilibrium from which we can derive equilibrium constants. In Section 4, we first present the structural characterization and then the stability analysis of the polymer fragments identified in the theory part in terms of their electronic energy within DFT. For all configurations, we conduct a conformational space sampling to estimate their structure–stability relationship further. The following subsection compares these results with our experimental Raman spectroscopy of the TBT monomer and the electro-polymerized PTBT polymer. Ultimately, we combine the statistical model with the stability analysis results to derive binding probability distributions depending on the concentration of sulfur in the vulcanization process. Finally, we calculate the average sulfur rank and standard deviations for these distributions and look at their temperature dependency. The paper ends with some concluding remarks.

## 2 Statistical binding model

### 2.1 Modeling the initial state of the charged cathode

In Fig. 2 the schematic illustration of the preparation of the S/PTBT cathode is shown. In a first step, the TBT monomers are electro-polymerized to form a PTBT polymer. Polymerization of the five-membered heterocyclic thiophene ring can occur through bonding at the  $\alpha$ - or  $\beta$ - (*i.e.* 2- or 3-) position (*cf.* Fig. 1). In the TBT monomer, the  $\beta$ -position is substituted by the benzenethiol group. It is well known that, in 3-substituted thiophene monomers, the  $\alpha$ -position is most reactive in the polymerization, and therefore  $\alpha,\alpha$ -linkages will be dominant in the resulting polymer. It is most likely that the long PTBT polymer chains that form during polymerization will then have the thiophene rings as the main-chain backbones with the benzenethiol groups as the lateral chain.<sup>35–38</sup>

During vulcanization, heating causes the ring-opening polymerization (ROP) of elemental S<sub>8</sub> monomers into linear polysulfanes with diradical chain ends, which subsequently



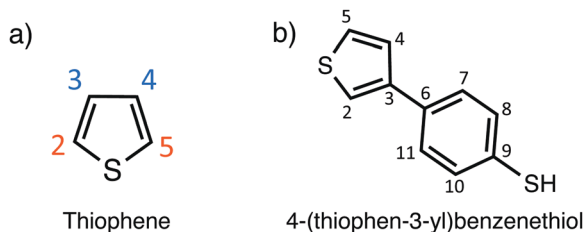


**Fig. 1** (a) Binding sites of the heterocyclic thiophene ring. The  $\alpha$ -positions are colored in red and the  $\beta$ -positions are colored in blue. (b) 4-(Thiophen-3-yl)benzenethiol (TBT) monomer with the substituted benzenethiol at the  $\beta$ -position of the thiophene ring.

polymerize.<sup>11</sup> Its diradical form is unstable and depolymerizes back into monomeric ring forms.<sup>34</sup> Quenching of the diradical ends *via* polymerization with the thiol ( $-\text{SH}$ ) groups of the lateral chain can stabilize sulfur in the PTBT polymer.

The difference between conventional and inverse vulcanization is that a small amount of sulfur is used in the former. In contrast, a large amount of sulfur is used together with a relatively modest amount of polymer in the latter. In the original sense, inverse vulcanization also means the copolymerization of elemental sulfur and small organic monomers as a bulk reaction.<sup>34</sup> Here, we do not observe a copolymerization process since the PTBT polymer is electropolymerized in the first step before sulfur is embedded into this framework in a subsequent step. Therefore, in the following, we will describe the process of adding sulfur as vulcanization.

Furthermore, the sulfur deposition process in experiments occurs without the presence of any additional solvent. This work focuses on the initial state of the charged cathode, that is, the vulcanized polymer, before it gets assembled into a battery. Hence, we will study the outcome of the vulcanization in the framework of a gas phase model reaction.

Based on the structure of the main chains of the PTBT polymer, we generally distinguish two different ways in which the polysulfide chains can bind to the TBT units. On the one hand, a sulfur chain can connect two adjacent TBT units of the same polymer chain to form an intra-chain sulfur cross-link (bottom left picture of Fig. 2). On the other hand, as shown on the right, sulfur can form an inter-chain cross-link between TBT monomers that belong to different polymer chains. Here, we implicitly assume that the polymer chains are sufficiently close to each other. It should be noted that, in addition to the linkage of adjacent TBT units, intra-chain cross-links may in principle also occur between monomers that are further apart within the chain under real conditions. The linkage of remote monomers would then reflect a scenario similar to an inter-chain cross-linking of different polymer backbones. The limitation of considering only intra-chain connections of neighboring TBT units allows us to choose a well-defined reference state for the PTBT polymer chains within a different scenario from the inter-chain cross-links.

In the following, we derive a model that reflects the reaction type (intra- or inter-chain) and the sulfur rank  $n$  depending on the amount of sulfur that is embedded into the polymer.

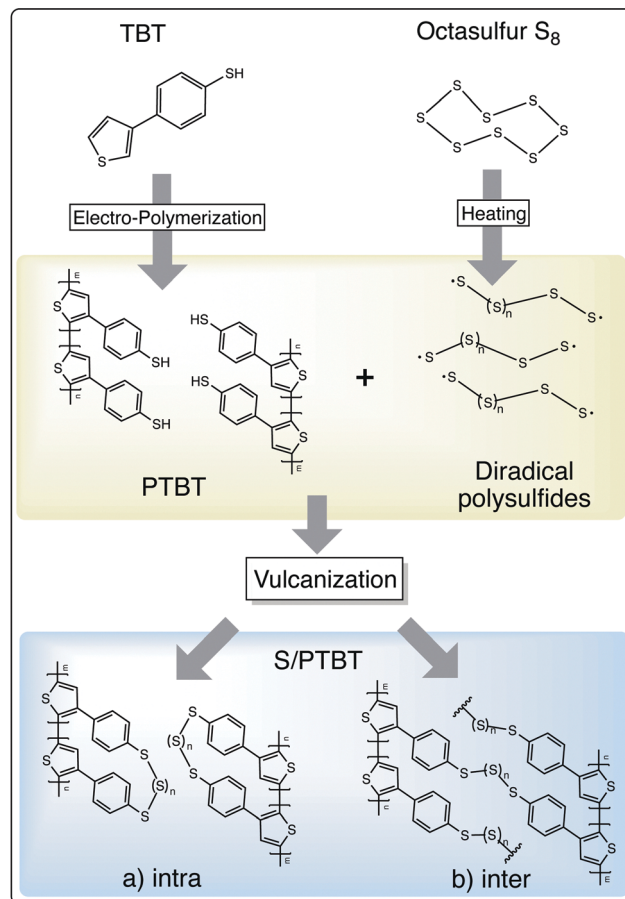


**Fig. 2** Schematic illustration of the preparation of the S/PTBT cathode. First, the TBT monomers are electro-polymerized to form a PTBT polymer. By a vulcanization process, sulfur is embedded into the PTBT network to form S/PTBT. Hereby, we distinguish between an (a) intra-chain and (b) inter-chain sulfur cross-link between two TBT units.

The sulfur rank  $n$  is defined as the total number of sulfur atoms in the chain that connects the two TBT units. We describe the PTBT polymer as a fixed configuration of binding sites ( $-\text{SH}$  groups) for the additional sulfur and the reactions of forming intra- or inter-chain sulfur links as two independent processes. Both reaction types include two  $-\text{SH}$  groups to be connected by a sulfur chain. Let us assume that the PTBT polymer consists of  $N$  thiol groups in total. Then the number of independent binding sites is  $n_{\text{BS}} = N/2$ . After vulcanization, a binding site can have an intra- or inter-configuration or be still empty (the two  $-\text{SH}$  groups have not reacted). The binding polynomial  $Q$ , which describes all possible outcomes of the vulcanization, is then a sum of the statistical weights of these three scenarios:

$$Q = 1 + p^{\text{intra}} + p^{\text{inter}}. \quad (1)$$

Next, we distinguish between the number of sulfur atoms that can form an intra- or inter-chain (the sulfur rank  $n$ ). Let us assume we have sulfur ranks ranging from  $n = 1$  to  $m$  ( $n = 0$  is the case of an 'empty state'). We consider the binding of sulfur chains with different lengths again as independent processes (for both intra- and inter-reactions). Therefore, the statistical



weights of intra- and inter-reactions are themselves sums over the weights of having  $n$  sulfur atoms bound:

$$p^{\text{intra}} = \sum_{n=1}^m p_n^{\text{intra}}, \quad p^{\text{inter}} = \sum_{n=1}^m p_n^{\text{inter}}. \quad (2)$$

where  $p_n^{\text{intra/inter}}$  are the statistical weights of having an intra/inter-chain of rank  $n$ .

In general, we can describe the vulcanization process as bringing the two reference states 'PTBT polymer' and 'elemental sulfur' together to form a product state 'vulcanized polymer'. We want to find out the most probable binding states in terms of intra- vs. inter-reaction, resolved by the sulfur rank  $n$ . To make computations feasible, we first have to reduce the complexity of the PTBT reference state, *i.e.* omit the long polymer chains. In our model, we have chosen a DiTBT molecule describing two neighboring, covalently bonded TBT monomers as the basic unit of a polymer chain. This DiTBT molecule represents one of many binding sites of the polymer. For the amount of sulfur embedded into the polymer, we take one-eighth of an  $S_8$  ring as the reference. In Fig. 3, we show a scheme for the two reaction types based on these new reference states.

These reactions are explained in the following. The formation of an intra-chain is already realized by connecting the two thiol groups of a DiTBT. The smallest chain would consist of one S atom ( $n = 1$ ). Since a DiTBT already has two S atoms as parts of the thiol groups, the second sulfur atom would react with the two hydrogen atoms to form the bi-product  $H_2S$ . To create the next larger chain with  $n = 2$ , one additional sulfur atom is needed to react with the hydrogen atoms. In every case, we consider the loss of one S atom by the formation of  $H_2S$ . The production of  $H_2S$  gas during inverse vulcanization was already confirmed in experiments with similar thiol-group containing polymers.<sup>19,30,32</sup> Therefore, the amount of sulfur atoms added is counted by the term  $(n - 1)/8 S_8$  giving

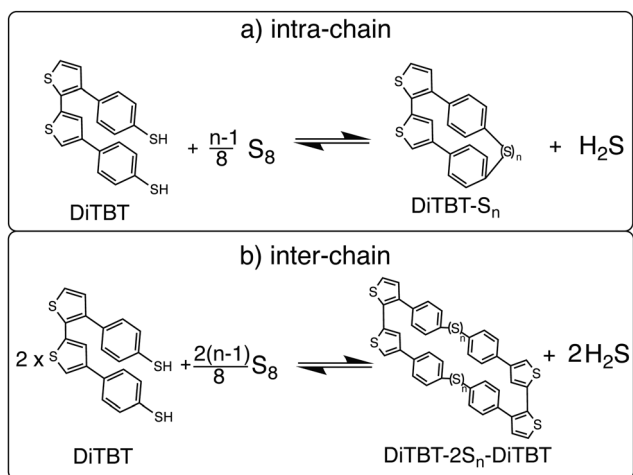
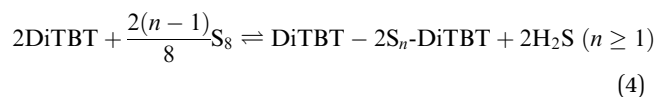


Fig. 3 The schematic of vulcanization to form (a) an intra-chain sulfur link in one DiTBT unit or (b) an inter-chain cross-link between two DiTBT units.

For the inter-chain process, we have to make an additional assumption. Since a DiTBT molecule is a fragment of one polymer chain, we need to consider two DiTBT molecules in order to model the process of connecting two polymer chains by a sulfur link. The DiTBT molecules now represent two different binding sites, and therefore we must also double the amount of sulfur atoms compared to the intra-reaction. This product state describes a pair of sulfur cross-links between four TBT monomers (two DiTBT units on each polymer chain). For more than one DiTBT per chain, this would lead to an organized ladder-like structure. However, inter-chain cross-links may occur more randomly in a real system, such that neighboring TBT units of a given chain bind to monomers of two different polymer chains. In order to be consistent with the intra-chain binding process, however, we here take the same reference state of two DiTBTs. The corresponding reaction equation is then



For both reactions, we define vulcanization energy<sup>33</sup> as the electronic energy difference between the products and the reactants, *i.e.*

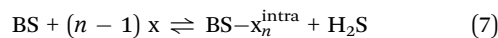
$$E_{\text{vul}}^{\text{intra}}(n) = E(\text{DiTBT-S}_n) + E(H_2S) - E(\text{DiTBT}) - \frac{n-1}{8} E(S_8) \quad (5)$$

and

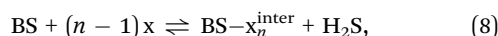
$$E_{\text{vul}}^{\text{inter}}(n) = \frac{1}{2} E(\text{DiTBT-}2S_n\text{-DiTBT}) + E(H_2S) - E(\text{DiTBT}) - \frac{n-1}{8} E(S_8). \quad (6)$$

In eqn (6), we divide the energy difference of products and reactants by two in order to normalize the vulcanization energy to one unit of DiTBT and  $(n - 1)/8 S_8$ . By doing this, we can compare the stability of different intra- and inter-reaction products in terms of their electronic energies.<sup>39</sup>

The next step in our model is to describe the final state after vulcanization as an equilibrium of intra- and inter-binding states resolved by the sulfur rank. We model the vulcanization as the binding process of a certain amount  $x = S_8/8$  of sulfur to a number of binding sites (BS). With these association reaction equilibria,



and



we can formulate the equilibrium binding constants:

$$K_n^{\text{intra}}([x]) = \frac{1}{v_0^{n-2}} \frac{[\text{BS-x}_n^{\text{intra}}][H_2S]}{[\text{BS}][x]^{n-1}} \quad (9)$$



and

$$K_n^{\text{inter}}([\text{x}]) = \frac{1}{\nu_0^{n-2}} \frac{[\text{BS} - x_n^{\text{inter}}][\text{H}_2\text{S}]}{[\text{BS}][\text{x}]^{n-1}}, \quad (10)$$

where the brackets denote the concentrations of reactants and products,<sup>40</sup> and  $\nu_0 = 1 \text{ mol}^{-1}$  is the standard binding volume.<sup>41–43</sup> Note that the binding fractions of the concentrations of products and reactants in eqn (9) and (10) have the dimension of volume <sup>$n-2$</sup> . Hence, we have to divide by the volume factor  $\nu_0^{n-2}$  to define the dimensionless equilibrium constants  $K_n$ .<sup>44</sup> The statistical weights of intra- and inter-binding in eqn (2) can be expressed in terms of these binding constants<sup>40</sup> by

$$P_n^{\text{intra/inter}}([\text{x}]) = K_n^{\text{intra/inter}}(\nu_0[\text{x}])^{n-1}. \quad (11)$$

At the same time, the binding constants can be associated with binding energies through

$$\Delta G_n = -k_B T \ln[K_n], \quad (12)$$

where  $k_B$  stands for the Boltzmann constant and  $T$  for the temperature during vulcanization. Formally,  $\Delta G_n$  denotes a free energy comprising internal entropic changes of the binding process.<sup>45</sup> As an approximation, we replace the free binding energies with the vulcanization energies taking only electronic energy differences into account:

$$K_n^{\text{intra/inter}} \approx \exp\left[-\frac{E_{\text{vul}}^{\text{intra/inter}}(n)}{k_B T}\right]. \quad (13)$$

It should be mentioned that, in general, the binding volumes for the intra- and inter-reactions will be different from each other. Since these quantities are computationally not accessible in our gas-phase calculations, we make a further approximation and assume an equal binding volume  $\nu_0$  for both processes. If we insert eqn (13) and (11) into eqn (1), we can finally write down the binding polynomial:

$$\begin{aligned} Q([\text{x}]) &= 1 + \sum_{n=1}^m (P_n^{\text{intra}}([\text{x}]) + P_n^{\text{inter}}([\text{x}])) \\ &= 1 + \sum_{n=1}^m (\nu_0[\text{x}])^{n-1} \left( \exp\left[-\frac{E_{\text{vul}}^{\text{intra}}(n)}{k_B T}\right] + \exp\left[-\frac{E_{\text{vul}}^{\text{inter}}(n)}{k_B T}\right] \right). \end{aligned} \quad (14)$$

## 2.2 Conformational space sampling and binding probabilities

With increasing sulfur chain length  $n$ , the number of degrees of freedom grows rapidly, and hence the search for a global minimum of the potential energy surface becomes a complex task itself. A typical strategy to solve this is a global conformational space search.<sup>46,47</sup> In this study, however, we pursue an approach that not only looks for the global minimum structures but also considers a manifold of different conformations of the product states DiTBT- $S_n$  and DiTBT- $2S_n$ -DiTBT for each sulfur chain length. The aim of this conformational space sampling is not to find all possible conformations to get the global minimum, but rather to get an estimate of the

structure–stability relationship of the products in the vulcanization process.

First, a set of diverse low-energy conformers that cover different shapes of the sulfur chain are generated and then pre-relaxed, employing a force-field (FF) from classical molecular dynamics.<sup>48</sup> These structures are then further optimized using density functional theory (DFT) to calculate their electronic energies. By making further distinction regarding the conformation of possible product states of the vulcanization, we have to adjust the binding polynomial according to

$$\begin{aligned} Q([\text{x}]) &= 1 + \sum_{n=1}^m \sum_{i=1}^{i_{\text{max}}(n)} (\nu_0[\text{x}])^{n-1} \\ &\times \left( \exp\left[-\frac{E_{\text{vul}}^{\text{intra}}(n, i)}{k_B T}\right] + \exp\left[-\frac{E_{\text{vul}}^{\text{inter}}(n, i)}{k_B T}\right] \right). \end{aligned} \quad (15)$$

Here, we introduced the index  $i$ , which accounts for the different conformations of the products. With the final binding polynomial at hand, we can calculate the binding probability distribution, for example, their first and second moments (mean and variance). The average sulfur rank for the intra- and inter-chain processes can be computed by

$$\bar{n}^{\text{intra/inter}}([\text{x}]) = \sum_{n=1}^m \sum_{i=1}^{i_{\text{max}}(n)} n \frac{P_{n,i}^{\text{intra/inter}}([\text{x}])}{Q([\text{x}])}, \quad (16)$$

with  $P_{n,i}^{\text{intra/inter}}([\text{x}])/Q([\text{x}])$  being the probability distribution of having an intra/inter-chain with sulfur rank  $n$  and conformation  $i$ . In the same way, we obtain the standard deviation of the distribution by

$$\sigma_n^{\text{intra/inter}}([\text{x}]) = \sqrt{\sum_{n=1}^m \sum_{i=1}^{i_{\text{max}}(n)} (\bar{n}^{\text{intra/inter}}([\text{x}]) - n)^2 \frac{P_{n,i}^{\text{intra/inter}}([\text{x}])}{Q([\text{x}])}}. \quad (17)$$

## 3 Methods

### 3.1 Experimental methods

The previously synthesized monomer 4-(thiophen-3-yl)benzenethiol (TBT) was directly polymerized on a nickel foam (thickness: 0.5 mm). The electro-polymerization was carried out in acetonitrile solution to form PTBT (4 mg ml<sup>-1</sup>) using 0.1 M tetrabutylammonium hexafluorophosphate (TBAPF6) as the solution electrolyte. This process was conducted by CV in a three-electrode system at a potential between  $-1.8$  and  $1.8$  V (100 mV s<sup>-1</sup>, 20 cycles) using an electrochemical workstation (GAMRY), Ag wire as the reference electrode, and platinum wire as the counter electrode. After electro-polymerization, the electrode was rinsed with ACN several times and then dried in a vacuum oven at 50 °C. Finally, a red-brown nickel foam electrode (PTBT@NF) was obtained and the mass loading of PTBT is  $\sim 1 \text{ mg cm}^{-2}$ .

Subsequently, the sulfur deposition was conducted through a vulcanization process: elemental sulfur dissolved in CS<sub>2</sub> (mg ml<sup>-1</sup>) was first embedded into the porous PTBT framework



at a low-temperature step, transferred under argon gas in a sealed vessel, and then heated up at 150 °C for one hour, followed by further heating at 170 °C for 8 hours, leading to ring-opening radical polymerization of elemental sulfur with the thiol groups of PTBT. Finally, the obtained S/PTBT@NF was rinsed with CS<sub>2</sub> to wash away the physically adsorbed sulfur and dried at room temperature before being used. The loading amount of sulfur in S/PTBT@NF is  $\sim 1.6 \text{ mg cm}^{-2}$ .

The Raman spectra were recorded using a micro-Raman setup with a confocal microscope (Dilor LabRAM) coupled to a CCD. The laser excitation was at 632.8 nm with a power density of about  $2 \text{ W cm}^{-2}$ . The acquisition time was 300 s.

### 3.2 Computational details

For the generation of the possible conformations and their pre-relaxation, Avogadro software<sup>49</sup> was used employing the MMFF94 force field<sup>50</sup> using steepest descent minimization. All DFT calculations were performed using the all-electron, full-potential electronic-structure code FHI-aims.<sup>51–53</sup> The exchange–correlation interactions were treated using the Perdew–Burke–Ernzerhof (PBE) functional<sup>54</sup> together with the Tkatchenko–Scheffler method<sup>55,56</sup> to include van der Waals (vdW) interactions. For comparison, we also used the hybrid PBE0 functional<sup>57</sup> as well as the many-body dispersion (MBD) method<sup>58</sup> to account for the long-range van der Waals interactions. FHI-aims-specific tier 2 basis sets and tight settings have been used. The convergence criterion for the total energy and the forces was set to  $10^{-6} \text{ eV}$  and  $10^{-5} \text{ eV \AA}^{-1}$ , respectively.

## 4 Results and discussion

### 4.1 Structural characterization of product states

We first look at the structural characteristics of the reactants and the products of the vulcanization process. In Fig. 4, the DFT-relaxed structures of elemental sulfur (S<sub>8</sub>), TBT, and DiTBT are shown as well as those for the lowest energy conformations of the reaction products for sulfur ranks  $n = 1$ –4. First, we look at the most stable configuration of our reference state DiTBT (*cf.* Fig. 4c). As can be seen in the top view, the arrangement of the two neighboring benzenethiol groups is similar to the  $\pi$ – $\pi$  stacked (parallel-displaced) conformation of benzene dimers.<sup>59</sup>

The distance of the two carbon atoms at the 9-position of TBT (the carbon atom binding to the thiol group, *cf.* Fig. 1) is  $d_{\text{CC}} = 4.38 \text{ \AA}$ . The thiophene rings have a dihedral angle of  $\gamma_{\text{SCCS}} = 55.4^\circ$  through the carbon atoms at the  $\alpha$ -positions of the thiophene rings.

We can now analyze the product states after DFT optimization with regard to these quantities to see how the structure of DiTBT gets altered by the insertion of sulfur chains. In Fig. 5, the C–C distance  $d_{\text{CC}}$ , the dihedral angle  $\gamma_{\text{SCCS}}$ , and the sulfur bond angle  $\alpha_{\text{SSS}}$  among three neighboring sulfur chain atoms are shown for all intra-chain (red) and inter-chain (blue) products and compared against their reference values of isolated DiTBT and S<sub>8</sub> (black dashed lines). For the products, we report the statistical mean and standard deviation of the

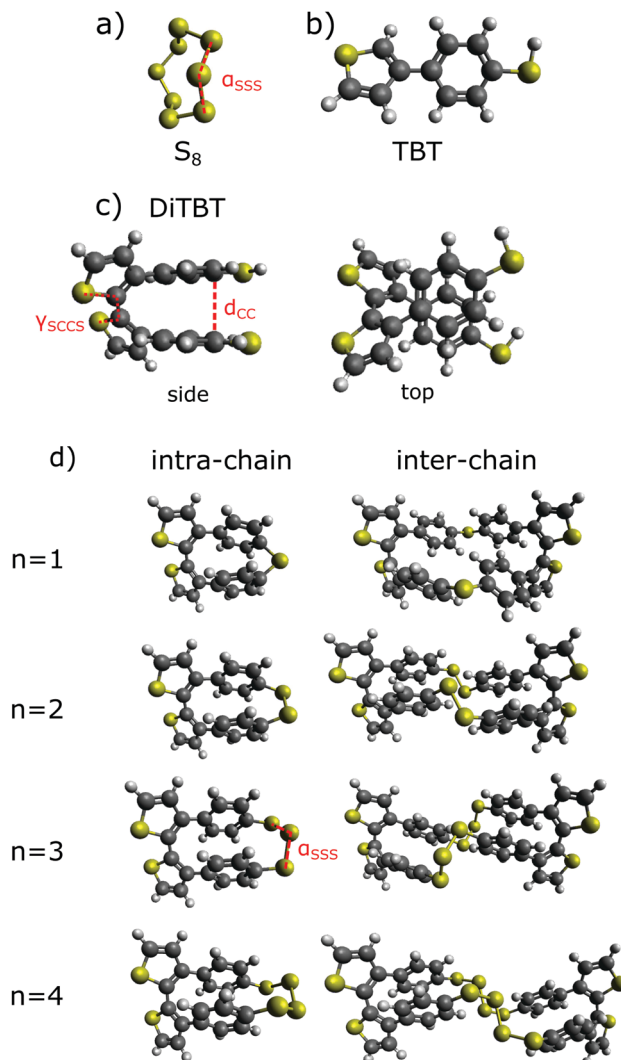
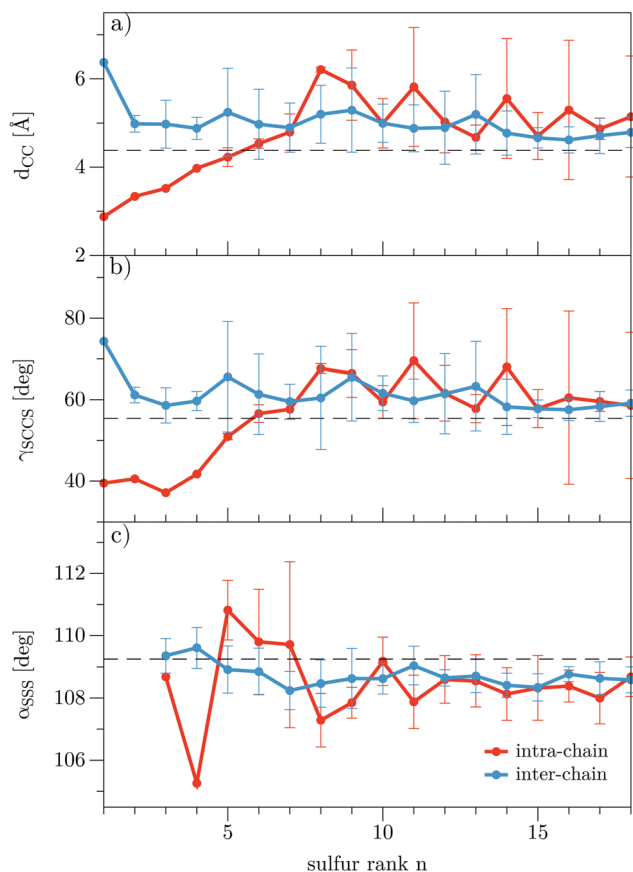


Fig. 4 Optimized structures of the reactants and products of the vulcanization process after relaxation with DFT: (a) cyclo-octa sulfur S<sub>8</sub>, (b) TBT, (c) side and top views of DiTBT, and (d) exemplary structures of the intra-chain and inter-chain reaction products DiTBT-S<sub>n</sub> and DiTBT-2S<sub>n</sub>-DiTBT for  $n = 1$ –4. Carbon (C), hydrogen (H), and sulfur (S) elements are displayed as spheres in grey, white, and yellow, respectively.  $d_{\text{CC}}$ ,  $\alpha_{\text{SSS}}$ , and  $\gamma_{\text{SCCS}}$  are indicated with red dashed lines.

conformational sample for the respective sulfur ranks. For all three quantities, we observe the largest deviations from the respective reference values for short chains ( $n = 1$ –4) and an approach towards them for increasing  $n$ . For the short-chain DiTBT-S<sub>n</sub> (red solid line in a),  $d_{\text{CC}}$  is shortened indicating that the benzenethioether rings are closer to each other than they are in DiTBT. This can be also clearly seen in Fig. 4d for  $n = 1, 2$ . At the same time, the dihedral angle between the thiophenes for short  $n$  is also smaller than the reference value. For the inter-chain DiTBT-2S<sub>n</sub>-DiTBT products, we observe the opposite behavior that, for short chains, the values  $d_{\text{CC}}$  and  $\gamma_{\text{SCCS}}$  are larger than the reference values.

With increasing sulfur rank, both properties align with the reference values. This can be explained by the greater flexibility





**Fig. 5** Structural analysis of the DFT-relaxed intra-chain (red) and inter-chain (blue) products depending on the sulfur rank  $n$ : (a) distance  $d_{CC}$  between the terminating C9 (*cf.* Fig. 4) carbon atoms belonging to the benzenethioether; (b) dihedral angle  $\gamma_{SCCS}$  between neighboring thiophene rings; and (c) sulfur bond angle  $\alpha_{SSS}$ . The solid lines show the average overall conformations for the respective rank, and error bars represent the standard deviation of the sample. The black dashed lines indicate the values for the reference DiTBT in (a) and (b) and for  $S_8$  in (c).

of the chains allowing the DiTBT in the product states to adopt conformations similar to the reference structure. Put another way, we can conclude that the insertion of short sulfur chains leads to modified conformations of the DiTBT. Due to the altered dihedral angle of the thiophenes, the resulting structures possess torsional strain.<sup>60</sup> In addition to that, the variation in distance between the benzenethioethers changes their van der Waals interaction and thus leads to steric strain.<sup>60</sup> In Fig. 5c, we can also see that the sulfur chains themselves possess angle strains compared with the crown conformation of an  $S_8$  ring.

What is noticeable is that, for longer chains, the curves of  $d_{CC}$  and  $\gamma_{SCCS}$  show a similar zigzag behavior. This can also be explained by the greater flexibility of the long chains. With increasing  $n$ , the chains can adopt a variety of stable conformations (*cf.* Fig. S1, ESI<sup>†</sup>), which are probed with our sampling approach. For  $n = 1$ , there is only one stable configuration for the intra- and inter-chain products. With increasing  $n$ , the flexibility of the chain leads to a variety of stable configurations with a broad range of dihedral angles. Shown here are two

extreme cases of the intra- and inter-chain processes, respectively. For the former, a wide range of dihedral angles is possible only for long chain lengths, while for the latter it can already be seen for short ranks. The jumps are probably due to the relatively small sample sizes (max. 10 conformations per sulfur rank). We also see that these fluctuations are less pronounced for the inter-chain configurations because the structures automatically lead to improved statistics (and hence smaller errors).

The S–S bond length for all products is in the interval of  $d_{SS} = [2.07, 2.09]$  Å which matches the experimental value of  $S_8$  and is in good agreement with similar chain-like  $-R-S_n-R-$  polysulfanes.<sup>61,62</sup>

## 4.2 Stability analysis

Next, we proceed with the stability analysis of all reaction products according to eqn (5) and (6). Here, we mean the electronic stability of the products relative to our defined reference states. The vulcanization energies for the intra-chain process (red) and the inter-chain process (blue) are compared in Fig. 6. The colored areas represent the overall results for all sampled conformations, while the solid lines show the average trends. As it can be seen, the inter-chain cross-link reaction leads to negative vulcanization energies  $E_{vul}^{inter}$  throughout almost the whole range of sulfur chains showing that this process can chemically stabilize the sulfur content. Only the shortest chains ( $n = 1, 2$ ) lead to a slightly positive energy. The intra-chain reaction on the other hand yields almost only positive values for  $E_{vul}^{intra}$ . Only for very long sulfur chains ( $n \geq 11$ ), we find some stable conformations, whereas particularly short sulfur chains ( $1 \leq n \leq 3$ ) are very unlikely to form.

The fact that the short sulfur chains are less stable in both processes can be directly related to the structural features discussed above. The structural changes of the two reactants DiTBT and  $S_8$  which go along with their binding process lead to different kinds of strain. The additional strain energy of the binding products raises their internal energy and thus makes it

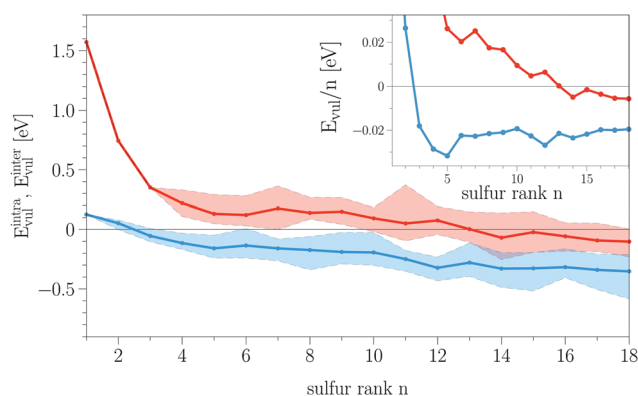


**Fig. 6** The vulcanization energies  $E_{vul}^{intra}$  (eqn (5)) for intra-chain reactions (red) and  $E_{vul}^{inter}$  (eqn (6)) for inter-chain reactions (blue). The colored areas represent the results of all sampled conformations, and the solid lines show the averaged trends. In the inset, the vulcanization energies normalized by the sulfur rank  $E_{vul}/n$  are shown.



unfavorable for them to form during the vulcanization process. We can also note that, although we made a rather small sampling of the conformational space, it can be seen that the stability of the reaction products is extremely sensitive to structural changes. Because of that we can also observe a similar zigzag behavior in the curves of  $E_{\text{vul}}^{\text{intra}}$  and  $E_{\text{vul}}^{\text{inter}}$ .

Besides the structure–stability relationship, the vulcanization energies show two additional features. Firstly, one can see a clear negative drift of the vulcanization energies with increasing sulfur rank. Even for the averaged curves, we observe a negative correlation on  $n$ . If we normalize the vulcanization energies by the sulfur rank (*cf.* the inset of Fig. 6), we can see that, for the inter-chain process,  $E_{\text{vul}}^{\text{inter}}/n$ , after reaching a minimum at  $n = 5$ , shows a plateau for  $n > 6$ . For the intra-chain process,  $E_{\text{vul}}^{\text{intra}}/n$  still goes down with increasing  $n$  but, for very long chains ( $n > 14$ ), we start to see a saturation. The limit of constant normalized energies for large  $n$  indicates that the stability of the reaction products depends linearly on  $n$  after reaching a certain chain length. The drift in  $E_{\text{vul}}$  suggests that wave-function hybridization of an S–S bond inside a polysulfide chain of the reaction products is energetically more favorable than that for the same bond inside an  $S_8$  ring given the formation of  $H_2S$ . Indeed, the plateau of  $E_{\text{vul}}^{\text{inter}}/n$  for sulfur ranks higher than  $n = 5$  shows that every additional S–S bond would yield a constant energy gain of about 20 meV, making the corresponding structure energetically more stable.

On the other hand, this energy gain per sulfur atom is in the order of the thermal energy  $k_B T$ , showing that the energy differences between the structures of different chain lengths are sensitive to temperature and entropy effects. This should be put into the context of contributions that were not taken into account for this electronic stability analysis. If we refer back to eqn (12), we see that the actual chemical reaction is governed by the Gibbs free energy  $G = U + pV - TS$ . If we assume the contribution of the  $pV$ -term to be minor in our gas-phase reaction, the important correction comes with including the entropy  $S$ . Its inclusion would mean that the longer chains are entropically penalized over the shorter chains and thus cause a destabilization of the structures with higher sulfur ranks. While, for low sulfur ranks, the main driving force for the addition of sulfur atoms would be the electronic stability, with increasing  $n$ , the only driving force would be the entropy which should overcome the energy drift in  $E_{\text{vul}}$  at a certain sulfur chain length. Indeed, experimental studies on the standard Gibbs free energy of equilibrium distributions of polysulfide chains have shown that pentasulfide chains ( $n = 5$ ) represent the most stable configuration.<sup>63,64</sup> This is in agreement with another DFT study of large sulfur rings ( $n = 8–20$ ) which showed that considering only the electronic energy would allow rings with  $n = 12, 14, 18$ , but the inclusion of entropic effects leads to an  $S_8$  ring as the only stable allotrope.<sup>65</sup>

For the most stable inter-chain products with sulfur rank  $n = 1–8$ , we also calculated the electronic energies with PBE + MBD and PBE0 + vdW (*cf.* Fig. S2, ESI†) and compared them with the results for PBE + vdW from Fig. 6. The comparison shows that all three methods give relatively similar results for

the stability analysis. Using the MBD method instead of the pairwise vdW correction to account for the dispersion interaction, we observe that as the sulfur rank  $n$  increases, the larger structures are less stable. This is a consequence of the inclusion of many-body interactions in the dispersion energy. Contrary to including only an attractive pairwise interaction *via* the vdW method, the inclusion of many-body effects becomes more relevant and less attractive when the chain consists of more sulfur atoms, yielding a less attractive long-range dispersion energy. This fact also points in the direction of an energy saturation in a real polymer chain where the many-body effects would become even larger. The comparison between PBE and PBE0 functionals shows that their curves are almost the same, but the PBE0 results decrease by about 0.03 eV.

### 4.3 Comparison to experimental Raman spectroscopy

The comparison of the stability of intra- and inter-reaction products shows that the latter process is more favorable in terms of electronic energies. The finding that inter-chain sulfur cross-links are dominant in the vulcanized polymer was also compared to the experimental Raman spectroscopy results of the monomer TBT and the electro-polymerized layer of TBT (PTBT) (*cf.* Fig. 7). Here, the spectrum of TBT (black line) shows a Raman signal around  $2560 \text{ cm}^{-1}$  due to the S–H stretching vibration of the thiol groups present at the benzene ring of the monomer.<sup>66</sup> These groups vanish after electrochemical polymerization (red line of PTBT). The vibrational signatures between  $600$  and  $1600 \text{ cm}^{-1}$  are part of the benzene and thiophene ring structures, respectively.<sup>67,68</sup> The Raman signature below  $600 \text{ cm}^{-1}$  is due to the formation of disulfide bonds, especially the signal around  $480 \text{ cm}^{-1}$ .<sup>69</sup>

The absence of the S–H stretching mode coupled with the simultaneous occurrence of the S–S Raman modes between  $300$  and  $480 \text{ cm}^{-1}$  indicates the formation of disulfides as a side reaction during the anodic polymerization of TBT. It is well

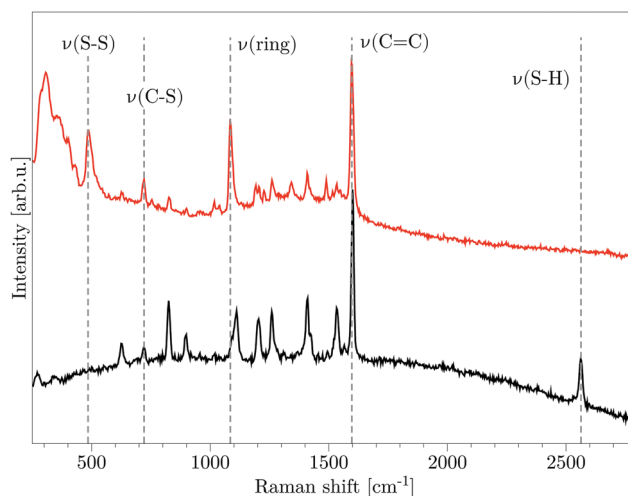


Fig. 7 Raman spectra of the monomer TBT (black) and the electrochemically prepared polymer layer PTBT (red). The gray dashed lines indicate several distinct vibrational modes  $\nu$  of the two samples.



known in the literature that disulfide formation is an oxidative process driven by oxidizing agents.<sup>70</sup> Hence, the thiol functional groups of TBT are activated to form disulfide bonds in the aqueous solution by the anodic oxidation process<sup>71</sup> that is needed to drive the polymerization of the thiophene groups. From an experimental point of view, it is not possible to distinguish between intra- and inter-chain bonds (*cf.* Fig. S3, ESI†). However, if we compare these findings with the stability analysis, we can exclude that the disulfide bonds represent intra-chain compounds with sulfur rank  $n = 2$  due to their high positive vulcanization energies. We can therefore say that S-S inter-chains are already present in the polymer before vulcanization. This result furthermore motivates the choice of reference states in our statistical binding model.

In summary, we see that the formation of inter-chain cross-links leads to more energetically stable structures than the intra-chain reaction. In the latter, we can already state that it would only lead to the formation of very long sulfur chains with rank  $n \geq 11$ . For the inter-chain process, already short chains with  $n \geq 2$  are possible to form. So far, we have only looked at the energetic stability as a criterion for the formation of certain reaction products, but what will also determine the microscopic structure of the vulcanized polymer is the feed ratio of the reactants as it was already shown.<sup>34</sup> Hence, we will now make use of our binding model derived in eqn (15) and vary the amount of sulfur to see how the binding probability distribution of sulfur chain lengths will change depending on the free sulfur concentration  $[x]$ .

#### 4.4 Binding probabilities

In Fig. 8a, the individual binding probabilities for the inter-chain process  $p_n^{\text{inter}}([x])$  are displayed *versus* the molar ratio of free sulfur and binding sites  $y = [x]/[\text{BS}]$ . We only show the binding curves for those sulfur ranks whose maximum probability is more than 10%. For the chosen range of  $y$ , we can qualitatively distinguish three different regions of short, medium-length, and long sulfur chains.

For low sulfur concentrations, only the reactions for  $n = 3, 4, 5$  have substantial contributions. These probabilities decrease with increasing  $y$ , and we observe the shift to longer sulfur ranks ( $n = 8, 12, 14, 15$ ). In the limit of high concentrations, the probability of forming medium-length chains also vanishes, and only the longest chain we have considered ( $n = 18$ ) contributes. It should also be noted that the binding probabilities for the intra-chain reaction are four orders of magnitude lower (*cf.* Fig. S4, ESI†) than those for the inter-chain process, which further corroborates that the latter one is the main reaction during vulcanization.

We can now relate these distributions to our previous stability analysis. The two smallest structures ( $n = 1, 2$ ) do not contribute because they are unstable. If we increase the amount of free sulfur, the next longer chains with  $n = 3, 4, 5$  will form. Interestingly, this behavior maximizes around  $n = 5$  (the peak maximum of  $n = 6, 7$  is less than 10%). Only if the sulfur concentration is substantially increased further, longer chains with  $n > 8$  will then be present. The presence of the  $p_5^{\text{inter}}([x])$

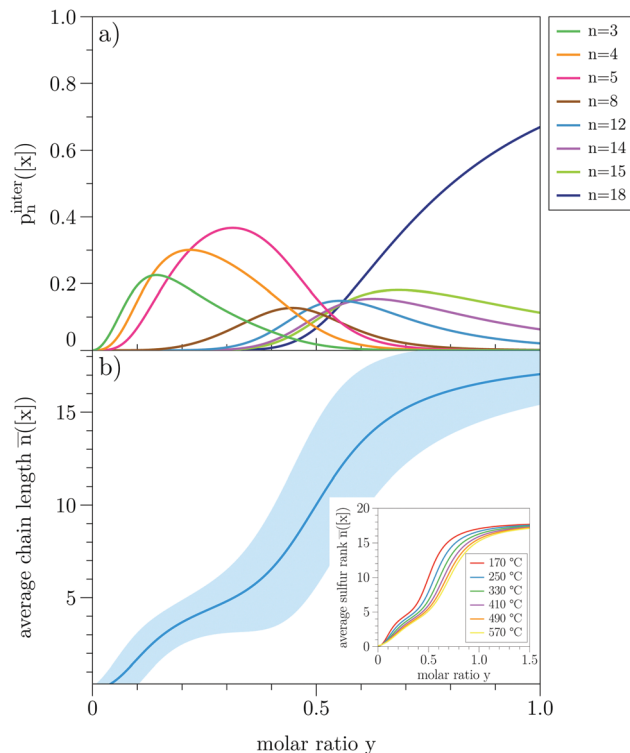


Fig. 8 The individual binding probability distributions for the inter-chain process  $p_n^{\text{inter}}([x])$  (a) and the respective average sulfur rank  $\bar{\nu}^{\text{inter}}([x])$  (solid line) and the standard deviation  $\sigma$  (colored area) as functions of the molar ratio of free sulfur and binding site  $y = [x]/[\text{BS}]$ . The inset in (b) shows the average sulfur rank  $\bar{n}^{\text{inter}}([x])$  for different vulcanization temperatures  $T$ .

curve over a relatively long range of  $y$  seems to correspond with the minimum of  $E_{\text{vul}}^{\text{inter}}$  at  $n = 5$  (*cf.* the inset of Fig. 6) indicating that a pentasulfide chain is the most probable outcome of the vulcanization for a certain range of free sulfur concentration. As discussed before, the temperature and (translational) entropy effects, included in the statistical mechanics model, lead to probable distributions of more but smaller ranks, especially the low energy state rank  $n = 5$ . Increasing the amount of sulfur then naturally pushes the system toward longer chains. The high stability of rank  $n = 5$  is also reflected by the average sulfur rank  $\bar{n}([x])$  (eqn (16)) for the inter-chain reaction (solid blue line, Fig. 8, panel b). It shows that the transition from short to long chains cannot be described by a strictly monotonically increasing function. Instead, it shows a small plateau around  $\bar{n} \approx 5$  before saturating to  $\bar{n} \approx 18$  for high concentrations. This again corresponds to the upper limit we have calculated vulcanization energies for. The result that we would find more stable structures by extending the chain would mean that the average chain length would increase continuously. This is, of course, due to the shortcomings of the electronic stability analysis. Furthermore, one should keep in mind the limitations of this model, considering only small gas-phase molecules. Certainly, in a real polymer, there will be constraints for the growth of the sulfur chain, such as steric, excluded volume, and packing effects, which we cannot assess with our approach.



In the experimental process of vulcanization, there is no precise definition of the temperature given that it is above the ROP-temperature (floor temperature) of  $S_8$  for initiating the process (although there might be some reasons related to the setup or the used material to choose a specific temperature). We, therefore, analyzed the temperature dependency of the average sulfur rank for the inter-chain process. In the inset of Fig. 8b, we see that the change of the isotherm vanishes with higher temperatures indicating an upper limit. The lower limit is the floor temperature of  $S_8$  which has to be exceeded. In between these limits, we can partially enhance sulfur embedding with the temperature by choosing a value just above the floor temperature. The results show that an increase in the temperature would decrease the average sulfur rank.

## 5 Conclusions

In this study, we used a combination of first-principles computational methods and statistical mechanics to explore the structural characteristics of the initial state of a vulcanized organic polymer which serves as the cathode for a Li-S battery.

We derived a statistical model to describe the outcome of the binding process of elemental sulfur to the thiol-containing PTBT polymer during vulcanization. The basis of this model is the fragmentation of the vulcanized S/PTBT polymer into small basic units for which simulations within electronic structure theory are feasible. By this, we can cover the essential features of the covalent binding process occurring on a local scale. The conformational space sampling, at the same time, allows us to study various structural configurations. The results of the DFT stability analysis are then fed back into our binding model. By calculating probability distributions and their quantitative measures, we can draw conclusions about the macroscopic features of the polymer. In that sense, our novel combination of methods can be described as a multi-scale approach to the structural characterization of the polymer.

Our results show that the main reaction of the vulcanization process leads to a sulfur chain cross-link between TBT units of different polymer backbones (inter-chain), whereas the binding of sulfur between adjacent TBT units of the same backbone is the side reaction (intra-chain). We could experimentally support this finding by Raman spectroscopy by identifying the S-S signal, which was detected already after electropolymerization, with our inter-chain structures. Based on our binding model, we calculated the average inter-chain sulfur rank for various sulfur concentrations and temperatures. Our results suggest that sulfur ranks around  $n = 5$  are most likely for a wide range of sulfur concentrations and can then be continuously extended by increasing the sulfur concentration (while in reality, at some points, steric constraints may occur). Moreover, for a given concentration, the embedding of sulfur would be most effective for a temperature just above the floor temperature of elemental sulfur.

This study provides insights into the fundamental understanding of the microscopic structure of a vulcanized organic polymer. By combining electronic structure theory with a

statistical mechanics model, we could draw more advanced conclusions than with pure DFT calculations. Hence, this approach seems beneficial when it comes to the structural characterization of novel cathode materials. Work to extend our model to describe the electronic properties of the polymer is in progress. An interesting aspect to investigate in future studies would be the comparison of the experimental Raman spectra to the calculated frequencies of the most representative structure.<sup>72,73</sup> Furthermore, this study is the first step into a multi-scale approach bridging classical and *ab initio* molecular dynamics simulations that will focus on larger solvated polymer structures<sup>74,75</sup> and spectroscopy calculations,<sup>76–78</sup> respectively.

## Conflicts of interest

There are no conflicts to declare.

## Acknowledgements

We thank Pouya Partovi-Azar, Michael Walter, Sebastian Risse, Shilin Mei, Sebastien Groh, and Diptesh Gayen for helpful discussions. The authors thank the HPC Service of ZEDAT (Curta<sup>79</sup>), Freie Universität Berlin, for computing time. We acknowledge funding of the project through the DFG Priority Programme “Polymer-based batteries” (SPP 2248, project number: 441211139).

## References

- 1 J. B. Goodenough and Y. Kim, *Chem. Mater.*, 2010, **22**, 587–603.
- 2 A. Manthiram, Y. Fu and Y.-S. Su, *J. Phys. Chem. Lett.*, 2013, **4**, 1295–1297.
- 3 X.-B. Cheng, R. Zhang, C.-Z. Zhao and Q. Zhang, *Chem. Rev.*, 2017, **117**, 10403–10473.
- 4 A. Fotouhi, D. J. Auger, K. Propp, S. Longo and M. Wild, *Renewable Sustainable Energy Rev.*, 2016, **56**, 1008–1021.
- 5 J. A. Poulis, J. P. François, C. H. Massen and L. C. V. Poucke, *Electrical Conductivity of Sulfur*, John Wiley & Sons, Ltd, 1990, ch. 15.2.2.2.14, p. 53.
- 6 Y. Diao, K. Xie, S. Xiong and X. Hong, *J. Power Sources*, 2013, **235**, 181–186.
- 7 X. He, J. Ren, L. Wang, W. Pu, C. Jiang and C. Wan, *J. Power Sources*, 2009, **190**, 154–156.
- 8 M. M. Islam, A. Ostadhosseini, O. Borodin, A. T. Yeates, W. W. Tipton, R. G. Hennig, N. Kumar and A. C. Van Duin, *Phys. Chem. Chem. Phys.*, 2015, **17**, 3383–3393.
- 9 P. T. Dirlam, R. S. Glass, K. Char and J. Pyun, *J. Polym. Sci., Part A: Polym. Chem.*, 2017, **55**, 1635–1668.
- 10 T. Danner, G. Zhu, A. F. Hofmann and A. Latz, *Electrochim. Acta*, 2015, **184**, 124–133.
- 11 F. Zhao, Y. Li and W. Feng, *Small Methods*, 2018, **2**, 1800156.
- 12 Q. Pang, X. Liang, C. Y. Kwok and L. F. Nazar, *Nat. Energy*, 2016, **1**, 1–11.
- 13 S. Walus, PhD thesis, Université Grenoble Alpes, 2015.



- 14 A. Manthiram, Y. Fu, S.-H. Chung, C. Zu and Y.-S. Su, *Chem. Rev.*, 2014, **114**, 11751–11787.
- 15 A. Narayanan Kirshnamoorthy, K. Oldiges, M. Winter, A. Heuer, I. Cekic-Laskovic, C. Holm and J. Smiatek, *Phys. Chem. Chem. Phys.*, 2018, **20**, 25701–25715.
- 16 G. Bieker, D. Diddens, M. Kolek, O. Borodin, M. Winter, P. Bieker and K. Jalkanen, *J. Phys. Chem. C*, 2018, **122**, 21770–21783.
- 17 M. D. Hager, B. Esser, X. Feng, W. Schuhmann, P. Theato and U. S. Schubert, *Adv. Mater.*, 2020, **32**, 2000587.
- 18 M. Wu, Y. Cui, A. Bhargav, Y. Losovyj, A. Siegel, M. Agarwal, Y. Ma and Y. Fu, *Angew. Chem., Int. Ed.*, 2016, **55**, 10027–10031.
- 19 S. Zeng, L. Li, L. Xie, D. Zhao, N. Wang and S. Chen, *ChemSusChem*, 2017, **10**, 3378–3386.
- 20 D. Y. Wang, W. Guo and Y. Fu, *Acc. Chem. Res.*, 2019, **52**, 2290–2300.
- 21 Y. Yang, G. Yu, J. J. Cha, H. Wu, M. Vosgueritchian, Y. Yao, Z. Bao and Y. Cui, *ACS Nano*, 2011, **5**, 9187–9193.
- 22 L. Xiao, Y. Cao, J. Xiao, B. Schwenzer, M. H. Engelhard, L. V. Saraf, Z. Nie, G. J. Exarhos and J. Liu, *Adv. Mater.*, 2012, **24**, 1176–1181.
- 23 S.-E. Cheon, K.-S. Ko, J.-H. Cho, S.-W. Kim, E.-Y. Chin and H.-T. Kim, *J. Electrochem. Soc.*, 2003, **150**, A796.
- 24 A. Manthiram, Y. Fu, S.-H. Chung, C. Zu and Y.-S. Su, *Chem. Rev.*, 2014, **114**, 11751–11787.
- 25 J. Liu, M. Wang, N. Xu, T. Qian and C. Yan, *Energy Storage Mater.*, 2018, **15**, 53–64.
- 26 X. Liu, Y. Lu, Q. Zeng, P. Chen, Z. Li, X. Wen, W. Wen, Z. Li and L. Zhang, *ChemSusChem*, 2020, **13**, 715–723.
- 27 M. Rao, X. Song, H. Liao and E. J. Cairns, *Electrochim. Acta*, 2012, **65**, 228–233.
- 28 W. Li, G. Zheng, Y. Yang, Z. W. Seh, N. Liu and Y. Cui, *Proc. Natl. Acad. Sci. U. S. A.*, 2013, **110**, 7148–7153.
- 29 W. Li, Q. Zhang, G. Zheng, Z. W. Seh, H. Yao and Y. Cui, *Nano Lett.*, 2013, **13**, 5534–5540.
- 30 H. Kim, J. Lee, H. Ahn, O. Kim and M. J. Park, *Nat. Commun.*, 2015, **6**, 7278.
- 31 A. Bhargav, M. E. Bell, Y. Cui and Y. Fu, *ACS Appl. Energy Mater.*, 2018, **1**, 5859–5864.
- 32 P. Sang, Y. Si and Y. Fu, *Chem. Commun.*, 2019, **55**, 4857–4860.
- 33 G. Gao, X. Sun and L.-W. Wang, *J. Mater. Chem. A*, 2020, **8**, 21711–21720.
- 34 W. J. Chung, J. J. Griebel, E. T. Kim, H. Yoon, A. G. Simmonds, H. J. Ji, P. T. Dirlam, R. S. Glass, J. J. Wie, N. A. Nguyen, B. W. Guralnick, J. Park, Á. Somogyi, P. Theato, M. E. Mackay, Y.-E. Sung, K. Char and J. Pyun, *Nat. Chem.*, 2013, **5**, 518–524.
- 35 R. M. S. Maior, K. Hinkelmann, H. Eckert and F. Wudl, *Macromolecules*, 1990, **23**, 1268–1279.
- 36 S. Hotta, S. D. Rughooputh, A. J. Heeger and F. Wudl, *Macromolecules*, 1987, **20**, 212–215.
- 37 S. Hotta, M. Soga and N. Sonoda, *Synth. Met.*, 1988, **26**, 267–279.
- 38 E. W. Tsai, S. Basak, J. P. Ruiz, J. R. Reynolds and K. Rajeshwar, *J. Electrochem. Soc.*, 1989, **136**, 3683–3689.
- 39 R. Kiani, D. Sebastiani and P. Partovi-Azar, *ChemPhysChem*, 2021, **1**, 1–6.
- 40 K. Dill, S. Bromberg and D. Stigter, *Molecular Driving Forces: Statistical Thermodynamics in Chemistry and Biology*, Garland Science, New York, NY, 2003.
- 41 X. Xu and J. Dzubiella, *Colloid Polym. Sci.*, 2020, **298**, 747–759.
- 42 P. Atkins and J. Paula, *Atkins' Physical Chemistry*, Oxford University press, New York, NY, 2008.
- 43 I. J. General, *J. Chem. Theory Comput.*, 2010, **6**, 2520–2524.
- 44 Y. Deng and B. Roux, *J. Phys. Chem. B*, 2009, **113**, 2234–2246.
- 45 D. McQuarrie and J. Simon, *Molecular Thermodynamics*, University Science Books, 1999.
- 46 M. Rossi, S. Chutia, M. Scheffler and V. Blum, *J. Phys. Chem. A*, 2014, **118**, 7349–7359.
- 47 M. Schneider, C. Masellis, T. Rizzo and C. Baldauf, *J. Phys. Chem. A*, 2017, **121**, 6838–6844.
- 48 K. Vollmayr-Lee, *Am. J. Phys.*, 2020, **88**, 401–422.
- 49 M. D. Hanwell, D. E. Curtis, D. C. Lonie, T. Vandermeersch, E. Zurek and G. R. Hutchison, *J. Cheminf.*, 2012, **4**, 17.
- 50 T. A. Halgren, *J. Comput. Chem.*, 1996, **17**, 490–519.
- 51 V. Blum, R. Gehrke, F. Hanke, P. Havu, V. Havu, X. Ren, K. Reuter and M. Scheffler, *Comput. Phys. Commun.*, 2009, **180**, 2175–2196.
- 52 V. W.-Z. Yu, F. Corsetti, A. Garca, W. P. Huhn, M. Jacquelin, W. Jia, B. Lange, L. Lin, J. Lu, W. Mi, A. Seifitokaldani, Á. Vázquez-Mayagoitia, C. Yang, H. Yang and V. Blum, *Comput. Phys. Commun.*, 2018, **222**, 267–285.
- 53 V. Havu, V. Blum, P. Havu and M. Scheffler, *J. Comput. Phys.*, 2009, **228**, 8367–8379.
- 54 J. P. Perdew, K. Burke and M. Ernzerhof, *Phys. Rev. Lett.*, 1996, **77**, 3865–3868.
- 55 A. Tkatchenko and M. Scheffler, *Phys. Rev. Lett.*, 2009, **102**, 6–9.
- 56 V. G. Ruiz, W. Liu, E. Zojer, M. Scheffler and A. Tkatchenko, *Phys. Rev. Lett.*, 2012, **108**, 2–6.
- 57 C. Adamo and V. Barone, *J. Chem. Phys.*, 1999, **110**, 6158–6170.
- 58 A. Ambrosetti, A. M. Reilly, R. A. DiStasio and A. Tkatchenko, *J. Chem. Phys.*, 2014, **140**, 18A508.
- 59 S. Grimme, *Angew. Chem., Int. Ed.*, 2008, **47**, 3430–3434.
- 60 R. T. Morrison and R. N. Boyd, *Organic Chemistry*, Allyn and Bacon, Boston, 2002, p. 1283.
- 61 B. Meyer, in *The Structures of Elemental Sulfur*, ed. H. Emeléus and A. Sharpe, Academic Press, 1976, vol. 18, of *Advances in Inorganic Chemistry and Radiochemistry*, pp. 287–317.
- 62 R. Steudel, *Chem. Rev.*, 2002, **102**, 3905–3945.
- 63 A. Kamyshny, A. Goifman, J. Gun, D. Rizkov and O. Lev, *Environ. Sci. Technol.*, 2004, **38**, 6633–6644.
- 64 A. Kamyshny, J. Gun, D. Rizkov, T. Voitsekovski and O. Lev, *Environ. Sci. Technol.*, 2007, **41**, 2395–2400.
- 65 R. Gleiter, G. Haberhauer and F. Rominger, *Eur. J. Inorg. Chem.*, 2019, 3846–3853.
- 66 D. M. Byler, H. Susi and H. M. J. Farrell, *Biopolymers*, 1983, **22**, 2507–2511.
- 67 K. B. Biggs, J. P. Camden, J. N. Anker and R. P. V. Duyne, *J. Phys. Chem. A*, 2009, **113**, 4581–4586.



- 68 X.-F. Wu, X. Zheng, H.-G. Wang, Y.-Y. Zhao, X. Guan, D. L. Phillips, X. Chen and W. Fang, *J. Chem. Phys.*, 2010, **133**, 134507.
- 69 H. E. Van Wart and H. A. Scheraga, *J. Phys. Chem.*, 1976, **80**, 1812–1823.
- 70 B. Mandal and B. Basu, *RSC Adv.*, 2014, **4**, 13854–13881.
- 71 L. F. Sgobbi, C. A. Razzino, I. G. Rosset, A. C. Burtoloso and S. A. Machado, *Electrochim. Acta*, 2013, **112**, 500–504.
- 72 P. Partovi-Azar and T. D. Kühne, *J. Comput. Chem.*, 2015, **36**, 2188–2192.
- 73 P. Partovi-Azar, T. D. Kühne and P. Kaghazchi, *Phys. Chem. Chem. Phys.*, 2015, **17**, 22009–22014.
- 74 C. Park, M. Kanduč, R. Chudoba, A. Ronneburg, S. Risse, M. Ballauff and J. Dzubiella, *J. Power Sources*, 2018, **373**, 70–78.
- 75 C. Park, A. Ronneburg, S. Risse, M. Ballauff, M. Kanduč and J. Dzubiella, *J. Phys. Chem. C*, 2019, **123**, 10167–10177.
- 76 M. Qureshi, S. H. Nowak, L. I. Vogt, J. J. Cotelesage, N. V. Dolgova, S. Sharifi, T. Kroll, D. Nordlund, R. Alonso-Mori, T. C. Weng, I. J. Pickering, G. N. George and D. Sokaras, *Phys. Chem. Chem. Phys.*, 2021, **23**, 4500–4508.
- 77 T. J. Zuehlsdorff and C. M. Isborn, *Int. J. Quantum Chem.*, 2019, **119**, 1–18.
- 78 K. H. Wujcik, T. A. Pascal, C. D. Pemmaraju, D. Devaux, W. C. Stolte, N. P. Balsara and D. Prendergast, *Adv. Energy Mater.*, 2015, **5**, 1500285.
- 79 L. Bennett, B. Melchers and B. Proppe, *Curta: A General-purpose High-Performance Computer at ZEDAT*, Freie Universität Berlin, 2020, DOI: 10.17169/refubium-26754.



## Supplementary Informations

### Combined first principles-statistical mechanics approach to sulfur structure in organic cathode hosts for polymer based lithium-sulfur (Li-S) batteries

Yannik Schütze,<sup>a,e</sup> Ranielle de Oliveira Silva,<sup>b,f</sup> Jiaoyi Ning,<sup>b,g</sup> Jörg Rappich,<sup>c</sup> Yan Lu,<sup>b,f</sup>  
Victor G. Ruiz,<sup>a</sup> Annika Bande,<sup>d</sup> and Joachim Dzubiella<sup>a,h</sup>

<sup>a</sup> Research Group for Simulations of Energy Materials, <sup>b</sup>Department Electrochemical Energy Storage, <sup>c</sup>Institute Silicon Photovoltaics, and <sup>d</sup>Young Investigator Group Theory of Electron Dynamics and Spectroscopy, Helmholtz-Zentrum Berlin für Materialien und Energie, Hahn-Meitner-Platz 1, 14109 Berlin, Germany;

E-mail: yannik.schuetze@helmholtz-berlin.de

<sup>e</sup> Theoretical Chemistry, Institute of Chemistry and Biochemistry, Freie Universität Berlin, Arnimallee 22, 14195 Berlin, Germany

<sup>f</sup> Institute of Chemistry, University of Potsdam, Am Neuen Palais 10, 14469 Potsdam Germany

<sup>g</sup> School of Advanced Materials, Peking University Shenzhen Graduate School, Peking University, 518055 Shenzhen, China

<sup>h</sup> Applied Theoretical Physics - Computational Physics, Physikalisches Institut, Albert-Ludwigs-Universität Freiburg, Herrmann-Herder-Straße 3, 79104 Freiburg, Germany;

E-mail: joachim.dzubiella@physik.uni-freiburg.de

## S1: Conformational space sampling of product states

For the sampling of different conformations of the vulcanization product states DiTBT- $S_n$  and DiTBT- $2S_n$ -DiTBT, we used the Avogadro software<sup>1</sup> employing the MMFF94 force field<sup>2</sup> with steepest descent minimization. The aim was to cover a wide range of sulfur chain conformations to estimate the structure-stability relationship of possible reaction products. Fig.S1 shows examples of the extreme cases probed by our sampling in terms of the dihedral angle  $\gamma_{SCCS}$  between the neighboring TBT units of a DiTBT. For  $n = 1$ , there is only one stable configuration for the *intra*- and *inter-chain* products. With increasing  $n$ , the chain's flexibility leads to various stable configurations with a broad range of dihedrals. Shown here are two extreme cases of the *intra*- and *inter-chain* process, respectively. For the former, a wide range of dihedrals is possible only for long chain lengths ( $n = 16$ ), while for the latter, it can already be seen for short ranks ( $n = 4$ ).

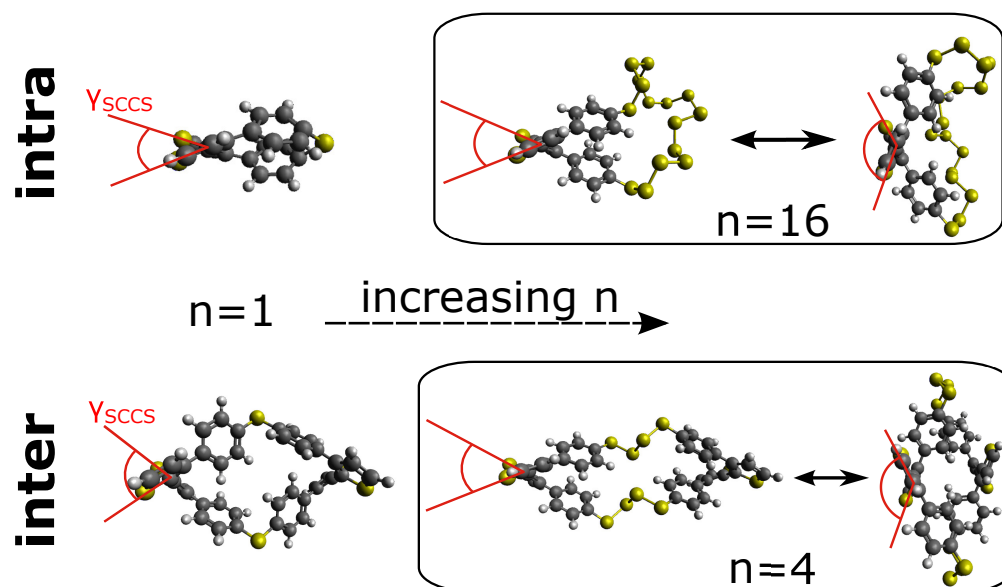
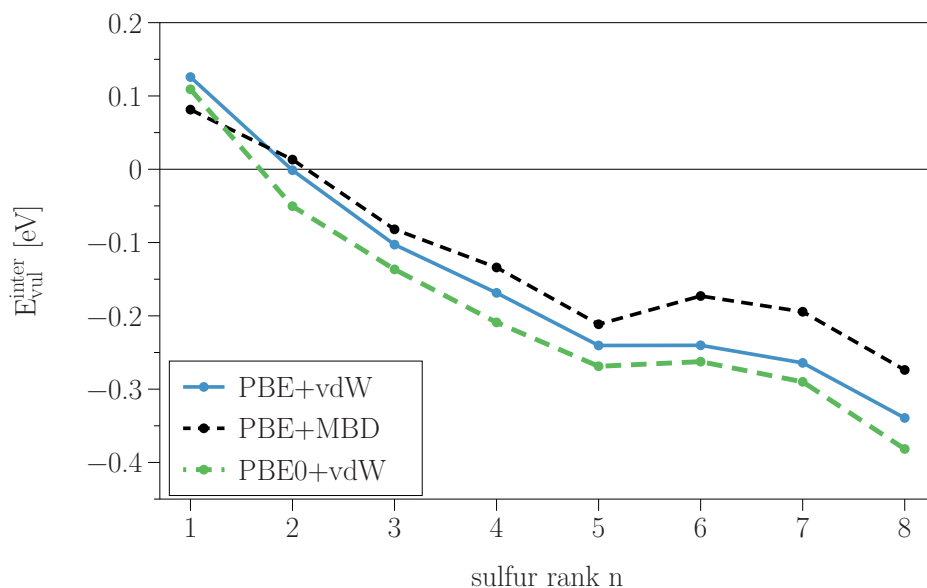


Fig. S1 Probing different configurations regarding the thiophene dihedral  $\gamma_{SCCS}$  in dependency of the sulfur rank  $n$ .

## S2: Stability analysis - comparison of DFT functionals and van der Waals interaction methods

We also did the stability analysis of reaction products by using the hybrid DFT functional PBE0<sup>3</sup> together with the pair-wise van der Waals correction<sup>4,5</sup> (PBE0+vdW) and also the PBE functional<sup>6</sup> together with the many-body dispersion method<sup>7</sup> (PBE+MBD) and compared it with the PBE+vdW method presented in the main text. All DFT calculations were performed using the all-electron, full-potential density-theory package FHI-aims<sup>8-10</sup> (convergence settings can be found in the computational details subsection of the main text). Fig.S2 shows that the two different functionals give relatively similar results for the vulcanization energies of the *inter-chain* process. The PBE0 results are decreased by about 0.03 eV against the PBE results. Using the MBD method instead of the pairwise vdW correction to account for the dispersion interaction, we observe that as the sulfur rank  $n$  increases, the larger structures are less stable. This is a consequence of the inclusion of many-body interactions in the dispersion energy. Contrary to including only an attractive pairwise interaction via the vdW-method, the inclusion of many-body effects becomes more relevant and less attractive when the chain consists of more sulfur atoms, yielding a less attractive long-range dispersion energy. This fact also points in the direction of an energy saturation in a real polymer chain, where the many-body effects would become even larger.



**Fig. S2** The comparison of vulcanization energies  $E_{\text{vul}}^{\text{inter}}$  of the most stable *inter-chain* products for different exchange-correlation functionals and different van der Waals interactions: PBE+vdW (solid blue line), PBE+MBD (dashed black line), and PBE0+vdW (dashed green line).

### S3: Raman spectroscopy of *intra-chain* and *inter-chain* bonds

Raman spectroscopy may be sensitive to the conformational modes of thiol groups. Therefore, we have repeated the Raman backscattering experiments with higher spectral resolution using an exposition time of 300 s. Fig. S3 shows the Raman spectra measured with lower ( $3\text{ cm}^{-1}$ , blue curve) and higher ( $1\text{ cm}^{-1}$ , green curve) spectral resolution. The spectrum with higher resolution shows some pronounced shoulders for the vibrational modes of the -S-S- group around  $500\text{ cm}^{-1}$ . As shown in the inset of Fig. S3, the peak centered around  $500\text{ cm}^{-1}$  can be deconvoluted in three components: the peaks at  $478\text{ cm}^{-1}$ ,  $492\text{ cm}^{-1}$ , and  $516\text{ cm}^{-1}$  originate from the S-S stretching modes in the *gauche-gauche-gauche* (GGG), *gauche-gauche-trans* (GGT), and the *trans-gauche-trans* (TGT) configurations<sup>11,12</sup>, respectively. These peaks have been shifted by about  $30\text{ cm}^{-1}$  to lower energy with respect to those from ref. 11,12. This may be a result of a different environment (polymer vs. human hair).

The three components were found for the as-prepared polymer PTBT leading to the assumption that all these configurations co-exist in the polymeric layer. So far, it is not possible to discriminate any preferential conformation for the molecules and associate them to the types of inter- and intra-molecular bonds by Raman spectroscopy. To do so, we need polymers with only GGG, GGT, TGT configuration and with only inter- or only intra-molecular bonding, which is nearly impossible from a synthesis point of view.

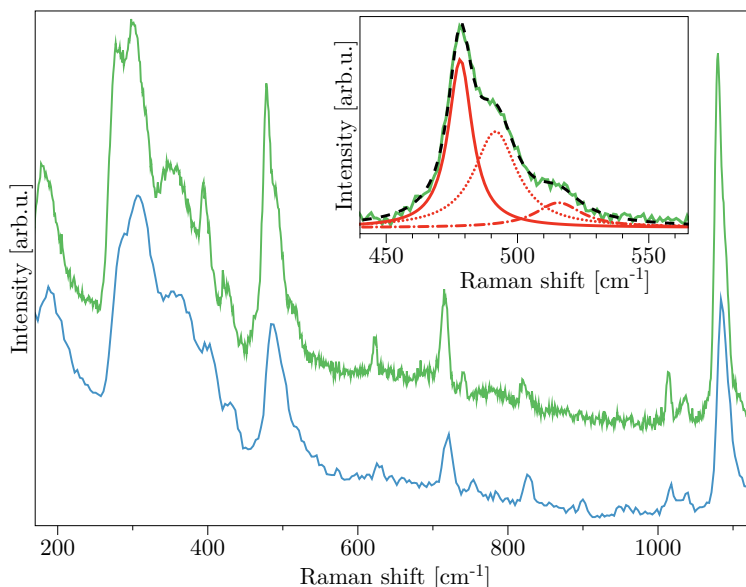


**Fig. S3** Raman spectra measured with lower ( $3\text{ cm}^{-1}$ , blue curve) and higher ( $1\text{ cm}^{-1}$ , green curve) spectral resolution. The spectrum recorded at higher resolution shows some pronounced shoulders for the vibrational modes of the -S-S- group around  $500\text{ cm}^{-1}$ . The inset shows the peak centered around  $500\text{ cm}^{-1}$  and its deconvolution into three components as described in the text.

## S4: Binding probability distributions for the *intra-chain* process

In Fig.S4, the individual binding probabilities for the *intra-chain* process  $p_n^{\text{intra}}([x])$  are displayed versus the molar ratio of free sulfur and binding sites  $y = [x]/[\text{BS}]$ . The maximum *intra-chain* binding probability  $p_{14}^{\text{intra}}$  is four orders of magnitude lower than for the *inter-chain* process (cf. Fig.8 in main text). This shows that the connection of adjacent TBT units of the same polymer backbone by a sulfur chain is the side reaction during vulcanization.

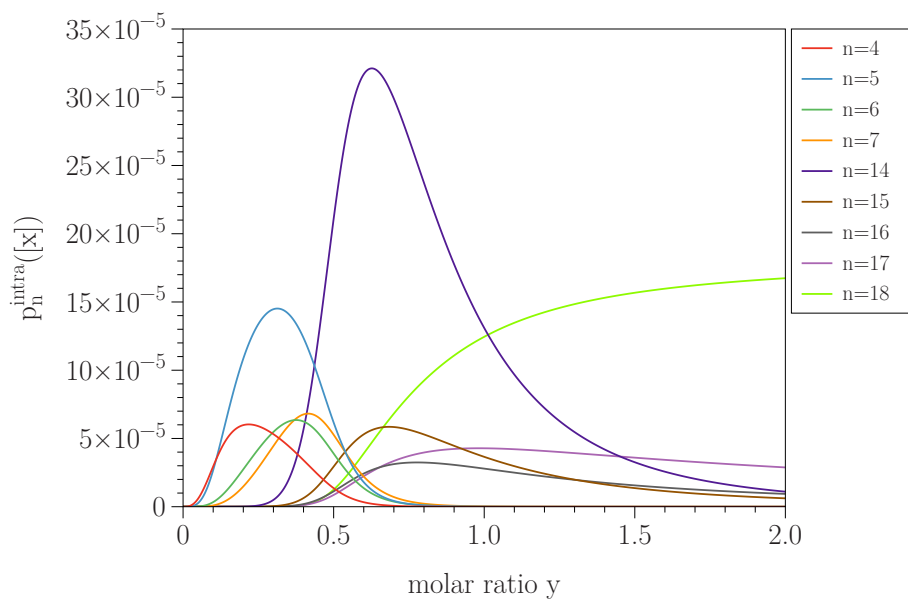


Fig. S4 The individual binding probabilities for the *intra-chain* process  $p_n^{\text{intra}}(x)$ .

## Notes and references

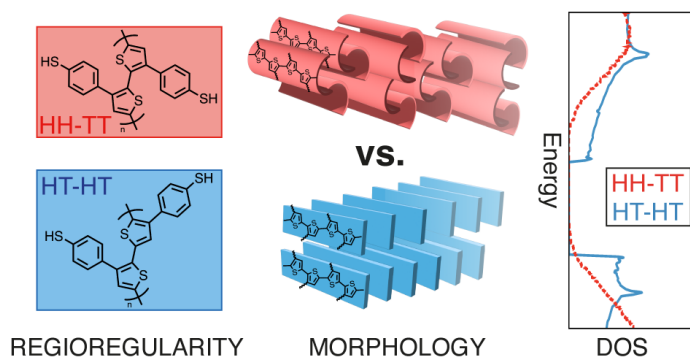
- 1 M. D. Hanwell, D. E. Curtis, D. C. Lonie, T. Vandermeersch, E. Zurek and G. R. Hutchison, *Journal of Cheminformatics*, 2012, **4**, 17.
- 2 T. A. Halgren, *Journal of Computational Chemistry*, 1996, **17**, 490–519.
- 3 C. Adamo and V. Barone, *The Journal of Chemical Physics*, 1999, **110**, 6158–6170.
- 4 A. Tkatchenko and M. Scheffler, *Physical Review Letters*, 2009, **102**, 6–9.
- 5 V. G. Ruiz, W. Liu, E. Zojer, M. Scheffler and A. Tkatchenko, *Physical Review Letters*, 2012, **108**, 2–6.
- 6 J. P. Perdew, K. Burke and M. Ernzerhof, *Physical Review Letters*, 1996, **77**, 3865–3868.
- 7 A. Ambrosetti, A. M. Reilly, R. A. DiStasio and A. Tkatchenko, *The Journal of Chemical Physics*, 2014, **140**, 18A508.
- 8 V. Blum, R. Gehrke, F. Hanke, P. Havu, V. Havu, X. Ren, K. Reuter and M. Scheffler, *Computer Physics Communications*, 2009, **180**, 2175–2196.
- 9 V. W.-Z. Yu, F. Corsetti, A. García, W. P. Huhn, M. Jacquelin, W. Jia, B. Lange, L. Lin, J. Lu, W. Mi, A. Seifitokaldani, Á. Vázquez-Mayagoitia, C. Yang, H. Yang and V. Blum, *Computer Physics Communications*, 2018, **222**, 267–285.
- 10 V. Havu, V. Blum, P. Havu and M. Scheffler, *Journal of Computational Physics*, 2009, **228**, 8367–8379.
- 11 R. Paquin and P. Colomban, *Journal of Raman Spectroscopy*, 2007, **38**, 504–514.
- 12 A. Kuzuhara, *Int J Cosmet Sci*, 2018, **40**, 34–43.

### A.3 How Regiochemistry Influences Aggregation Behavior and Charge Transport in Conjugated Organosulfur Polymer Cathodes for Lithium–sulfur Batteries

Yannik Schütze, Diptesh Gayen, Karol Palczynski, Ranielle de Oliveira Silva, Yan Lu, Michael Tovar, Pouya Partovi-Azar, Annika Bande, Joachim Dzubiella

*ACS Nano*, **2023**, 17, 8, 7889–7900

DOI: 10.1021/acsnano.3c01523



**Author Contributions:** This project was a cooperation between the groups of Joachim Dzubiella (JD), Yan Lu (YL), and Annika Bande (AB). The project idea was conceived by JD, AB, Victor G. Ruiz (VR), and Yannik Schütze (YS). All synthesis was carried out by Ranielle de Oliveira Silva (RS). X-ray diffraction measurements were performed by Michael Tovar (MT). All theoretical calculations were performed by YS, including the re-parametrization of the MD force field, which has been constructed by Diptesh Gayen (DG) and YS. RS, MT, and YS analyzed and compared the XRD data to the theoretical diffractograms. The manuscript was mainly written by YS, with RS responsible for the experimental chapter and the remaining authors proofreading. All authors contributed to the final version of the manuscript.

On the following pages, the publication, including the supporting information, is provided with permission of the American Chemical Society in accordance with the creative commons attribution 4.0 international licence for Yannik Schütze *et al.*, A.3, 2023.

# How Regiochemistry Influences Aggregation Behavior and Charge Transport in Conjugated Organosulfur Polymer Cathodes for Lithium–Sulfur Batteries

Yannik Schütze, Diptesh Gayen, Karol Palczynski, Ranielle de Oliveira Silva, Yan Lu, Michael Tovar, Pouya Partovi-Azar, Annika Bande, and Joachim Dzubiella\*



Cite This: *ACS Nano* 2023, 17, 7889–7900



Read Online

ACCESS |



Metrics & More



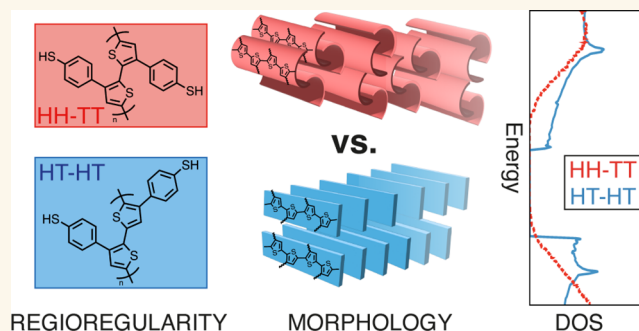
Article Recommendations



Supporting Information

**ABSTRACT:** For lithium–sulfur (Li–S) batteries to become competitive, they require high stability and energy density. Organosulfur polymer-based cathodes have recently shown promising performance due to their ability to overcome common limitations of Li–S batteries, such as the insulating nature of sulfur. In this study, we use a multiscale modeling approach to explore the influence of the regiochemistry of a conjugated poly(4-(thiophene-3-yl)benzenethiol) (PTBT) polymer on its aggregation behavior and charge transport. Classical molecular dynamics simulations of the self-assembly of polymer chains with different regioregularity show that a head-to-tail/head-to-tail regularity can form a well-ordered crystalline phase of planar chains allowing for fast charge transport. Our X-ray

**KEYWORDS:** lithium–sulfur battery, conjugated polymer, regularity, self-assembly, charge transport, molecular dynamics simulations, X-ray diffraction



Lithium–sulfur (Li–S) batteries are among the most promising next-generation energy storage systems that have the potential to surpass traditional lithium-ion batteries in terms of both energy density and cost.<sup>1–3</sup> These batteries are composed of a lithium anode and a sulfur cathode and operate through a redox reaction in which lithium ions are transferred between the two electrodes. This reaction allows Li–S batteries to store more energy per unit weight than lithium-ion batteries, making them an attractive option for a wide range of applications.<sup>4,5</sup> However, despite their potential advantages, Li–S batteries have faced several challenges in terms of their performance and stability, such as the insulating nature of the elemental sulfur<sup>6</sup> and the shuttle effect of dissolvable lithium polysulfides.<sup>7</sup>

Conjugated polymers are a class of polymeric materials that exhibit alternating single and double carbon bonds in their main chain, which gives them characteristic electrical, optical,

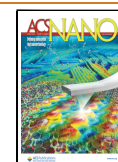
and mechanical properties.<sup>8–11</sup> In the context of Li–S batteries, conjugated polymers can be used as cathode material to improve the electrical conductivity<sup>12–14</sup> of the sulfur cathode and to prevent the dissolution of the active materials by forming strong chemical bonds with sulfur.<sup>15–19</sup> Among these, thiol-containing polymers are one example where the –SH groups can be cross-linked with sulfur via covalent bonding.<sup>20–22</sup>

In a recent study of ours, we presented a fabrication strategy to construct a binder- and carbon additive-free organosulfur

Received: February 16, 2023

Accepted: March 29, 2023

Published: April 4, 2023



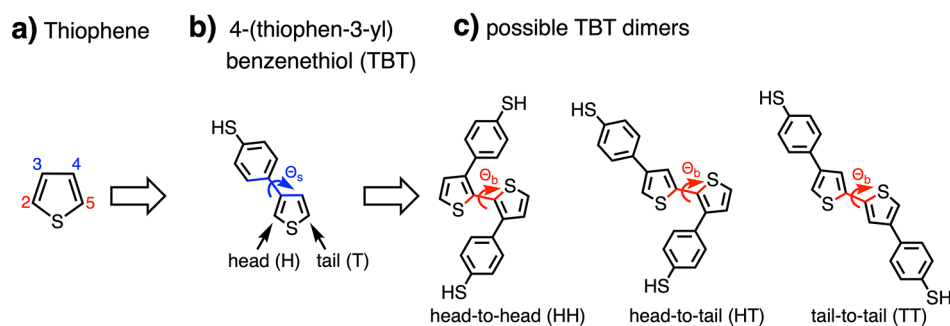


**Figure 1.** (a) Binding sites of the heterocyclic thiophene ring. The labels on the  $\alpha$ -positions (2, 5) are colored in red, and those at the  $\beta$ -positions (3, 4) in blue. (b) The TBT monomer with the substituted benzenethiol at the  $\beta$ -position of the thiophene ring. The side chain dihedral  $\Theta_s$  is colored in blue. (c) Illustration of the three possible connections, HH, HT, and TT, between two asymmetric TBT units. The backbone dihedral  $\Theta_b$  is colored in red for the three structures.

cathode based on a thiol-containing conducting polymer poly(4-(thiophene-3-yl)benzenethiol) (PTBT).<sup>22</sup> The PTBT features the polythiophene main chain as a highly conducting framework and the benzenethiol side chain to copolymerize<sup>23,24</sup> with sulfur and form a cross-linked organosulfur polymer. We have been able to show the significant fixing effect of the sulfur species by operando X-ray imaging. This synthesis approach maintains the conductivity and flexibility of the polymer framework and therefore seems promising to overcome typical drawbacks of Li–S batteries. In a further study, we used a combination of *first-principles* computational methods and statistical mechanics to explore the structural characteristics of the initial state of a vulcanized PTBT polymer.<sup>25</sup> Our calculations showed that the main reaction of the vulcanization process leads to high-probability states of sulfur chains cross-linking TBT units belonging to different polymer backbones, with a dominant sulfur chain length of 5 atoms. Similar results have been reported for different sulfur/carbon copolymers.<sup>14,26</sup>

The morphology of a polymer can greatly impact its conductive behavior. In general, polymers with more ordered and aligned structures allow for more efficient transport of charges and tend to have higher conductivity than those with disordered structures. The morphology of the polymer can be controlled through various synthesis techniques.<sup>27–29</sup> Understanding the relationship between morphology and conductivity can allow for the design of polymers with improved conductive behavior.<sup>30–32</sup> Thiophene-based conjugated polymers such as the well-known poly(3-hexylthiophene) (P3HT),<sup>33–36</sup> poly(2,5-bis(3-alkylthiophen-2-yl)thieno[3,2-*b*]thiophene) (PBTTT),<sup>37–39</sup> or poly-3,4-ethylenedioxythiophen (PEDOT)<sup>40–42</sup> have been extensively studied over the last decades to demonstrate morphology-transport relationships, but many fundamental questions in this field of polymeric organic semiconductors remain unanswered. Furthermore, it is often not possible to directly use the theoretical description of similar thiophene-based polymers when investigating a different material without introducing errors. Therefore, special care must be taken to describe the PTBT's microstructure accurately.

One important factor influencing the charge transport properties of all of these systems is the regioregularity of their backbones.<sup>43–47</sup> In order to elucidate this relationship for our PTBT polymer from a theoretical point of view, the knowledge of an accurate atomistic model of the material is crucial for a structural description and the calculation of its electronic properties. In this work, we employ classical

molecular dynamics (MD) simulations to explore the self-assembly process of conjugated PTBT chains of different backbone regularities. To validate our structure predictions, we compare experimental X-ray diffraction (XRD) measurements of the electropolymerized PTBT polymer with simulated diffraction patterns. Taking the generated structures as input, we then use electronic structure theory to investigate how the structural changes of the polymer influence its electronic and charge transport properties. Finally, we employ Boltzmann transport and deformation potential theory as a quantitative approach to estimating the intrinsic transport limit of the PTBT polymer. Our theoretical multiscale approach, combined with the experiments, allows us to precisely describe the interplay between polymer regularity, structural morphology, and charge transfer properties.

## RESULTS AND DISCUSSION

**Aggregation Behavior of Regioregular PTBT Polymer Chains.** In a recent study of ours,<sup>48</sup> we investigated the conformational behavior of a single oligomeric PTBT chain in solution by means of MD simulations. Due to the conjugated nature of our system, one of the most important terms to be considered when evaluating the force field is the energetic profile governing the dihedral dynamics between neighboring monomers. The electropolymerization of TBT monomers results in the formation of conjugated PTBT polymer chains. The polymerization of the five-membered heterocyclic thiophene ring can take place through bonding at the  $\alpha$ - or  $\beta$ - positions (2- or 3-positions, cf. Figure 1a). In the TBT monomer, the  $\beta$ -position is substituted with a benzenethiol group. It is well established that the  $\alpha$ -position is the most reactive position in the polymerization of 3-substituted thiophene monomers, leading to the dominance of  $\alpha,\alpha$ -linkages in the resulting polymer. As a result, the long PTBT polymer chains that form during polymerization will likely have thiophene rings as the main-chain backbones with benzenethiol groups as the lateral chains.<sup>49–52</sup>

A key feature of the TBT monomer is the breaking of reflection symmetry between each end of the molecule (along the direction of the polymer backbone). This intrinsic asymmetry allows for three possible connections, head-to-head (HH), head-to-tail (HT), and tail-to-tail (TT), between two TBT repeat units (cf. Figure 1c). The general terms 'head' and 'tail' distinguish the substituted groups at the  $\beta$ -positions of consecutive thiophene rings (here, the benzenethiol group is depicted as a head (H), and the hydrogen at the 4-position is

the tail (T)).<sup>53</sup> For our system, we identify two critical dihedrals that will govern the aggregation behavior of the polymer chain: the backbone dihedral  $\Theta_b$  between the thiophene rings of neighboring TBT units (Figure 1c) and the side chain dihedral  $\Theta_s$  between the thiophene ring and the benzenethiol group within one monomer (Figure 1b). Details on the results of the reparametrization and the validation of the optimized force field can be found in Table S1 and Figures S1–S5 of the SI.

In a real polymer system, on larger scales, both crystalline and amorphous domains will be present. As the first step in our investigation of charge transfer properties, we do not describe the polymer chains as oligomers but as periodically repeated chains of infinite length. Throughout the rest of this paper, we will apply periodic boundary conditions (PBC) along the axis of the polymer backbone. As a further simplification, we only consider regioregular (RR)-conjugated polymer chains,<sup>46</sup> which follow a strict orientation of the alternating asymmetric repeating TBT units throughout the polymer backbone. This is, of course, an idealization of the real system in which the degree of regioregularity depends on synthetic conditions.<sup>47,49,54</sup> Given the three possible connections between two TBT units (HH, HT, TT), there are two feasible RR-chains, namely HH-TT and HT-HT (cf. Figure 2).

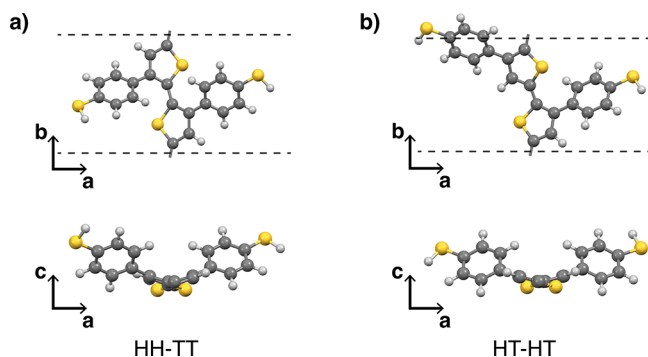


**Figure 2.** Illustration of the two possible regioregularities, (a) HH-TT and (b) HT-HT, of a conjugated PTBT chain. The upper two panels show the side view (*ab*-plane), and the lower two panels show the top view along the backbone direction (*ac*-plane). Dashed lines indicate the height of the unit cell along the *b*-direction.

We compare the structural properties of these regioregularities obtained from MD and DFT (cf. Table S2). Our results show that the presence of the benzenethiol groups leads to a deviation of the backbone planarity compared to the unsubstituted planar polythiophene chain.<sup>55</sup> Such distortions from planarity have been observed for polythiophene systems substituted with similar bulky aromatic groups and can be related to steric effects between the side groups.<sup>56,57</sup> For the HH-TT regularity, this is more prominent than for the HT-HT regularity because of the proximity of the benzenethiol groups in the HH intermonomer junction (cf. Figure S5, Table S2, and Supporting Text).

Next, we take the optimized single-chain structures to set up supercells of  $N = 100$  PTBT chains for both regioregularities. Since there is no experimental data on the structural properties of this polymer present in the literature, we will simulate the self-assembly of conjugated PTBT chains from scratch. This means we let the system self-associate by temperature annealing from a very high temperature, isotropic phase to

room-temperature conditions. Such an approach has been used successfully for similar systems.<sup>58,59</sup> The initial systems are cooled down from 1500 to 300 K at a pressure of 1 bar in the *NPT* ensemble over a time period of 10 ns (cf. Figure S6). After the systems are equilibrated at room-temperature, all polymer chains have aggregated into one big cluster, respectively (cf. Figure 3). In the HT-HT system, we observe

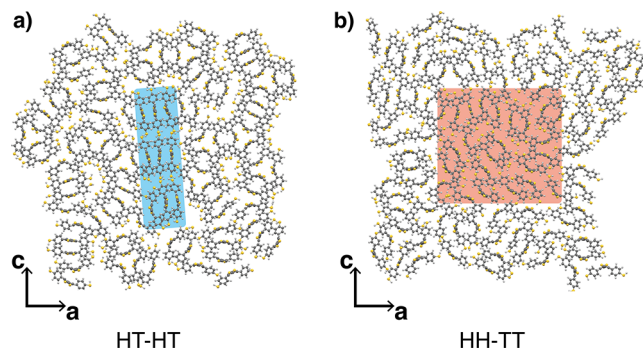


**Figure 3.** Comparison of the grown clusters at  $T = 300$  K after annealing. The systems are shown in the *ac*-plane with the view along the polymer backbones. (a) The HT-HT system forms an ordered phase with a two-dimensional translational ordering along the *a*- and *c*-axes (blue-colored area). (b) The HH-TT system does not show long-range ordering in the *ac*-plane. For further investigation, we cut out a representative subset of the cluster's center (red-colored area).

neighboring chains forming an ordered region in the center of the cluster, where the backbones are planar and stacked together in a face-to-face manner along the crystal (growth) *a*-axis. The blue-colored area depicts three stacks of chains arranged in a lamellar fashion along the *c*-axis. Going to the outer regions of such a cluster, its ordering decreases due to surface effects which lead to backbone bending and distortion of the crystalline alignment. Here, we observe a mix of different substructures (small stacks similar to the center, pairs of bent chains, and even bigger arrangements of those chain pairs; cf. Figure S6).

On the other hand, the HH-TT does not show ordered regions in the center of the grown cluster. Here, the backbones are still twisted, as is the case for the isolated chain. Thus, we see no stacking of multiple chains but rather arrangements of pairs. In contrast to the HT-HT system, we cannot observe any sign of long-range order, which suggests that the HH-TT polymer system cannot form crystalline phases. This can be related to the increased steric hindrance of the single chains making it harder for the HH-TT chains to adapt a planar configuration and thus aggregate into stacks.

In the following, we will investigate the structural and electronic properties of the two systems. For the HT-HT regularity, we will focus on the ordered phase without any surface effects. However, for HH-TT, this separation is not feasible due to its unordered behavior. Instead, we take a smaller subset of the cluster's center as a representative system (red-colored area in Figure 3).

**Structural and Electronic Properties of the Crystalline (HT-HT) and Unordered (HH-TT) Phase.** We start with the characterization of the HT-HT single-crystal by cutting a representative subset from the center of the grown cluster after the *NPT* annealing. This subset consists of  $3 \times 3$  neighboring chains (blue colored area in Figure 3). From this, we create a

**Table 1. Crystallographic Data of the HT-HT Single-Crystal Phase from *NPT* Equilibration Simulations at  $T = 300$  K and from DFT Optimization of the Primitive Cell<sup>a</sup>**

	$a$ (Å)	$b$ (Å)	$c$ (Å)	$\alpha$ (Å)	$\beta$ (deg)	$\gamma$ (deg)	$\rho$ (g/cm <sup>3</sup> )
MD average	8.12(3)	7.68(1)	14.50(4)	92.5(2)	84.4(4)	108.4(4)	1.480(4)
DFT	7.44	7.78	14.45	89.2	89.7	90.2	1.51

<sup>a</sup>The first row denotes the block average over the ensemble of the  $12 \times 12$  chains in the  $ac$ -plane with the standard deviation due to thermal fluctuations at room temperature in parentheses. The bottom row shows the DFT-optimized (PBE+MBD) results.

periodic crystal by replicating the structures  $4 \times 4$  times in the  $ac$ -plane. This homogeneous crystal, consisting of  $N = 144$  polymer chains ( $12 \times 12$  in the  $ac$ -plane), is then equilibrated in another *NPT* run at 300 K for 5 ns. Afterward, a final *NPT* run for 1 ns is performed to collect structural data from the trajectory. The unit cell parameters, such as lattice lengths, angles, and mass density, are then averaged over the ensemble.

The results and their respective standard deviations due to temperature and pressure fluctuations are summarized in Table 1. We see that all angles differ from each other and do not contain the  $90^\circ$  angle typical for monoclinic crystals. Thus, the HT-HT forms a triclinic crystal structure at room-temperature. The crystal shows only minimal deviations from its equilibrium configuration due to thermal fluctuation (the standard deviation of the  $a$ - and  $c$ -axes is 0.3% and of the  $b$ -axis <0.1%).

From the final *NPT* run, we take a snapshot of the homogeneous single-crystal, cut out the primitive unit cell, and optimize it with DFT at the PBE+MBD level of theory (bottom row of Table 1). The DFT optimization at 0 K mainly leads to a shortening of the  $a$ -axis by 8% corresponding to a tighter stacking of neighboring polymer backbones. This is also evident in the increased mass density (1.51 g/cm<sup>3</sup> for the DFT compared to 1.48 g/cm<sup>3</sup> for the MD run). We also notice that in the DFT structure, all angles are very close to  $90^\circ$  (with less than 1% deviation), suggesting an orthorhombic crystal. As already seen in the *NPT* run, in the crystal structure, the stacked chains now adopt a planar backbone conformation in contrast to the nonplanar isolated chains (Figure 4a). In Figure

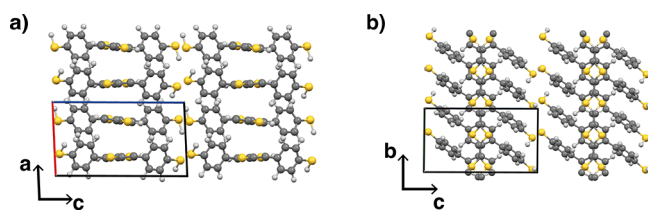


**Figure 4. DFT optimized crystal structure of the HT-HT primitive unit cell. (a) The  $ac$ -plane and (b)  $bc$ -plane of the HT-HT crystal.**

4b, we see that the thiophene rings of neighboring chains (along the short stacking axis in  $a$ -direction) are not aligned on top of each other, but instead, they are shifted along the backbone direction ( $b$ -direction in Figure 4a) by one thiophene-thiophene distance. This creates space for the benzenethiol groups making the side chains from adjacent layers staggered and thus sterically less contentious. The thiol groups of neighboring stacks just touch each other, and there is no interdigitation of the side groups along the long stacking axis in  $c$ -direction.

In order to validate our structure prediction, we calculate XRD patterns based on the optimized HT-HT crystal and compare them to experimentally observed XRD diffractograms (cf. Figure 5). Measurements were performed on two different samples. The first sample is the PTBT polymer film deposited

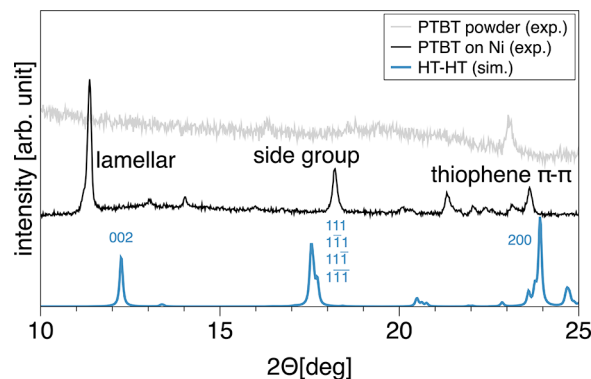


**Figure 5. Comparison between the simulated XRD pattern for the theoretical crystal structure of HT-HT (blue) and two experimentally observed diffractograms for the PTBT film on a nickel foam (black) and as a powder (gray). For the simulated spectrum, Miller indices ( $hkl$ ) are added to the main peaks.**

on a nickel surface, as it is prepared during the electropolymerization. With prolonged electropolymerization time, the PTBT film becomes thicker and looser, from which the outer layer is likely to fall off.<sup>22</sup> The detached part of the PTBT polymer (called ‘PTBT powder’) was collected as the second sample. The PTBT polymer attached to the nickel surface (black line) shows strong diffraction with clearly observable crystal peaks. In contrast, the PTBT powder sample (gray line) shows no distinct peaks except one centered at  $2\Theta = 23^\circ$ . For the ‘PTBT on Ni’ sample, we also observe strong peaks originating from the nickel itself (cf. Figure S9). Since these peaks occur at much higher Bragg angles ( $2\Theta > 40^\circ$ ), they are easily distinguishable from the polymer signals. For the simulated diffractogram (blue line in Figure 5), we can assign Miller indices of the crystal lattice planes to the main peaks. Comparing the simulated pattern against that of the polymer attached to nickel allows us to distinguish three regions. The first peak of the measured pattern at around  $2\Theta = 11.4^\circ$  is close to the secondary peak (002) of the theoretical one along the  $c$ -direction (long stacking axis). We, therefore, denote this as the lamellar peak. The next peak in the simulated diffractogram is a convolution of four different peaks originating from the planes defined by the four benzenethiol groups within the primitive cell (111,  $1\bar{1}1$ ,  $11\bar{1}$ , and  $1\bar{1}\bar{1}$ ). Hence, we suggest that the experimental peak at around  $2\Theta = 18.2^\circ$  stems from the reflections of the side groups. Lastly, we observe several signals at higher Bragg angles with two pronounced peaks at  $2\Theta = 21.3^\circ$  and  $23.6^\circ$  in the experimental spectrum. Using Bragg’s law  $n\lambda = 2d \sin(\Theta)$ , this corresponds to distances of  $d = [3.7, 4.1]$  Å which are in the range of typical  $\pi$ - $\pi$  stacking distances of similar polythiophene-based polymers.<sup>60–62</sup> The simulated spectrum also features a distinct peak at  $2\Theta = 23.9^\circ$ , corresponding to the stacking of thiophene backbones along the short  $a$ -axis. We can also relate the stacking distance  $d$  to the unit cell parameters by

$$\frac{1}{d^2} = \frac{h^2}{a^2} + \frac{k^2}{b^2} + \frac{l^2}{c^2} \quad (1)$$

with the Miller indices  $hkl$ . If we take the experimental peaks at  $11.4^\circ$  and  $23.6^\circ$  together with the Miller indices of the simulated pattern, we can get the lattice lengths  $a$  and  $c$ . The peak at  $18.2^\circ$  then gives us the lattice length  $b$ . From this, we calculate the following unit cell parameters based on the experimental diffractogram:  $a = 7.53 \text{ \AA}$ ,  $b = 7.01 \text{ \AA}$ , and  $c = 15.56 \text{ \AA}$ . Compared to the DFT results (cf. Table 1), this gives deviations of 1.1%, 11.6%, and 7.2% (for  $a$ ,  $b$ , and  $c$ , respectively).

The overall agreement with the simulated pattern suggests that the peaks of the PTBT-on-nickel sample mainly come from crystalline phases of chains with HT-HT regularity. The fact that the experimentally measured diffractogram can only be associated with the HT-HT crystal structure again emphasizes the importance of distinguishing between different regularities. Furthermore, the absence of crystallinity in the powder sample shows that, as the PTBT film becomes thicker during electropolymerization, its outer layers will lose most of its structural order. In the initial stage of electropolymerization, there is sufficient electrical contact between the polymer layers formed at the electrode surface. At this point, the polymer chains are short and efficient adhesion avoids twisting of the chains, forming higher regular and crystalline zones.<sup>63</sup> As polymerization proceeds, large polymer chains tend to form disordered amorphous domains that affect the microstructure of the film. As the number of cycles increases, the film gradually becomes thicker, with a dense and rough surface.<sup>64</sup> This is in agreement with similar electropolymerized thiophene-based polymers.<sup>60,65,66</sup> Only the peak at  $2\Theta = 23^\circ$  indicates that thiophene  $\pi$ - $\pi$  stacking will remain to some degree in the PTBT-powder sample.

Further, we looked at the electronic properties of the crystalline polymer phase. The band structure shows the HT-HT crystal to be a direct band gap semiconductor with a band gap of 0.58 eV at the  $\Gamma$ -point (cf. Figure 6). From the projected density of states (PDOS), we see that the shallow valence band and conduction band (CB) are mainly determined by the  $sp^2$ -hybridized carbon atoms within the

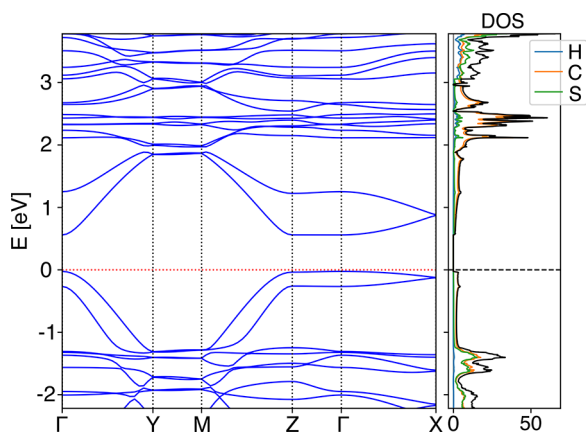


**Figure 6.** Band structure, DOS, and PDOS (hydrogen (H), carbon (C), and sulfur (S) are depicted with blue, orange, and green, respectively) for the HT-HT crystal. The band energies are shifted relative to the Fermi level. The Fermi level is indicated with a red dotted and gray dashed line.

thiophene rings. In contrast, the thiophene sulfur atoms only contribute to the latter. The width of the CB along the  $\Gamma Y$  direction (direction of the conjugated backbones) is four times larger than that along the  $\Gamma X$  direction (short stacking direction) (1.29 and 0.31 eV, respectively). The bandwidth is almost zero in the direction of the long stacking axis ( $\Gamma Z$ ). Large bandwidths are usually a characteristic feature of high mobility. Therefore, the band structure already suggests a two-dimensional charge transport with the main direction along the polymer backbones. Such a feature is typical for conjugated polymers which stack in a lamellar fashion.<sup>40,41,67</sup>

In order to investigate the HH-TT system, we cut out a representative subset of the cluster's center containing  $N = 23$  polymer chains (cf. Figure 3b, red shaded area). This subsystem is then again equilibrated over 5 ns using an NPT simulation at  $T = 300 \text{ K}$ . We randomly select five representative configurations for the electronic structure calculations from the last 10 ps of the equilibrated MD trajectory. The obtained MD structures are not further optimized with DFT but directly used due to the large system size. To estimate the band gap of the unordered HH-TT, we take an average over the values obtained from the five selected configurations. In Figure 7, the DOS of the crystalline HT-HT

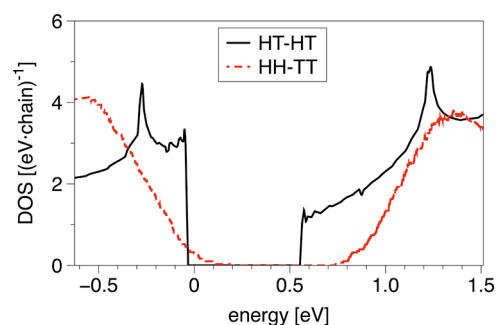


**Figure 7.** Comparison of the DOS of the crystalline HT-HT phase (black solid line) and the averaged DOS over five representative configurations of the unordered HH-TT phase (red dashed line).

phase is compared with the averaged one of the selected HH-TT systems. As can be seen, the band gap of the disordered HH-TT phase (red dashed line) is larger by 24% than that of the crystalline HT-HT aggregates (black solid line), mainly due to a shift of the CB edge toward higher energies. The band gap is  $E_g = 0.72 \pm 0.07 \text{ eV}$  for the HH-TT system.

When comparing the systems in Figure 3, it can be seen that the polymer backbones in the HH-TT phase exhibit greater deviations from planarity than those in the ordered HT-HT phase (cf. also Figure S7 for a quantitative analysis), which indicates a break in conjugation in the former. It has already been observed for similar conjugated polymers that the band gap of their amorphous phases is much higher compared to that in well-ordered domains,<sup>44,68</sup> which can be related to the reduced conjugation length (i.e., the length of periodicity<sup>69</sup>) along the polymer backbones of the amorphous phase. The DOS also displays a broadening of the tails near the band gap in the HH-TT system compared to the sharp band edges of the HT-HT phase. It is known that this broadening is caused by structural disorder, or so-called paracrystallinity,<sup>70,71</sup> in the  $\pi$ -stacks of the system and the width of the DOS tails is a measure for the energetic disorder, that is, variations in the energy levels across the material.<sup>68,72</sup>

Furthermore, the broadening induces electronic states within the band gap of the crystalline HT-HT phase. It has been shown that disorder in the  $\pi$ -stacks of conjugated polymer chains causes the creation of deep tails of electronic states, which are much more localized than states inside of the bands.<sup>37,73</sup> Thus, these states can act as traps for charge carriers, limiting their transport through the polymer.<sup>74,75</sup> Beyond the static disorder of the HH-TT phase, dynamic disorder, that is, structural fluctuations over time, might be even more crucial in this domain as the relative position of neighboring chains will significantly influence their electronic coupling.<sup>31</sup> The larger range of possible backbone dihedrals of HH-TT chains (cf. Figure S7) indicates an increased dynamic disorder in this phase compared to the HT-HT system.

Overall, the structural disorder in the HH-TT phase, caused by decreased packing efficiency, leads to an energetic disorder manifested in an enlarged band gap and the formation of potential trapping states within the band gap. In a heterogeneous microstructure where HT-HT and HH-TT phases coexist, the ordered HT-HT regions would be largely responsible for charge transport. If the band gap offset between the two phases is large enough so that the energetic overlap of electronic states vanishes, charges would be hindered from migrating between disordered and ordered regions.<sup>68</sup> Charge carriers would then remain confined in the crystalline HT-HT phase.

Depending on the structural order of a material, one has to decide between different transport mechanisms. There is a wealth of literature on the topic of charge transport in molecular materials, but generally, one distinguishes two limiting regimes of band transport and charge hopping.<sup>76</sup> Building on Bloch's theorem,<sup>77,78</sup> which describes very delocalized charge carriers, band-like approaches are by construction restricted to ordered and defect-free crystals. In our case, we will hence apply this 'band' picture only to the crystalline HT-HT phase. Given the morphological disorder of the HH-TT system, it is more appropriate to describe the charge transport herein either with a hopping model,<sup>79,80</sup> assuming the charges to be localized on discrete sites or by trapping and releasing from localized states into higher energy mobile states.<sup>81–83</sup> It should be noted that the models mentioned above still rely heavily on assumptions limiting their applicability, especially when it comes to intermediate cases of charge transport, which do not adhere to the limiting regimes.<sup>76</sup> The development of methods<sup>84–86</sup> that bridge the gap between these regimes to advance the understanding of charge transport in organic semiconducting materials is an ongoing field.

**Band-like Charge Transport in the HT-HT Phase.** As a quantitative approach to estimate the intrinsic limits of charge transport in the PTBT polymer, we describe the charge transport in the HT-HT crystal within the band transport regime. The constant relaxation time approximation of the Boltzmann transport equation<sup>87,88</sup> (eq 3) is employed to calculate the electrical conductivity and mobility. We first compute the relaxation time within the deformation potential theory (cf. eqs S2, S6, and S7) are used to calculate the deformation potential  $D_{\text{def},ii}$  and the elastic constant  $C_i$  of the dilated unit cells along the three lattice directions ( $i = a, b,$  and  $c$ ), respectively. With eq S8, we also compute the transport effective masses of the CB at its extrema. With these three parameters at hand, we obtain the electron/acoustic phonon scattering relaxation time  $\tau_{ii}$  at 300 K.

From the results in Table 2, we see that the band structure's anisotropy also manifests itself in the charge transfer

**Table 2.** Calculated Deformation Potential  $D_{\text{def},ii}$  (in eV), Elastic Constant  $C_i$ , Effective Transport Mass  $m_{\text{eff}}$ , and Relaxation Time  $\tau_{ii}$  along the Three Lattice Directions ( $i = a, b,$  and  $c$ ) at 300 K

crystal direction $i$	$D_{\text{def},ii}$ (eV)	$C_i$ (eV/Å)	$m_{\text{eff}}$ ( $m_e$ )	$\tau_{ii}$ (fs)
$a$	2.02	9.87	1.80	8.12
$b$	0.40	93.61	0.14	$7.71 \times 10^3$
$c$	0.14	9.76	96.12	$2.37 \times 10^2$

properties. The flat CB along the  $c$ -axis ( $\Gamma Z$ ) leads to a very high effective mass ( $m_{\text{eff}} = 96.12m_e$ ) compared to the other two directions with a modest ( $\Gamma X$ ) and high band dispersion ( $\Gamma Y$ , cf. Figure 6). The elastic constant along the conjugated backbone in the  $b$ -direction is 1 order of magnitude higher than along the directions where the polymer chains are only bound by dispersive forces. Interestingly, the deformation potential, which describes the interaction strength of the charge carrier with the acoustic phonons, is largest for the transport along the  $a$ -axis with the tightly stacked thiophene backbones. The van der Waals interactions between neighboring chains which mainly govern the crystal structure in  $a$ - and  $c$ -directions are strongest in the direction of the  $\pi$ - $\pi$  stacking of neighboring thiophene backbones. Thus, the total energy is more prone to structural deformations along the short stacking axis. This, in turn, leads then to a very short relaxation time along  $a$  of only a few femtoseconds. In comparison, the relaxation time along the conjugated backbone is 3 orders of magnitude higher, which shows that charge carriers can move relatively freely through the extended  $\pi$ -electron system along the backbone.

With the band structure and the relaxation times, we can calculate the electrical conductivity  $\sigma$  in dependency of the charge carrier concentration  $N$  (by varying the chemical potential  $\mu_{\text{chem}}$ ) according to eq 3. In Figure 8, we plot the conductivity  $\sigma_a(N)$  (black solid line),  $\sigma_b(N)$  (blue solid line), and  $\sigma_c(N)$  (red solid line) along the  $a$ -,  $b$ -, and  $c$ -directions,

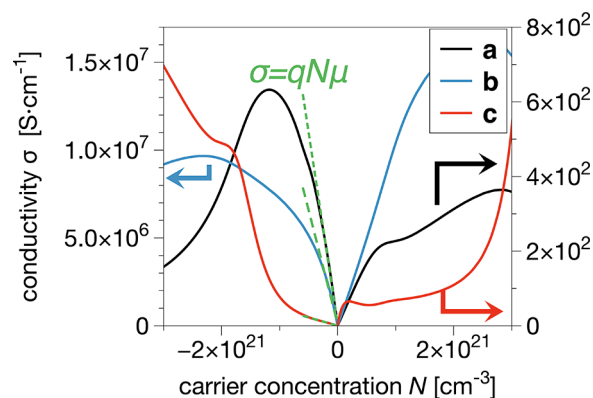


**Figure 8.** Plot of the band-like conductivity  $\sigma_a$  (black solid line),  $\sigma_b$  (blue solid line), and  $\sigma_c$  (red solid line) along the  $a$ ,  $b$ , and  $c$  directions, respectively, as a function of the charge carrier concentration  $N$  (the colored arrows associate the lines to their corresponding scales on the  $y$ -axis). The slope of the positive (negative) linear region of the conductivity over  $N$  gives the hole (electron) mobility according to eq 2 (green dashed lines, shown here for negative  $N$ ).

respectively. As the chemical potential shifts, the dominant charge carriers change from electrons (negative  $x$ -axis) to holes (positive  $x$ -axis). A negative (positive) charge carrier concentration  $N$  resembles then n-type (p-type) doping of the polymer.

The electrical conductivity is apparently anisotropic. Along the conjugated backbones ( $b$ -direction),  $\sigma_b$  is 5 orders of magnitude larger than  $\sigma_a$  along the  $\pi$ - $\pi$  stacking axis of the thiophene backbones and  $\sigma_c$  along the lamellar stacking (note the different scales on the  $y$ -axis in Figure 8). For a vanishing charge carrier concentration, we see that the intrinsic conductivity is zero in all cases, which is typical for semiconducting materials. Due to the system's band gap, no thermally excited charge carriers contribute to conduction. This shows that an optimized doping state is crucial to guarantee the high conductivity of the system. Therefore, one would have to reduce the PTBT polymer to decrease or oxidate to increase the amount of doped anions. By comparing  $\sigma_b$  along the main transport direction for positive and negative  $N$ , we see that p-doping is favorable compared to n-doping since it leads to higher conductivities. This is the opposite for charge transport along the  $a$ - and  $c$ -directions.

Finally, we can determine the mobilities for charge transport along individual lattice directions by fitting the linear regions in Figure 8 according to eq 2. The mobility is given here by the slope of the linear fit. We calculate the electron mobilities as  $\mu_a = 6.4 \text{ cm}^2/(\text{V s})$ ,  $\mu_b = 8.1 \times 10^4 \text{ cm}^2/(\text{V s})$ , and  $\mu_c = 0.3 \text{ cm}^2/(\text{V s})$ . Again, the mobility along the polymer chains is much higher than in the other two directions. Although intrachain charge transport is expected to be faster than transport between different chains, the interchain charge transfer between backbones is known to be crucial for transport in a real polymeric system since macroscopic transport can not only be provided by single chains.<sup>89,90</sup> The mobilities along the latter two directions are already at the lower end of the range where the picture of band-like charge transport is valid.<sup>76</sup> Such anisotropic behavior has also been experimentally observed for polythiophene-based polymers.<sup>91–93</sup> For instance, a high mobility anisotropy of  $\mu_{\parallel}/\mu_{\perp} \approx 1000$  (where  $\mu_{\parallel}$  and  $\mu_{\perp}$  are the field-effect mobility along and orthogonal to the backbone orientation direction, respectively) was reported for highly oriented films of PBTBT.<sup>94</sup> A similar anisotropy of the mobility of  $4 \times 10^3$  was found in poly(3-octylthiophene) single crystals.<sup>95</sup> Yu et al. reported a mobility of up to  $2.3 \text{ cm}^2/(\text{V s})$  along the  $\pi$ -stacking direction of mesocrystalline P3HT.<sup>96</sup> Luo et al. measured interchain mobilities along the  $\pi$ - $\pi$  stacking direction of  $1\text{--}2 \text{ cm}^2/(\text{V s})$  for highly oriented nanocrystalline thiophene-based polymers.<sup>91</sup> Overall, the agreement of our results with recent experimental values shows that a band-like description is able to explain the charge transport in well-ordered polymer systems.

As discussed, introducing disorder in crystalline structures can negatively affect their charge transport by introducing defects into the crystal lattice, causing domain boundaries and decreasing packing efficiency. Therefore, our results are an estimate of what might be ultimately achievable in a highly crystalline, defect-free polymer. An interesting aspect to investigate in future studies is to quantitatively assess the charge transport properties of the disordered phase as well. This, of course, necessitates an adequate theoretical model which accounts for any of the above-mentioned structural deviations from the well-ordered case. Another direction would be the band gap engineering of the system, for example, by

explicit doping with ions to further improve the polymer's transport properties.<sup>97,98</sup>

## CONCLUSIONS

In this study, we used a multiscale modeling approach to explore charge transport in conjugated organosulfur polymers for Li–S batteries. In particular, the focus has been set on the PTBT polymer, which has been extensively studied as an alternative cathode material.<sup>22,25</sup> By using classical MD, for which we reparametrized important force field parameters based on DFT calculations, we simulated the self-assembled aggregation of polymer chains with different regioregularity. We found that the polymer chains can form crystalline phases only for a regioregular head-to-tail/head-to-tail (HT-HT) regularity, whereas for a head-to-head/tail-to-tail (HH-TT) regularity, the system did not show any long-range order after annealing. We can explain this structural difference by the increased steric constraints between neighboring TBT units within individual polymer chains in the HH-TT phase. Experimental XRD measurements confirmed the existence of crystalline phases in the electropolymerized PTBT, which we can relate to our predicted HT-HT crystal structure. We employed electronic structure theory to calculate the band structure and DOS of the different structural phases. It was observed that the polymer shows a semiconducting behavior. Further, we observed how the structural disorder in the HH-TT phase leads to an energetic disorder that can potentially limit the charge transport herein. Our calculations of conductivity as a function of charge carrier density offer a quantitative approach to estimating the intrinsic limit of the band-like mobility of the HT-HT phase along its crystal directions. Our results are in agreement with recent mobility measurements of similar crystalline thiophene-based polymers.

This study provides insights into the complex interplay between the microstructure and electrical properties of conjugated polymers, which serve as the cathode material for Li–S batteries. Specifically, the effects of polymer chain regioregularity on the morphology and the polymer's electronic structure and charge transfer properties are demonstrated. Our work thus highlights the importance of polymer regularity and morphology modifications to design high-mobility crystalline phases, which would optimize the electrochemical performance of the cathode material. Work is in progress to extend our model to more realistic cathode structures and geometries, for example, including the influence of cross-linking sulfur between polymer chains as well as the solvent and electrolyte degrees of freedom. Hence, our study prepares future work on the described Li–S battery system.

## METHODS

**Synthesis of PTBT.** The monomer 4-(thiophen-3-yl)benzenethiol (TBT) was polymerized on a nickel foam (NF) with a thickness of 0.5 mm using a solution electrolyte of 0.1 M tetrabutylammonium hexafluorophosphate (TBAPF6) in acetonitrile (ACN). The electropolymerization process was carried out using a three-electrode system under potential range of  $-1.8\text{--}1.8 \text{ V}$  ( $100 \text{ mV/s}$ ,  $n = 20$ ) with an electrochemical workstation (GAMRY). An Ag wire was used as the reference electrode, and a platinum wire as the counter electrode. The resulting red-brown PTBT@NF electrode was obtained after rinsing the polymerized electrode with acetonitrile several times and drying it in a vacuum oven at  $50 \text{ }^\circ\text{C}$ . During electropolymerization, the outer parts of the polymer detached from the electrode and were collected in the reaction vessel. After the polymerization reaction, the detached polymer was separated from the reaction medium (TBT and TBAPF6

in ACN) through 3 cycles of centrifugation using fresh acetonitrile to wash. After that, the remaining powdered PTBT polymer was dried in the same way as the one deposited on the nickel foam.

**XRD Characterization.** X-ray diffraction (XRD) data were collected at Bruker D8 Advance for powder diffraction hosted by the HZB X-ray Corelab. The instrument makes use of a focusing X-ray beam consisting of characteristic copper wavelengths  $K\alpha_{1+2}$  and is equipped with a 1D LynxEye detector for fast powder diffraction data collection. Samples were prepared in a 9-fold sample flip-stick. Applied measuring time was 4 h per sample with a step size of  $0.02^\circ$  in the range of  $10\text{--}130^\circ$  for  $2\Theta$ . All measurements were carried out under ambient conditions.

**MD Simulations.** Our systems are simulated on an *all-atom level* using the large-scale atomic/molecular massively parallel simulator package<sup>99</sup> in combination with the OPLS force field.<sup>100,101</sup> Details on the Hamiltonian of the force field and its adjustments regarding our specific system can be found in ref 48 and the Supporting Information (SI). The simulations are performed in an isothermal–isobaric (*NPT*) ensemble with periodic boundary conditions. The temperature and pressure are held constant with a Nosé–Hoover thermostat and barostat<sup>102</sup> with a relaxation time of 100 and 1000 fs, respectively. The pressure is set to 1 bar.

We used a steepest descent algorithm to optimize the single chains. We also allowed the simulation box to relax in the periodic direction of the chains. In the other two directions, we set the box length to 40 Å to ensure a large distance between the periodic images of the chains. The aggregation process was explored using temperature annealing followed by an equilibrium simulation for a total period of 10 ns. To enhance the conformational sampling, the runs were started at an artificially high temperature of 1500 K and are then cooled down to 300 K (cooling rate of 0.12 K/ps). A time step of 1 fs was used in all simulations. The initial systems of  $N = 100$  chains were set in orthogonal boxes, and during the run, we only applied the barostat to the *b*-direction of the box. After the initial *NPT* simulations, we took out representative subsets from the center of the resulting clusters to prepare another set of simulation cells. These systems were again equilibrated in an *NPT* ensemble simulation for 5 ns at  $T = 300$  K. This time, we applied the barostat to all dimensions, and we also allowed the simulation boxes to adopt a triclinic shape.

**Electronic Structure Calculations.** Electronic structure calculations are done at DFT level<sup>103</sup> using the all-electron, full-potential density-theory package FHI-aims.<sup>104–106</sup> The exchange–correlation interactions were treated using the Perdew–Burke–Erzerhof (PBE) functional<sup>107</sup> together with the many-body dispersion (MBD) method<sup>108</sup> to account for long-range van der Waals interactions. For comparison, we also used the hybrid PBE0 functional.<sup>109</sup> The FHI-aims-specific tier 2 basis set and tight settings have been used. The convergence criterion for the total energy was set to  $10^{-5}$  eV.

A  $\Gamma$ -centered  $k$ -grid of  $1 \times 8 \times 1$  was used for the optimization of the single chain structures and that of  $8 \times 8 \times 4$  for the optimization of the HT-HT crystal unit cell. The band structure of the HT-HT crystal was calculated on a finer  $k$  of  $32 \times 32 \times 12$ . For the bigger HH-TT supercells, a coarse  $k$ -grid of  $1 \times 8 \times 1$  was used.

**Charge Transport Calculations.** In general, the electrical conductivity of any material is determined by the concentration of mobile charge carriers  $N$  and their mobility  $\mu$  by

$$\sigma = qN\mu \quad (2)$$

where  $q$  is the charge of the carrier. We model the charge transport of PTBT in the crystalline HT-HT phase using the Boltzmann transport equation:<sup>87,88</sup>

$$\sigma = e^2 \sum_{\mathbf{k}} \left( -\frac{\partial f(\epsilon_{\mathbf{k}})}{\partial \epsilon_{\mathbf{k}}} \right) \mathbf{v}_{\mathbf{k}} \mathbf{v}_{\mathbf{k}} \tau_{\mathbf{k}} \quad (3)$$

where  $f(\epsilon_{\mathbf{k}}) = 1/(e^{(\epsilon_{\mathbf{k}} - \epsilon_F)/k_B T} + 1)$  is the Fermi–Dirac distribution function,  $\mathbf{v}_{\mathbf{k}} = \nabla_{\mathbf{k}} \epsilon_{\mathbf{k}}/\hbar$ , the group velocity of a charge carrier in a given band,  $\epsilon_{\mathbf{k}}$  is the band energy at a given  $\mathbf{k}$ -point,  $\epsilon_F$  is the Fermi-energy (the chemical potential at  $T = 0$  K),  $k_B$  is the Boltzmann constant, and  $T$  the temperature. This equation describes the steady-state

distribution of charge carriers in an electric field, considering the acceleration of the charges by the field and the restoration of the distribution through collisions with phonons and impurities.<sup>110</sup> The so-called relaxation time  $\tau_{\mathbf{k}}$  describes the average time between these scattering events.<sup>88</sup> In the crystalline phase of the polymer, we can neglect the influence of impurities and consider only scattering events with acoustic phonons,<sup>88</sup> using the deformation potential theory<sup>111</sup> to calculate the relaxation time along a crystal direction. The necessary parameters to assess the relaxation time can be determined by parabolic and linear fitting procedures.<sup>112,113</sup> Together with the band structure of the system and for a given temperature, one can calculate the conductivity as a function of the charge carrier concentration by varying the chemical potential (more details on the derivation and the numerical schemes can be found in eqs S1–S11 of the SI).

## ASSOCIATED CONTENT

### Supporting Information

The Supporting Information is available free of charge at <https://pubs.acs.org/doi/10.1021/acsnano.3c01523>.

Computational details of the charge transport property calculations. Force field dihedral reparametrization and validation. Structural properties of single PTBT chains. Aggregation behavior: Annealing and crystal growth. Structural analysis of the HT-HT and HH-TT phase. Calculation of the deformation potential and elastic constant. X-ray diffractogram of the PTBT polymer attached to nickel. Geometry of the optimized HT-HT crystal structure (PDF)

## AUTHOR INFORMATION

### Corresponding Author

Joachim Dzubiella – Research Group for Simulations of Energy Materials, Helmholtz-Zentrum Berlin für Materialien und Energie GmbH, 14109 Berlin, Germany; Applied Theoretical Physics - Computational Physics, Physikalisches Institut, Albert-Ludwigs-Universität Freiburg, 79104 Freiburg, Germany; [orcid.org/0000-0001-6751-1487](https://orcid.org/0000-0001-6751-1487); Email: [joachim.dzubiella@helmholtz-berlin.de](mailto:joachim.dzubiella@helmholtz-berlin.de), [joachim.dzubiella@physik.uni-freiburg.de](mailto:joachim.dzubiella@physik.uni-freiburg.de)

### Authors

Yannik Schütze – Research Group for Simulations of Energy Materials, Helmholtz-Zentrum Berlin für Materialien und Energie GmbH, 14109 Berlin, Germany; Theoretical Chemistry, Institute of Chemistry and Biochemistry, Freie Universität Berlin, 14195 Berlin, Germany; [orcid.org/0000-0002-7934-0969](https://orcid.org/0000-0002-7934-0969)

Diptesh Gayen – Applied Theoretical Physics - Computational Physics, Physikalisches Institut, Albert-Ludwigs-Universität Freiburg, 79104 Freiburg, Germany; [orcid.org/0000-0001-9054-5685](https://orcid.org/0000-0001-9054-5685)

Karol Palczynski – Research Group for Simulations of Energy Materials, Helmholtz-Zentrum Berlin für Materialien und Energie GmbH, 14109 Berlin, Germany; [orcid.org/0000-0003-2979-4281](https://orcid.org/0000-0003-2979-4281)

Ranielle de Oliveira Silva – Department Electrochemical Energy Storage, Helmholtz-Zentrum Berlin für Materialien und Energie GmbH, 14109 Berlin, Germany

Yan Lu – Department Electrochemical Energy Storage, Helmholtz-Zentrum Berlin für Materialien und Energie GmbH, 14109 Berlin, Germany; Institute of Chemistry, University of Potsdam, 14469 Potsdam, Germany; [orcid.org/0000-0003-3055-0073](https://orcid.org/0000-0003-3055-0073)

Michael Tovar – Department Structure and Dynamics of Energy Materials, Helmholtz-Zentrum Berlin für Materialien und Energie GmbH, 14109 Berlin, Germany

Pouya Partovi-Azar – Institute for Chemistry, Martin Luther Universität Halle-Wittenberg, 06120 Halle (Saale), Germany; [orcid.org/0000-0001-5568-1315](https://orcid.org/0000-0001-5568-1315)

Annika Bande – Theory of Electron Dynamics and Spectroscopy, Helmholtz-Zentrum Berlin für Materialien und Energie GmbH, 14109 Berlin, Germany; [orcid.org/0000-0003-3827-9169](https://orcid.org/0000-0003-3827-9169)

Complete contact information is available at:  
<https://pubs.acs.org/10.1021/acsnano.3c01523>

## Notes

Schütze, Y.; Gayen, D.; Palczynski, K.; de Oliveira Silva, R.; Lu, Y.; Tovar, M.; Partovi-Azar, P.; Bande, A.; Dzubilla, J. How Regiochemistry Influences Aggregation Behavior and Charge Transport in Conjugated Organosulfur Polymer Cathodes for Lithium–Sulfur Batteries. *ChemRxiv*, 2023. <https://chemrxiv.org/engage/chemrxiv/article-details/63ea5cc79da0bc6b33dd0b71> (accessed March 28, 2023).

The authors declare no competing financial interest.

## ACKNOWLEDGMENTS

The authors thank V. G. Ruiz and S. Groh for helpful discussions. We thank the HPC Service of ZEDAT (Curta<sup>14</sup>), Freie Universität Berlin, for computing time. We acknowledge funding of the project through the Priority Programme “Polymer-based batteries” of the Deutsche Forschungsgemeinschaft (DFG) (SPP 2248, project number 441211139). P.P.-A. gratefully acknowledges DFG funding via projects PA3141/3 (project number 420536636) and PA3141/5 (project number 446879138).

## ABBREVIATIONS

MD, molecular dynamics; DFT, density functional theory; XRD, X-ray diffraction; TBT, 4-(thiophene-3-yl)benzenethiol; PTBT, poly(4-(thiophene-3-yl)benzenethiol); PBTBT, poly(2,5-bis(3-alkylthiophen-2-yl)thieno[3,2-b]-thiophene); P3HT, poly(3-hexylthiophene); OPLS, optimized potentials for liquid simulations; NPT, isothermal–isobaric ensemble; PBE, Perdew–Burke–Ernzerhof functional; PBE0, Perdew–Burke–Ernzerhof zero functional; MBD, many-body dispersion; HT, head-to-tail; HH, head-to-head; TT, tail-to-tail; HT-HT, head-to-tail/head-to-tail; HH-TT, head-to-head/tail-to-tail; DOS, density of states; PDOS, partial density of states; RBA, rigid band approximation; SP, single point; FF, force field; RB, Ryckaert–Bellmanns; PBC, periodic boundary conditions; RR, regioregular

## REFERENCES

- (1) Goodenough, J. B.; Kim, Y. Challenges for Rechargeable Li Batteries. *Chem. Mater.* **2010**, *22*, 587–603.
- (2) Manthiram, A.; Fu, Y.; Su, Y.-S. In Charge of the World: Electrochemical Energy Storage. *J. Phys. Chem. Lett.* **2013**, *4*, 1295–1297.
- (3) Fotouhi, A.; Auger, D. J.; Propp, K.; Longo, S.; Wild, M. A Review on Electric Vehicle Battery Modelling: From Lithium-ion Toward Lithium-Sulphur. *Renewable Sustainable Energy Rev.* **2016**, *56*, 1008–1021.
- (4) Lochala, J.; Liu, D.; Wu, B.; Robinson, C.; Xiao, J. Research Progress Toward the Practical Applications of Lithium-Sulfur Batteries. *ACS Appl. Mater. Interfaces* **2017**, *9*, 24407–24421.

- (5) Fotouhi, A.; Auger, D. J.; O'Neill, L.; Cleaver, T.; Walus, S. Lithium-Sulfur Battery Technology Readiness and Applications-A Review. *Energies* **2017**, *10*, 1937.

- (6) Zuckerman, J. J.; Hagen, A. P. *Inorganic Reactions and Methods: Oligomerization and Polymerization Formation of Intercalation Compounds*; John Wiley & Sons: New York, 1990; Vol. 17; pp 53–53.

- (7) Diao, Y.; Xie, K.; Xiong, S.; Hong, X. Shuttle Phenomenon – The Irreversible Oxidation Mechanism of Sulfur Active Material in Li-S Battery. *J. Power Sources* **2013**, *235*, 181–186.

- (8) Kaloni, T. P.; Giesbrecht, P. K.; Schreckenbach, G.; Freund, M. S. Polythiophene: From Fundamental Perspectives to Applications. *Chem. Mater.* **2017**, *29*, 10248–10283.

- (9) Swager, T. M. 50th Anniversary Perspective: Conducting/Semiconducting Conjugated Polymers. A Personal Perspective on the Past and the Future. *Macromolecules* **2017**, *50*, 4867–4886.

- (10) Lu, H.; Li, X.; Lei, Q. Conjugated Conductive Polymer Materials and Its Applications: A Mini-Review. *Front. Chem.* **2021**, *9*, 732132.

- (11) Palani, P.; Karpagam, S. Conjugated Polymers - a Versatile Platform for Various Photophysical, Electrochemical and Biomedical Applications: A Comprehensive Review. *New J. Chem.* **2021**, *45*, 19182–19209.

- (12) Manthiram, A.; Fu, Y.; Chung, S.-H.; Zu, C.; Su, Y.-S. Rechargeable Lithium–Sulfur Batteries. *Chem. Rev.* **2014**, *114*, 11751–11787.

- (13) Chen, X.; Wang, Y.; Wang, J.; Liu, J.; Sun, S.; Zhu, L.; Ma, Q.; Zhu, N.; Wang, X.; Chen, J.; Yan, W. A COF-Like Conductive Conjugated Microporous Poly(Aniline) Serving as a Current Collector Modifier for High-Performance Li-S Batteries. *J. Mater. Chem. A* **2022**, *10*, 1359–1368.

- (14) Partovi-Azar, P. Sulfur/Polyacrylonitrile-Based N-Terminated Graphene Nanoribbon Cathodes for Li-S Batteries. *Phys. Rev. Appl.* **2022**, *18*, 044072.

- (15) Yang, Y.; Yu, G.; Cha, J. J.; Wu, H.; Vosgueritchian, M.; Yao, Y.; Bao, Z.; Cui, Y. Improving the Performance of Lithium-Sulfur Batteries by Conductive Polymer Coating. *ACS Nano* **2011**, *5*, 9187–9193.

- (16) Xiao, L.; Cao, Y.; Xiao, J.; Schwenzler, B.; Engelhard, M. H.; Saraf, L. V.; Nie, Z.; Exarhos, G. J.; Liu, J. A Soft Approach to Encapsulate Sulfur: Polyaniline Nanotubes for Lithium-Sulfur Batteries with Long Cycle Life. *Adv. Mater.* **2012**, *24*, 1176–1181.

- (17) Liu, J.; Wang, M.; Xu, N.; Qian, T.; Yan, C. Progress and Perspective of Organosulfur Polymers as Cathode Materials for Advanced Lithium-Sulfur Batteries. *Energy Storage Mater.* **2018**, *15*, 53–64.

- (18) Liu, X.; Lu, Y.; Zeng, Q.; Chen, P.; Li, Z.; Wen, X.; Wen, W.; Li, Z.; Zhang, L. Trapping of Polysulfides with Sulfur-Rich Poly Ionic Liquid Cathode Materials for Ultralong-Life Lithium-Sulfur Batteries. *ChemSusChem* **2020**, *13*, 715–723.

- (19) Zhang, Q.; Huang, Q.; Hao, S. M.; Deng, S.; He, Q.; Lin, Z.; Yang, Y. Polymers in Lithium-Sulfur Batteries. *Adv. Sci.* **2022**, *9*, 2270008.

- (20) Kim, H.; Lee, J.; Ahn, H.; Kim, O.; Park, M. J. Synthesis of Three-Dimensionally Interconnected Sulfur-Rich Polymers for Cathode Materials of High-Rate Lithium–Sulfur Batteries. *Nat. Commun.* **2015**, *6*, 7278.

- (21) Zhao, F.; Li, Y.; Feng, W. Recent Advances in Applying Vulcanization/Inverse Vulcanization Methods to Achieve High-Performance Sulfur-Containing Polymer Cathode Materials for Li-S Batteries. *Small Methods* **2018**, *2*, 1800156.

- (22) Ning, J.; Yu, H.; Mei, S.; Schütze, Y.; Risse, S.; Kardjilov, N.; Hilger, A.; Manke, I.; Bande, A.; Ruiz, V. G.; Dzubilla, J.; Meng, H.; Lu, Y. Constructing Binder- and Carbon Additive-Free Organosulfur Cathodes Based on Conducting Thiol-Polymers through Electropolymerization for Lithium-Sulfur Batteries. *ChemSusChem* **2022**, *15*, No. e202200434.

- (23) Chung, W. J.; Griebel, J. J.; Kim, E. T.; Yoon, H.; Simmonds, A. G.; Ji, H. J.; Dirlam, P. T.; Glass, R. S.; Wie, J. J.; Nguyen, N. A.; Guralnick, B. W.; Park, J.; Somogyi, Á.; et al. The Use of Elemental

Sulfur as an Alternative Feedstock for Polymeric Materials. *Nat. Chem.* **2013**, *5*, 518–524.

(24) Dirlam, P. T.; Simmonds, A. G.; Kleine, T. S.; Nguyen, N. A.; Anderson, L. E.; Klever, A. O.; Florian, A.; Costanzo, P. J.; Theato, P.; Mackay, M. E.; Glass, R. S.; Char, K.; Pyun, J. Inverse Vulcanization of Elemental Sulfur with 1,4-Diphenylbutadiyne for Cathode Materials in Li-S Batteries. *RSC Adv.* **2015**, *5*, 24718–24722.

(25) Schütze, Y.; de Oliveira Silva, R.; Ning, J.; Rappich, J.; Lu, Y.; Ruiz, V. G.; Bande, A.; Dzubiella, J. Combined First-Principles Statistical Mechanics Approach to Sulfur Structure in Organic Cathode Hosts for Polymer Based Lithium-Sulfur (Li-S) Batteries. *Phys. Chem. Chem. Phys.* **2021**, *23*, 26709–26720.

(26) Kiani, R.; Sebastiani, D.; Partovi-Azar, P. On the Structure of Sulfur/1,3-Diisopropenylbenzene Co-Polymer Cathodes for Li-S Batteries: Insights from Density-Functional Theory Calculations. *ChemPhysChem* **2022**, *23*, No. e202100519.

(27) Skotheim, T. A.; Reynolds, J. *Conjugated Polymers: Theory, Synthesis, Properties, and Characterization*, 3rd ed.; Taylor and Francis: Boca Raton, 2006; pp 1–49.

(28) Okamoto, K.; Luscombe, C. K. Controlled Polymerizations for the Synthesis of Semiconducting Conjugated Polymers. *Polym. Chem.* **2011**, *2*, 2424–2434.

(29) Xu, P.; Han, X.; Zhang, B.; Du, Y.; Wang, H.-L. Multifunctional Polymer-Metal Nanocomposites via Direct Chemical Reduction by Conjugated Polymers. *Chem. Soc. Rev.* **2014**, *43*, 1349–1360.

(30) Kline, R. J.; McGehee, M. D. Morphology and Charge Transport in Conjugated Polymers. *J. Macromol. Sci., Polym. Rev.* **2006**, *46*, 27–45.

(31) Schmaltz, T.; Gothe, B.; Krause, A.; Leitherer, S.; Steinrück, H.-G.; Thoss, M.; Clark, T.; Halik, M. Effect of Structure and Disorder on the Charge Transport in Defined Self-Assembled Monolayers of Organic Semiconductors. *ACS Nano* **2017**, *11*, 8747–8757.

(32) Kukhta, N. A.; Luscombe, C. K. Gaining Control over Conjugated Polymer Morphology to Improve the Performance of Organic Electronics. *Chem. Commun.* **2022**, *58*, 6982–6997.

(33) Do, K.; Huang, D. M.; Faller, R.; Moulé, A. J. A Comparative MD Study of the Local Structure of Polymer Semiconductors P3HT and PBTTT. *Phys. Chem. Chem. Phys.* **2010**, *12*, 14735–14739.

(34) Poelking, C.; Daoulas, K.; Troisi, A.; Andrienko, D. In *P3HT Revisited – From Molecular Scale to Solar Cell Devices*; Ludwigs, S., Ed.; Springer: Berlin, Heidelberg, 2014; pp 139–180.

(35) Alberga, D.; Perrier, A.; Ciofini, I.; Mangiatordi, G. F.; Lattanzi, G.; Adamo, C. Morphological and Charge Transport Properties of Amorphous and Crystalline P3HT and PBTTT: Insights from Theory. *Phys. Chem. Chem. Phys.* **2015**, *17*, 18742–18750.

(36) Greco, C.; Melnyk, A.; Kremer, K.; Andrienko, D.; Daoulas, K. C. Generic Model for Lamellar Self-Assembly in Conjugated Polymers: Linking Mesoscopic Morphology and Charge Transport in P3HT. *Macromolecules* **2019**, *52*, 968–981.

(37) Rivnay, J.; Noriega, R.; Northrup, J. E.; Kline, R. J.; Toney, M. F.; Salleo, A. Structural Origin of Gap States in Semicrystalline Polymers and the Implications for Charge Transport. *Phys. Rev. B* **2011**, *83*, 121306.

(38) Poelking, C.; Cho, E.; Malafeev, A.; Ivanov, V.; Kremer, K.; Risko, C.; Brédas, J.-L.; Andrienko, D. Characterization of Charge-Carrier Transport in Semicrystalline Polymers: Electronic Couplings, Site Energies, and Charge-Carrier Dynamics in Poly(bithiophene-alt-thienothiophene) [PBTTT]. *J. Phys. Chem. C* **2013**, *117*, 1633–1640.

(39) Liu, T.; Troisi, A. Understanding the Microscopic Origin of the Very High Charge Mobility in PBTTT: Tolerance of Thermal Disorder. *Adv. Funct. Mater.* **2014**, *24*, 925–933.

(40) Shi, W.; Zhao, T.; Xi, J.; Wang, D.; Shuai, Z. Unravelling Doping Effects on PEDOT at the Molecular Level: From Geometry to Thermoelectric Transport Properties. *J. Am. Chem. Soc.* **2015**, *137*, 12929–12938.

(41) Franco-Gonzalez, J. F.; Zozoulenko, I. V. Molecular Dynamics Study of Morphology of Doped PEDOT: From Solution to Dry Phase. *J. Phys. Chem. B* **2017**, *121*, 4299–4307.

(42) Rolland, N.; Franco-Gonzalez, J. F.; Volpi, R.; Linares, M.; Zozoulenko, I. V. Understanding Morphology-Mobility Dependence in PEDOT:Tos. *Phys. Rev. Mater.* **2018**, *2*, 045605.

(43) Loewe, R. S.; McCullough, R. D. Effects of Structural Regularity on the Properties of Poly(3-Alkylthiophenevinylenes). *Chem. Mater.* **2000**, *12*, 3214–3221.

(44) McMahon, D. P.; Cheung, D. L.; Goris, L.; Dacuña, J.; Salleo, A.; Troisi, A. Relation between Microstructure and Charge Transport in Polymers of Different Regioregularity. *J. Phys. Chem. C* **2011**, *115*, 19386–19393.

(45) Coughlin, J. E.; Zhugayevych, A.; Wang, M.; Bazan, G. C.; Tretiak, S. Charge Delocalization Characteristics of Regioregular High Mobility Polymers. *Chem. Sci.* **2017**, *8*, 1146–1151.

(46) Ying, L.; Huang, F.; Bazan, G. C. Regioregular Narrow-Bandgap-Conjugated Polymers for Plastic Electronics. *Nat. Commun.* **2017**, *8*, 14047.

(47) Amna, B.; Siddiqi, H. M.; Hassan, A.; Ozturk, T. Recent Developments in the Synthesis of Regioregular Thiophene-Based Conjugated Polymers for Electronic and Optoelectronic Applications Using Nickel and Palladium-Based Catalytic Systems. *RSC Adv.* **2020**, *10*, 4322–4396.

(48) Gayen, D.; Schütze, Y.; Groh, S.; Dzubiella, J. Solvation Structure of Conjugated Organosulfur Polymers for Lithium-Sulfur Battery Cathodes. *ChemRxiv*, 2023. <https://chemrxiv.org/engage/chemrxiv/article-details/63ea00621d2d1840636905f3> (accessed March 28, 2023)

(49) Maior, R. M. S.; Hinkelmann, K.; Eckert, H.; Wudl, F. Synthesis and Characterization of Two Regiochemically Defined Poly-(dialkylbithiophenes): A Comparative Study. *Macromolecules* **1990**, *23*, 1268–1279.

(50) Hotta, S.; Rughooputh, S. D.; Heeger, A. J.; Wudl, F. Spectroscopic Studies of Soluble Poly(3-Alkylthiophenes). *Macromolecules* **1987**, *20*, 212–215.

(51) Hotta, S.; Soga, M.; Sonoda, N. Novel Organosynthetic Routes to Polythiophene and Its Derivatives. *Synth. Met.* **1988**, *26*, 267–279.

(52) Tsai, E. W.; Basak, S.; Ruiz, J. P.; Reynolds, J. R.; Rajeshwar, K. Electrochemistry of Some  $\beta$ -Substituted Polythiophenes: Anodic Oxidation, Electrochromism, and Electrochemical Deactivation. *J. Electrochem. Soc.* **1989**, *136*, 3683–3689.

(53) Hodge, P.; Hellwich, K. H.; Hiorns, R. C.; Jones, R. G.; Kahovec, J.; Luscombe, C. K.; Purbrick, M. D.; Wilks, E. S. A Concise Guide to Polymer Nomenclature for Authors of Papers and Reports in Polymer Science and Technology (IUPAC Technical Report). *Pure Appl. Chem.* **2020**, *92*, 797–813.

(54) Barbarella, G.; Bongini, A.; Zambianchi, M. Regiochemistry and Conformation of Poly(3-hexylthiophene) via the Synthesis and the Spectroscopic Characterization of the Model Configurational Triads. *Macromolecules* **1994**, *27*, 3039–3045.

(55) Kaloni, T. P.; Schreckenbach, G.; Freund, M. S. Band Gap Modulation in Polythiophene and Polypyrrole-Based Systems. *Sci. Rep.* **2016**, *6*, 1–18.

(56) Vikramaditya, T.; Saisudhakar, M.; Sumithra, K. A PBC-DFT Study of Electronic Properties of Substituted Polythiophenes. *J. Phys. Org. Chem.* **2015**, *28*, 695–702.

(57) Mehmood, U.; Al-Ahmed, A.; Hussein, I. A. Review on Recent Advances in Polythiophene Based Photovoltaic Devices. *Renewable Sustainable Energy Rev.* **2016**, *57*, 550–561.

(58) Palczynski, K.; Heibel, G.; Heyda, J.; Dzubiella, J. Growth and Characterization of Molecular Crystals of Para-Sexiphenyl by All-Atom Computer Simulations. *Cryst. Growth Des.* **2014**, *14*, 3791–3799.

(59) Huang, Y. C.; Lu, T. C.; Huang, C. I. Exploring the Correlation Between Molecular Conformation and UV-Visible Absorption Spectra of Two-Dimensional Thiophene-Based Conjugated Polymers. *Polymer* **2013**, *54*, 6489–6499.

(60) Tokuda, T.; Hoshino, K. Electropolymerized Films of 3-Methoxythiophene with a Potential Sweep-Induced Gold-Like Luster. *Polym. J. (Tokyo, Jpn.)* **2016**, *48*, 1141–1149.

- (61) Aasmundtveit, K.; Samuelsen, E.; Pettersson, L.; Ingas, O.; Johansson, T.; Feidenhans'l, R. Structure of Thin Films of Poly(3,4-ethylenedioxythiophene). *Synth. Met.* **1999**, *101*, 561–564.
- (62) Lebert, J.; Kratzer, E. M.; Bourdick, A.; Coric, M.; Gekle, S.; Herzig, E. M. Directing the Aggregation of Native Polythiophene During in Situ Polymerization. *ACS Omega* **2018**, *3*, 6388–6394.
- (63) Rendón-Enríquez, I.; Palma-Cando, A.; Körber, F.; Niebisch, F.; Forster, M.; Tausch, M. W.; Scherf, U. Thin Polymer Films by Oxidative or Reductive Electropolymerization and Their Application in Electrochromic Windows and Thin-Film Sensors. *Molecules* **2023**, *28*, 883.
- (64) Tassinari, F.; Amsellem, D.; Bloom, B. P.; Lu, Y.; Bedi, A.; Waldeck, D. H.; Gidron, O.; Naaman, R. Spin-Dependent Enantioselective Electropolymerization. *J. Phys. Chem. C* **2020**, *124*, 20974–20980.
- (65) Chen, S.; Luan, T.; Di, C.; Lu, M. H.; Yan, X. J.; Song, C.; Deng, T. Thickness Dependent Thermal Performance of a Poly(3,4-Ethylenedioxythiophene) Thin Film Synthesized: Via an Electrochemical Approach. *RSC Adv.* **2022**, *12*, 1897–1903.
- (66) Seki, Y.; Takahashi, M.; Takashiri, M. Effects of Different Electrolytes and Film Thicknesses on Structural and Thermoelectric Properties of Electropolymerized Poly(3,4-Ethylenedioxythiophene) Films. *RSC Adv.* **2019**, *9*, 15957–15965.
- (67) Johansson, E.; Larsson, S. Electronic Structure and Mechanism for Conductivity in Thiophene Oligomers and Regioregular Polymer. *Synth. Met.* **2004**, *144*, 183–191.
- (68) Noriega, R.; Rivnay, J.; Vandewal, K.; Koch, F. P.; Stingelin, N.; Smith, P.; Toney, M. F.; Salleo, A. A General Relationship Between Disorder, Aggregation and Charge Transport in Conjugated Polymers. *Nat. Mater.* **2013**, *12*, 1038–1044.
- (69) Kuzmany, H.; Kürti, J. The Physical Meaning of the Conjugation Length in Polymers. *Synth. Met.* **1987**, *21*, 95–102.
- (70) Bonart, R.; Hosemann, R.; McCullough, R. The Influence of Particle Size and Distortions upon the X-Ray Diffraction Patterns of Polymers. *Polymer* **1963**, *4*, 199–211.
- (71) Hindeleh, A. M.; Hosemann, R. Paracrystals Representing the Physical State of Matter. *J. Phys. C: Solid State Phys.* **1988**, *21*, 4155–4170.
- (72) Abutaha, A.; Kumar, P.; Yildirim, E.; Shi, W.; Yang, S. W.; Wu, G.; Hippalgaonkar, K. Correlating Charge and Thermoelectric Transport to Paracrystallinity in Conducting Polymers. *Nat. Commun.* **2020**, *11*, 1–8.
- (73) Street, R. A.; Northrup, J. E.; Salleo, A. Transport in Polycrystalline Polymer Thin-Film Transistors. *Phys. Rev. B* **2005**, *71*, 165202.
- (74) Salleo, A.; Chen, T. W.; Völkel, A. R.; Wu, Y.; Liu, P.; Ong, B. S.; Street, R. A. Intrinsic Hole Mobility and Trapping in a Regioregular Poly(thiophene). *Phys. Rev. B* **2004**, *70*, 115311.
- (75) Nenashev, A. V.; Valkovskii, V. V.; Oelerich, J. O.; Dvurechenskii, A. V.; Semeniuk, O.; Reznik, A.; Gebhard, F.; Baranovskii, S. D. Release of Carriers from Traps Enhanced by Hopping. *Phys. Rev. B* **2018**, *98*, 155207.
- (76) Oberhofer, H.; Reuter, K.; Blumberger, J. Charge Transport in Molecular Materials: An Assessment of Computational Methods. *Chem. Rev.* **2017**, *117*, 10319–10357.
- (77) Bloch, F. Über die Quantenmechanik der Elektronen in Kristallgittern. *Zeitschrift für Physik* **1929**, *52*, 555–600.
- (78) Kittel, C. *Introduction to Solid State Physics*, 8th ed.; John Wiley & Sons: New York, 2004; pp 167–168.
- (79) Marcus, R. A. On the Theory of Oxidation-Reduction Reactions Involving Electron Transfer. I. *J. Chem. Phys.* **1956**, *24*, 966–978.
- (80) Marcus, R. A. Electron Transfer Reactions in Chemistry. Theory and Experiment. *Rev. Mod. Phys.* **1993**, *65*, 599–610.
- (81) Mott, N. F. Conduction in Non-Crystalline Materials. *Philos. Mag.* **1969**, *19*, 835–852.
- (82) Vissenberg, M. C. J. M.; Matters, M. Theory of the Field-Effect Mobility in Amorphous Organic Transistors. *Phys. Rev. B* **1998**, *57*, 12964–12967.
- (83) Merlo, J. A.; Frisbie, C. D. Field Effect Transport and Trapping in Regioregular Polythiophene Nanofibers. *J. Phys. Chem. B* **2004**, *108*, 19169–19179.
- (84) Giannini, S.; Carof, A.; Blumberger, J. Crossover from Hopping to Band-Like Charge Transport in an Organic Semiconductor Model: Atomistic Nonadiabatic Molecular Dynamics Simulation. *J. Phys. Chem. Lett.* **2018**, *9*, 3116–3123.
- (85) Carof, A.; Giannini, S.; Blumberger, J. How to Calculate Charge Mobility in Molecular Materials from Surface Hopping Non-Adiabatic Molecular Dynamics - Beyond the Hopping/Band Paradigm. *Phys. Chem. Chem. Phys.* **2019**, *21*, 26368–26386.
- (86) Fratini, S.; Mayou, D.; Ciuchi, S. The Transient Localization Scenario for Charge Transport in Crystalline Organic Materials. *Adv. Funct. Mater.* **2016**, *26*, 2292–2315.
- (87) Harris, S. *An Introduction to the Theory of the Boltzmann Equation*, 1st ed.; Dover Publications: New York, 2004; pp 121–130.
- (88) Ziman, J. M. *Principles of the Theory of Solids*, 2nd ed.; Cambridge University Press: Cambridge, 1972; pp 211–230.
- (89) Kim, N.; Lee, B. H.; Choi, D.; Kim, G.; Kim, H.; Kim, J.-R.; Lee, J.; Kahng, Y. H.; Lee, K. Role of Interchain Coupling in the Metallic State of Conducting Polymers. *Phys. Rev. Lett.* **2012**, *109*, 106405.
- (90) Thomas, E. M.; Brady, M. A.; Nakayama, H.; Popere, B. C.; Segalman, R. A.; Chabiny, M. L. X-Ray Scattering Reveals Ion-Induced Microstructural Changes During Electrochemical Gating of Poly(3-Hexylthiophene). *Adv. Funct. Mater.* **2018**, *28*, 1803687.
- (91) Luo, C.; Kyaw, A. K. K.; Perez, L. A.; Patel, S.; Wang, M.; Grimm, B.; Bazan, G. C.; Kramer, E. J.; Heeger, A. J. General Strategy for Self-Assembly of Highly Oriented Nanocrystalline Semiconducting Polymers with High Mobility. *Nano Lett.* **2014**, *14*, 2764–2771.
- (92) Wang, Z.; Song, X.; Jiang, Y.; Zhang, J.; Yu, X.; Deng, Y.; Han, Y.; Hu, W.; Geng, Y. A Simple Structure Conjugated Polymer for High Mobility Organic Thin Film Transistors Processed from Nonchlorinated Solvent. *Adv. Sci.* **2019**, *6*, 1902412.
- (93) Lenz, J.; Weitz, R. T. Charge Transport in Semiconducting Polymers at the Nanoscale. *APL Mater.* **2021**, *9*, 110902.
- (94) Kumari, N.; Pandey, M.; Nagamatsu, S.; Nakamura, M.; Pandey, S. S. Investigation and Control of Charge Transport Anisotropy in Highly Oriented Friction-Transferred Polythiophene Thin Films. *ACS Appl. Mater. Interfaces* **2020**, *12*, 11876–11883.
- (95) Xiao, X.; Wang, Z.; Hu, Z.; He, T. Single Crystals of Polythiophene with Different Molecular Conformations Obtained by Tetrahydrofuran Vapor Annealing and Controlling Solvent Evaporation. *J. Phys. Chem. B* **2010**, *114*, 7452–7460.
- (96) Yu, L.; Pavlica, E.; Li, R.; Zhong, Y.; Silva, C.; Bratina, G.; Müller, C.; Amassian, A.; Stingelin, N. Conjugated Polymer Mesocrystals with Structural and Optoelectronic Coherence and Anisotropy in Three Dimensions. *Adv. Mater.* **2022**, *34*, 2103002.
- (97) Uejii, K.; Ohno, M.; Takeya, J.; Watanabe, S. Correlation Between Coherent Charge Transport and Crystallinity in Doped  $\pi$ -Conjugated Polymers. *Appl. Phys. Express* **2019**, *12*, 011004.
- (98) Yamashita, Y.; Tsurumi, J.; Kurosawa, T.; Uejii, K.; Tsuneda, Y.; Kohno, S.; Kempe, H.; Kumagai, S.; Okamoto, T.; Takeya, J.; Watanabe, S. Supramolecular Cocrystals Built Through Redox-Triggered Ion Intercalation in  $\pi$ -Conjugated Polymers. *Commun. Mater.* **2021**, *2*, 45.
- (99) Thompson, A. P.; Aktulga, H. M.; Berger, R.; Bolintineanu, D. S.; Brown, W. M.; Crozier, P. S.; in 't Veld, P. J.; Kohlmeyer, A.; Moore, S. G.; Nguyen, T. D.; Shan, R.; Stevens, M. J.; Tranchida, J.; Trott, C.; Plimpton, S. J. LAMMPS - A Flexible Simulation Tool for Particle-Based Materials Modeling at the Atomic, Meso, and Continuum Scales. *Comput. Phys. Commun.* **2022**, *271*, 108171.
- (100) Jorgensen, W. L.; Tirado-Rives, J. The OPLS [Optimized Potentials for Liquid Simulations] Potential Functions for Proteins, Energy Minimizations for Crystals of Cyclic Peptides and Crambin. *J. Am. Chem. Soc.* **1988**, *110*, 1657–1666.
- (101) Jorgensen, W. L.; Maxwell, D. S.; Tirado-Rives, J. Development and Testing of the OPLS All-Atom Force Field on Conforma-

tional Energetics and Properties of Organic Liquids. *J. Am. Chem. Soc.* **1996**, *118*, 11225–11236.

(102) Nosé, S. A Unified Formulation of the Constant Temperature Molecular Dynamics Methods. *J. Chem. Phys.* **1984**, *81*, 511–519.

(103) Kohn, W.; Sham, L. J. Self-Consistent Equations Including Exchange and Correlation Effects. *Phys. Rev.* **1965**, *140*, A1133–A1138.

(104) Blum, V.; Gehrke, R.; Hanke, F.; Havu, P.; Havu, V.; Ren, X.; Reuter, K.; Scheffler, M. Ab Initio Molecular Simulations with Numeric Atom-Centered Orbitals. *Comput. Phys. Commun.* **2009**, *180*, 2175–2196.

(105) Yu, V. W.-Z.; Corsetti, F.; García, A.; Huhn, W. P.; Jacquelin, M.; Jia, W.; Lange, B.; Lin, L.; Lu, J.; Mi, W.; Seifitokaldani, A.; Vázquez-Mayagoitia, A.; Yang, C.; Yang, H.; Blum, V. ELSI: A Unified Software Interface for Kohn–Sham Electronic Structure Solvers. *Comput. Phys. Commun.* **2018**, *222*, 267–285.

(106) Havu, V.; Blum, V.; Havu, P.; Scheffler, M. Efficient O(N) Integration for All-Electron Electronic Structure Calculation Using Numeric Basis Functions. *J. Comput. Phys.* **2009**, *228*, 8367–8379.

(107) Perdew, J. P.; Burke, K.; Ernzerhof, M. Generalized Gradient Approximation Made Simple. *Phys. Rev. Lett.* **1996**, *77*, 3865–3868.

(108) Ambrosetti, A.; Reilly, A. M.; DiStasio, R. A.; Tkatchenko, A. Long-Range Correlation Energy Calculated from Coupled Atomic Response Functions. *J. Chem. Phys.* **2014**, *140*, 18A508.

(109) Adamo, C.; Barone, V. Toward Reliable Density Functional Methods Without Adjustable Parameters: The PBE0 Model. *J. Chem. Phys.* **1999**, *110*, 6158–6170.

(110) Licker, M.; Hill, M. *McGraw-Hill Concise Encyclopedia of Physics*, 1st ed.; McGraw-Hill Book Company: New York, 2005; pp 70–75.

(111) Bardeen, J.; Shockley, W. Deformation Potentials and Mobilities in Non-Polar Crystals. *Phys. Rev.* **1950**, *80*, 72–80.

(112) Tang, L.; Long, M.; Wang, D.; Shuai, Z. The Role of Acoustic Phonon Scattering in Charge Transport in Organic Semiconductors: A First-Principles Deformation-Potential Study. *Sci. China, Ser. B: Chem.* **2009**, *52*, 1646–1652.

(113) Xi, J.; Long, M.; Tang, L.; Wang, D.; Shuai, Z. First-Principles Prediction of Charge Mobility in Carbon and Organic Nanomaterials. *Nanoscale* **2012**, *4*, 4348–4369.

(114) Bennett, L.; Melchers, B.; Proppe, B. Curta: A General-Purpose High-Performance Computer at ZEDAT, Freie Universität Berlin. *Refubium* 2020. <https://refubium.fu-berlin.de/handle/fub188/26993> (accessed April 4, 2023).

## Recommended by ACS

### An Investigation of Conjugated Sulfonamide Materials as Binders for Organic Lithium-Ion Batteries

Jiang Tian Liu, Dwight S. Seferos, *et al.*

NOVEMBER 09, 2023

CHEMISTRY OF MATERIALS

READ 

### Solvation Structure of Conjugated Organosulfur Polymers for Lithium–Sulfur Battery Cathodes

Diptesh Gayen, Joachim Dzubiella, *et al.*

JUNE 10, 2023

ACS APPLIED POLYMER MATERIALS

READ 

### Low-Cost Organodisulfide Polymer for Ultrafast High-Capacity Cathode Materials

Shao-Zhong Zeng, Peigang Han, *et al.*

AUGUST 14, 2023

ACS APPLIED ENERGY MATERIALS

READ 

### Evaluating the Impact of Conjugation Break Spacer Incorporation in Poly(3,4-propylenedioxythiophene)-Based Cathode Binders for Lithium-Ion Batteries

Pratyusha Das, Barry C. Thompson, *et al.*

JANUARY 31, 2024

CHEMISTRY OF MATERIALS

READ 

Get More Suggestions >

# Supporting Information:

## How Regiochemistry Influences Aggregation Behavior and Charge Transport in Conjugated Organosulfur Polymer Cathodes for Lithium-Sulfur Batteries

Yannik Schütze,<sup>†,‡</sup> Diptesh Gayen,<sup>¶</sup> Karol Palczynski,<sup>†</sup> Ranielle de Oliveira Silva,<sup>§</sup> Yan Lu,<sup>§,||</sup> Michael Tovar,<sup>⊥</sup> Pouya Partovi-Azar,<sup>#</sup> Annika Bande,<sup>@</sup> and Joachim Dzubiella<sup>\*,†,¶</sup>

<sup>†</sup>*Research Group for Simulations of Energy Materials, Helmholtz-Zentrum Berlin für Materialien und Energie GmbH, Hahn-Meitner-Platz 1, 14109 Berlin, Germany*

<sup>‡</sup>*Theoretical Chemistry, Institute of Chemistry and Biochemistry, Freie Universität Berlin, Arnimallee 22, 14195 Berlin, Germany*

<sup>¶</sup>*Applied Theoretical Physics - Computational Physics, Physikalisches Institut, Albert-Ludwigs-Universität Freiburg, Hermann-Herder-Straße 3, 79104 Freiburg, Germany*

<sup>§</sup>*Department Electrochemical Energy Storage, Helmholtz-Zentrum Berlin für Materialien und Energie GmbH, Hahn-Meitner-Platz 1, 14109 Berlin, Germany*

<sup>||</sup>*Institute of Chemistry, University of Potsdam, Am Neuen Palais 10, 14469 Potsdam, Germany*

<sup>⊥</sup>*Department Structure and Dynamics of Energy Materials, Helmholtz-Zentrum Berlin für Materialien und Energie GmbH, Hahn-Meitner-Platz 1, 14109 Berlin, Germany*

<sup>#</sup>*Institute for Chemistry, Martin Luther Universität Halle-Wittenberg, Von-Danckelmann-Platz 4, 06120 Halle (Saale), Germany*

<sup>@</sup>*Theory of Electron Dynamics and Spectroscopy, Helmholtz-Zentrum Berlin für Materialien und Energie GmbH, Hahn-Meitner-Platz 1, 14109 Berlin, Germany*

E-mail: joachim.dzubiella@helmholtz-berlin.de, joachim.dzubiella@physik.uni-freiburg.de

# Computational details of the charge transport property calculations

We model the charge transport of the PTBT in the crystalline phase with the Boltzmann transport equation (BTE).<sup>S1,S2</sup> The BTE expresses how a charge carrier distribution evolves in an electric field. The equation describes the steady-state situation between the acceleration of the charge by the external field, which drives the distribution out of equilibrium, and the collision with phonons and impurities, which restores the distribution.<sup>S3</sup> A common way to solve the BTE is the so-called relaxation time approximation. Here, one linearizes the relaxation of an electron distribution in a specific band, resulting in a time constant  $\tau$  as the average time between scattering events that reset the charge distribution in this band.<sup>S4</sup> In the linearized version of the BTE, the electrical conductivity  $\sigma$  can be expressed as

$$\sigma = e^2 \sum_{\mathbf{k}} \left( - \frac{\partial f(\epsilon_{\mathbf{k}})}{\partial \epsilon_{\mathbf{k}}} \right) \mathbf{v}_{\mathbf{k}} \mathbf{v}_{\mathbf{k}} \tau_{\mathbf{k}}. \quad (1)$$

Here,  $f(\epsilon_{\mathbf{k}}) = 1/(e^{(\epsilon_{\mathbf{k}} - \epsilon_F)/k_B T} + 1)$  is the Fermi-Dirac distribution function,  $\mathbf{v}_{\mathbf{k}} = \nabla_{\mathbf{k}} \epsilon_{\mathbf{k}} / \hbar$  the group velocity of a charge carrier in a given band,  $\epsilon_{\mathbf{k}}$  the band energy at a given  $\mathbf{k}$ -point,  $\epsilon_F$  the Fermi-energy (the chemical potential  $\mu_{\text{chem}}$  at  $T = 0$  K),  $k_B$  the Boltzmann constant, and  $T$  the temperature. We obtain the group velocities from the  $\mathbf{k}$ -space derivatives of the quasi-particle energies given by the band structure. For this, we use the BoltzTraP2 software package, which applies a smoothed Fourier interpolation method to obtain an analytic expression for the band structure in order to calculate the  $\mathbf{v}_{\mathbf{k}}$ 's.<sup>S5,S6</sup> We interpolate the  $\mathbf{k}$ -grid of the self-consistent band structure calculation onto a five times finer grid to obtain converged results for the conductivity.

In eqn (1), the relaxation time  $\tau_{\mathbf{k}}$  is energy- and  $\mathbf{k}$ -dependent. In general, the relaxation time accounts for scattering mechanisms such as elastic collisions of the charge carrier wave packet with impurities, as well as with optical and acoustic phonons.<sup>S2</sup> Since we apply the above theory only to the crystalline phase of the polymer, we can neglect any influence of

impurities. In such a molecular crystal, the coherence length of a delocalized charge carrier extends over several lattice constants. In this picture, the transport behavior of such a delocalized charge is mainly influenced by scattering events with acoustic phonons.<sup>S7,S8</sup> We here make use of the well-known deformation potential theory<sup>S9</sup> to calculate the relaxation time along a direction  $i$  due to charge carrier-acoustic phonon interactions<sup>S10</sup>

$$\tau_{ii} = \frac{C_i \hbar^2}{\sqrt{k_B T m_{\text{eff},ii}} D_{\text{def},ii}^2}. \quad (2)$$

Three quantities are introduced in eqn (2). The deformation potential in direction  $i$ ,  $D_{\text{def},ii}$ , is the response of the energy eigenvalue of the band in question at an extremal  $\mathbf{k}$ -point ( $\mathbf{k}_e$ ) to a lattice deformation  $\delta l_i$  along direction  $i$

$$D_{\text{def},ii} = \left. \frac{\partial \epsilon(\mathbf{k})}{\partial \delta l_i} \right|_{\mathbf{k}=\mathbf{k}_e}. \quad (3)$$

As we aim to investigate the charge transport of electrons in our polymer, we are interested in the conduction band. The elastic constant of the crystal,  $C_i$ , is the response of the total electronic energy to a dilation in direction  $i$

$$C_i = \frac{1}{l_i} \frac{\partial^2 E_{\text{tot}}}{\partial \delta l_i^2}, \quad (4)$$

where  $l_i$  is the length of the respective lattice vector of the non-deformed crystal unit cell, and  $E_{\text{tot}}$  is the total electronic energy of the unit cell. The third term is the effective mass,  $m_{\text{eff},ii}$ , which, in its conventional definition, is given by the curvature of the band dispersion relation

$$m_{\text{eff},ii} = \frac{1}{\hbar^2} \frac{\partial^2 \epsilon(\mathbf{k})}{\partial k_i^2}. \quad (5)$$

Again, as we focus on electron transport, the reference point for the derivative is the conduction band minimum (CBM). Also notice the double indices in eqn (2), (3), and (5).

They occur because the relaxation time, in its general form, is a second-rank tensor. For simplicity, we assume a transformation into the principal axes of the crystal to only consider the diagonal elements.<sup>S4</sup> In order to obtain the deformation potential, we dilate (stretch and compress) the unit cell in all three Cartesian directions up to 3% and calculate the energy change of the conduction band with the lattice dilation. Since there is the inherent problem of DFT to calculate the absolute position of an energy level with respect to the vacuum level in an infinite periodic crystal, it is difficult to obtain absolute energy changes by comparing calculations with different lattice constants.<sup>S7,S8</sup> Therefore, we adopt an approximation by Wei and Zunger, which takes the energy of the lowest band as a reference to obtain absolute energy changes of the CBM, assuming that the 1s core level is not affected by small deformations of the unit cell.<sup>S11</sup> The deformation potential in eqn (3) is then fitted by

$$E_i^{\text{CBM}} - E^{\text{1s}} = D_{\text{def},ii} \frac{\delta l_i}{l_i}. \quad (6)$$

For the elastic constant, the same stretching and compressing of the crystal must be done. The change of the total electronic energy is fitted to the cell dilation by<sup>S11</sup>

$$\frac{E_{\text{tot}} - E_{\text{tot}}^{\text{eq}}}{l_i} = \frac{C_i}{2} \left( \frac{\delta l_i}{l_i} \right)^2, \quad (7)$$

with the total energy of the undeformed unit cell  $E_{\text{tot}}^{\text{eq}}$  as the reference. Further, we use the EFFMASS package to obtain the effective mass for the different extremal points of the conduction band.<sup>S12</sup> In order to account for any non-parabolicity in the band structure, instead of eqn (5), we use a Kane quasi-linear dispersion relation<sup>S13</sup>

$$\frac{\hbar^2 k^2}{2m_{\text{eff},ii}^t} = \epsilon(\mathbf{k})(1 + \alpha\epsilon(\mathbf{k})), \quad (8)$$

with the so-called transport effective mass  $m_{\text{eff},ii}^t$ . In eqn (8),  $\alpha$  accounts for the amount of non-parabolicity due to the flattening of an energy band (for  $\alpha = 0$ , one recovers the dispersion relation of a parabolic band).

With the band structure and the relaxation times, we can calculate the electrical conductivity at room temperature according to eqn. (1). Note that in the Fermi-Dirac distribution, the temperature  $T$  and the chemical potential  $\mu$  are external parameters. As we fix the temperature, the latter is still to be determined. For any real system, the chemical potential is determined by the experimental conditions applied during the synthesis (including defects and/or doping). This experimentally variable quantity cannot be captured within DFT. In a semiconducting material, the DFT would place the chemical potential (which at  $T = 0$  K is the Fermi level) simply in the band gap to fulfill charge neutrality.

In general, the conductivity of any material is determined by the concentration of mobile charge carriers  $N$  and their mobility  $\mu$  by

$$\sigma = qN\mu, \quad (9)$$

with  $q$  as the charge of the carrier. The carrier density can be separated into the intrinsic carrier density, which is due to thermally excited states of the band structure, and the carrier density originating from extrinsic contributions such as doping. The concentrations of electrons in the conduction band and holes in the valence band are given by<sup>S14</sup>

$$\rho_e = \int_{\text{CB}} d\epsilon \rho(\epsilon) f(\epsilon), \text{ and} \quad (10)$$

$$\rho_h = \int_{\text{VB}} d\epsilon \rho(\epsilon) (1 - f(\epsilon)), \quad (11)$$

with the density of states (DOS)  $\rho(\epsilon)$ . The charge carrier concentration  $N$  is the net concentration defined as the difference between electron and hole concentrations. Within the so-called rigid band approximation (RBA), we can model the effect of doping by simply changing the value of the chemical potential  $\mu_{\text{chem}}$  and, by this, the density of mobile electrons or holes. This assumes that changing  $\mu_{\text{chem}}$  does not affect the band structure. Moving  $\mu_{\text{chem}}$

into the conduction bands would lead to a higher electron density, resulting in an n-type material. Moving it into the valence bands would increase the hole density and produce a p-type material. Within the RBA, we then obtain the electrical conductivity as a function of charge carrier concentration by varying the value of the chemical potential.

## Force field dihedral re-parametrization and validation

The force field parameters we have used so far to describe the conjugated PTBT system<sup>S15</sup> using classical molecular dynamics simulation are taken from the original OPLS-AA force field.<sup>S16</sup> As this was the first approach to describe a new polymeric system, we aim to improve the description of our conjugated polymer further. In order to gain a better understanding of the crystallization behavior of the PTBT system, we need accurate dihedral energies. We, therefore, re-parametrize specific dihedral potentials by adopting the general force-field parametrization scheme by Wildman.<sup>S17</sup>

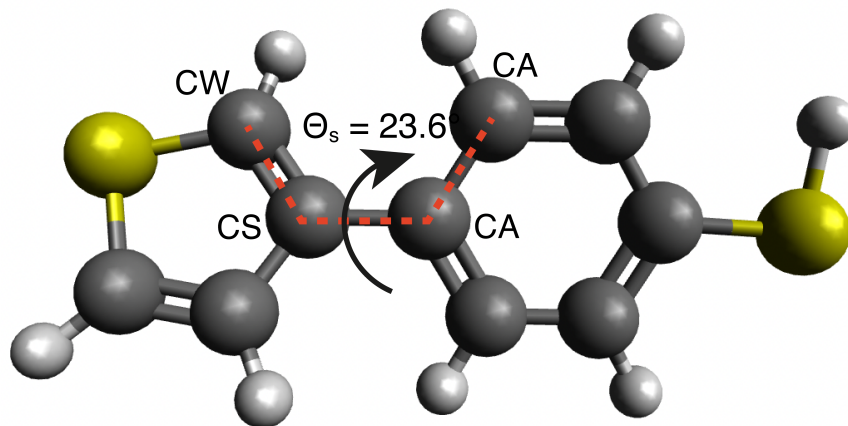


Figure S1: DFT optimized structure of a TBT monomer. The junction between the thio-phenyl and benzene ring is governed by the side chain dihedral  $\Theta_s$  (exemplified here by the atom set CW-CS-CA-CA). The most stable conformation features a dihedral angle of  $\Theta = 23.6^\circ$ . Carbon, hydrogen, and sulfur elements are displayed as spheres in grey, white, and yellow, respectively.

First, we identify the critical dihedrals of our system. Starting with the basic repeating unit of the polymer (cf. Figure S1), we notice the bond between the thiophene ring and the benzenethiol group allows for a rotation of the two rings against each other. This junction is of special interest as the torsion between the rings will influence the orientation of  $\pi$ -orbitals and, therefore, the overall electronic structure and charge transfer properties. The DFT-optimized structure shows an inter-ring dihedral of  $\Theta_s = 23.6^\circ$ .

In order to determine the dihedral energy parameters, we first scan the dihedral in steps of  $10^\circ$ , obtaining a series of relaxed molecular geometries. The geometry optimizations were carried out using the functional PBE. We then calculate the change of the total electronic energy  $E_{\text{DFT}}$  of the whole system (encompassing all dispersive and electrostatic interactions between electrons and nuclei) in dependency of the dihedral angle  $\Theta_s$ . As a validation, we also adopted a two-step 'Scan - single point (SP)' approach<sup>S18</sup> where we used the hybrid PBE0 functional to calculate SP energies of the PBE-optimized structures (cf. Figure S2). The comparison shows a good agreement between the two functionals. Only the energies at the conjugation barrier ( $90^\circ$ ) appear different. This difference is  $\sim 0.2$  kcal/mol, which at  $\sim 7\%$  of the barrier itself is a negligible deviation. Given the similar results and the computational expense of using a hybrid functional, we chose PBE for all further calculations.

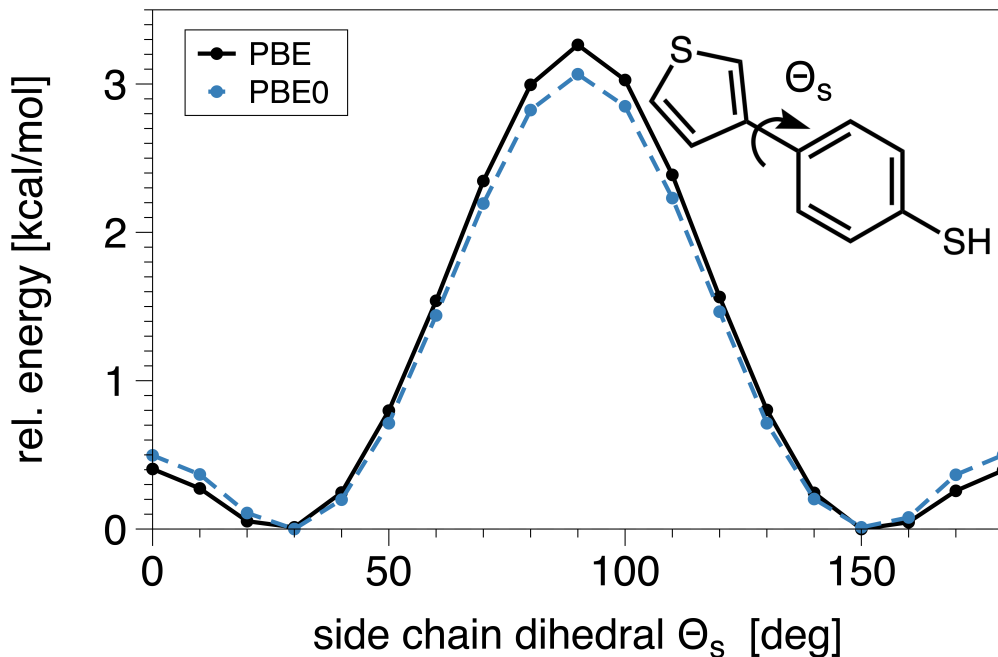


Figure S2: DFT scan of the TBT side chain dihedral  $\Theta_s$  profile. All geometries were optimized with PBE (black solid line). In addition, we also calculated single point (SP) energies with the PBE0 functional (dashed blue line). The inset shows the molecular structure of a TBT monomer with the dihedral of interest.

Note that the DFT profile is not the same as the desired dihedral potential profile. In order to obtain the 'bare' dihedral profile, we have to isolate the energy of the dihedral from all other force field contributions. We, therefore, perform the same scan with our force field, but we set the energy terms of the dihedral to zero (see Figure S3, red solid line (FF)). If we then subtract the FF energy profile from the DFT profile, we obtain the effective dihedral potential and can fit it to a fifth-order Ryckaert-Bellmanns (dashed pink line (RB)) function<sup>S19,S20</sup>

$$V_{\text{RB}}(\Theta) = \sum_{n=0}^5 C_n \cos(\Phi)^n, \quad (12)$$

with  $\Phi = \Theta - 180^\circ$ , where we adopt the 'polymer convention' casting the *trans* conformation at  $0^\circ$ .<sup>S21</sup> The 'complete' force field profile (dashed yellow line (FF + RB fit)) given by the addition of the FF scan and the fitted RB profile now matches the DFT profile to a

very high degree.

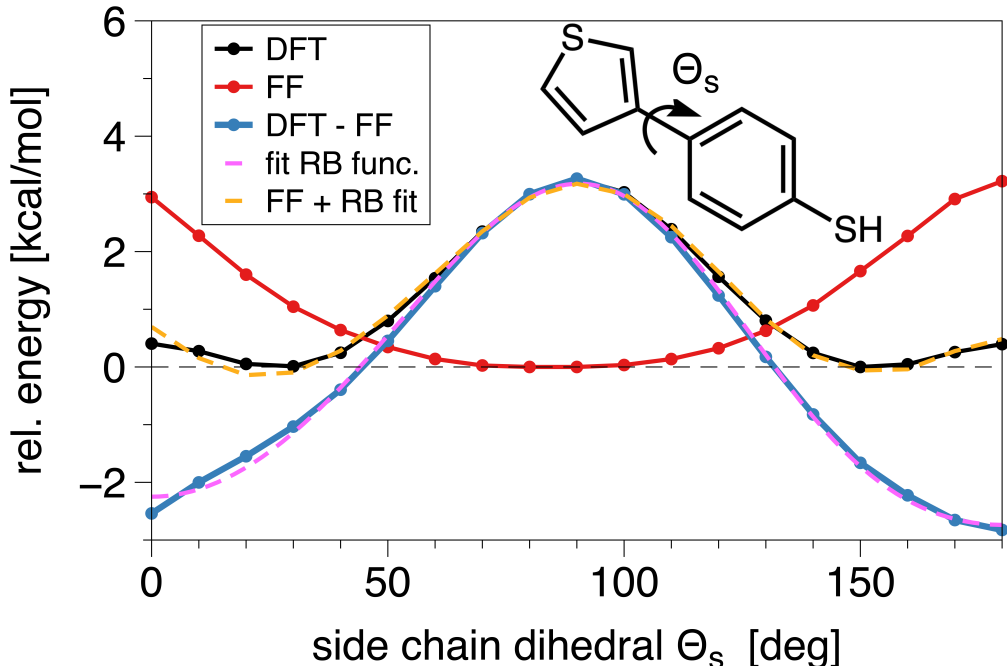


Figure S3: Illustration of the individual steps of the parametrization scheme for the inter-ring dihedral of one TBT monomer. The figure shows the DFT (PBE) profile (black), the profile obtained from the FF scan which excludes the dihedral contribution (red), the resulting subtracted profile of the former two (blue), the fit of the subtracted profile to a fifth-order Ryckaert-Bellmans function (dashed pink), and the 'complete' profile given by the addition of the FF scan profile and the fitted profile (dashed yellow).

We now turn to the case of two neighboring, covalently bound TBT units. As explained in the main text, three possible connections (HH, HT, TT) can be formed between two TBT monomers during electro-polymerization (cf. Figure 1). Therefore, we must distinguish between these three configurations when parametrizing the dihedral potential  $\Theta_b$  for the intermonomer junction. We apply the same procedure as for the TBT monomer to the parametrization of the three intermonomer junctions (cf. Figure S4). The force field parameters  $C_n$  (cf. eqn. (12)) obtained from the above procedure are summarized in Table S1, in a form suitable for use with the LAMMPS MD package.<sup>S22</sup>

Table S1: Dihedral angle parameters  $C_n$  (in kcal/mol) of the inter-ring torsion  $\Theta_s$  within a TBT unit and the three possible intermonomer torsions  $\Theta_b$  between two neighboring TBT units. The dihedral profiles were fitted with Ryckaert-Bellmanns functions according to eqn (12).

dihedral angle	$C_0$	$C_1$	$C_2$	$C_3$	$C_4$	$C_5$
TBT	0.794	-0.030	-1.892	0.334	0.474	-0.243
head-to-head (HH)	0.410	1.058	-0.356	-2.008	-0.904	0.643
head-to-tail (HT)	0.749	0.110	-1.837	-0.103	0.829	0.018
tail-to-tail (TT)	0.542	0.334	-1.388	-0.809	0.285	0.326

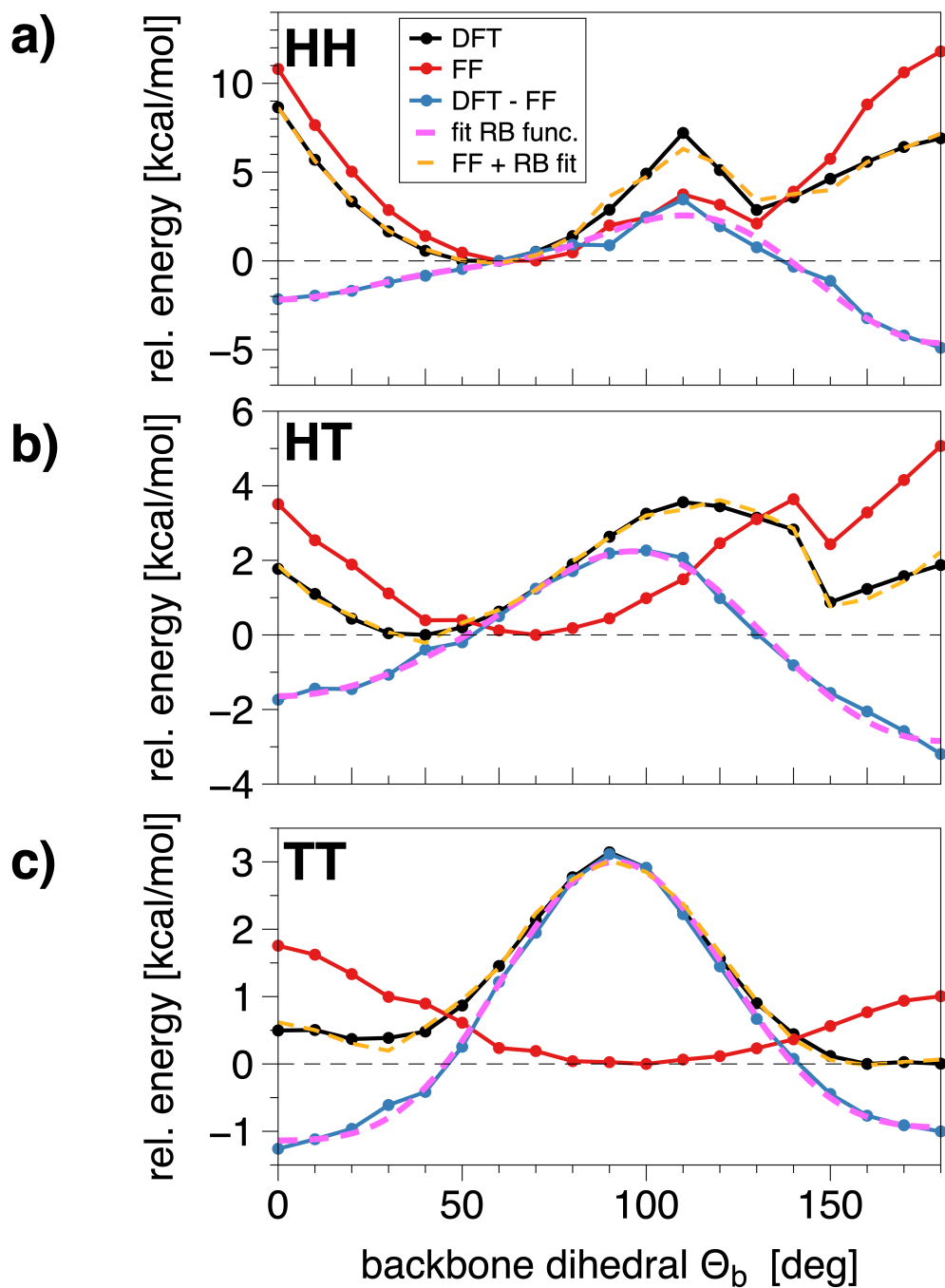


Figure S4: Illustration of the individual steps of the parametrization scheme for the three possible backbone dihedrals (HH, HT, TT). The figures show the DFT profile (black), the profile obtained from the FF scan which excludes the dihedral contribution (red), the resulting subtracted profile of the former two (blue); the fit of the subtracted profile to a fifth-order Ryckaert-Bellmans function (dashed pink), and the 'complete' profile given by the addition of the FF scan profile and the fitted profile (dashed yellow). (Legend applies to all graphs).

In order to validate the performance of the re-parametrized force field, we compute the potential energy surface with respect to all four individual dihedrals and compare them with the DFT results (cf. Figure S5). The TBT side chain scan (upper panel) clearly shows that with the original parameters<sup>S15</sup> (dashed blue line), the energy barrier ( $90^\circ$ ) between the planar configurations ( $0^\circ$  and  $180^\circ$ ) was strongly overestimated by more than 22 kcal/mol. Because of this, the overall force field described a very rigid structure where the benzenethiol group had no flexibility to rotate but was kept at the planar conformation. With the improved 'new' parameters (red solid line), the energies match the DFT results (black solid line). For the three backbone dihedrals in the bottom figures, we additionally included calculations using only the improved side chain parameters while keeping the original backbone parameters (green dashed lines). This way, we can quantify how the adjustment of the side chain dihedral already improves the description of the backbone dihedral. For the HH case (second from above), we indeed see that adjusting the side chain already leads to a significantly improved backbone dihedral profile (green dashed line). This significant impact of the side chain can be explained by the proximity between the two benzenethiol groups in the HH structure (cf. Figure 1c). Due to their greater flexibility they can adapt more to the rotation of the backbone. This leads to less steric hindrance between the two monomers and, therefore, to a lowering of the total energy. The side chain's influence on the backbone's behavior is not as pronounced for the HT case as for the HH structure because the side groups are further apart. This is even more so for the TT case, as the benzenethiols are at the opposite ends of the dimer structure. Therefore, only adjusting the side chain dihedral does not improve the contribution of the backbone to the total energy (lower panel: the green dashed line still matches the blue dashed line). This fact underlines the importance of assessing both side chain and backbone dihedrals to improve the force field model.

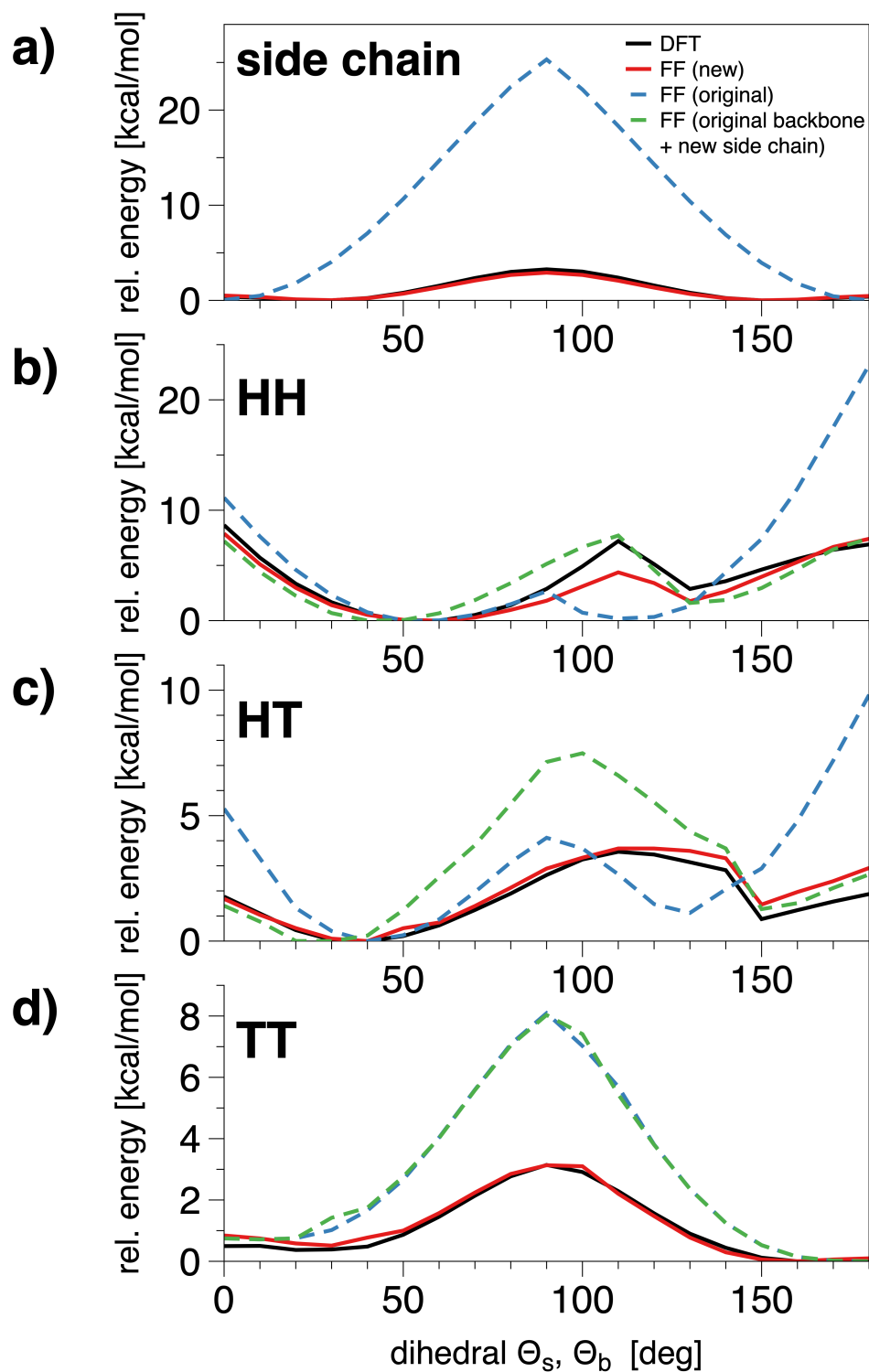


Figure S5: Comparison of the dihedral scans with the original force field<sup>S15</sup> (blue dashed line) and the improved 'new' force field of this study (red solid line) with the DFT results (black solid line). For the backbone dihedrals (HH, HT, TT), we also performed scans with the old backbone dihedral parameters in combination with the improved side dihedral parameters (green dashed line). (Legend applies to all graphs).

# Structural properties of single PTBT chains

We compare the results of the geometry optimization of the TBT monomer and two regioregular single chains between our force field and DFT. In Table S2, the structural properties of these three systems are summarized for the MD and two different DFT methods (PBE+MBD and PBE0+MBD). For better comparability of the dihedral angles, we report their deviation from planarity ( $\Delta\Theta_x = |180^\circ - \Theta_x|$ , with  $x = s, b$ ). For the TBT monomer, we compare the side chain dihedral. The periodic structures contain two monomers in the unit cell. Since two dihedrals constitute the chains, we have to consider two dihedrals for the side chain and backbone, respectively. For the dihedral angles, we obtain a maximum deviation of about  $3 - 4^\circ$  between the MD and PBE0+MBD result, that is, approximately 10%. We also compare the height of the unit cell  $L$ , that is, the length of two repeating units along the chain between MD and DFT. Here, MD underestimates  $L$  by roughly 1% compared to DFT. Comparing these structural features demonstrates that our classical force field accurately represents the monomeric and single-chain properties.

Comparing the two regularities, we notice that the two backbone dihedrals of an HT-HT chain are identical, whereas, in the case of an HH-TT chain, they differ by  $15^\circ$ . This is a consequence of the ordering of the side groups. In the HH-TT chain, the interaction of the benzenethiol groups between neighboring TBT units (HH) leads to a much higher deviation from planarity ( $\Delta\Theta_b = 41.4^\circ$  with PBE0) of the backbone than if the two hydrogens (TT) are adjacent ( $\Delta\Theta_b = 26.4^\circ$  with PBE0). Interestingly, both regularities are almost similar in their total electronic energy calculated by DFT (difference of  $\delta E = 5$  meV with PBE0).

Table S2: Comparison of structural properties of an optimized TBT monomer and two isolated, periodic chains (HH-TT, HT-HT regularity). For the unit cell structures of the single chains, we have to consider two side chain and backbone dihedrals, respectively. For the backbone dihedral of the HH-TT chain, the upper value belongs to the HH case and the lower value to the TT case.

model	TBT	HH-TT			HT-HT		
	side chain $\Delta\Theta_s$ [deg]	side chain $\Delta\Theta_s$ [deg]	backbone $\Delta\Theta_b$ [deg]	$L^a$ [Å]	side chain $\Delta\Theta_s$ [deg]	backbone $\Delta\Theta_b$ [deg]	$L$ [Å]
PBE	27.9	47.3	37.3	7.78	55.5	22.3	7.80
		46.5	19.5		55.5	22.1	
PBE0	28.9	46.7	41.4	7.75	53.5	28.3	7.76
		45.2	26.4		53.9	28.4	
OPLS (MD)	31.8	49.5	43.3	7.64	52.9	26.7	7.66
		41.8	22.9		57.6	29.3	

<sup>a</sup> $L$  is the height of the unit cell along the chain axis.

## Aggregation behavior: Annealing and crystal growth

To study the aggregation of PTBT polymer chains, we set up supercells of  $N = 100$  chains for both regioregularities. Figure S6 shows exemplarily selected snapshots of the annealing process of the HT-HT system at several temperatures. As the temperature of the systems goes down, chains begin to aggregate and form many small clusters. Around a temperature of  $T \approx 830$  K, chains start to stack together. Further cooling leads then to the growth of these aggregates by subsequent attachment of chains until these clusters eventually unite into a single large cluster. In the center of the cluster, neighboring chains form an ordered region with lamellar stacks (blue-colored area). In the outer regions of the cluster, the polymer chains have more freedom to bend due to thermal fluctuations. These surface effects lead to a distortion of the crystalline alignment where chains still form small stacks, but they also arrange in pairs of bent polymer chains. Interestingly, we can observe another substructure that almost looks like a micelle, in which chain pairs are arranged with all thiol groups pointing inward (black dashes line).

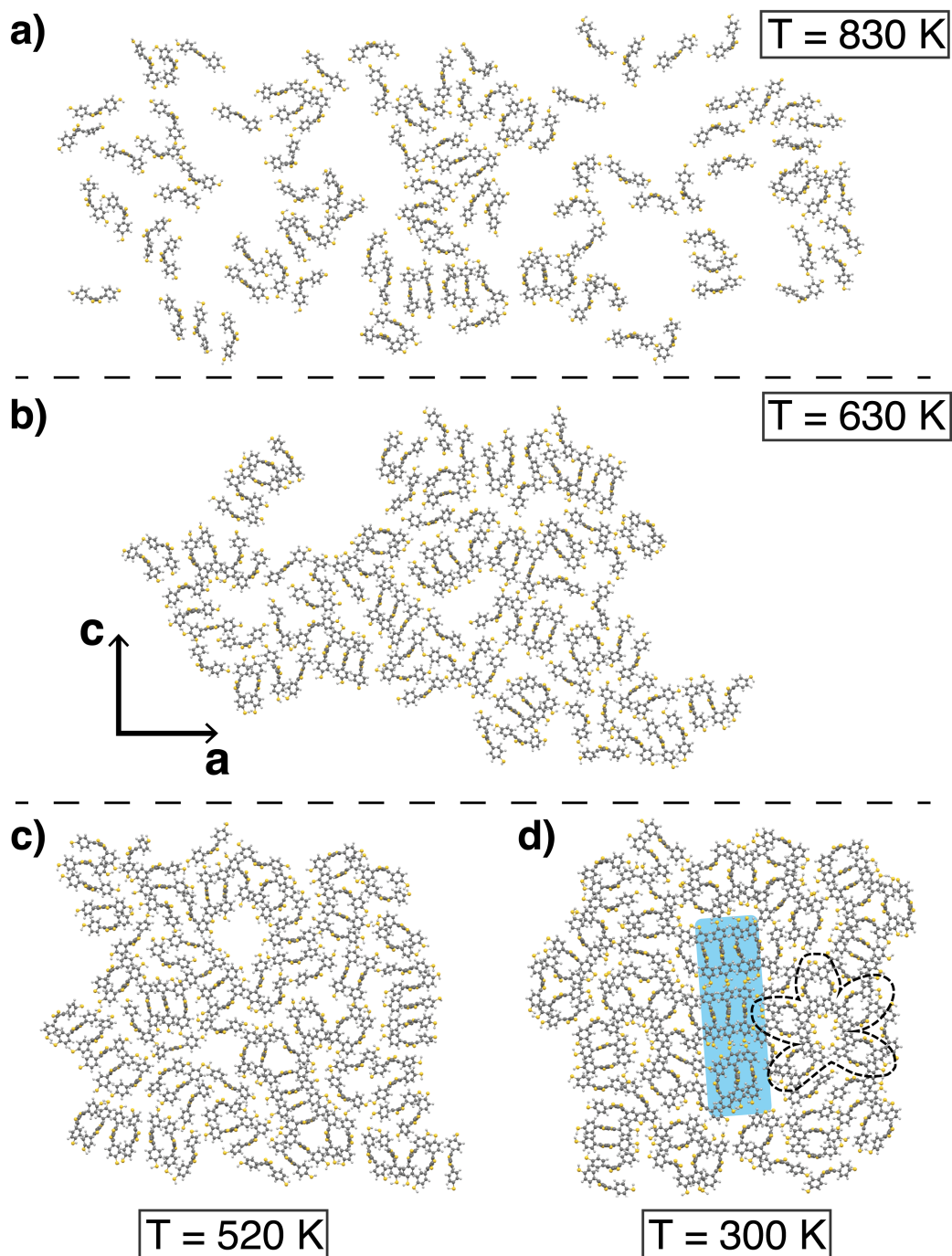


Figure S6: Snapshots of the aggregation process of the HT-HT PTBT polymer with respect to the annealing temperature  $T$ . (a) Pairs of chains start to stack together, with their backbones facing each other. (b) A big cluster starts to form. (c) The cluster becomes denser, with more and more chains forming stacks with their backbones aligning in a face-to-face manner. (d) A crystalline phase forms in the cluster's center with three stacks of chains arranged in a lamella (blue-colored area). Surface effects in the cluster's outer layers allow the chains to arrange in less ordered substructures, e.g., a micelle-like arrangement of chain pairs (black dashed line). All snapshots are shown in the  $ac$ -plane with the view along the polymer backbones.

## Structural analysis of the HT-HT and HH-TT phase

For both systems (HT-HT and HH-TT), we cut out representative subsets from the center of the grown clusters after the *NPT* annealing (cf. section 4.2 in the main text for more details). For a quantitative analysis of the two phases, we sample the backbone dihedrals  $\Theta_b$  of all polymer chains over the last 10 ps of their respective *NPT* runs. In Figure S7, we observe a clear difference in the distributions of backbone dihedrals of the two systems. As expected, the crystalline HT-HT (blue) shows one maximum at the planar backbone configuration ( $\Theta_b = 180^\circ$ ). The system's finite temperature during the sampling ( $T \approx 300$  K) causes thermal fluctuations of its equilibrium configuration, leading to a broadening of the distribution. On the other hand, the HH-TT system features two distinct and equally populated maxima, which deviate both by about  $30^\circ$  from the planar configuration. Furthermore, the total range of possible backbone dihedrals is much larger for the HH-TT than for the HT-HT phase.

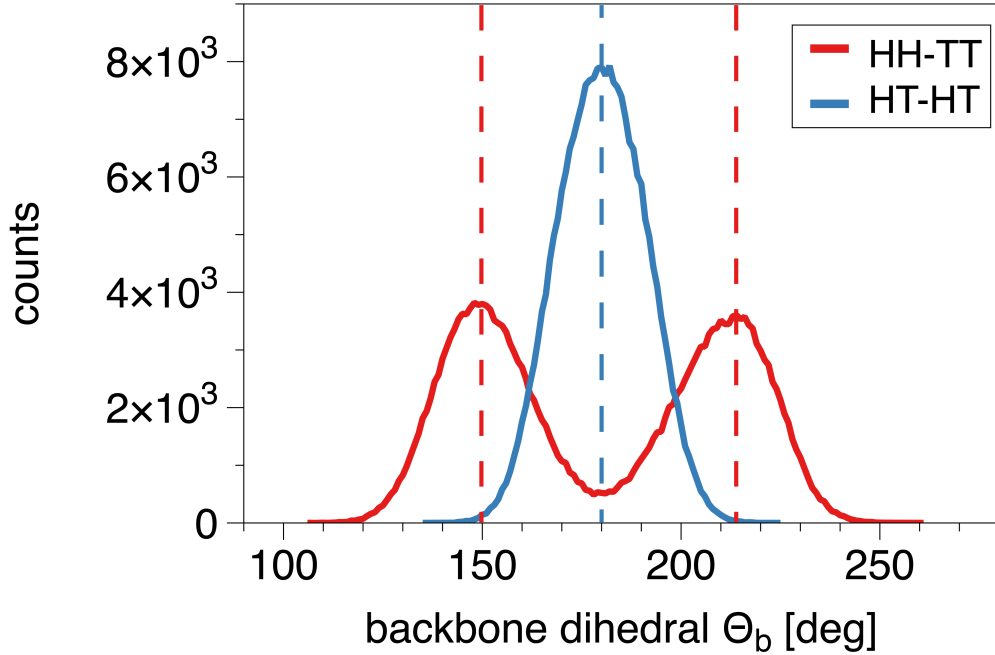


Figure S7: Distribution plot of the backbone dihedrals  $\Theta_b$  of all polymer chains in the unordered HH-TT subset (red) and the homogeneous HT-HT crystal (blue) (cf. section 4.2 and Figure 3 in the main text for more details). The data was sampled from the last 10 ps of their respective *NPT* runs. The dashed lines serve as a guide to the eye to depict the maxima.

## Calculation of the deformation potential and elastic constant

In order to assess the relaxation time  $\tau$  along the crystal directions of the HT-HT phase, we calculate the deformation potential and the elastic constant. As explained in the computational details, both parameter can be determined from a number of DFT geometry optimizations in stretched and compressed unit cells. Eq. (6) and (7) are then used to fit the change of the conduction band energy and the total energy to the lattice dilation, respectively (cf. Figure S8).

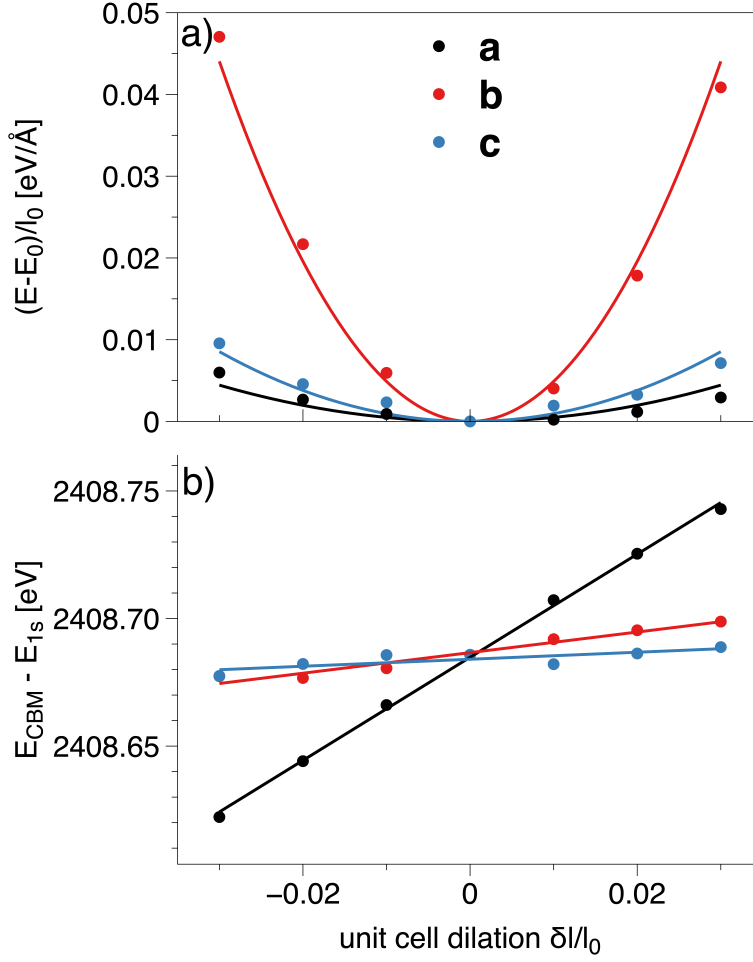


Figure S8: Numerical scheme to fit the elastic constant  $C$  and the deformation potential  $D_{\text{def}}$ . (a) The total electronic energy  $E$  of the unit cell (referenced to the energy  $E_0$  of the undeformed cell) in dependency of the dilation  $\delta l/l_0$  along the lattice vectors **a**, **b**, and **c** (in black, red, and blue, respectively). The parabolic fit according to eqn. (S7) yields the elastic constant. (b) The shifts of the conduction band energy  $E_{\text{CBM}}$  (with respect to the lowest energy level  $E_{1s}$ ) *versus* lattice dilation. The linear fits according to eqn. (S6) give the deformation potential as the slope.

## X-ray diffractogram of the PTBT polymer attached to nickel

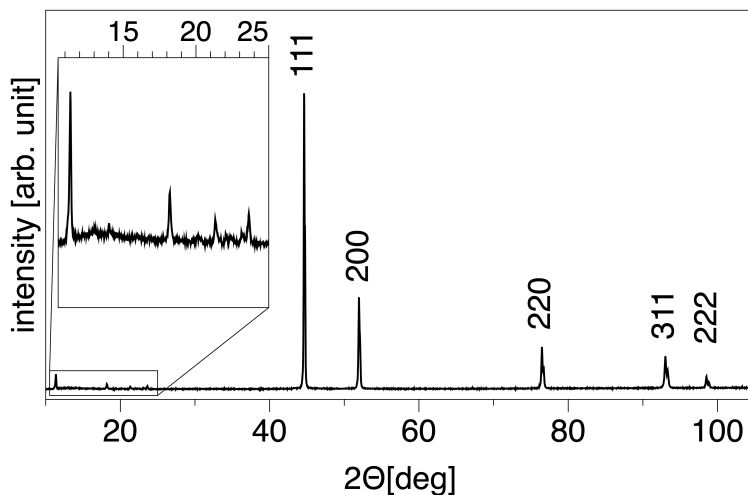


Figure S9: X-ray diffraction pattern of the PTBT film on a nickel (Ni) foam. The diffractogram shows the typical pattern of a face-centered cubic (fcc) phase of Ni (Miller indices are assigned to the main peaks).<sup>S23,S24</sup> The inset shows the signals of the PTBT polymer at lower Bragg angles.

## Geometry of the optimized HT-HT crystal structure

lattice\_vector 7.43824238 0.08176976 0.03602299

lattice\_vector -0.11706210 7.77782144 0.07550361

lattice\_vector 0.00807419 0.07101866 14.45370871

atom 2.68768098 3.36657492 3.37504874 C

atom 1.70271259 3.07670674 5.64150195 C

atom 1.86134347 1.67775986 5.75817778 C

atom 1.98616530 1.03396834 4.88947463 H

atom 1.70968321 3.72399197 4.31916204 C

atom 0.72367183 4.64673790 3.93209401 C

atom 0.72164501 5.21459403 2.66080602 C

atom 1.71773505 4.86552848 1.73822444 C  
atom -0.06871199 4.90859550 4.63161980 H  
atom -0.06278777 5.91821429 2.38348835 H  
atom 1.74017447 5.49681545 0.07885606 S  
atom 1.32387768 6.76343752 0.36126138 H  
atom 2.69780941 3.93298071 2.10443157 C  
atom 1.71999455 6.40953693 6.22048101 S  
atom 3.50406992 6.55881183 3.69928627 H  
atom 1.50706164 5.06791475 7.30025791 C  
atom 1.61798921 2.50323784 8.16379799 S  
atom 1.68477118 7.57881616 7.51102870 C  
atom 1.51422456 6.93918459 8.74377876 C  
atom 1.80723838 1.18348928 7.05388277 C  
atom 1.39084933 5.53956416 8.60184707 C  
atom 1.23441645 4.88251369 9.45549664 H  
atom 1.46638378 7.58273928 10.06787135 C  
atom 2.61082679 0.65728739 10.42823569 C  
atom 0.42146247 7.29418876 10.96079499 C  
atom 0.51211563 0.06717563 12.16315818 C  
atom 1.54088494 0.92409108 12.58168799 C  
atom 7.05959877 6.70368100 10.68838424 H  
atom 7.13144878 -0.09177053 12.87657911 H  
atom 1.46188572 1.59564158 14.22211400 S  
atom 2.59085906 1.22134752 11.70024066 C  
atom 2.79930360 1.86246119 14.32439763 H  
atom 1.55883965 3.69346447 6.89107667 C  
atom 5.25054892 7.06213328 5.68826001 C

atom 5.13371595 5.65948872 5.80913109 C  
atom 5.01576591 5.01123962 4.94277945 H  
atom 5.21529581 7.70306849 4.36362769 C  
atom 6.28173059 0.88294772 3.89419050 C  
atom 4.25200374 7.30139958 3.42195215 C  
atom 6.26294520 1.43956884 2.61833007 C  
atom 4.33813655 0.07847290 2.07123873 C  
atom 5.28280115 1.04380425 1.69761224 C  
atom 7.06409005 1.18013385 4.59077964 H  
atom 7.01991744 2.17061852 2.33589153 H  
atom 5.24161292 1.65984344 0.03398588 S  
atom 5.62794808 2.93792819 0.30930674 H  
atom 3.46328228 2.65092843 3.64704244 H  
atom 5.25084127 2.61849534 6.19454174 S  
atom 3.56342770 -0.22639422 1.36852035 H  
atom 3.48354430 3.66335720 1.39974872 H  
atom 3.63186862 5.82183495 12.06259324 H  
atom 3.61944436 4.83020825 9.80764361 H  
atom 5.38970512 7.68517941 6.93531049 C  
atom 3.44472663 0.87473483 9.76170328 H  
atom 5.21753241 5.16869618 7.10448917 C  
atom 5.26538430 3.78706737 7.48675997 C  
atom 5.46506311 3.15061303 8.71704687 C  
atom 5.51795441 1.28272524 7.26930633 C  
atom 5.63130672 1.75584885 8.57045096 C  
atom 5.81568896 1.10222728 9.42119661 H  
atom 5.49523048 3.78683288 10.04494969 C

atom 4.45103327 4.61981033 10.47926563 C  
atom 6.53461298 3.50399994 10.94596328 C  
atom 4.44997516 5.17063190 11.75701661 C  
atom 6.54047578 4.04220581 12.22949992 C  
atom 5.49511602 4.87956540 12.64618514 C  
atom 7.34720737 2.84533132 10.64034319 H  
atom -0.08138457 3.72482467 12.87574954 H  
atom 5.54437681 5.53656951 14.29360666 S  
atom 4.19882213 5.76415371 14.38786845 H  
atom 5.38517629 6.49509389 8.20996688 S  
atom 3.39565349 1.88840525 12.00712721 H

The absolute energy of the optimized structure is  $-4736.90$  Ha.

## References

- (S1) Harris, S. *An Introduction to the Theory of the Boltzmann Equation*; Dover Publications: New York, 2004; pp 121–130.
- (S2) Ziman, J. M. *Principles of the Theory of Solids*, 2nd ed.; Cambridge University Press: Cambridge, 1972; pp 211–230.
- (S3) Licker, M.; Hill, M. *McGraw-Hill Concise Encyclopedia of Physics*, 1st ed.; McGraw-Hill Book Company: New York, 2005; pp 70–75.
- (S4) Herring, C.; Vogt, E. Transport and Deformation-Potential Theory for Many-Valley Semiconductors with Anisotropic Scattering. *Phys. Rev.* **1956**, *101*, 944–961.
- (S5) Madsen, G. K. H. Automated Search for New Thermoelectric Materials: The Case of LiZnSb. *Journal of the American Chemical Society* **2006**, *128*, 12140–12146.

- (S6) Madsen, G. K.; Carrete, J.; Verstraete, M. J. BoltzTraP2, a Program for Interpolating Band Structures and Calculating Semi-Classical Transport Coefficients. *Comput. Phys. Commun.* **2018**, *231*, 140 – 145.
- (S7) Tang, L.; Long, M.; Wang, D.; Shuai, Z. The Role of Acoustic Phonon Scattering in Charge Transport in Organic Semiconductors: A First-Principles Deformation-Potential Study. *Sci. China, Ser. B: Chem.* **2009**, *52*, 1646–1652.
- (S8) Xi, J.; Long, M.; Tang, L.; Wang, D.; Shuai, Z. First-Principles Prediction of Charge Mobility in Carbon and Organic Nanomaterials. *Nanoscale* **2012**, *4*, 4348–4369.
- (S9) Bardeen, J.; Shockley, W. Deformation Potentials and Mobilities in Non-Polar Crystals. *Phys. Rev.* **1950**, *80*, 72–80.
- (S10) Beleznay, F. B.; Bogár, F.; Ladik, J. Charge Carrier Mobility in Quasi-One-Dimensional Systems: Application to a Guanine Stack. *Journal of Chemical Physics* **2003**, *119*, 5690–5695.
- (S11) Wei, S.-H.; Zunger, A. Predicted Band-Gap Pressure Coefficients of All Diamond and Zinc-Blende Semiconductors: Chemical Trends. *Phys. Rev. B* **1999**, *60*, 5404–5411.
- (S12) Whalley, L. D.; Frost, J. M.; Morgan, B. J.; Walsh, A. Impact of Nonparabolic Electronic Band Structure on the Optical and Transport Properties of Photovoltaic Materials. *Physical Review B* **2019**, *99*, 1–11.
- (S13) Kane, E. O. Band Structure of Indium Antimonide. *Journal of Physics and Chemistry of Solids* **1957**, *1*, 249–261.
- (S14) Kittel, C. *Introduction to Solid State Physics*, 8th ed.; John Wiley & Sons: New York, NY, 2004; pp 167–168.
- (S15) Gayen, D.; Schütze, Y.; Groh, S.; Dzubiella, J. Solvation Structure of Conjugated Organosulfur Polymers for Lithium-Sulfur Battery Cathodes. *ChemRxiv*, 2023.

<https://chemrxiv.org/engage/chemrxiv/article-details/63ea00621d2d1840636905f3> (accessed March 28, 2023).

- (S16) Jorgensen, W. L.; Maxwell, D. S.; Tirado-Rives, J. Development and Testing of the OPLS All-Atom Force Field on Conformational Energetics and Properties of Organic Liquids. *Journal of the American Chemical Society* **1996**, *118*, 11225–11236.
- (S17) Wildman, J.; Repiščák, P.; Paterson, M. J.; Galbraith, I. General Force-Field Parametrization Scheme for Molecular Dynamics Simulations of Conjugated Materials in Solution. *Journal of Chemical Theory and Computation* **2016**, *12*, 3813–3824.
- (S18) Dubay, K. H.; Hall, M. L.; Hughes, T. F.; Wu, C.; Reichman, D. R.; Friesner, R. A. Accurate Force Field Development for Modeling Conjugated Polymers. *Journal of Chemical Theory and Computation* **2012**, *8*, 4556–4569.
- (S19) Ryckaert, J.-P.; Bellemans, A. Molecular Dynamics of Liquid n-Butane Near Its Boiling Point. *Chemical Physics Letters* **1975**, *30*, 123–125.
- (S20) Ryckaert, J.-P.; Bellemans, A. Molecular Dynamics of Liquid Alkanes. *Faraday Discuss. Chem. Soc.* **1978**, *66*, 95–106.
- (S21) Chanda, M. *Introduction to Polymer Science and Chemistry: A Problem-Solving Approach*, 2nd ed.; Taylor & Francis: New York, 2013; pp 35–37.
- (S22) Thompson, A. P.; Aktulga, H. M.; Berger, R.; Bolintineanu, D. S.; Brown, W. M.; Crozier, P. S.; in 't Veld, P. J.; Kohlmeyer, A.; Moore, S. G.; Nguyen, T. D.; Shan, R.; Stevens, M. J.; Tranchida, J.; Trott, C.; Plimpton, S. J. LAMMPS - A Flexible Simulation Tool for Particle-Based Materials Modeling at the Atomic, Meso, and Continuum Scales. *Comput. Phys. Commun.* **2022**, *271*, 108171.
- (S23) Jović, V. D.; Maksimović, V.; Pavlović, M. G.; Popov, K. I. Morphology, Internal

Structure and Growth Mechanism of Electrodeposited Ni and Co Powders. *J. Solid State Electrochem.* **2006**, *10*, 373–379.

- (S24) Wang, H.; Kou, X.; Zhang, J.; Li, J. Large Scale Synthesis and Characterization of Ni Nanoparticles By Solution Reduction Method. *Bull. Mater. Sci.* **2008**, *31*, 97–100.



# Bibliography

- (1) Crutzen, P. J. *Nature* **2002**, *415*, 23–23.
- (2) Steffen, W. *Ambio* **2011**, *40*, 739–761.
- (3) Steffen, W. *Ambio* **2021**, *50*, 1784–1787.
- (4) Kurzweil, P. J. *Power Sources* **2010**, *195*, 4424–4434.
- (5) Jeyaseelan, C.; Jain, A.; Khurana, P.; Kumar, D.; Thatai, S. In *Rechargeable Batteries*; John Wiley & Sons, Ltd: 2020; Chapter 9, pp 177–194.
- (6) Arya, S.; Verma, S. In *Rechargeable Batteries*; John Wiley & Sons, Ltd: 2020; Chapter 8, pp 131–175.
- (7) Yoshino, A. *Angew. Chem., Int. Ed.* **2012**, *51*, 5798–5800.
- (8) Goodenough, J. B.; Park, K.-S. *J. Am. Chem. Soc.* **2013**, *135*, 1167–1176.
- (9) The Element Sulfur, <https://education.jlab.org/itselemental/ele016.html>, Accessed: 2023-11-10.
- (10) Chung, W. J. et al. *Nat. Chem.* **2013**, *5*, 518–524.
- (11) Herbert, D.; Ulam, J. Electric dry cells and storage batteries, U.S. Patent 3.043.896, 1962.
- (12) Ji, X.; Lee, K. T.; Nazar, L. F. *Nat. Mater.* **2009**, *8*, 500–506.
- (13) Dirlam, P. T.; Glass, R. S.; Char, K.; Pyun, J. *J. Polym. Sci., Part A: Polym. Chem.* **2017**, *55*, 1635–1668.
- (14) Danner, T.; Zhu, G.; Hofmann, A. F.; Latz, A. *Electrochim. Acta* **2015**, *184*, 124–133.
- (15) Zhao, F.; Li, Y.; Feng, W. *Small Methods* **2018**, *2*, 1800156.
- (16) Pang, Q.; Liang, X.; Kwok, C. Y.; Nazar, L. F. *Nat. Energy* **2016**, *1*, 1–11.
- (17) Walus, S. Lithium/Sulfur batteries : development and understanding of the working mechanisms, Ph.D. Thesis, Université Grenoble Alpes, 2015.
- (18) Manthiram, A.; Fu, Y.; Chung, S.-H.; Zu, C.; Su, Y.-S. *Chem. Rev.* **2014**, *114*, 11751–11787.

- (19) Narayanan Kirshnamoorthy, A.; Oldiges, K.; Winter, M.; Heuer, A.; Cekic-Laskovic, I.; Holm, C.; Smiatek, J. *Phys. Chem. Chem. Phys.* **2018**, *20*, 25701–25715.
- (20) Bieker, G.; Diddens, D.; Kolek, M.; Borodin, O.; Winter, M.; Bieker, P.; Jalkanen, K. *The J. Phys. Chem. C* **2018**, *122*, 21770–21783.
- (21) Yang, L.; Li, Q.; Wang, Y.; Chen, Y.; Guo, X.; Wu, Z.; Chen, G.; Zhong, B.; Xiang, W.; Zhong, Y. *Ionics* **2020**, *26*, 5299–5318.
- (22) Mori, R. *J. Solid State Electrochem.* **2023**, *27*, 813–839.
- (23) Eftekhari, A.; Kim, D.-W. *J. Mater. Chem. A* **2017**, *5*, 17734–17776.
- (24) Li, Y.; Shapter, J. G.; Cheng, H.; Xu, G.; Gao, G. *Particuology* **2021**, *58*, 1–15.
- (25) Licker, M.; Hill, M., *McGraw-Hill Concise Encyclopedia of Physics*, 1st ed.; McGraw-Hill Book Company: New York, 2005, pp 70–75.
- (26) Bardeen, J.; Shockley, W. *Phys. Rev.* **1950**, *80*, 72–80.
- (27) Arote, S. A., *Lithium-ion and Lithium–Sulfur Batteries*; IOP Publishing: Bristol, 2022; Chapter 1, pp 1–21.
- (28) Goodenough, J. B.; Kim, Y. *Chem. Mater.* **2010**, *22*, 587–603.
- (29) Li, M.; Lu, J.; Chen, Z.; Amine, K. *Adv. Mater.* **2018**, *30*, 1800561.
- (30) Cheng, X.-B.; Zhang, R.; Zhao, C.-Z.; Zhang, Q. *Chem. Rev.* **2017**, *117*, 10403–10473.
- (31) Dahl, C.; Prange, A.; Steudel, R. In *Biopolymers Online*; John Wiley & Sons, Ltd: 2005.
- (32) Jana, M.; Xu, R.; Cheng, X.-B.; Yeon, J. S.; Park, J. M.; Huang, J.-Q.; Zhang, Q.; Park, H. S. *Energy Environ. Sci.* **2020**, *13*, 1049–1075.
- (33) Li-S Energy achieves 45% increase in volumetric energy density with new 20-layer semi-solid state lithium sulfur battery, <https://shorturl.at/rtJ24>, Accessed: 2024-03-05.
- (34) Farjana, S. H.; Huda, N.; Mahmud, M. P. *J. Sustain. Min.* **2019**, *18*, 150–161.
- (35) Mikhaylik, Y. V.; Akridge, J. R. *J. Electrochem. Soc.* **2004**, *151*, A1969.
- (36) Zhang, S.; Ueno, K.; Dokko, K.; Watanabe, M. *Adv. Energy Mater.* **2015**, *5*.
- (37) Cheon, S.-E.; Ko, K.-S.; Cho, J.-H.; Kim, S.-W.; Chin, E.-Y.; Kim, H.-T. *J. Electrochem. Soc.* **2003**, *150*, A796.

- (38) Peng, H.-J.; Zhang, G.; Chen, X.; Zhang, Z.-W.; Xu, W.-T.; Huang, J.-Q.; Zhang, Q. *Angew. Chem.* **2016**, *128*, 13184–13189.
- (39) Dean, J.; Lange, N., *Lange's Handbook of Chemistry*; Lange's handbook of chemistry Bd. 15; McGraw-Hill: 1999.
- (40) Zheng, G.; Yang, Y.; Cha, J. J.; Hong, S. S.; Cui, Y. *Nano Lett.* **2011**, *11*, 4462–4467.
- (41) Zheng, G.; Zhang, Q.; Cha, J. J.; Yang, Y.; Li, W.; Seh, Z. W.; Cui, Y. *Nano Lett.* **2013**, *13*, 1265–1270.
- (42) Wang, H.; Yang, Y.; Liang, Y.; Robinson, J. T.; Li, Y.; Jackson, A.; Cui, Y.; Dai, H. *Nano Lett.* **2011**, *11*, 2644–2647.
- (43) Wang, C.; Wang, X.; Yang, Y.; Kushima, A.; Chen, J.; Huang, Y.; Li, J. *Nano Lett.* **2015**, *15*, 1796–1802.
- (44) Visco, S. J.; Dejonghe, L. C. *J. Electrochem. Soc.* **1988**, *135*, 2905–2909.
- (45) M. M. Doeff M. M. Lerner, S. J. V.; Jonghe, L. C. D. *J. Electrochem. Soc.* **1992**, *139*, 2077–2081.
- (46) Tsutsumi, H.; Okada, K.; Fujita, K.; Oishi, T. *J. Power Sources* **1997**, *68*, 735–738.
- (47) Tsutsumi, H.; Oyari, Y.; Onimura, K.; Oishi, T. *J. Power Sources* **2001**, *92*, 228–233.
- (48) Xue, L.; Li, J.; Hu, S.; Zhang, M.; Zhou, Y.; Zhan, C. *Electrochem. Commun.* **2003**, *5*, 903–906.
- (49) Li, J.; Zhan, H.; Zhou, L.; Deng, S.; Li, Z.; Zhou, Y. *Electrochem. Commun.* **2004**, *6*, 515–519.
- (50) Deng, S. R.; Kong, L. B.; Hu, G. Q.; Wu, T.; Li, D.; Zhou, Y. H.; Li, Z. Y. *Electrochim. Acta* **2006**, *51*, 2589–2593.
- (51) Amaike, M.; Iihama, T. *Synth. Met.* **2006**, *156*, 239–243.
- (52) Gavrilov, A.; Kovalev, I.; Skotheim, T. In *The Electrochemical Society Meet.* San Antonio, US, 1996.
- (53) Skotheim, T.; Trofimov, B.; Grigorevna, M.; Koralev, I. *J. Power Sources* **1997**, *67*, 337–337.
- (54) A. Gorkovenko, T. A. S. (Moltech Corp), US WO 99/33130, 1999.
- (55) Sang, P.; Si, Y.; Fu, Y. *Chem. Commun.* **2019**, *55*, 4857–4860.

- (56) Chisholm, H., *The Encyclopaedia Britannica: A Dictionary of Arts, Sciences, Literature and General Information*; The Encyclopædia Britannica: A Dictionary of Arts, Sciences, Literature and General Information Bd. 23; At the University Press: 1911.
- (57) Goodyear, C. Improvement in India-Rubber Fabrics, U.S. Patent US3633A, 1844.
- (58) Kennedy, S. J.; Wheeler, J. C. *J. Phys. Chem.* **1983**, *87*, 3961–3966.
- (59) Steudel, R.; Strauss, R.; Koch, L. *Angew. Chem., Int. Ed. Engl.* **1985**, *24*, 59–60.
- (60) Steudel, R., *Elemental Sulfur and Sulfur-Rich Compounds I*; Elemental sulfur and sulfur-rich compounds; Springer Berlin Heidelberg: 2003; Chapter 2, pp 81–116.
- (61) Simmonds, A. G.; Griebel, J. J.; Park, J.; Kim, K. R.; Chung, W. J.; Oleshko, V. P.; Kim, J.; Kim, E. T.; Glass, R. S.; Soles, C. L.; Sung, Y. E.; Char, K.; Pyun, J. *ACS Macro Lett.* **2014**, *3*, 229–232.
- (62) Gomez, I.; Leonet, O.; Blazquez, J. A.; Mecerreyes, D. *ChemSusChem* **2016**, *9*, 3419–3425.
- (63) Gomez, I.; Mecerreyes, D.; Blazquez, J. A.; Leonet, O.; Youcef, H. B.; Li, C.; Gómez-Cámer, J. L.; Bondarchuk, O.; Rodriguez-Martinez, L. *J. Power Sources* **2016**, *329*, 72–78.
- (64) Zhang, Y.; Griebel, J. J.; Dirlam, P. T.; Nguyen, N. A.; Glass, R. S.; Mackay, M. E.; Char, K.; Pyun, J. *J. Polym. Sci., Part A: Polym. Chem.* **2017**, *55*, 107–116.
- (65) Chiang, C. K.; Fincher, C. R.; Park, Y. W.; Heeger, A. J.; Shirakawa, H.; Louis, E. J.; Gau, S. C.; MacDiarmid, A. G. *Phys. Rev. Lett.* **1977**, *39*, 1098–1101.
- (66) Brédas, J. L.; Marder, S. R.; Salaneck, W. R. *Macromolecules* **2002**, *35*, 1137–1139.
- (67) Li, W.; Zhang, Q.; Zheng, G.; Seh, Z. W.; Yao, H.; Cui, Y. *Nano Letters* **2013**, *13*, 5534–5540.
- (68) Dirlam, P. T.; Simmonds, A. G.; Shallcross, R. C.; Arrington, K. J.; Chung, W. J.; Griebel, J. J.; Hill, L. J.; Glass, R. S.; Char, K.; Pyun, J. *ACS Macro Lett.* **2015**, *4*, 111–114.
- (69) Oschmann, B.; Park, J.; Kim, C.; Char, K.; Sung, Y.-E.; Zentel, R. *Chem. Mater.* **2015**, *27*, 7011–7017.

- (70) Chang, A.; Wu, Q.; Du, X.; Chen, S.; Shen, J.; Song, Q.; Xie, J.; Wu, W. *Chem. Commun.* **2016**, *52*, 4525–4528.
- (71) Zeng, S.; Li, L.; Xie, L.; Zhao, D.; Wang, N.; Chen, S. *ChemSusChem* **2017**, *10*, 3378–3386.
- (72) Schrödinger, E. *Phys. Rev.* **1926**, *28*, 1049–1070.
- (73) Hamilton, W. R., *On a general method of expressing the paths of light, & of the planets, by the coefficients of a characteristic function*; P.D. Hardy Dublin: Dublin, 1833; Vol. 1, pp 795–826.
- (74) Hartree, D. R. *Math. Proc. Camb. Philos. Soc.* **1928**, *24*, 111–132.
- (75) Fock, V. *Z. Physik* **1930**, *61*, 126–148.
- (76) Bruus, H.; Flensberg, K., *Many-Body Quantum Theory in Condensed Matter Physics: An Introduction*; Oxford Graduate Texts; OUP Oxford: 2004, pp 65–71.
- (77) Slater, J. C. *Phys. Rev.* **1929**, *34*, 1293–1322.
- (78) Pauli, W. *Z. Physik.* **1925**, *31*, 765–783.
- (79) Čížek, J. *J. Chem. Phys.* **1966**, *45*, 4256–4266.
- (80) Nagy Otto, B. In *Computational Theoretical Organic Chemistry*, Springer Netherlands: Dordrecht, 1981, pp 77–100.
- (81) Sholl, D. S.; Steckel, J. A. In *Density Functional Theory*; John Wiley & Sons, Ltd: 2009; Chapter 1, pp 1–33.
- (82) Hohenberg, P.; Kohn, W. *Phys. Rev* **1964**, *136*, B864.
- (83) Kohn, W. *Rev. Mod. Phys.* **1999**, *71*, 1253–1266.
- (84) Born, M.; Oppenheimer, R. *Ann. Phys. (Berlin, Ger.)* **1927**, *389*, 457–484.
- (85) Thomas, L. H. *Math. Proc. Cambridge Philos. Soc.* **1927**, *23*, 542–548.
- (86) Fermi, E. *Z. Physik.* **1928**, *48*, 73–79.
- (87) Kohn, W.; Sham, L. J. *Phys. Rev.* **1965**, *140*, A1133–A1138.
- (88) Parr, R. G.; Weitao, Y., *Density-Functional Theory of Atoms and Molecules*; Oxford University Press: 1995, pp 142–168.
- (89) Capelle, K. *Braz. J. Phys.* **2006**, *36*, 1318–1343.
- (90) Mardirossian, N.; Head-Gordon, M. *Mol. Phys.* **2017**, *115*, 2315–2372.
- (91) Perdew, J. P.; Burke, K.; Ernzerhof, M. *Phys. Rev. Lett.* **1996**, *77*, 3865–3868.

- (92) Meier de Andrade, A.; Kullgren, J.; Broqvist, P. *Phys. Rev. B* **2020**, *102*, 075115.
- (93) Adamo, C.; Barone, V. *J. Chem. Phys.* **1999**, *110*, 6158–6170.
- (94) Becke, A. D. *J. Chem. Phys.* **1993**, *98*, 1372–1377.
- (95) Becke, A. D. *J. Chem. Phys.* **1993**, *98*, 5648–5652.
- (96) Gupta, V., *Principles and Applications of Quantum Chemistry*; Elsevier Science: London, 2015, pp 103–110.
- (97) Blum, V.; Gehrke, R.; Hanke, F.; Havu, P.; Havu, V.; Ren, X.; Reuter, K.; Scheffler, M. *Comput. Phys. Commun.* **2009**, *180*, 2175–2196.
- (98) Yu, V. W.-Z.; Corsetti, F.; Garcia, A.; Huhn, W. P.; Jacquelin, M.; Jia, W.; Lange, B.; Lin, L.; Lu, J.; Mi, W.; Seifitokaldani, A.; Vazquez-Mayagoitia, A.; Yang, C.; Yang, H.; Blum, V. *Comput. Phys. Commun.* **2018**, *222*, 267–285.
- (99) Havu, V.; Blum, V.; Havu, P.; Scheffler, M. *J. Comput. Phys.* **2009**, *228*, 8367–8379.
- (100) Jensen, S. R.; Saha, S.; Flores-Livas, J. A.; Huhn, W.; Blum, V.; Goedecker, S.; Frediani, L. *J. Phys. Chem. Lett.* **2017**, *8*, 1449–1457.
- (101) Tkatchenko, A.; Scheffler, M. *Phys. Rev. Lett.* **2009**, *102*, 6–9.
- (102) Ambrosetti, A.; Reilly, A. M.; DiStasio, R. A.; Tkatchenko, A. *The J. Chem. Phys.* **2014**, *140*, 18A508.
- (103) Bohm, D.; Pines, D. *Phys. Rev.* **1951**, *82*, 625–634.
- (104) Pines, D.; Bohm, D. *Phys. Rev.* **1952**, *85*, 338–353.
- (105) Bohm, D.; Pines, D. *Phys. Rev.* **1953**, *92*, 609–625.
- (106) Rapaport, D. C. In *The Art of Molecular Dynamics Simulation*, 2nd ed.; Cambridge University Press: 2004, pp 11–43.
- (107) Park, C.; Kanduč, M.; Chudoba, R.; Ronneburg, A.; Risse, S.; Ballauff, M.; Dzubiella, J. *J. Power Sources* **2018**, *373*, 70–78.
- (108) Park, C.; Ronneburg, A.; Risse, S.; Ballauff, M.; Kanduč, M.; Dzubiella, J. *J. Phys. Chem. C* **2019**, *123*, 10167–10177.
- (109) Dubouis, N.; Park, C.; Deschamps, M.; Abdelghani-Idrissi, S.; Kanduč, M.; Colin, A.; Salanne, M.; Dzubiella, J.; Grimaud, A.; Rotenberg, B. *ACS Cent. Sci.* **2019**, *5*, 640–643.
- (110) Jorgensen, W. L.; Tirado-Rives, J. *J. Am. Chem. Soc.* **1988**, *110*, 1657–1666.

- 
- (111) Jorgensen, W. L.; Maxwell, D. S.; Tirado-Rives, J. *J. Am. Chem. Soc.* **1996**, *118*, 11225–11236.
- (112) Lorentz, D. *Ann. Phys.* **1881**, *248*, 127–136.
- (113) Berthelot, H. A. *C. R. Hebd. Seances Acad. Sci.* **1898**, *126*, 1703–1855.
- (114) Lennard-Jones, J. E. *Proc. Phys. Soc.* **1931**, *43*, 461.
- (115) Eisenschitz, R.; London, F. *Z. Physik* **1930**, *60*, 491–527.
- (116) Socrates, G., *Infrared and Raman Characteristic Group Frequencies: Tables and Charts*; John Wiley & Sons: 2004, pp 50–51.
- (117) Boltzmann, L., *Vorlesungen über Gastheorie*; J.A. Barth, Leipzig: 1923, p 89.
- (118) Halley, J. W. In *Statistical Mechanics: From First Principles to Macroscopic Phenomena*; Cambridge University Press: 2006, pp 7–26.
- (119) Nolting, W., *Grundkurs Theoretische Physik 6: Statistische Physik*; Springer-Lehrbuch; Springer Berlin Heidelberg: 2013, pp 1–4.
- (120) Gibbs, J., *Elementary Principles in Statistical Mechanics: Developed with Especial Reference to the Rational Foundations of Thermodynamics*; C. Scribner's sons New York: 1902, pp 5–8.
- (121) Nose, S. *J. Chem. Phys.* **1984**, *81*, 511–519.
- (122) Martyna, G. J.; Tobias, D. J.; Klein, M. L. *J. Chem. Phys.* **1994**, *101*, 4177–4189.
- (123) Clausius, R. *Philos. Mag. (1798-1977)* **1870**, *40*, 122–127.
- (124) Marx, D.; Hutter, J., *Ab Initio Molecular Dynamics: Basic Theory and Advanced Methods*; Cambridge University Press: 2009, pp 5–19.
- (125) Groenhof, G. *Methods Mol. Biol. (N. Y.)* **2013**, *924*, 43–66.
- (126) Dill, K.; Bromberg, S.; Stigter, D., *Molecular Driving Forces: Statistical Thermodynamics in Chemistry and Biology*; Garland Science: New York, NY, 2003, pp 560–563.
- (127) General, I. J. *J. Chem. Theory Comput.* **2010**, *6*, 2520–2524.
- (128) Xu, X.; Dzubiella, J. *Colloid Polym. Sci.* **2020**, *298*, 747–759.
- (129) McQuarrie, D.; Simon, J., *Molecular Thermodynamics*; University Science Books: 1999, pp 477–485.
- (130) Lennard-Jones, J. E. *Trans. Faraday Soc.* **1929**, *25*, 668–686.
- (131) Hückel, E. *Z. Phys.* **1931**, *70*, 204–286.

- (132) Hückel, E. *Z. Phys.* **1931**, *72*, 310–337.
- (133) Hückel, E. *Z. Phys.* **1932**, *76*, 628–648.
- (134) Hückel, E. *Z. Phys.* **1933**, *83*, 632–668.
- (135) Peierls, R., *Quantum Theory of Solids*; Clarendon Press: 1996, pp 75–100.
- (136) Bredas, J.-L.; Marder, S. R., *The WSPC Reference on Organic Electronics: Organic Semiconductors*; World Scientific: 2016; Vol. 1, pp 1–18.
- (137) Bloch, F. *Z. Phys.* **1929**, *52*, 555–600.
- (138) Setyawan, W.; Curtarolo, S. *Comput. Mater. Sci.* **2010**, *49*, 299–312.
- (139) Kittel, C., *Introduction to Solid State Physics*. 8th ed.; John Wiley & Sons: New York, 2004, pp 167–168.
- (140) Kittel, C.; Kroemer, H., *Thermal Physics*; W. H. Freeman & Co. Ltd: New York, 1980, pp 355–363.
- (141) Ziman, J. M., *Principles of the Theory of Solids*, 2nd ed.; Cambridge University Press: Cambridge, 1972, pp 211–230.
- (142) Herring, C.; Vogt, E. *Phys. Rev.* **1956**, *101*, 944–961.
- (143) Harris, S., *An Introduction to the Theory of the Boltzmann Equation*, 1st ed.; Dover books on physics; Dover Publications: New York, 2004, pp 121–130.
- (144) Singh, J., *Modern Physics for Engineers*; John Wiley & Sons, Ltd: 1999; Chapter Appendix B, pp 353–363.
- (145) Ashcroft, N. W.; Mermin, N. D., *Solid State Physics*; Holt-Saunders: 1976, pp 323–324.
- (146) Harrison, W. A. *Phys. Rev.* **1956**, *104*, 1281–1290.
- (147) Dirac, P. A. M. *Math. Proc. Cambridge Philos. Soc.* **1939**, *35*, 416–418.
- (148) Beleznay, F. B.; Bogar, F.; Ladik, J. *J. Chem. Phys.* **2003**, *119*, 5690–5695.
- (149) Maior, R. M. S.; Hinkelmann, K.; Eckert, H.; Wudl, F. *Macromolecules* **1990**, *23*, 1268–1279.
- (150) Hotta, S.; Rughooputh, S. D.; Heeger, A. J.; Wudl, F. *Macromolecules* **1987**, *20*, 212–215.
- (151) Hotta, S.; Soga, M.; Sonoda, N. *Synth. Met.* **1988**, *26*, 267–279.
- (152) Tsai, E. W.; Basak, S.; Ruiz, J. P.; Reynolds, J. R.; Rajeshwar, K. *J. Electrochem. Soc.* **1989**, *136*, 3683–3689.
- (153) Kim, H.; Lee, J.; Ahn, H.; Kim, O.; Park, M. J. *Nat. Commun.* **2015**, *6*, 7278.

- 
- (154) Nasir, M.; Teh, G. *Eur. Polym. J.* **1988**, *24*, 733–736.
- (155) Flory, P. J.; Rabjohn, N.; Shaffer, M. C. *J. Polym. Sci.* **1949**, *4*, 435–455.
- (156) Krejsa, M. R.; Koenig, J. L. *Rubber Chem. Technol.* **1993**, *66*, 376–410.
- (157) Barai, P.; Mistry, A.; Mukherjee, P. P. *Extreme Mech. Lett.* **2016**, *9*, Mechanics of Energy Materials, 359–370.
- (158) Waluś, S.; Offer, G.; Hunt, I.; Patel, Y.; Stockley, T.; Williams, J.; Purkayastha, R. *Energy Storage Mater.* **2018**, *10*, 233–245.
- (159) Vikramaditya, T.; Saisudhakar, M.; Sumithra, K. *J. Phys. Org. Chem.* **2015**, *28*, 695–702.
- (160) Mehmood, U.; Al-Ahmed, A.; Hussein, I. A. *Renewable Sustainable Energy Rev.* **2016**, *57*, 550–561.
- (161) Tokuda, T.; Hoshino, K. *Polym. J.* **2016**, *48*, 1141–1149.
- (162) Aasmundtveit, K.; Samuelsen, E.; Pettersson, L.; Inganas, O.; Johansson, T.; Feidenhans'l, R. *Synth. Met.* **1999**, *101*, 561–564.
- (163) Lebert, J.; Kratzer, E. M.; Bourdick, A.; Coric, M.; Gekle, S.; Herzig, E. M. *ACS Omega* **2018**, *3*, 6388–6394.
- (164) Rudyak, V. Y.; Gavrilov, A. A.; Guseva, D. V.; Tung, S.-H.; Komarov, P. V. *Mol. Syst. Des. Eng.* **2020**, *5*, 1137–1146.
- (165) Johansson, E.; Larsson, S. *Synth. Met.* **2004**, *144*, 183–191.
- (166) Franco-Gonzalez, J. F.; Zozoulenko, I. V. *J. Phys. Chem. B* **2017**, *121*, 4299–4307.
- (167) Shi, W.; Zhao, T.; Xi, J.; Wang, D.; Shuai, Z. *J. Am. Chem. Soc.* **2015**, *137*, 12929–12938.
- (168) Kuzmany, H.; Kürti, J. *Synth. Met.* **1987**, *21*, 95–102.
- (169) McMahon, D. P.; Cheung, D. L.; Goris, L.; Dacuña, J.; Salleo, A.; Troisi, A. *J. Phys. Chem. C* **2011**, *115*, 19386–19393.
- (170) Noriega, R.; Rivnay, J.; Vandewal, K.; Koch, F. P.; Stingelin, N.; Smith, P.; Toney, M. F.; Salleo, A. *Nat. Mater.* **2013**, *12*, 1038–1044.
- (171) Bonart, R.; Hosemann, R.; McCullough, R. *Polymer* **1963**, *4*, 199–211.
- (172) Hindeleh, A. M.; Hosemann, R. *J. Phys. C: Solid State Phys.* **1988**, *21*, 4155–4170.
- (173) Abutaha, A.; Kumar, P.; Yildirim, E.; Shi, W.; Yang, S. W.; Wu, G.; Hippalgaonkar, K. *Nat. Commun.* **2020**, *11*, 1–8.

- (174) Rivnay, J.; Noriega, R.; Northrup, J. E.; Kline, R. J.; Toney, M. F.; Salleo, A. *Phys. Rev. B* **2011**, *83*, 121306.
- (175) Street, R. A.; Northrup, J. E.; Salleo, A. *Phys. Rev. B* **2005**, *71*, 165202.
- (176) Salleo, A.; Chen, T. W.; Völkel, A. R.; Wu, Y.; Liu, P.; Ong, B. S.; Street, R. A. *Phys. Rev. B* **2004**, *70*, 115311.
- (177) Nenashev, A. V.; Valkovskii, V. V.; Oelerich, J. O.; Dvurechenskii, A. V.; Semeniuk, O.; Reznik, A.; Gebhard, F.; Baranovskii, S. D. *Phys. Rev. B* **2018**, *98*, 155207.
- (178) Luo, C.; Kyaw, A. K. K.; Perez, L. A.; Patel, S.; Wang, M.; Grimm, B.; Bazan, G. C.; Kramer, E. J.; Heeger, A. J. *Nano Lett.* **2014**, *14*, 2764–2771.
- (179) Wang, Z.; Song, X.; Jiang, Y.; Zhang, J.; Yu, X.; Deng, Y.; Han, Y.; Hu, W.; Geng, Y. *Adv. Sci.* **2019**, *6*, 1902412.
- (180) Lenz, J.; Weitz, R. T. *APL Mater.* **2021**, *9*, 110902.
- (181) Kumari, N.; Pandey, M.; Nagamatsu, S.; Nakamura, M.; Pandey, S. S. *ACS Appl. Mater. Interfaces* **2020**, *12*, 11876–11883.
- (182) Xiao, X.; Wang, Z.; Hu, Z.; He, T. *J. Phys. Chem. B* **2010**, *114*, 7452–7460.
- (183) Wang, Y.; Li, M. *Curr. Opin. Electrochem.* **2022**, *33*, 100952.